MICROBUBBLE DRAG REDUCTION PHENOMENON STUDY IN A CHANNEL FLOW

A Dissertation

by

JOSE ALFREDO JIMENEZ BERNAL

Submitted to the Office of Graduate Studies of
Texas A&M University
in partial fulfillment of the requirements for the degree of

DOCTOR OF PHILOSOPHY

August 2004

Major Subject: Mechanical Engineering

MICROBUBBLE DRAG REDUCTION PHENOMENON STUDY IN A CHANNEL FLOW

A Dissertation

by

JOSE ALFREDO JIMENEZ BERNAL

Submitted to Texas A&M University
in partial fulfillment of the requirements
for the degree of

DOCTOR OF PHILOSOPHY

Approved as to style and content by:

Yassin A. Hassan (Co-Chair of Committee)	Denis Phares (Co-Chair of Committee)
Kalyan Annamalai (Member)	William Marlow (Member)
Dennis O'Neal (Interim Head of Department)	

August 2004

Major Subject: Mechanical Engineering

ABSTRACT

Microbubble Drag Reduction Phenomenon Study in a Channel Flow. (August 2004)

Jose Alfredo Jimenez Bernal, B.S., Acapulco Institute of Technology (Mexico);

M.S., National Polytechnic Institute (Mexico)

Co-Chairs of Advisory Committee: Dr. Yassin A. Hassan
Dr. Denis Phares

An experimental study on drag reduction by injection of microbubbles was performed in the upper wall of a rectangular channel at Re = 5128. Particle Image Velocimetry measurement technique (PIV) was used to obtain instantaneous velocity fields in the x-y plane. Microbubbles, with an average diameter of 30μm, were produced by electrolysis using platinum wires with a diameter of 76 μm. They were injected in the buffer layer producing several different values of local void fraction. A maximum drag reduction of 38.45% was attained with a local void fraction of 4.8 %. The pressure drop in the test station was measured by a reluctance pressure transducer. Several parameters such as velocity profile, turbulent intensities, skewness, flatness, joint probability density function (JPDF), enstrophy, one and two-dimensional energy spectra were evaluated. The results indicate that microbubbles reduced the intermittency of the streamwise fluctuating component in the region near the wall. At the same time they destroy or reduce the vortical structures regions (high shear zones) close to the wall. They also redistribute the energy among different eddy sizes. An energy shift from larger

wavenumbers to lower wavenumbers is observed in the near wall region (buffer layer). However, outside this region, the opposite trend takes place. The JPDF results indicate that there is a decrease in the correlation between the streamwise and the normal fluctuating velocities, resulting in a reduction of the Reynolds stresses. The results of this study indicate that pursuing drag reduction by injection of microbubbles in the buffer layer could result in great saving of energy and money.

The high wavenumber region of the one dimensional wavenumber spectra was evaluated from PIV spatial information, where the maximum wavenumber depends on the streamwise length (for streamwise wavenumber) of the recorded image and the minimum wavenumber depends on the distance between vectors. On the other hand, the low wavenumber region was calculated from the PIV temporal information by assuming Taylor's frozen hypothesis. This new approach allows obtaining the energy distribution of a wider wavenumber region.

ACKNOWLEDGMENTS

I would like to thank my advisor and committee Co-Chair, Dr. Yassin A. Hassan, for his guidance whenever requested and his patience, knowledge, and enthusiasm during the development of this project. I would also like to thank Dr. Denis Phares (Co-Chair), and my other committee members, Dr. Kalyan Annamalai and Dr. William Marlow. Thanks are also due to my friends and fellow graduate students, Elvis Efren Dominguez-Ontiveros, Carlos Estrada-Perez, and Juan Gabriel Barbosa-Saldaña. I want to thank my fellow graduate student and wife, Claudia del Carmen Gutierrez Torres, for her support, love, dedication, motivation, and patience. Thanks are due to my parents, Tomas Jimenez Vazquez and Maria Asuncion Bernal Ortega for their unconditional love and motivation. Thanks to my mother in law, Concepcion Torres Garcia, for her friendship and for giving birth to my lovely wife.

I want to thank Mexican National Polytechnic Institute (Instituto Politecnico Nacional) for its support during my studies.

I also want to thank ANUIES (Asociacion Nacional de Universidades) for sponsoring my studies.

TABLE OF CONTENTS

LIST OF FIGURES

FIGURE Page

FIGURE Page

FIGURE Page

FIGURE Page

FIGURE Page

FIGURE Page

CHAPTER I

INTRODUCTION

1.1 Motivation

Everyday, energy is used for keeping the motion of a fluid over a solid surface and moving a solid body through a fluid. Unfortunately, a great amount of it is spent on overcoming drag, which results in loss and degradation of energy. Therefore, a decrease of the drag could have a worldwide impact on environment and economy. The reduction of drag, which is a complex phenomenon, can be utilized in several engineering and industrial applications such as hydraulic machines, oil well operations, pumping systems, slurry pipeline systems, oil pipeline transport, automobiles, aircraft, submarines, ships, etc. Pursuing a better understanding of the drag reduction phenomenon could also allow the design of more efficient systems and faster transportation vehicles; it means that savings in fuel by doing the same work with less energy and a decrease of contaminant emissions due to less burning fossil fuels would be viable. According to Wood (2003) the transportation sector consumption exceeded the USA oil production by 85 % in 2002; this deficit is expected to be 140 % by 2020. Moreover, 25 % of the energy consumed in USA is used to overcome aerodynamic drag.

This dissertation follows the format and style of the *Journal of Fluid Mechanics.*

If aerodynamic drag were reduced by 50 %, yearly costs savings in the 30 billion dollar range could be obtained. These facts make drag reduction an attractive issue for research. Furthermore, there is not yet a unique theory that can describe this complicated phenomenon, despite the significant theoretical and practical studies of the last three decades.

1.2 Background

A drag force is produced in the direction of the flow when a fluid moves over a solid body, and it is the resultant of two forces. One is due to skin friction drag or friction drag, which is directly related to the wall shear stress; the other is the result of pressure drag, which is associated with the normal stresses. Skin friction, a consequence of the no-slip boundary on the surface, can be either laminar at low Reynolds numbers or turbulent at high Reynolds numbers (Bushnell & Moore 1991). Most of the practical situations where drag reduction could produce significant savings of energy and money take place in turbulent flow conditions. The total shear stress in a turbulent flow is higher than laminar and is defined as

$$\tau_{tot} = \tau + \tau_{turb} = \mu \frac{dU}{dy} - \rho \overline{uv} \qquad (1)$$

where y is the distance from the wall; U is the local mean velocity; μ is the absolute

viscosity or dynamic viscosity; $\overline{uv}$ is the Reynolds stress, and ρ is the density of the fluid.

The dynamics of the turbulence near the wall should be understood because turbulent boundary layer structures are responsible for most of the dissipation of energy. Furthermore, these structures can be incoherent and coherent (vortices), which lie down parallel and close to the wall. The coherent structures, oriented in the streamwise direction, account for 80% of the turbulent fluctuating energy (Lumley & Blossey 1998). They have a diameter in wall units that goes from 20 to 50 (Kim 2003) and are found in the buffer layer (y^+ = 10-50). Moreover, streaks of low and high velocity and high skin friction are also attributed to coherent structures.

Nature has been the most efficient in terms of energy consumption through the years. It is one of the main reasons that studies have performed to observe and carry out experiments with birds and free swimming aquatic animals such as squids, fishes and whales to elucidate how nature achieves drag reduction. For instance, sharks have small riblets (with parallel, converging and diverging patterns) on their skin, which are assumed to improve their swimming performance (Koeltzsch et al. 2002). Some other species also deploy roughness by projecting bands near the position of maximum body girth to ensure the presence of turbulent flow over the afterbody to avoid flow separation, which would increase the pressure drag. Furthermore, investigations indicate most fish slim, which contains high molecular weight polymer and surfactants, manifest a considerable drag reduction behavior with maximum effectiveness taking place close to the wall region. It suggests that drag reduction by addition of additives and surfactants

is present in nature (Bushnell & Moore 1991). Hence, it is clear that some of the technology applied to skin friction reduction can be identified in several natural systems.

1.3 Drag reduction techniques

Despite, most of the research related to drag reduction that has been carried out by academic institutions, industries and government agencies such as Defense Advanced Research Projects Agency (DARPA), the main dilemma is to take these techniques from the laboratory environment to practical systems and to clarify why and how drag reduction occurs.

The techniques to reduce skin friction drag are categorized as laminar flow control (delay of transition to turbulence) and reduction of friction drag in the boundary layer. They are also subdivided as active control when they involve energy consumption and passive control when they require no external activities.

Several hypotheses have been suggested to elucidate the decrease of drag. However, there is no consensus about one specific hypothesis that can clarify this phenomenon. A review of some experimental and numerical results about drag reduction by riblets, addition of polymers and microbubbles injection is reported below.

1.3.1 Drag reduction by riblets

There is no doubt about the applicability and effectiveness of riblets (Wilkinson et al. 1988; Jimenez & Pinelli 1997). However, the physics of the drag reduction mechanism

by this technique is not yet well understood and several approaches are still being developed to clarify it.

The use of riblets, which is a passive technique for turbulent drag reduction and enhancement of heat transfer, has been studied for more than two decades by several research groups. Riblets can have different shapes (V, U, and L-grooves, etc.) and have to be aligned with the flow direction. The most significant parameters to describe a riblet are spacing riblet (s), height of the riblet (h), and the spacing of the riblet in wall units, which is shown in the equation (2), where u_τ is the friction velocity and ν is the kinematic viscosity of the fluid.

$$s^+ = \frac{s u_\tau}{\nu} \tag{2}$$

The practical applicability of riblets was demonstrated by a rowing boat team in the Olympic Games in 1984 and in the America's cup in 1987; furthermore, swimming suits with riblets were used in the Olympic Games in 2000. Moreover, a flight test of an airbus aircraft with riblets in the fuselage and wings was carried out in 1989 with a net 2% of drag reduction (Karniadakis & Choi 2003).

Baron & Quadrio (1993) performed some experiments using V riblets (figure 1) in a wind tunnel with a length of 170 cm, a width of 30 cm and a height of 9.3 cm. The test section was located in the lower wall of the tunnel at 65 cm downstream of the leading edge. Experiments were carried out using smooth and V riblet surfaces, which have to be

flushed to the wall. The velocity was measured by a constant temperature hot wire anemometer with a sample frequency of 6.25 kHz during 30 seconds. The velocity of the air ranged from 0 to 20 m/s with s = 0.07 cm. The best performance of the riblets was achieved at $s^+ = 12$ for a skin friction reduction of 6 percent. The turbulent intensity with riblets is lower than without them and the maximum value of the turbulent intensity is achieved about $y^+ = yu_\tau/\nu \approx 10$.

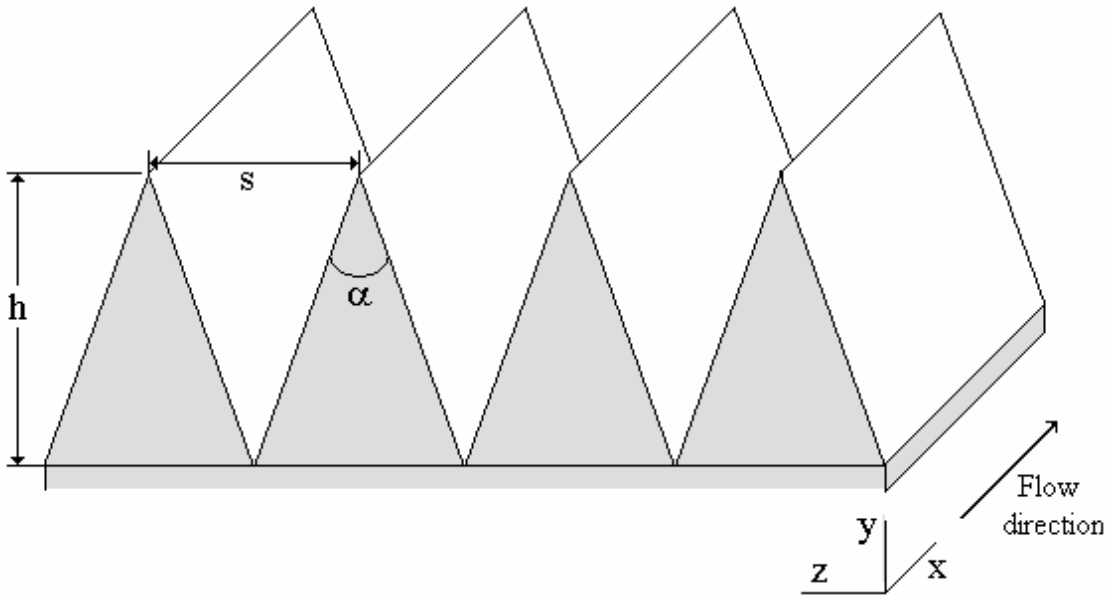

FIGURE 1. Parameters for V-riblets.

Choi & Orchard (1997) performed an experiment in the lower wall of a flat plate with a width of 51 cm and a length of 250 cm. The plate was located inside a low speed wind

tunnel with a total length of 300 cm. This investigation is very interesting; because both an increase in heat transfer and a drag reduction effect took place at the same time. A constant heat flux was transmitted at constant temperature to the test plate, which was situated at 190 cm far from the leading edge of the flat plate; the longitudinal pressure gradient at this region was nearly zero. The V-riblets, which are shown in figure 1, were mounted with the peaks flushed with the surrounding flat plate. Riblets with an s/h =1 and s = 0.183 cm were tested using a free stream velocity of 250 cm/s. Not only an increase of 10 % in the heat transfer coefficient, but also a roughly 6 % of drag reduction was observed. Furthermore, the turbulent intensity profile for the riblets case is lower than without them, and in both cases the maximum value was reported for $y^+ = yu_\tau/\nu = 13$ (where y is the distance from the wall). Turbulent energy of the spectra showed a reduction at almost the whole frequency range, when riblets are present. The velocity information was obtained from a boundary layer type hot wire probe that operates at constant temperature (Dantec 55P15); it has a platinum wire with a length of 0.125 cm and a diameter of 5 mm.

A study was performed in a Plexiglas flat plate with a length of 240 cm, a width of 18 cm and 1 cm thick (Wang et al. 2000). The plate was located in an open channel with 18 cm wide, 22.5 cm high and 300 cm long. The test station, which was located at 68 cm downstream the leading edge of the flat plate, was machined with spaced V type riblets whose dimensions are s = 0.2 cm and h = w = s/2. Figure 2 displays the parameters of this kind of riblet. The velocity measurements were obtained by Laser Doppler Velocimetry (LDV) technique along the center lane of the test station. A tripping rod

(figure 3) was situated at 10 cm downstream the sharp leading edge to reduce the distance to get fully developed flow in the test station. Water was run over the flat plate at 17.5 cm/s. The turbulent intensity profile with riblets was higher than without them. Furthermore, it was reported that the thickness of the viscous layer for the plate with riblets was larger than for the plate without them; no difference was reported for the evaluation of both skewness and flatness between the plate with riblets and the plate without them.

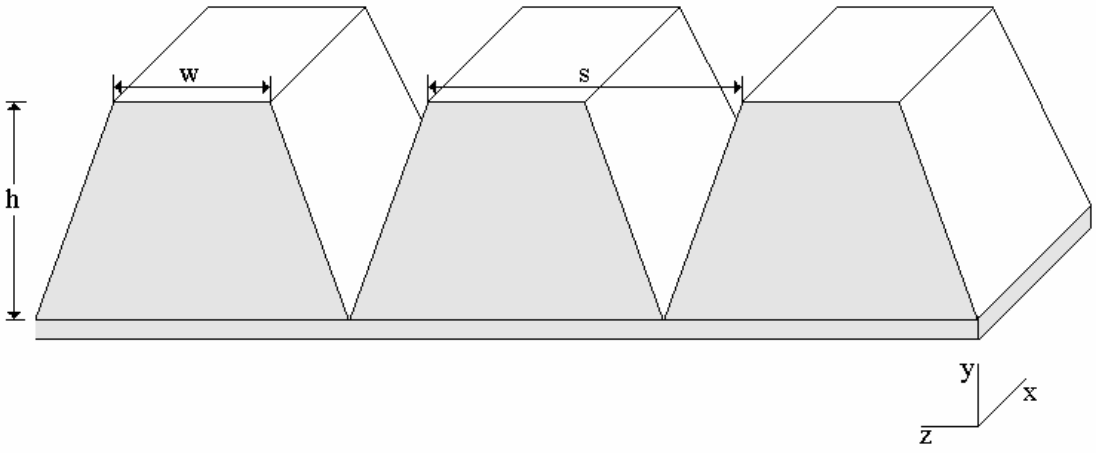

FIGURE 2. Parameters of V-space riblets.

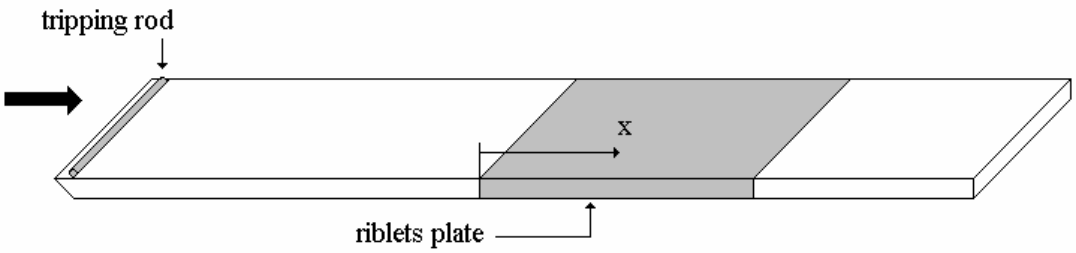

FIGURE 3. Location of the tripping wire and the riblets.

Bechert et al. (1997) tested several regular configurations to elucidate how drag reduction by riblets can be improved. In their experiments, baby oil was flown through a rectangular channel with a width of 25 cm and a height of 85 cm. A shear stress balance was used to measure the shear stress at the wall. The results for the **V** riblet shape with $\alpha = 60^{o}$ and s =3.034 mm indicated that the maximum drag reduction around 5% was attained at $s^{+} \approx 15$. However, for an $\alpha = 90^{o}$ the maximum drag reduction was lower than 4 % and was roughly maintained in a range from $s^{+} \approx 17$ to 24. Moreover, an increase of drag was reported after $s^{+} \approx 28$ for $\alpha = 60^{o}$ and $s^{+} \approx 34$ for $\alpha = 90^{o}$. For the semicircular scalloped with increase groove depth and with h/s = 1, t/s = 0.018 where t is ridge width, and s = 0.4 cm, the maximum drag reduction was around 6 % for $s^{+} \approx 14$; for h/s = 0.7, t/s = 0.035, and s = 0.631 cm the highest drag reduction was about 6.5 % at $s^{+} \approx 15$; h/s = 0.7, t/s = 0.015 and s = 0.34 cm the greatest drag reduction was approximately 7.5 % for $s^{+} \approx 14$. Bechert et al. (2000) also tested the channel with an array of three dimensional trapezoidal riblets, which occupied 64 % of a test plate with dimensions 40 cm x 50 cm; this array is illustrated in figure 4. In this experiment, a maximum drag reduction of 6.89 % was achieved for the following conditions t = 0.01 cm, a = 0.23 cm, w/s = 1.5, h/s = 0.3, $\alpha = 45^{o}$, s = 0.46 cm and $s^{+} \approx 28$. Likewise, the greatest value of drag reduction obtained for t = 0.01 cm, a = 0.46 cm, w/s = 2, h/s = 0.4, $\alpha = 45^{o}$, s = 0.46 cm and $s^{+} \approx 20$ was 7.29%. Finally, the highest value for the t = 0.01 cm, a = 0.92 cm, w/s = 3, h/s = 0.85, $\alpha = 45^{o}$, s = 0.46 cm and, $s^{+} \approx 16$ was 6.85 %. It was reported that two dimensional riblets could produce larger drag reduction than three dimensional riblets.

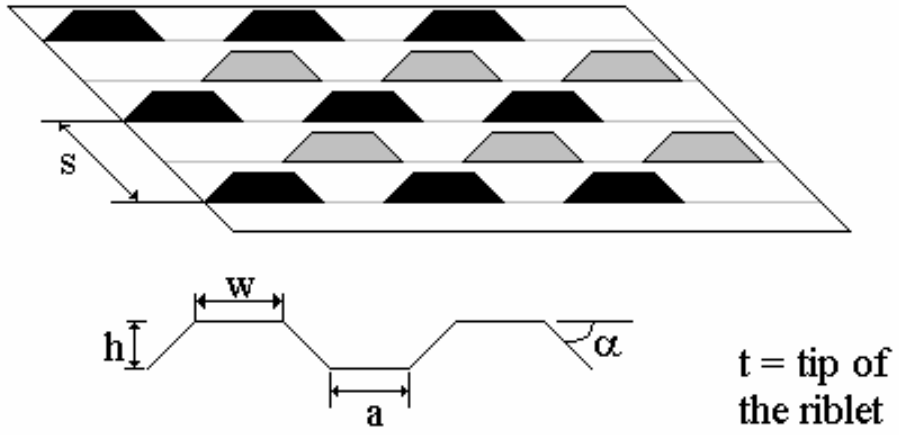

FIGURE 4. Configuration of the array of 3-D trapezoidal riblets.

Experiments with semicircular riblets were carried out in a closed type subsonic wind tunnel by Lee & Lee (2001). A sharp flat plate with a length of 620 cm was installed in the test section of a wind tunnel. Roughness elements were situated at 50 cm downstream the leading edge of the flat plate to get a fully developed flow at the measurement station, which is located at 541 cm downstream the leading edge. The measurements are performed in two exchangeable plates with 30 cm wide and 60 cm long, one of them is smooth and the other has riblets. The plate with riblets was aligned to the flat plate by using the virtual origin of the riblets. They have semicircular grooves with an s = 0.3 cm. Moreover, instantaneous velocity fields in y-z plane (vertical plane) with an area of 6.75 x 6.75 mm^2 were obtained by Particle Image Velocimetry (PIV) measurement technique. Their PIV system was in general composed of an Nd:YAG laser with a maximum frequency of 40 Hz (width pulse about 7ns, and approximately 25

mJ/pulse), and high speed CCD camera (model speed-cam+) with a frame rate from 31-1000 frames per second and a resolution of 512 x 512 pixels. The thickness of the laser light sheet was 4 mm. The measurements were taken at two free stream velocities (3 and 5 m/s). A reduction of drag was reported at the lowest velocity with $s^+ = 25.2$. However, the opposite trend occurred for the highest velocity at $s^+ = 40.6$.

1.3.2 Drag reduction by addition of polymers

Modification of the boundary layer structure can produce a significant reduction of skin friction on laminar and turbulent flows by the addition of insoluble particles or fibers and soluble long chain polymers or association colloids (White & Hemmings 1976). Although, most of the experimental and numerical studies that have been carried out for more than half of a century have been focused on addition of polymers, the physical mechanism of this method is not yet completely comprehended. However, good agreement is observed for the evaluation of some statistical parameters such as Reynolds stress and root mean square of the fluctuating velocities in a turbulent flow by all investigations (Warholic et al. 1999).

According to White & Hemmings (1976) the first study on drag reduction by additives can be attributed to Hele-Shaw, who in 1897 was investigating the skin friction on marine animals. He added bile to water in order to investigate the slime of fishes. The observations from his flow visualization indicated that skin friction was reduced. Lumley (1969) reported that several polymers could be added to different fluids to

obtain a decrease of drag for instance polyisobutyline (PIB) in cyclohexane and in benzene, polymethacrylate (PMM) in toluene, polyethylene oxide (PEO), which is uncomplicated to manipulate in water.

Toms (1977) conducted in 1946 one of the most famous experiments, which practically started the modern era of drag reduction by addition of polymers. His flow apparatus consisted of a tube that was fitted between two glass aspirator jars; the fluid was moved from one jar to the other by creating a pressure gradient (ΔP) between them. ΔP was created by maintaining one of the jars at atmospheric pressure while reducing the pressure in the other. Both jars were submersed in a water tank to maintain constant temperature (25^{o} C). A U mercury manometer was used to measure the pressure. At the beginning of each test ($\Delta P = 0$) the jars were half their capacity. The amount of flow was evaluated taking the time the solution spends to go from one jar to the other. From the experiments it was concluded that Newtonian fluids leave the laminar region at $2000 < Re < 4000$. On the other hand the conclusion about polymer solution reducing the drag was achieved because the rate of flow at constant pressure was increased as the concentration of polymer was increased.

Warholic et al. (1999) reported an investigation on drag reduction by addition of Percol 727 (Copolymer of polyacylamide and sodium acrilate). This study was conducted on a channel with a length of 1100 cm, a height of 5.1 cm, and a width of 61 cm; several polymer concentrations (from 5 to 200 ppm) were studied. Moreover, a Validyne pressure transducer (DP103) was used to measure the pressure drop (Δp) with polymer and without polymer over a distance (Δx) of 154 cm. These Δp values were

used to evaluate the wall shear stress τ_w as

$$\tau_w = -\frac{\Delta p}{\Delta x} H \tag{3}$$

where H is half height of the channel. Furthermore, measurements of two components of the velocity at different distances from the wall were performed at fully developed flow by LDV. The results for a drag reduction lower than 35 % can be summarized as follow. The root mean square of the fluctuating velocities (turbulent intensities) is made dimensionless by the friction velocity; it was observed that the streamwise turbulent intensity is increased as drag reduction increment from 14 to 33 %. The opposite trend is observed for the normal component. The Reynolds Stresses are made dimensionless by τ_w, and show a decrease when the drag reduction increased. The average stress that was assumed to be added by polymer had a positive value in the viscous sublayer. However, it reduced drastically above y/H = 0.2.

Another set of experiments for drag reduction by addition of Percol 727 was also carried out in the channel described above, but in this case PIV measurement technique was used to measure instantaneous velocity fields in the x-y and x-z planes (Warholic et al. 2001). The PIV system was composed of a pulsed ruby-laser with energy of 1 J/pulse, a CCD camera with a resolution of 256 x 256 pixels; the time difference between pulses was 4 μs and a cylindrical lens was used to transform the beam of laser-light into a sheet of light with a thickness of 1mm. Streamwise turbulent intensity profiles increased when the drag reduction augments. However, after y/H ≈ 0.5 the opposite trend occurs.

Normal turbulent intensity profile decreases when the drag reduction increases for the whole range of y/H. The Reynolds stress decreased as the drag reduction is incremented. A reduction of the burst production was observed when drag reduction is present; it can be interpreted as the turbulence production close to the wall is being diminished by the addition of the polymers.

1.3.3 Drag reduction by injection of microbubbles

Attempting to reduce drag of water vehicles by air injection is not new. Several patents were granted by the end of the 19th century and beginning of the 20th century; most of them consisted in placing an air film between the hull and the boundary layer (Latorre 1997). However, the first study on drag reduction in the United States of America (USA) by injection of bubbles was reported by McCormick & Bhattacharya (1973). This experiment was carried out in a fully submersed axisymetric body of revolution (SABR) with a length of 91.44 cm and a maximum diameter of 12.7 cm. The total drag force was measured by a dynamometer that was mounted to the SABR. Hydrogen bubbles were produced by driving an electrical current through a wrapped wire (0.6 cm in diameter) to the SABR, the mass rate of hydrogen produced by electrolysis was evaluated as

$$\dot{m}_H = 7.11x10^{-10}\left(\frac{IW}{Z}\right) \tag{4}$$

where I is the applied electrical current in amperes, W and Z are the atomic weight and valence number of the gas, respectively. For Hydrogen W = 1.008 and z = +1. The bubbles were injected beneath the boundary layer, and a maximum total drag reduction of approximately 30 % was measured. The total drag reduction was lower at higher Reynolds number. The drag reduction could be imputed to the decrease of the viscosity near the wall, which could also stop the transmission of the small viscous shear stresses from the turbulent region of the boundary layer to the wall. The size of the bubbles was not reported on this study.

Experimentation about drag reduction by saturating the boundary layer with bubbles was performed in a plate and in the initial channel section in the former USSR (Bogdevich et al. 1977). The plate had a length of 95.5 cm, width of 24.4 cm, and a thickness of 4 cm. The bubbles were produced by injecting air through a porous aluminum plate that was flushed 8 cm downstream the leading edge of the plate. The skin friction was measured by probes with floating surface elements. A gas bubble concentration was estimated by probes sensitive to the medium electrical conductivity. The pressure fluctuations measurements were accomplished by a probe with sensitive piezoceramics element with a diameter of 0.14 mm. If the void fraction is kept constant, the drag reduction increased when the Reynolds number was augmented. Moreover, when the void fraction increased so did the drag reduction until a maximum value was achieved; after that maximum value of void fraction the opposite trend is observed. The same shape and location of the peak value for the distribution of the bubbles were observed at different void fractions.

Experiments were carried out at the top and bottom of a rectangular test section (length of 76.2 cm and a cross section of 50.8 cm x 11.4 cm) of a water channel by Madavan et al. (1984). Laser Dopler anemometer (LDA) technique was used to measure velocity profiles. Microbubbles were produced by driving air into a sintered stainless steel plate and injected in the boundary layer. A floating element force balance was used for the integrated skin friction evaluation, and a flush mounted hot film probe was used to measure the local skin friction. The skin friction reduction in the bottom wall is less than in the upper wall at low velocities. This performance could be originated by buoyancy effects, because at higher velocities the buoyancy effects can be neglected. The maximum integrated skin friction reduction was more than 80 %. Differences of the velocity and turbulent intensities with and without bubbles are slight outside the boundary layer. It was reported that microbubbles modify only the boundary layer. Moreover, spectra results showed that there is a shift of the turbulent energy toward lower frequencies when the bubbles are introduced in the boundary layer; this loss of high frequency can be interpreted as a decrease in the turbulent Re due to the decrease of density and increase of viscosity of the air.

The mixing length model was used was used in a numerical study for drag reduction by microbubbles (Madavan et al. 1985). During the analysis, the viscosity and density were locally changed as a function of a trapezoidal concentration profile. Two mathematical models were used to evaluate the viscosity with microbubbles; they are reported in equation (5) and equation (6), where μ' is the viscosity of the liquid-bubble mixture, μ is the viscosity of the liquid, and ϕ is the bubble concentration in the

boundary layer.

$$\mu' = \mu(1 + 2.5\phi) \tag{5}$$

$$\mu' = \frac{\mu}{1 - 1.09\phi^{1/3}} \tag{6}$$

A maximum drag reduction of 50 % was obtained in this numerical study and it was shown that the skin friction depends on the concentration, location, and distribution of the bubbles in the boundary layer. The bubbles are most efficient when they are located in the buffer layer. They can also maintain the reduction of skin friction over long distances if remained in the boundary layer. The void fraction was observed to decrease in the streamwise direction.

Experiments were carried out using an axisymmetric body (AB) with a length of 63.2 cm and diameter of 8.9 cm; it was totally submerged in a water tunnel with a diameter of 305 mm (Deutsch & Castano 1986). Velocities profiles measurements were done by Laser Doppler Velocimetry (LDV) measurement technique. A wire with a diameter of 0.035 cm was located 4.6 cm downstream the leading edge of the AB in order to trip the boundary layer and reduce the distance to get fully developed flow. A force balance was used to evaluate the integrated skin friction. Injection of helium and air were tested separately to elucidate which of them is more effective to reduce the skin friction. Maximum 80% integrated skin friction reduction by injection of helium was measured at high velocities. The greatest value of drag reduction by injection of air was 55 % and

was obtained at low velocities. These results shown that the increase of drag reduction by injection of helium (about 80 %) is larger than that by injection of air (about 40%) at the highest mean velocity. However the opposite performance is observed at the lowest velocity (15 % for helium and 20 % for air). Both size and distribution of the bubbles were not reported on this work.

A test was conducted by Lance & Bataille (1991) in a bubbly flow, which was developed in vertical channel with a length of 200 cm and a square cross section of 45 x 45 cm. A grid constituted of 260 equally spaced injectors of air with 0.08 cm in diameter was located perpendicular to the streamwise direction of the flow. This grid helped to obtain isotropic turbulence. The size of the bubbles was measured photographically and the mean equivalent diameter of the bubbles was about 0.5 cm. The void fraction, ranges from 0 to 0.5, was evaluated by optical probe that is able to sense the variation of the optical index of the medium. The measurements of the velocity fluctuations were obtained from hot-film and laser Doppler anemometry. The isotropy was practically not altered with the increase of the void fraction. Energy of the higher frequency of the spectra without bubbles is lower than with a void fraction of 1.9 %. However, the opposite trend is observed in the lower frequency range.

Kato et al. (1994) conducted some experiments in water tunnel, which had a test section with a rectangular cross section (12 cm x 5 cm) that was located in the bottom wall of the channel. LDV was used as a measurement technique and a mixture of both water and air was injected within the boundary layer to reduce the drag by a slit in the surface. It was reported that the bubbles decrease their drag reduction effect when the

amount of injected water in the mixture was increased. Finally, the disadvantage of this technique to reduce the drag is due to the high energy consumption of the mixture and injection of air-water in the boundary layer.

Guin et al. (1996) carried out some experiments in a water channel with an aspect ratio equal to 10. Bubbles were produced by injecting air through porous plates, which were flushed to the upper and bottom walls of the channel, they were located at 60 channel height downstream the channel inlet. The void fraction was measure by a fiber optic probe and a sort of isokinetic sampling probe. The shear stress with bubbles and without bubbles was measured by a floating element transducer. The injection of bubbles in the upper wall produced a maximum drag reduction about 20 %. However, when the bubbles were injected in the bottom wall the maximum drag reduction was about 14 %.

A valuable approach was suggested by Fontaine et al. (1999) by injecting micro bubbles with homogeneous polymer and surfactant solutions. They run some experiments in axisymmetric body with a length of 63.2 cm and a diameter of 8.9 cm. A wire with a diameter of 0.035 was located at 4.6 cm form the leading edge of the body to assure fully developed flow in the test section. Measurements of integrated skin friction were obtained from a force sensor, which was located at 19.6 cm from the leading edge of the body. The measurements were performed for a combination of homogeneous polymer, surfactants and microbubble. It was observed that the reduction of drag for a combination of polymer and microbubbles was greater than that obtained for polymer or microbubbles alone. A drag reduction higher than 80 % was measured with a polymer concentration of 20 ppm and 10 m^3/s of gas. It was concluded that polymers probably

modify the turbulence close to the wall in such way that the effectiveness of the microbubbles was increased. Furthermore, it was observed that reducing the bubble size by the addition of a surfactant did not modify the characteristics of drag reduction by microbubbles.

Kodama et al. (2000) reported some experimental results, which were obtained in a water channel flow whose test section length, height, and width were 300 cm, 10 cm and 1.5 cm, respectively. The bubbles were produce by flowing air through a porous plate, which is located in the upper wall of the channel at 103.8 cm downstream the inlet of the channel. The skin friction was measured with bubbles and without bubbles by a skin friction sensor at three different positions in the streamwise direction. Measurements at three different positions and velocities (5, 7, and 10 m/s) were reported. When the void fraction was increased so was skin friction reduction. Furthermore, the maximum skin friction reported was 30 %.

A numerical investigation was conducted by Kanai & Miyata (2001) to clarify the interaction between wall turbulence and bubbles. Two computational domains of 1 x 1 x 1 and 2 x 1 x 2 in the x, y, and z directions were used for a turbulent Poiseuille flow under gravitational force and for a turbulent Couette flow, respectively. In the former, when the bubbles were present in the buffer layer, it was observed that the fluctuations of the streamwise velocity were decreased, and the velocity profile was modified. For the turbulent Couette flow, a peak was observed in the distribution of the bubbles at $y^+ = 18$ when drag reduction occurred, and the velocity profile was also altered by the presence of the bubbles. Moreover, a reduction of the bursting process was observed.

CHAPTER II

EXPERIMENTAL SET UP AND PIV SYSTEM

This section describes the experimental setup where the measurements were carried out, the calibration, synchronization, and the basics of the Particle Image Velocimetry (PIV) measurement technique, which was used to measure instantaneous velocity fields close to the upper wall of a turbulent water channel. Furthermore, the pressure drop measurement in the test station and the electrolysis production array that was used to produce the microbubbles are described.

2.1 Test facility

The experiments were carried out in a flow test facility, which was constituted by a rectangular channel as shown at figure 5. The channel has a length of 483 cm, a width of 20.5 cm and a height of 5.6 cm; it was built with Plexiglas due to the optical properties of this material. Water was pumped from the lower tank to the upper tank by 3 pumps with power consumptions of 1/6, 1/4, 1/2 HP, respectively. The upper tank was designed to have a constant pressure head, which provides a constant rate flow for the channel. The flow of water was controlled by two globe valves and one butterfly valve. Water, flowed through the channel by gravity to avoid the flow oscillations of the pumps, was quantified by two digital turbine flow meters (GPI, 0-50 GPM) and a float meter or more often called rotameter (Dwyer, 0-10 GPM).

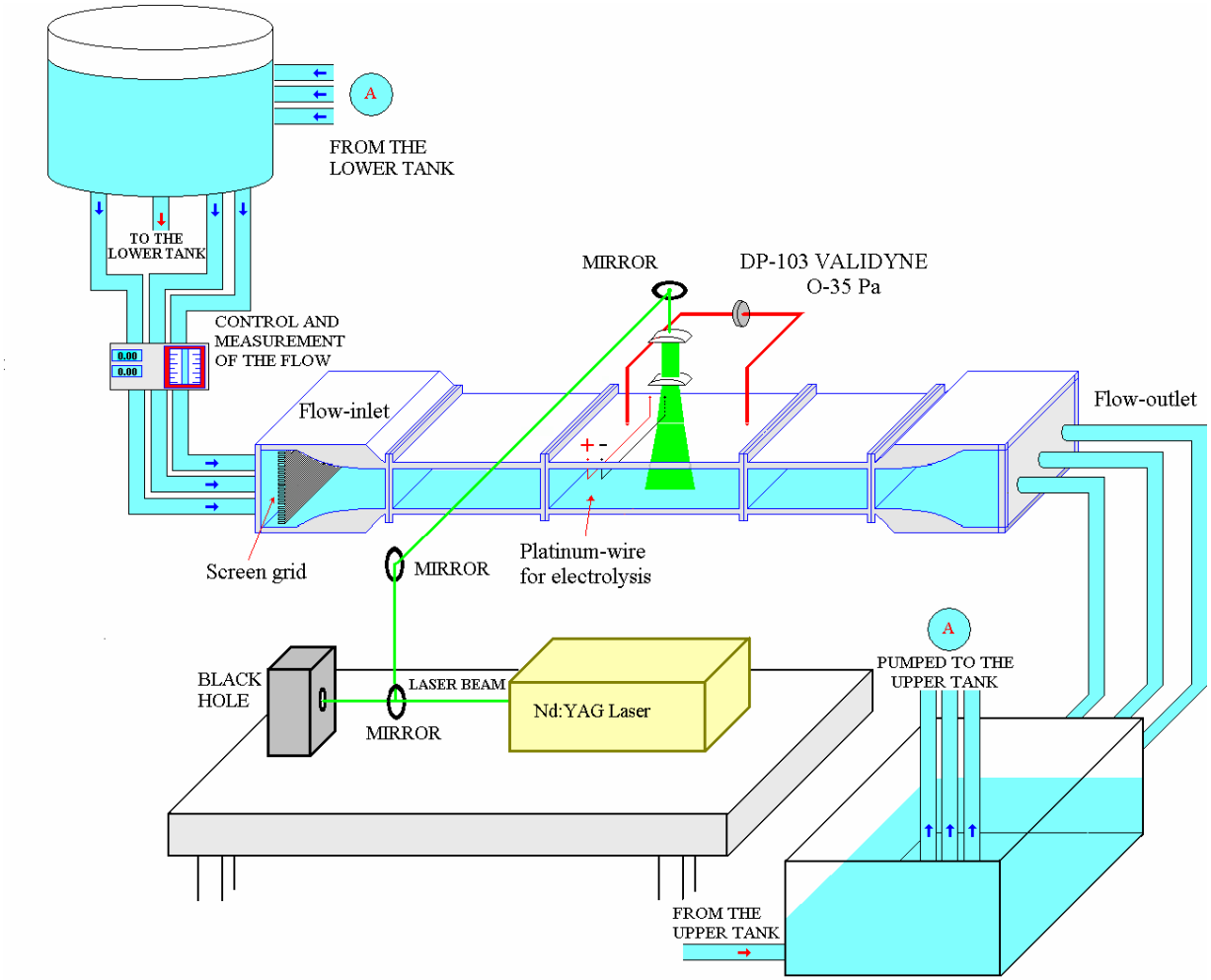

FIGURE 5. Schematic diagram of the experimental set up.

A honeycomb and a screen grid with an array of 400 equally spaced holes with a diameter of 0.4 cm and a length of 1cm was placed at the inlet of the channel to flat the velocity profile, to reduce the distance to attain fully developed flow, and to get rid of the bigger vortices that are created in the inlet of the channel. The water flow was seeded by polystyrene neutrally buoyant particles with a diameter that goes from 6 to 9 μm, and a density of 1.050 g/cm^{-3}. These particles can reflect enough light to be detected by the CCD (Charge Couple Device) camera; they were injected and mixed thoroughly in the lower tank before turning the pumps on. Through the entire experiment the particles were assumed to follow the flow. The channel was filled slowly to avoid pulverizing trapped air in the flow that occurred when the channel was filled rapidly. Henceforward, the flow conditions were adjusted by the valves.

2.2 Microbubble production

Most of the bubbles production methods reported in the literature have been chiefly focused on porous media plates and electrolysis. While there is a lot of information about evaluation of total void fraction and distribution of the bubbles, there is a lack of information about the size of bubbles and their exact location in the turbulent boundary layer. In this experiment, an in-house arrangement to generate microbubbles by electrolysis was developed; the configuration is constituted of two parallel platinum wires with a diameter of 76 μm, which are used as cathode an anode, respectively. They are parallel and separated each other by a distance 2.54 cm. The anode is located at 10

cm upstream the test station and 0.5 cm far from the upper wall. The cathode is separated 1 cm far from the wall. This array was proposed to inject the majority of the microbubbles in the buffer layer. The ratio between the distance from the closest wire to test station and the wire diameter is equal to 1315. Hence, the wire effect on the test station can be neglected. Furthermore, an electrical current of 25 mA was driven through the wires to break up the water molecules to produce microbubbles of hydrogen and oxygen, and an average diameter of 30 μm was observed for the former.

2.3 Pressure measurements

Measurements of the pressure drop in the streamwise direction are mandatory during the study of near wall turbulence and drag reduction. This parameter is very important to evaluate the shear stress at the wall and subsequently the total shear stress. The former will allow the estimation of the friction velocity, which is the near wall scaling parameter. The experiments were run at a low Reynolds number, $Re = U_bH/\nu = 5128$ (considering half height of the channel, the kinematic viscosity of water and the bulk velocity). At low Reynolds number, the pressure drop is very small and consequently very difficult to measure. Fortunately, there was in the market a reluctance differential pressure transducer (Validyne DP-103), which was able to measure a pressure drop range from 0-35 Pa. This device was installed in the upper wall of the channel, two 1/8 “ NPT holes were drilled with a depth of 0.75 times the thickness of the wall. Soon after, one hole of 1/32’’ of diameter was perforated in the center of each hole through the wall

as shown in figure 6; the holes were separated by a distance of 154 cm. Then, an acrylic pipe with a diameter 1/4'' was installed from the pressure transducer to the holes mentioned above by fast fitting connectors, which facilitated the dismounting and assembling of the device.

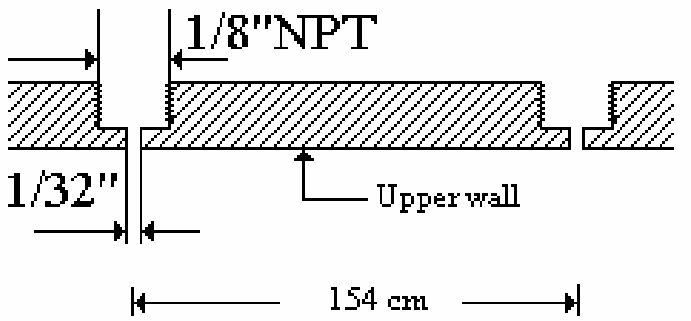

FIGURE 6. Description of the holes to connect the pressure transducer.

2.4 Particle Image Velocimetry (PIV)

Most of the instantaneous flow information reported in drag reduction studies has been acquire in the vicinity of the wall, which is the region that has to be studied to clarify this phenomenon. It is also clear that detailed qualitative and quantitative data are necessary in order to obtain better conclusion about the properties of the flow. Several techniques such hot film or hot-wire anemometry, Doppler Velocimetry (LDV) or Laser Doppler Anemometry (LDA), and Particle Image Velocimnetry (PIV) have

been used to measure instantaneous velocities.

Hot-wire and hot-film are one-point intrusive measurement techniques, which are able to measure the velocity fluctuations at one point. It is assumed that there is a relationship between the heat removed from the wire by convection and the velocity of the fluid. This technique can be also very accurate and suitable even to measure the components of the velocity at two different points at the same instant, which allows the evaluations of statistics that can not be obtained from on point measurements. Several precautions, such as maintaining constant fluid temperature, avoiding impurities in the fluid that can damage or adhere to the wire, and keeping the wire free of bubbles in a bubbly flow have to be taken. If a velocity field wants to be obtained the probe has to be located at different positions, which is an extremely time consuming procedure. The sample frequency of this technique can be expressed in MHz.

LDA or LDV is a non intrusive measurement technique, which does not need calibration. The velocity is measured from the Doppler laser frequency shift in laser light scattered by the seeding particles in the flow. This is only a one point technique that offers the information covering an interval of time. A velocity field can be obtained by moving the measuring volume, which has the size of the region intersected by the laser beams. The frequency sample can be measured in kHz.

2.4.1 PIV basics

Particle Image Velocimetry (PIV), which is an optical and non-intrusive measurement

technique, has the extraordinary ability to measure instantaneous velocity fields. It allows the evaluation of invaluable information about spatial structures and properties of the flow such as velocity profiles, turbulent intensities, Reynolds stress, vorticity, enstrophy, spatial derivatives, etc. It is clear that PIV overcomes the other techniques mentioned above when spatial information is necessary. However, the temporal history of the flow is limited due to the kind of recording devices, and energy and frequency of the Laser used to illuminate the seeding particles. Optical access in perpendicular planes was required to place the sheet of light and the camera of the PIV system that was used to estimate instantaneous velocity fields in the x-y plane in this experiment.

The basic operation principle of this technique is described as follow. Lasers, which are used as source of illumination due to their emission of monochromatic light, produce a beam that is transformed into a sheet of light by an array of cylindrical lenses. This sheet of light illuminates a plane in the seeded flow. The scattered light from the seeding particles can be recorded in a photographical negative or in a CCD camera; the recording process can be performed in a single or double exposure mode.

While in the film camera the image need to be digitalized by a scanner and then saved in the computer for post processing, the CCD camera produces digitalized images that can be recorded directly in the computer as soon as they are taken.

The basic idea for measuring the velocity consists on evaluating the displacement Δx and Δy of the seeding particles in two consecutive frames, which are separated each other by a time Δt. It can be represented mathematically in the equation (7) and equation (8) and graphically in figure 7.

$$u = \frac{\Delta x}{\Delta t} \tag{7}$$

$$v = \frac{\Delta y}{\Delta t} \tag{8}$$

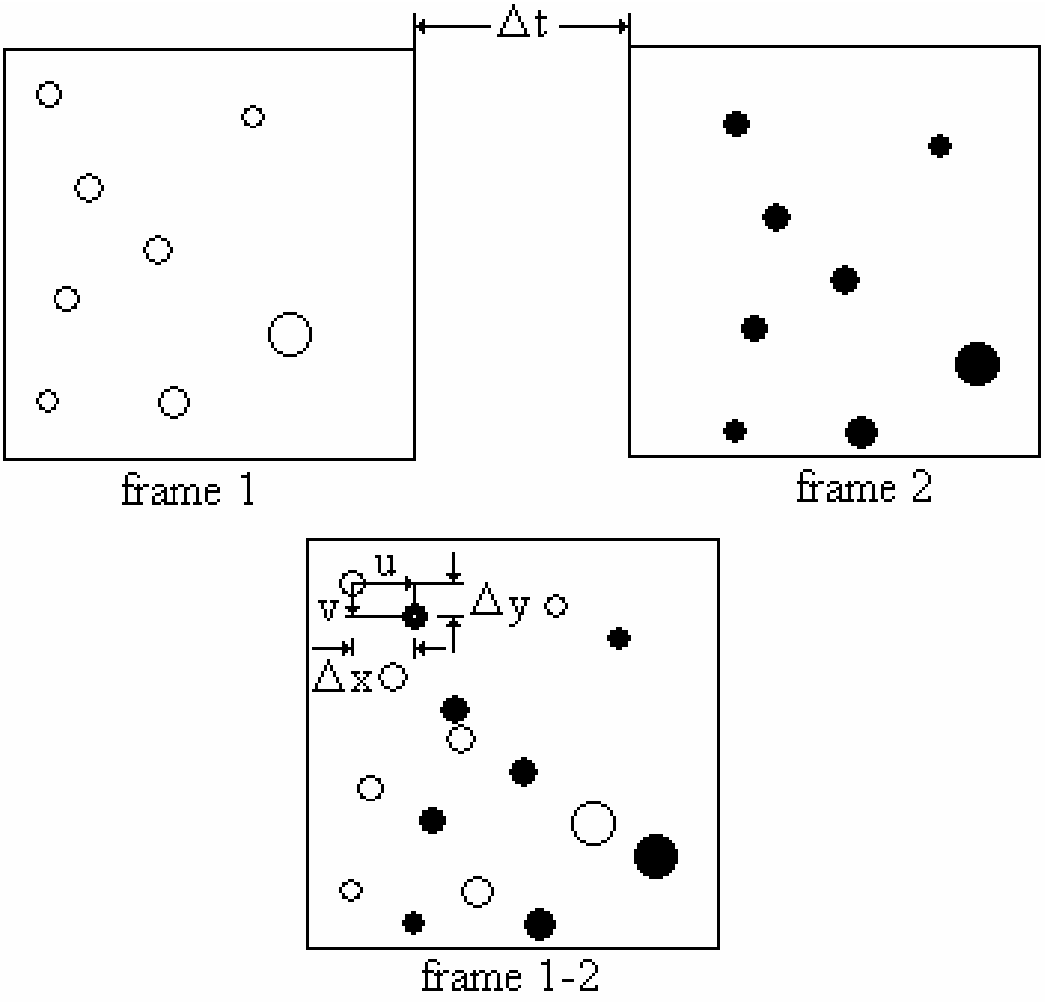

FIGURE 7. Graphic representation of the velocity of tracer particles.

2.4.2 PIV system

In this experiment, two hundred pictures per set were recorded by a CCD Kodak camera (model Megaplus ES 1.0/1.0) with a resolution of 1008 x 1018 pixels. The camera has the trigger double exposure capability, which permits measurements at high velocity flows. The seeded flow was illuminated by dual oscillator Nd:Yag laser with a power of 300-350 mJ/pulse and a wavelength of 532 nm (green light). The pulse duration was approximately 7 ns. The incident laser beam was transformed into a 1 mm thickness sheet of light by an array of cylindrical and spherical lenses.

Two successive images were necessary to obtain a velocity field by statistical methods; hence, one hundred velocity fields per set were obtained. The duration time between two consecutive pictures was 1 ms, and the time between velocity fields was 32 ms.

2.4.3 PIV synchronization

The commercial frame rate of the CCD camera was increased from 30 to 60 fps by doing a precise synchronization between the laser light pulsing and the double exposure capability of the CCD camera. A high accuracy pulse generator (Stanford Research System Inc., model DG535) with a four channel digital delay/pulse with an accuracy of picoseconds was used to synchronize the PIV system.

Two exposure times were used for the odd and even frames in order to attain the 60

fps, 0.128, and 32.4 ms, respectively. The diagram of the synchronization and timing used on this study is shown in figure 8.

2.4.4 PIV calibration

A calibration grid with adjacent white dots regularly divided, is located at the viewing plane, in order to obtain a scale for the physical measurement. This scale can also be obtained from the focal length, the angles and the distances, actual position of the lens plane, lens distortion. However, this approach is very complex because an exact knowledge of these parameters is necessary.

2.4.5 Image processing

Image preprocessing was indispensable to clear away the noise, background, and reflection effects that could provoke a mismatch of the seeding particles through consecutive frames. The illumination of the odd and even image may vary due to different exposure times (0.128 and 32.4 ms, respectively). The preprocessing of the odd and even images was made separately and can be summarized as follow. First, the original set of odd images was averaged. Second, the odd average image was subtracted from each original odd image of the set. Finally, the images from the subtracting process were equalized. The same procedure was applied to the even images.

After the preprocessing step the images were processed by two different particle

tracking software (PIV analysis process), which use a cross-correlation algorithm. One of the codes works on a windows platform and can use directly the images from the preprocessing process. Likewise, this code allows the user to have different image threshold and tracking parameter for each pair of images (Yamamoto et al. 2002). The second software is an in-house code (Hassan et al. 1992), which works on UNIX platform and need the images to be transformed to ASCII files before processing. This transformation was made by a program developed in Lab VIEW programming language.

The resulting velocity vectors from each application were compared, corrected and combined. This hybrid technique widely increment the number of vectors used for the flow field analysis. Moreover, the velocity vectors went through two separated filtering process. The first filter got rid of the vectors that had a lower cross-correlation value than the average value (~50% of the vectors). The second filter took away the vectors that were not within +/- standard deviation value of the magnitude and direction of the representative velocity vector within a small window (~20 X 20 pixels). About 40% of the initial vectors of each velocity field remain after performing the filtering processes. Then, the resulting vectors of both filtering process for each velocity field, are combined to get one single file, and compared to remove repeated vectors. The average number of velocity vector for each velocity field is about 1500 in an area of ~1.28 cm^2. Finally, these vectors are interpolated using the inverse distance algorithm in a window of 20 x 20 pixels to obtain 100 instantaneous velocity fields per set in an ordered grid of 50 x 50 vectors.

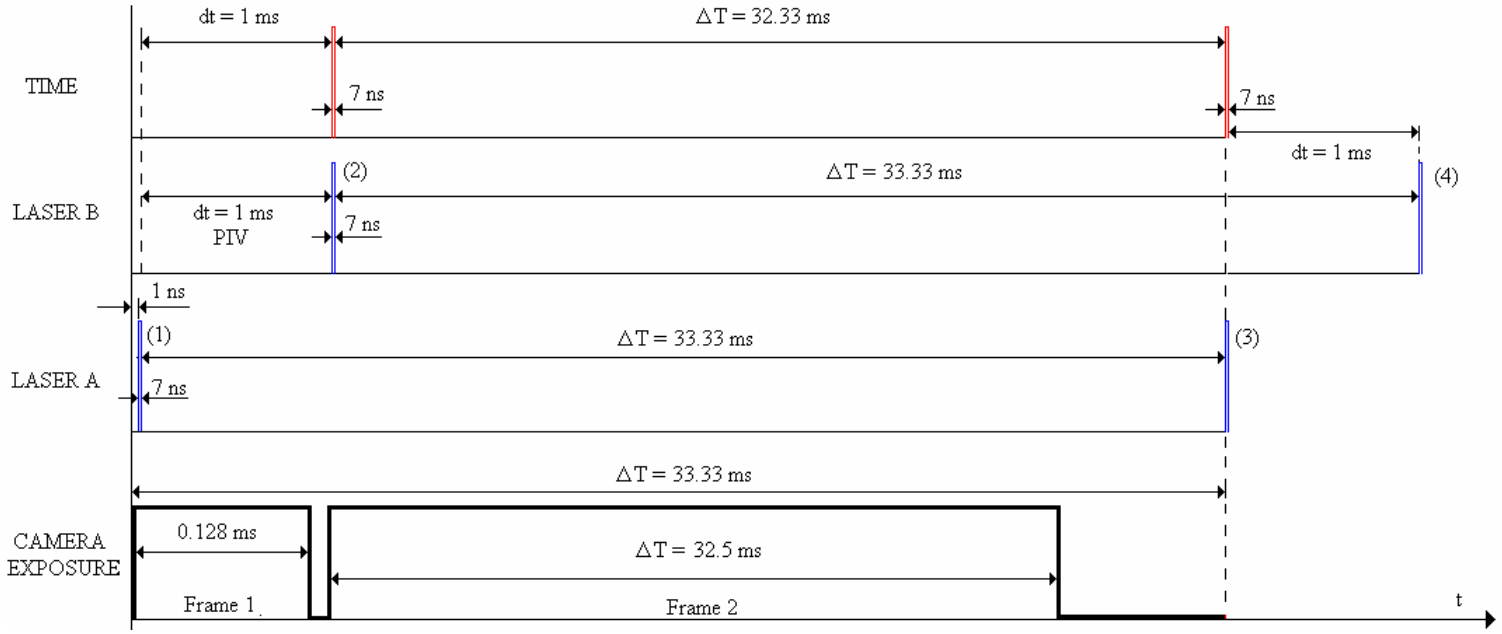

FIGURE 8. Schematic-diagram for the synchronization stage.

CHAPTER III

TURBULENT CHANNEL FLOW

Drag reduction by injection of microbubbles is a very complex phenomenon. It is very difficult if not impossible to obtain a deterministic model that can represent the whole physical mechanism due to the randomness of turbulence. Hence, statistical methods become the best option. In this study the evaluation of several statistical parameters with microbubbles and without microbubbles in a turbulent channel flow was performed. It allowed clarifying how the injection of microbubbles affects the turbulent intensity, skewness, flatness, vorticity, enstrophy, spectra, and probability density functions of the streamwise and normal fluctuating components of the velocity.

3.1 Equations of motion

There are two basic mathematical models that can attempt to describe the mean flow quantities of an adiabatic, incompressible, and Newtonian fluid. One is the conservation of mass equation also called continuity equation, which is represented by equation (9). The other is the Navier-Stokes (N-S) equation or momentum equation, which is described by equation (10), where $\tilde{u}_i$ is the instantaneous velocity component in the direction (x_i), $\tilde{p}$ is the instantaneous static pressure, ν is the kinematic viscosity, and ρ is the density of the fluid.

$$\frac{\partial \tilde{u}_i}{\partial x_i} = 0 \tag{9}$$

$$u_j \frac{\partial \tilde{u}_i}{\partial x_j} = -\frac{1}{\rho}\frac{\partial \tilde{p}}{\partial x_i} + \nu \frac{\partial^2 \tilde{u}_i}{\partial x_j^2} \tag{10}$$

3.2 Reynolds decomposition

It is frequently stated that turbulence is one of the great unsolved problems of classical physics (Nelkin 1992). Turbulent flows are ubiquitous and occur at high Reynolds numbers, they are characterized by high diffusivity and dissipation levels. Reynolds decomposition is a valuable approach during the analysis of turbulent flows; it splits up the instantaneous component of the velocity and the pressure into an average and a fluctuating part as shown at equation (11) and equation (12).

$$\tilde{u}_i = U_i + u_i \tag{11}$$

$$\tilde{p} = P + p \tag{12}$$

The average value of the velocity and pressure over an interval of time can be obtained from equation (13) and equation (14), respectively; the symbol < > means time average.

$$U = \frac{1}{T}\int_0^{\infty} \tilde{u}dt = <\tilde{u}> \tag{13}$$

$$P = \frac{1}{T}\int_0^{\infty} \tilde{p}dt = <\tilde{p}> \tag{14}$$

The time average of fluctuating quantities has to be zero (<u> = 0). It can is illustrated in figure 9. This evaluation has to be performed during the analysis of a turbulent flow to assure the measurements are right.

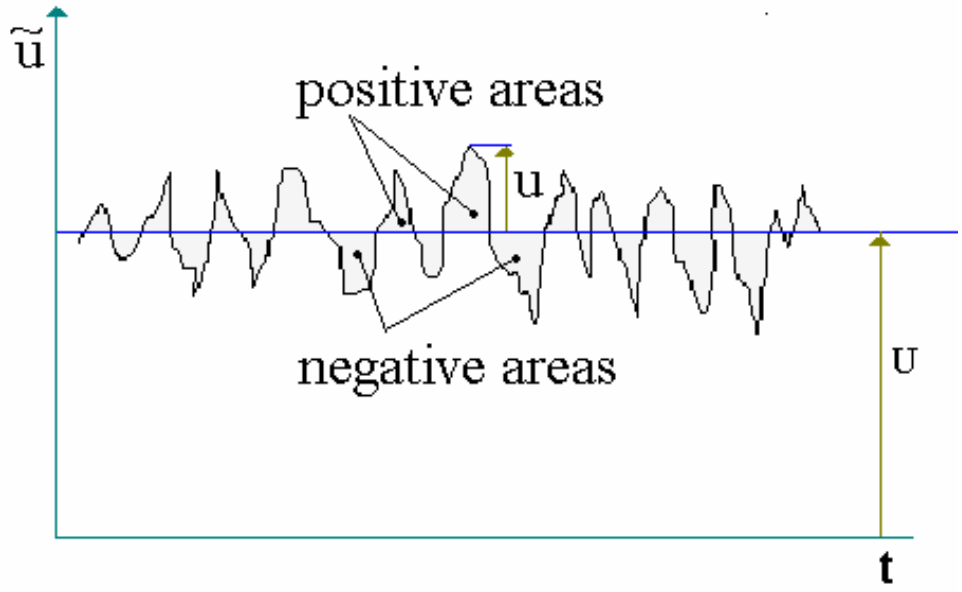

FIGURE 9. Components of the instantaneous velocity

Substituting equation (11) an equation (12) into equation (10), and making the time average leads to

$$U_j \frac{\partial U_i}{\partial x_j} = -\frac{1}{\rho}\frac{\partial P}{\partial x_i} + \frac{\partial}{\partial x_j}\left(\nu \frac{\partial U_i}{\partial x_j} - \overline{u_i u_j} \right) \tag{15}$$

The second term on the right hand of equation (15) represents the transport of momentum due to fluctuating velocities. The term $\overline{u_i v_j}$ is called the Reynolds shear stress, which is the contribution of the turbulent motion to the mean stress tensor. When the N-S equations are timed average information about the structures of the flow is lost and distilled in the Reynolds stresses, which are not known. It means that more unknowns have been produced during the time average process and the number of equations is insufficient to solve the system of equations (closure problem).

3.3 Turbulent quantities

Not only the role of near wall streamwise vortices has been found to be very important in the wall bounded turbulent flow but also downward sweep motion by streamwise vortices near the wall is closely correlated with skin friction (Choi et al. 2002). The study of the region close to the wall is very important to clarify skin friction reduction. Hence, the evaluation several near wall parameters with microbubbles and without microbubbles will allow a comparison, which would conduct to elucidate the

effect of the microbubbles in the drag reduction phenomenon.

The kinematic viscosity and the wall shear stress are the most important parameters near the wall region. They can help to scale several characteristics dimensions of turbulent flows. The wall shear stress can be represented by

$$\tau_w = \mu\left(\frac{dU}{dy}\right)_{y=0} \tag{16}$$

and practically evaluated by equation (3). For a channel flow, it is clear that τ_w is totally independent of the Reynolds stress, which is zero at the wall and at the center of a close channel. In a turbulent flow several scales exist; most of them are obtained by the friction velocity u_τ, which is also associated with the wall shear stress τ_w. The evaluation of the friction velocity can be done by equation (17), where ρ is the density of the fluid.

$$u_\tau = \sqrt{\frac{\tau_w}{\rho}} \tag{17}$$

Equation (18) and equation (19) represents the velocity U and the distance from the wall y in wall units, respectively. These dimensionless quantities have been used extensively in the literature to describe turbulent flows.

$$u^+ = \frac{U}{u_\tau} \tag{18}$$

$$y^+ = \frac{y\nu}{u_\tau^2} \tag{19}$$

There are several turbulent time scales in turbulent wall flows that can be evaluated. They are associated with the velocities and length scales of the flow. More energetic turbulent events are related with small time scales or small eddies. On the other hand, calm events tend to have longer time scales or big sizes (Christensen & Adrian 2002). The inner time scale which is associated with smaller eddies is defined by the equation (20) while the outer scale which is related to the bigger eddies is calculated by equation (21).

$$t^* = \frac{\nu}{u_\tau^2} \tag{20}$$

$$t_o = \frac{\nu}{u_\tau^2} \tag{21}$$

The evaluation of the time scale, velocity scale, length scale and dissipation of the smallest eddies is attributed to Kolmogorov. These scales are known as Kolmogorov scales and represented as follow.

$$\text{(Length scale)} \qquad \eta = \left(\frac{\nu^3}{\varepsilon}\right)^{1/4} \tag{22}$$

$$\text{(Velocity scale)} \qquad u_\eta = (\varepsilon\nu)^{1/4} \tag{23}$$

$$\text{(Time scale)} \qquad \tau_\eta = \left(\frac{\nu}{\varepsilon}\right)^{1/2} \tag{24}$$

$$\text{(Dissipation)} \qquad \varepsilon = \frac{\nu}{\tau_\eta^2} \tag{25}$$

According to Christensen & Adrian (2002) the last equation can be also approximated by

$$\varepsilon_B = \frac{U_{CL} u_\tau^2}{H} \tag{26}$$

where H is half height of the channel and U_{CL} is the center line velocity.

Statistical description of turbulence allows examining how fluctuations are distributed around an average value and how adjacent fluctuations (next to each other in time or space) are related (Tennekes & Lumley 1972). Statistical moments were evaluated for the instantaneous velocity fields obtained from PIV in this drag reduction study. The first moment corresponds to the mean value. The second moment is the variance or the square of the standard deviation; in fluid mechanics the root mean square (rms) is the

turbulent intensity. The third moment is known as skewness, and finally, the fourth moment is the flatness. Equations used to evaluate these parameters are depicted below.

$$U = \frac{1}{N}\sum_{i=1}^{N} \tilde{u} \tag{27}$$

$$\overline{u^2} = \frac{1}{N}\sum_{i=1}^{N} (\tilde{u} - U)^2 \tag{28}$$

$$u' = rms = \sqrt{\overline{u^2}} \tag{29}$$

$$S = \frac{1}{N\overline{u^2}^{3/2}}\sum_{i=1}^{N} (\tilde{u} - U)^3 \tag{30}$$

$$F = \frac{1}{N\overline{u^2}^{2}}\sum_{i=1}^{N} (\tilde{u} - U)^4 \tag{31}$$

3.4 Vorticity and enstrophy

Vorticity is a peculiarity of turbulent flows, which is directly related to the viscous effects and has dimensions of (sec^{-1}). It is also a well known that fluid particles can only

be set up in rotation by an unbalanced shear stress. Hence, vorticity is an indicator of body rotation. On the other hand, pressure forces and gravity forces act through the center of mass of a particle and can not produce rotation (Panton 1996). The vorticity of the small scales eddies is very much larger than that of the large-scale motion; it indicates that the small scale energy is little compared to the large scale energy. This is typical of all turbulence. Furthermore, most of the energy is associated with large scale motion and most of the vorticity is associated with small scale motion (Tennekes & Lumley 1972). The vorticity can be evaluated by equation (32), where V is the velocity vector.

$$\omega = \nabla x V \tag{32}$$

However, in this study of drag reduction there was only information to evaluate the spanwise vorticity. Hence, equation (32) becomes.

$$\omega_z = \left(\frac{\partial v}{\partial x} - \frac{\partial u}{\partial y} \right) \tag{33}$$

Several structures can be found in turbulent flows. They are present even in homogeneous and isotropic turbulence. However, not much information exists about their nature. The primary evidence is related to spatial localization of subregions with large enstrophy (Tsinober 2001). While the vorticity conserves the sign information, the enstrophy does not. It permits a better location of the turbulent structures in the spatial

domain. The enstrophy is defined as the dot product of the vorticity as shown in equation (34); it means that it is not a vector. It is one the parameters that highlights the power of the spatial resolution offered by PIV measurement technique compared with other one-point measurement techniques.

$$\text{Enstrophy} = \omega.\omega \tag{34}$$

3.5 Spectra

In a turbulent flow, there is a very complex phenomenon of transference of energy between eddies of different size. To explain this process is necessary to define an eddy as a spatial structure that lasts for a short period of time; it can be like a vortex, an imbedded jet, a mushroom shape, or any other recognizable form (Panton 1996). Furthermore, small eddies (small scales) exist inside larger eddies (large scales) and even smaller eddies subsist inside small eddies. Turbulence takes kinetic energy from the mean flow (turbulence production) at the largest eddies. Then, this energy is transferred by inviscid processes to smaller scales (inertial subrange) and so on until at the smallest scales the energy is dissipated by viscous action. The parameter that allows getting an idea of how eddies with different size exchange energy with each other is spectra. It can also be defined as a function that produces the total energy content when is integrated over all wavenumbers or over all frequencies.

Although turbulence is a three dimensional (3D) phenomenon, most of the spectra

evaluations reported in the literature have come from data measured by stationary one point measurements techniques (hot wire). First of all, the evaluation of a temporal correlation (autocorrelation) has to be performed as shown at equation (35). Then, the application of twice the Fourier transform to the autocorrelation gives the one-dimensional frequency spectra as illustrated in equation (36).

$$R(t') = u(t)u(t+t') \tag{35}$$

$$E(f) = 2\int_{-\infty}^{\infty} R(t')e^{-i2\pi ft'}dt' = 4\int_{0}^{\infty} R(t')e^{-i2\pi ft'}dt' \tag{36}$$

In the last two equations f represents the frequency in Hz, t is the time of the sample, and t' is the temporal increment that is analyzed.

PIV offers spatial information that allows the evaluation of spectra in the wavenumber domain. First of all, the calculation of a spatial correlation has to be performed as shown at equation (37). Then, the application of twice the Fourier transform to the spatial correlation gives the one-dimensional wavenumber spectra as illustrated in equation (36).

$$R(s_x) = u(x)u(x+s_x) \tag{37}$$

$$E(k_1) = 2\int_{-\infty}^{\infty} R(s_x)e^{-i2\pi k_1 S_x}\,ds_x = 4\int_{0}^{\infty} R(s)e^{-i2\pi k_1 S_x}\,ds_x \tag{38}$$

In the last two equations, k_1 represents the streamwise wavenumber, x is the streamwise direction, and s_x is the increment that is being analyzed.

To transform from frequency spectra to wavenumber spectra the assumption of Taylor's frozen hypothesis is necessary. This theory that regards a relationship between frequency and wavenumber spectra was developed by G. I. Taylor in 1938; he presumed that the changes in the streamwise fluctuating velocity with time at the fix measurement point could be due to the passage of a frozen pattern of turbulent motion past the point, provided that the mean (or free stream) velocity carrying the turbulent eddies was much larger than the turbulent fluctuations, which can interpreted as the velocity field at different instants could be related by the transformation portrayed in equation (39) and the local time derivative at a point could be replaced by the convective derivative as shown in equation (40) (McComb 1990).

$$u(x,t) = u(x - Ut,0) \tag{39}$$

$$\frac{\partial}{\partial t} = -U\frac{\partial}{\partial x} \qquad \text{if} \quad u << U \tag{40}$$

The transformation of the spectra from the frequency domain to the wavenumber

domain by assuming frozen Taylor's hypothesis can be performed by equation (41).

$$E(f) = UE(k_1) \tag{41}$$

In this study, one of the most important parameters that wase evaluated from the PIV's spatial information is the two dimensional spectra, which was calculated for the plane x-y. The two dimensional spectra is evaluated by equation (42), where k_1 and k_2 are the wavenumbers in the streamwise and normal direction, respectively. Furthermore, s_x and s_y corresponds to the increments analyzed in the respective direction (Geckinli & Yavuz 1983).

$$E(k_1, k_2) = \iint R(s_x, s_y) e^{-j(2\pi k_1 s_x + k_2 s_y)} ds_x ds_y \tag{42}$$

3.6 Joint probability density function

If u and v are assumed as variables with zero mean, the joint probality density function is proportional to the time that the moving point spends in a small window between u and u + Δu, v and v + Δv. The probability density function of u for a Gaussian distribution can be evaluated by the equation (43) as described by Pope (2000).

$$\mathrm{PDF}(u) = < \frac{1}{\sigma_u \sqrt{2\pi}} e^{0.5(u-a)^2/\sigma_u^2} > \tag{43}$$

In the equation (43), σ is the standard deviation, which was calculated by equation (44), where u is the fluctuating velocity, a represents the limit where u and v velocities are evaluated.

$$\sigma^2 = \frac{1}{N-1} \sum_{i=1}^{N} \left(\tilde{u}_i - U\right)^2 \tag{44}$$

CHAPTER IV

EXPERIMENTAL RESULTS AND ANALYSIS

Instantaneous velocity fields in the x-y plane were measured by Particle Image Velocimetry (PIV) measurement technique in the upper wall of a turbulent water channel flow at 315 cm downstream the inlet of the channel. The water was run through the channel at a Reynolds number, $Re = U_bH/\nu = 5128$. Electrolysis was used to produce microbubbles, which were injected in the boundary layer. Several low-local void fractions were tested. The use of low-local values of void fraction caused a decrease of undesirable speckles effects and an absence of extreme brightness provoked by high bubble saturation. Then, the uncertainty of the PIV measurements was reduced when the microbubbles were present.

4.1 Experimental results

Four different void fraction conditions were investigated. They were locally evaluated in a small control volume (CV) whose dimensions were the viewing area times the thickness of the laser sheet or 1.28 cm^2 x 0.1 cm. Microbubbles and tracer particles images were simultaneously recorded on the same frame at Re = 5128. The light reflection intensity of the microbubbles was higher than the correspondent to the tracer particles. Furthermore, the size of the bubbles was larger than the size of the tracer particles. A computer program was used to separate the bubbles from the tracer particles

(Hassan et al. 1992). The information of the bubbles was used to evaluate the gas volume in the measurement window. The hydrogen microbubbles that were produced by electrolysis had an average diameter about 30 μm. The values of friction velocity, average microbubble diameter, average microbubble diameter in wall units, void fraction, and drag reduction are reported in table 1.

		Re = 5128		
u_τ [mm/s]	10.88	10.6	9.7	9.1
d [μm]	30	30	30	30
d^+	0.33	0.31	0.29	0.27
α	2.38%	3.44%	4.4%	4.8%
DR	12.06%	16.6%	29.81%	38.45%

TABLE 1. Drag reduction values at Re = 5128 with various void fractions.

The average velocity distribution as function of the distance from the wall is an important characteristic of any turbulent flow. It is expected that the most significant changes will be observed in the region close to the wall due to the no-slip condition and viscous effects. Traditionally, most of the velocity profiles have been obtained using one fixed-point measurement techniques (hot-wire measurements). If a velocity field is required several sensors can be placed simultaneously in different points of the

measurement region or one sensor can be moved to different positions in the required measurement region at distinct times; this is a high time consuming task if a large velocity field is needed. However, PIV overcomes those difficulties because this measurement technique provides instantaneous velocity fields in a two dimensional plane. For instance, the velocity field of the average streamwise velocity in wall units for a single phase flow at Re = 5128 is illustrated in figure 10; it was obtained by averaging 100 velocity fields, which were separated each other by 32 ms.

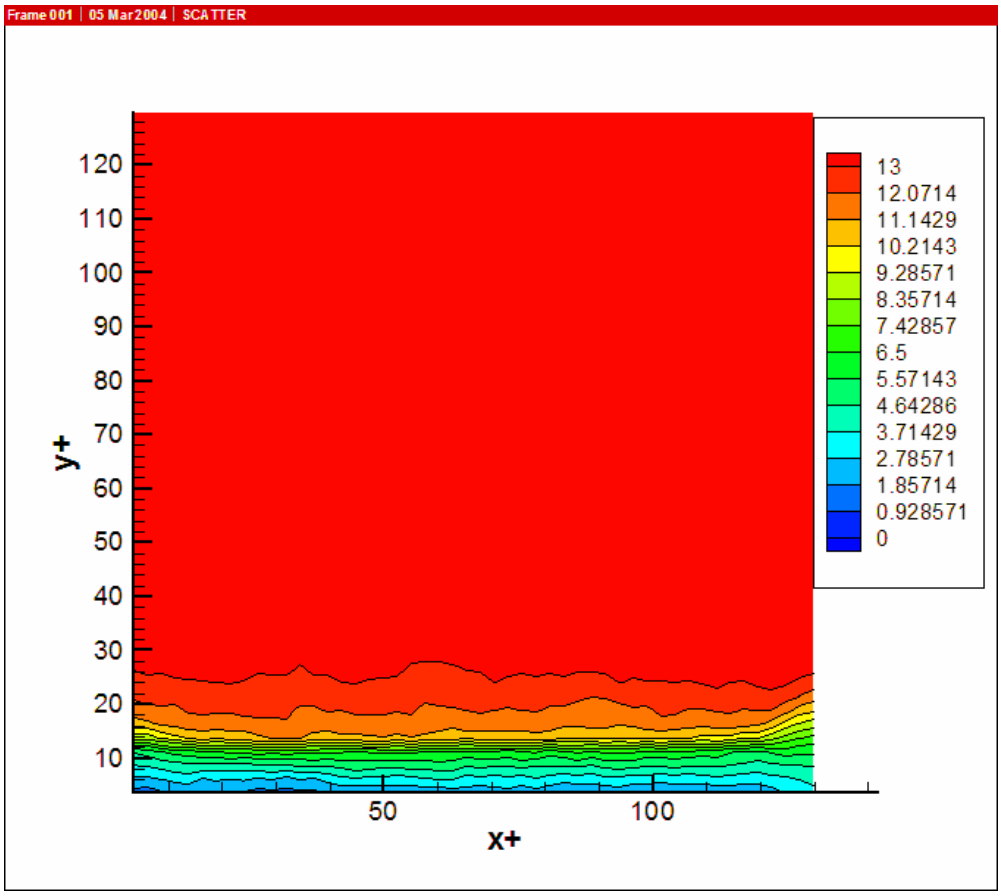

FIGURE 10. Streamwise velocity map for single phase flow in wall units.

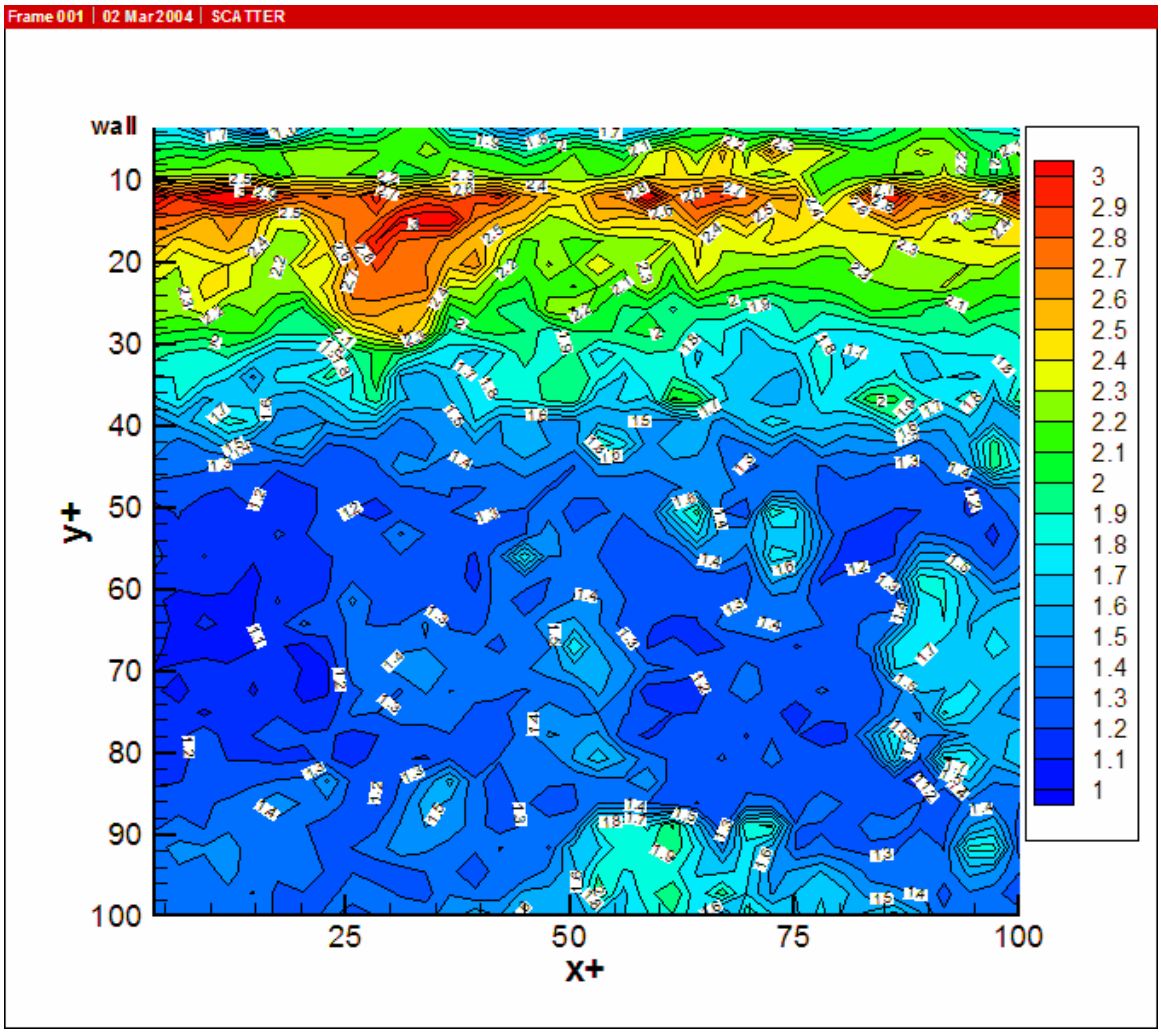

FIGURE 11. Turbulent intensity map for u fluctuating component (single phase).

The streamwise turbulent intensity (u') maps for single phase and for the maximum drag reduction are depicted in figure 11 and figure 12, respectively. They are made dimensionless by using the corresponding friction velocity. It is observed that the maximum value of u' for single phase occurs about $y^+ \approx 14$; a similar value was observed in other works (Günter et al. 1998; Warholic 1997; Warholic et al. 1999). The

values of u' for a maximum drag reduction of 38.45 % are larger than those of single phase flow.

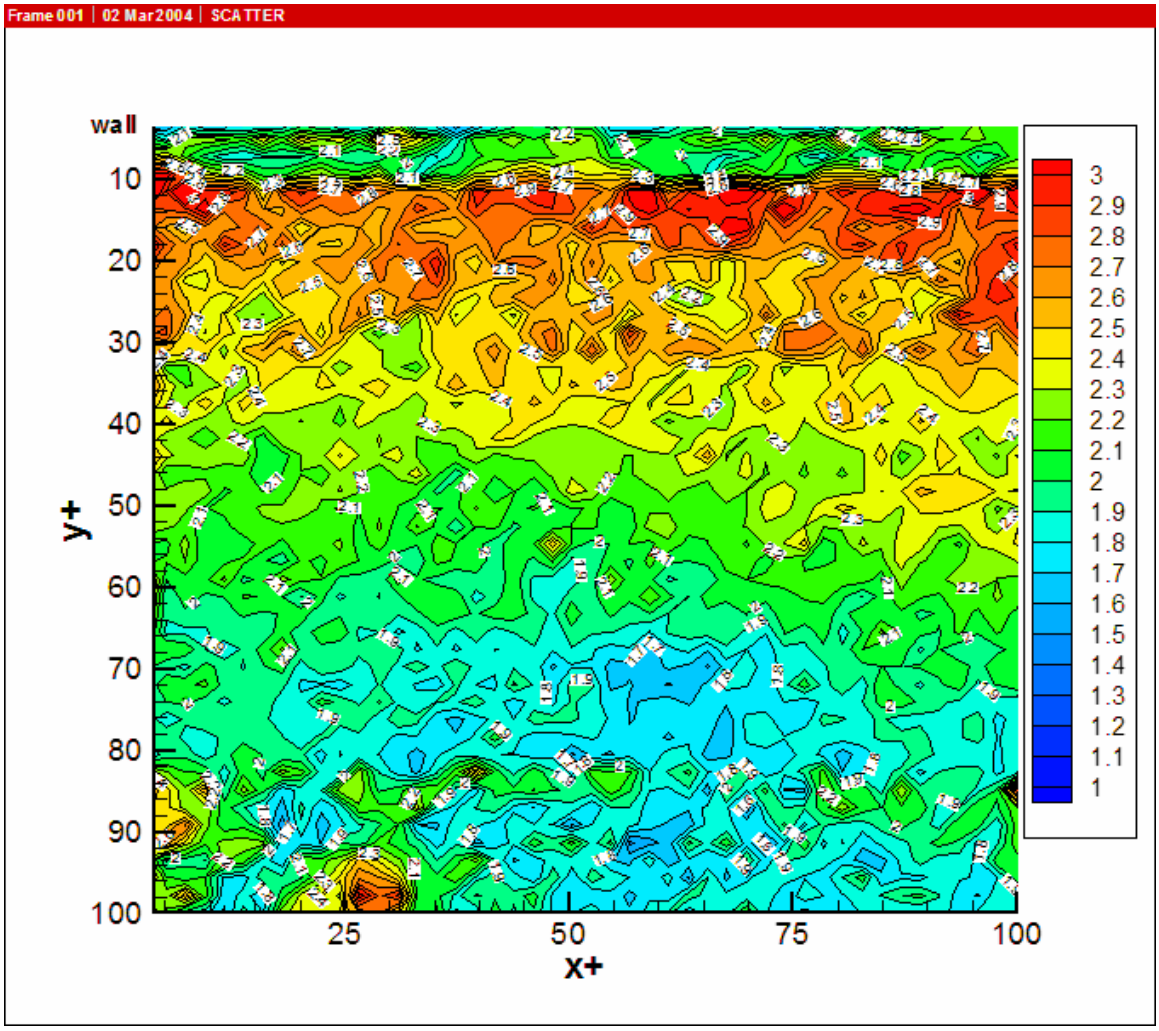

FIGURE 12. Turbulent intensity map for u fluctuating component (DR = 38.45 %).

The normal turbulent intensity (v') maps for single phase and for the maximum drag reduction (38.45 %) are depicted in figure 13 and figure 14, respectively. They are also

made dimensionless by using the corresponding friction velocity. It is observed that most of the maximum values of v' for single phase occurs about $y^+ \approx 70$; a similar value is observed in other works (Günter et al. 1998). The value of v' is increased for a drag reduction equal to 38.45 %. The changes of the turbulent intensity suggest that microbubbles produce a redistribution of the turbulent structures near the wall region.

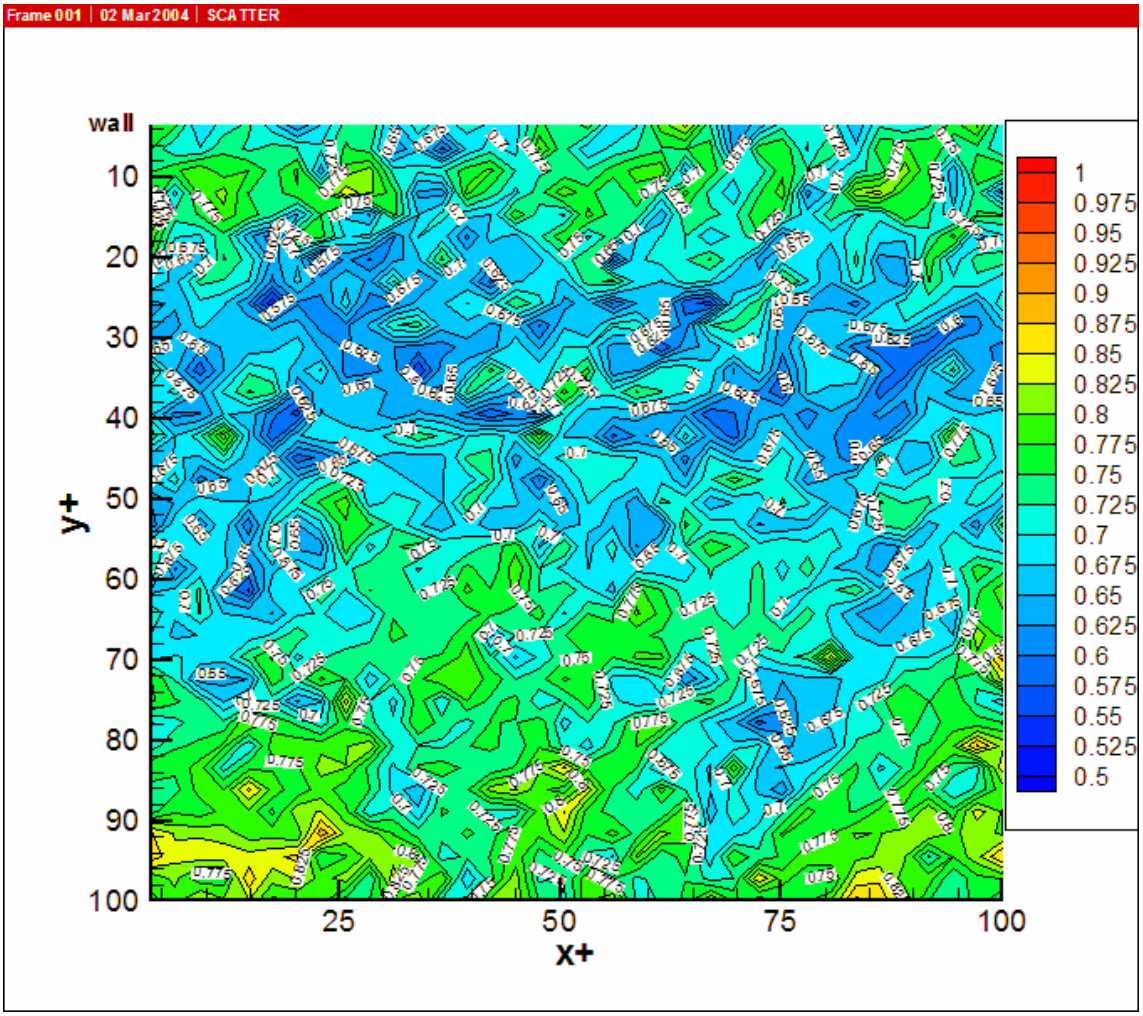

FIGURE 13. Turbulent intensity map for v fluctuating component (single phase).

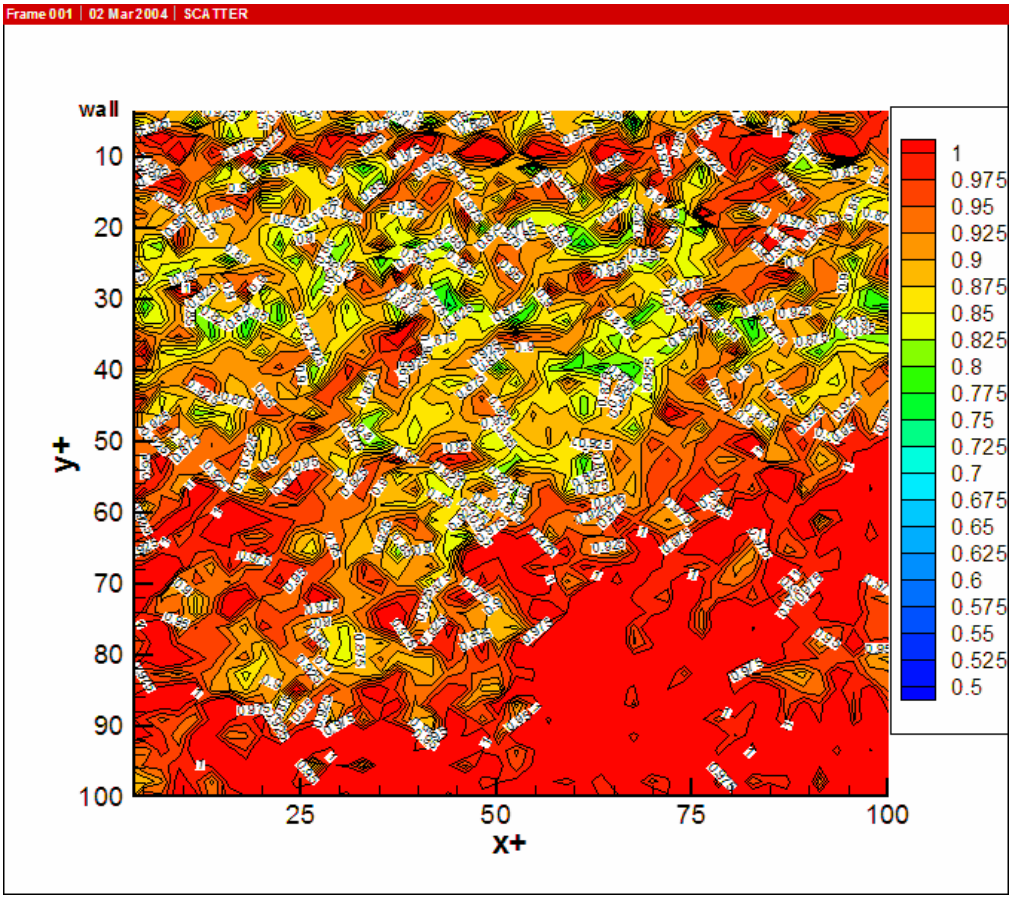

FIGURE 14. Turbulent intensity map for v fluctuating component (DR = 38.45%).

Higher order moments such as skewness (S) and flatness (F) must be evaluated to obtain more specific information about turbulence. They offer information about the intermittency of the variable that is analyzed. Skewness is the third order moment, which is used to describe the asymmetry of the probability density function. In this part of the study, skewness and flatness of the streamwise and normal velocity fluctuations were evaluated. When a signal is Gaussian the probability distribution has a probability distribution symmetric about the mean value with S = 0 and F = 3, respectively.

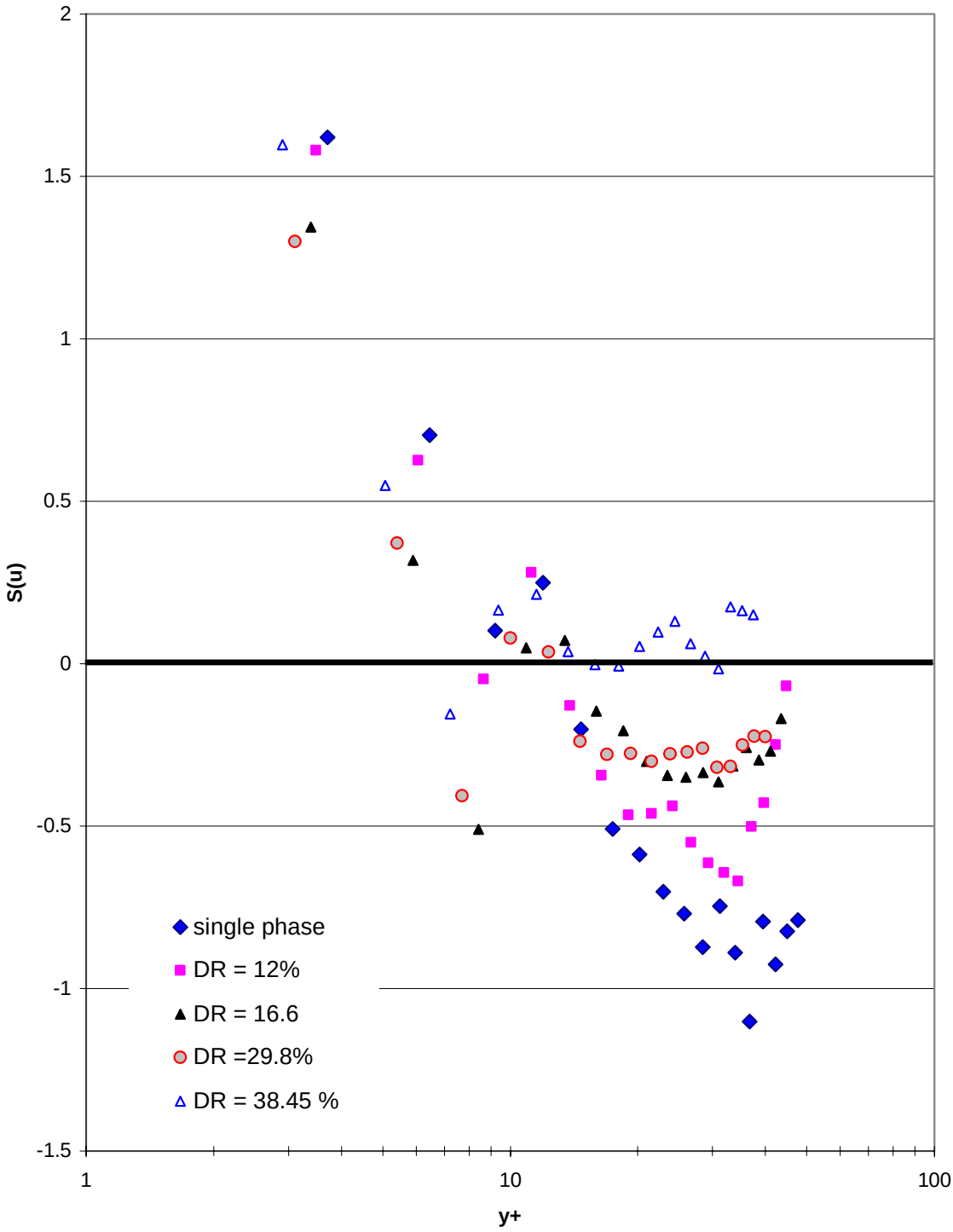

FIGURE 15. Skewness factor of the streamwise fluctuating velocity S(u) versus the distance from the wall in wall units.

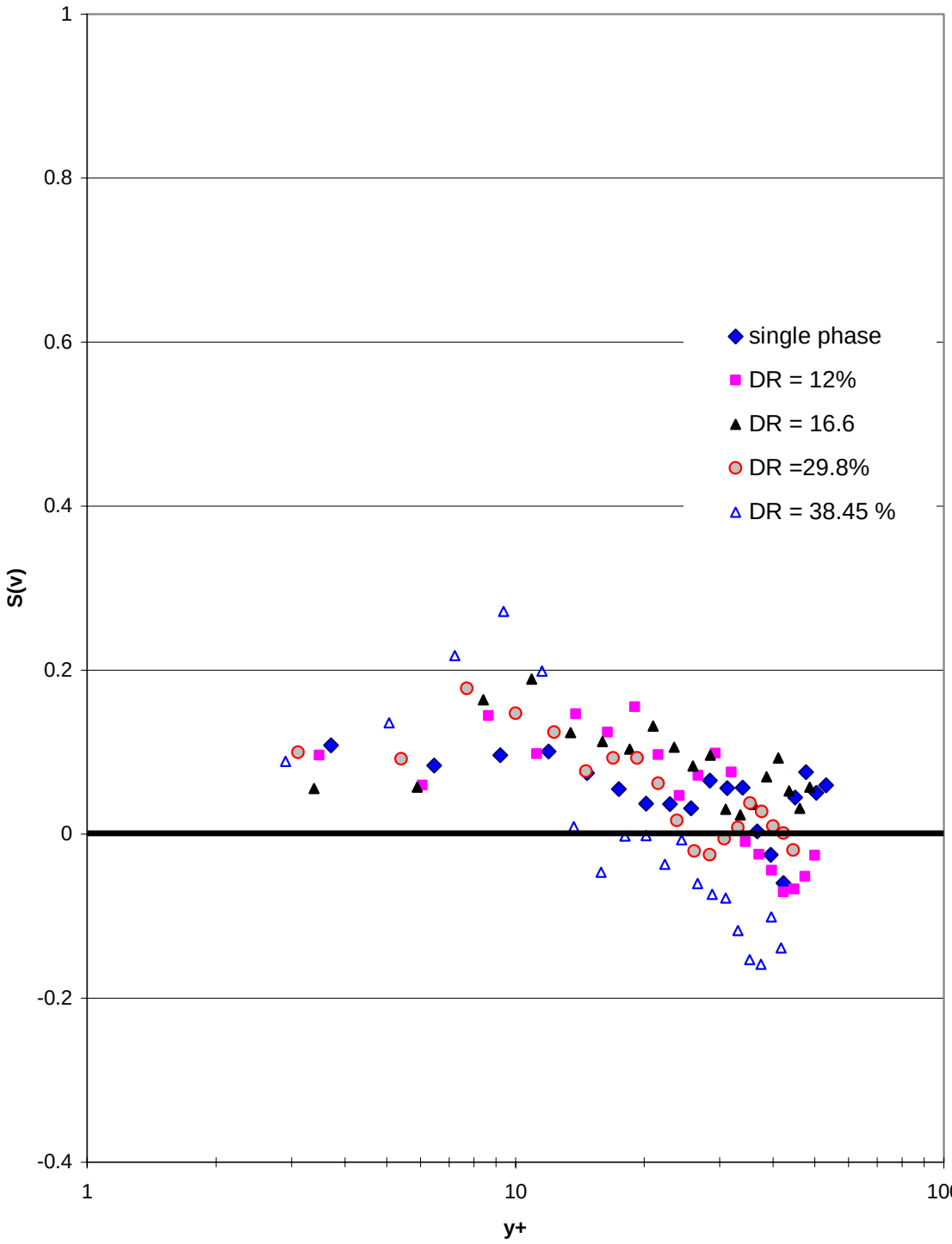

FIGURE 16. Skewness factor of the normal fluctuating velocity S(v) versus the distance from the wall in wall units.

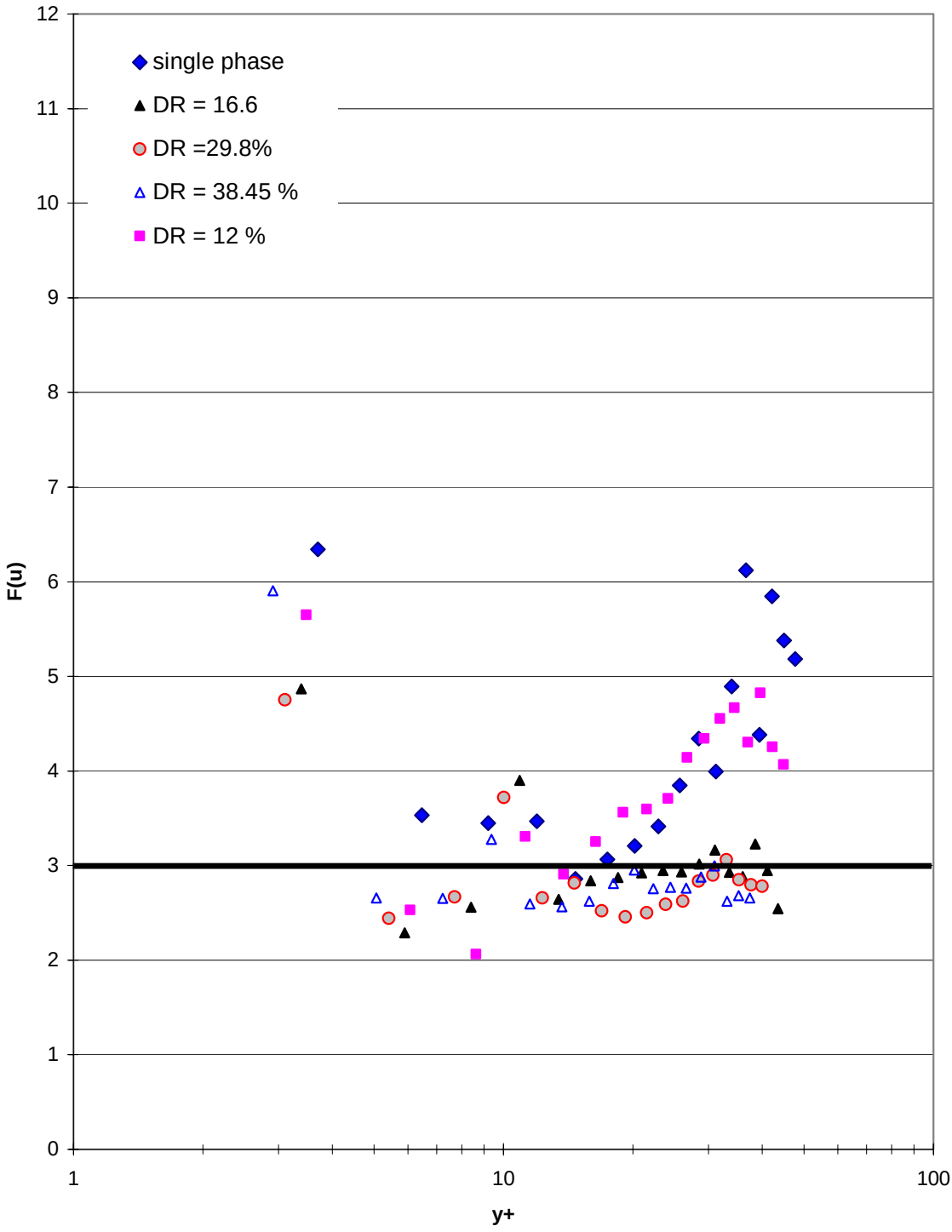

FIGURE 17. Flatness factor of the streamwise fluctuating velocity F(u) versus the distance from the wall in wall units.

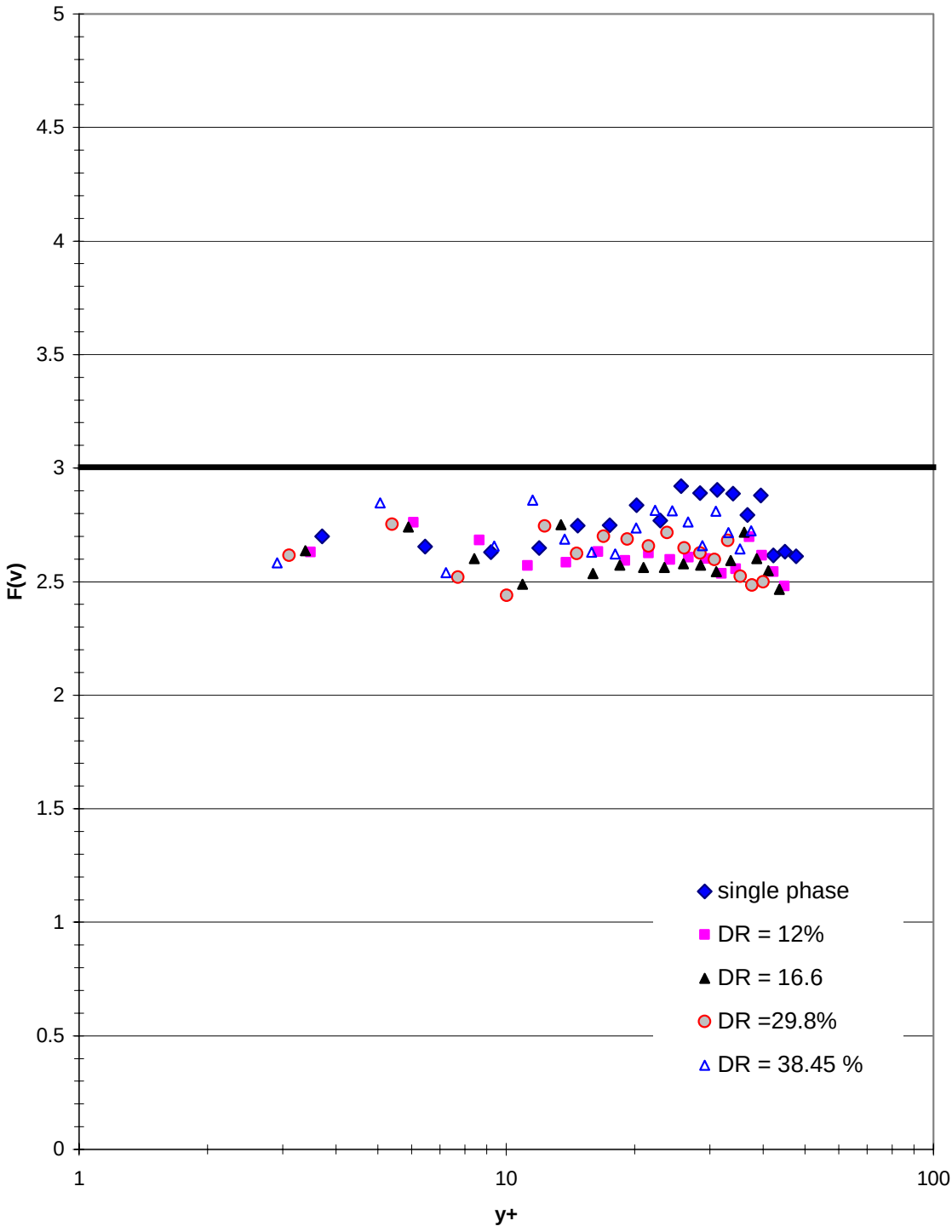

FIGURE 18. Flatness factor of the normal fluctuating velocity F(v) versus the distance from the wall in wall units.

The skewness of the streamwise velocity fluctuation is shown in figure 15; a maximum value of skewness is observed close to the wall and it crosses 0 around y^+ = 14 for single phase flow (this trend is similar to the one portrayed by Warholic (1997) for Re = 5100). The intermittency seems to be higher most of the time for the single phase flow; it could mean that the microbubbles reduce the randomness of the streamwise velocity fluctuation and modify the energy content along the different values of wavenumber. On the other, the skewness of the normal fluctuating component, which is portrayed in figure 16, is not affected in the same way that the streamwise fluctuation velocity. The maximum value for S(v) is not observed near the wall region and S(v) crosses 0 about $y^+ = 36$.

The flatness of the streamwise fluctuating velocity, F(u) shows a great intermittency at $y^+>35$ (see figure 17) for single phase. However, when microbubbles are present the intermittency is decreased. Figure 18 illustrates the flatness of the normal fluctuating velocity, F(v); it is observed that the effect of the microbubbles in the near wall region is negligible. However, far from the microbubbles increase the intermittency.

The evaluation of one dimensional spectra was one of the most essential results that were obtained in this study. This evaluation gives information about the distribution and interchange of fluctuating turbulent kinetic energy between eddies of different size. The calculation of spectra was performed to a single phase flow and to a two phase flow (drag reduction) in order to observe the effect of the microbubbles in the different wavenumer regions. The one dimensional spectra for the streamwise fluctuating velocity $E_{uu}(k_1)$, for normal fluctuating component $E_{vv}(k_1)$ and for the product of the two

components $E_{uv}(k_1)$ were evaluated in the streamwise wavenumber k_1. The spectra were not made dimensionless to show if the energy distribution is really being reduced or not when the microbubbles are present.

The spectra for single phase and maximum drag reduction are compared at several distances from the wall. The maximum value of 38.45 % drag reduction was obtained with a local void fraction of 4.8 %. Most of the results of wavenumber spectra reported in the literature have been done using data from hot wire measurements, which are transformed from frequency spectra into wavenumber spectra by assuming Taylor's frozen hypothesis.

The PIV spatial information was used to evaluate the spectra in the streamwise wavenumber; the length of the PIV window (L_x) was related to the maximum eddy size (minimum wavenumber) and the space between vectors (ΔX) was related to the minimum eddy size (maximum wavenumber) as shown by Murai et al. (2000). These considerations, allowed obtaining a minimum dimensionless wavenumber $(k_1H)_{min} = H/L_x = 28mm/(11.9mm) = 2.3$ and maximum $(k_1H)_{max} = H/2\Delta X = 58.8$ from the spatial information. However, there was still information in the one hundred velocity fields for dimensionless wavenumbers lower than 2.3; this information was obtained from the temporal information by assuming Taylor's frozen hypothesis. This new approach of using the temporal and spatial information of the fluctuating velocity fields allowed a larger wavenumber range.

The existence of a plateau-like region was observed in the higher wavenumber region of $E_{uu}(k_1)$, $E_{uv}(k_1)$ and $E_{vv}(k_1)$. This could be attributed to the energy contribution of

higher wavenumber components that can not be resolved from the spatial resolution and to noise. To reduce the effects of noise on the one dimensional spectra results, the area under the portion of the curve that corresponds the plateau-like region is integrated to obtain the energy content in that zone. A percentage of this energy is subtracted from each of the components of the spectra that were obtained from the PIV spatial information. The percentage that is subtracted is chosen as a function of the best fitting of the inertial subrange to the -5/3 slope for single phase. This process was applied to the results of $E_{uu}(k_1)$, $E_{uv}(k_1)$ and $E_{vv}(k_1)$ that are shown in figure 19 to figure 65.

The one-dimensional spectra for the streamwise fluctuating velocity at different positions from the wall are shown from figure 19 to figure 34. It is observed from the evaluation of $E_{uu}(k_1)$ in the viscous region ($y^+ = 3.7$) and part of the buffer layer ($y^+ =$ 6.5, 9.2, 12, 14.7, 17.4, 20.2, and 22.9) that the energy contain of single phase flow is larger than that of two phase flow (see figure 19 to figure 26). Furthermore, there is a redistribution of energy from high wavenumber to low wavenumbers; this shift of energy is analogous to the one reported by Wei & Willmarth (1992) for drag reduction by polymer injection. It is plausible that microbubbles redistribute the large coherent structures near the wall region. On other hand, the energy is shifted from lower to larger wavenumbers outside the buffer layer. These results indicates that the interactions that takes place outside the buffer layer do not have a big effect in the reduction of drag because the higher production and dissipation occurs between $y^+ = 10$-20.

When the results of $E_{vv}(k_1)$ from Taylor's frozen hypothesis and the results from the spatial information were plotted together a discontinuity was observed at $k_1H = 2.3$. This

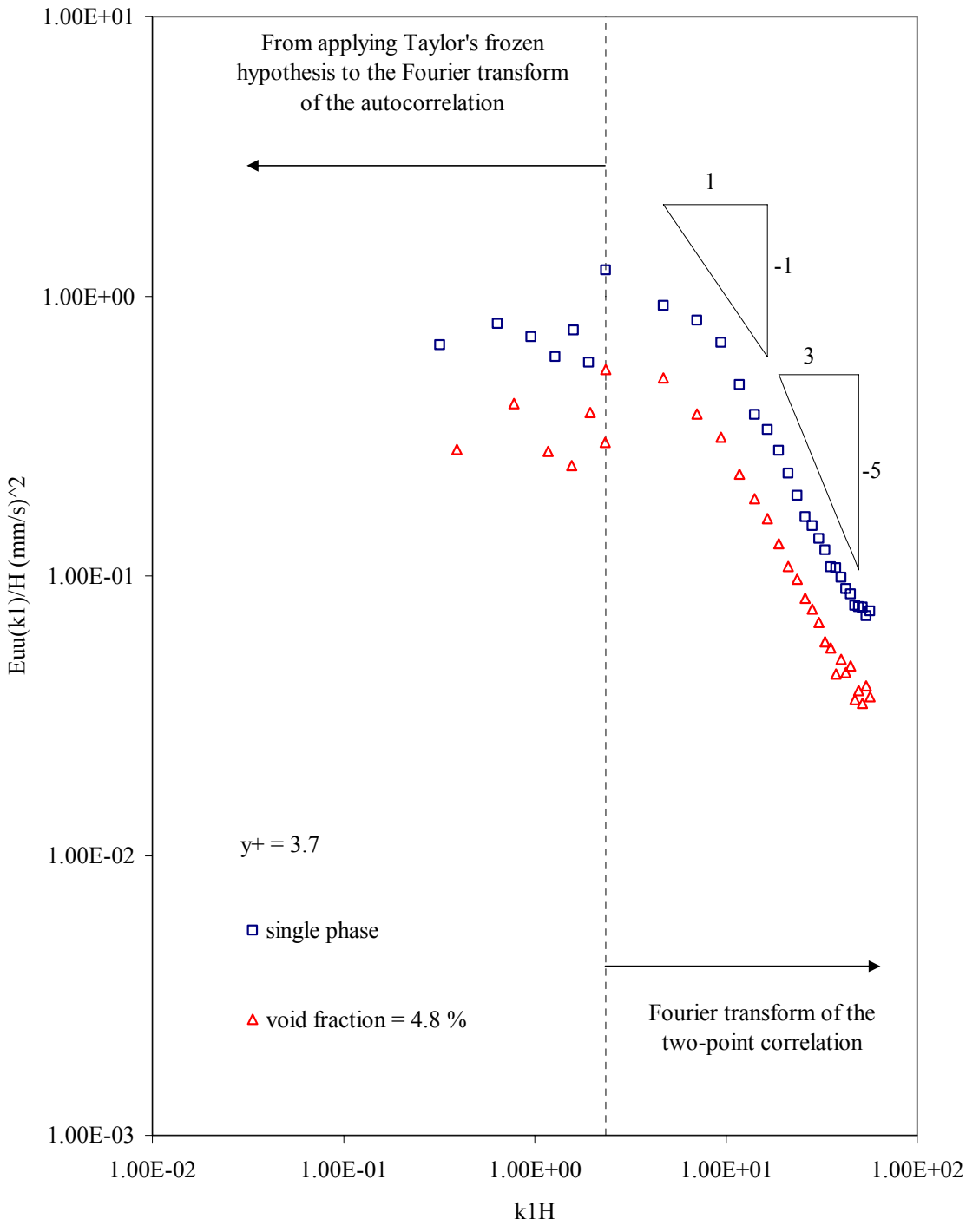

FIGURE 19. Dimensional streamwise spectra versus non-dimensional wavenumber at y/H = 0.01.

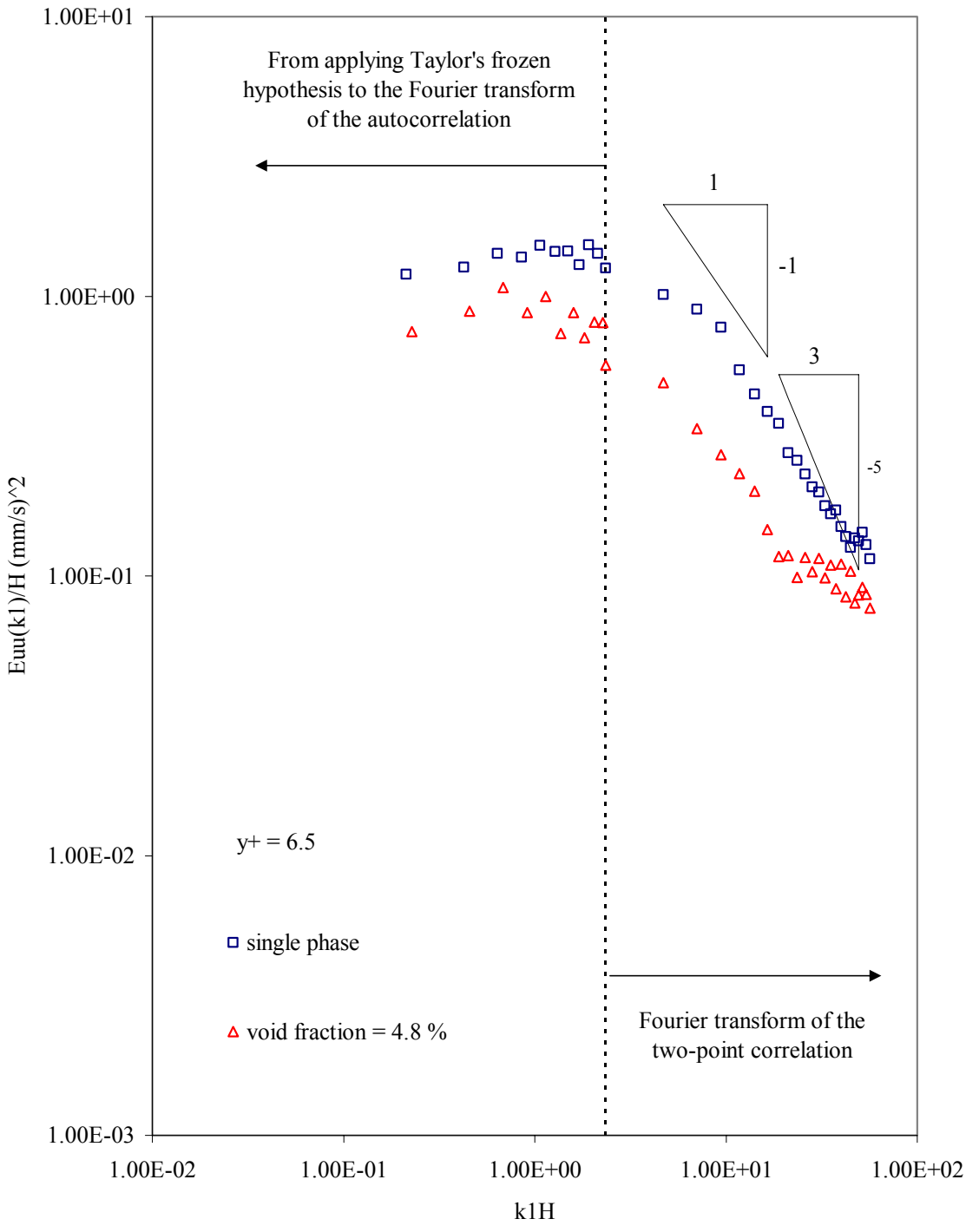

FIGURE 20. Dimensional streamwise spectra versus non-dimensional wavenumber at y/H = 0.019.

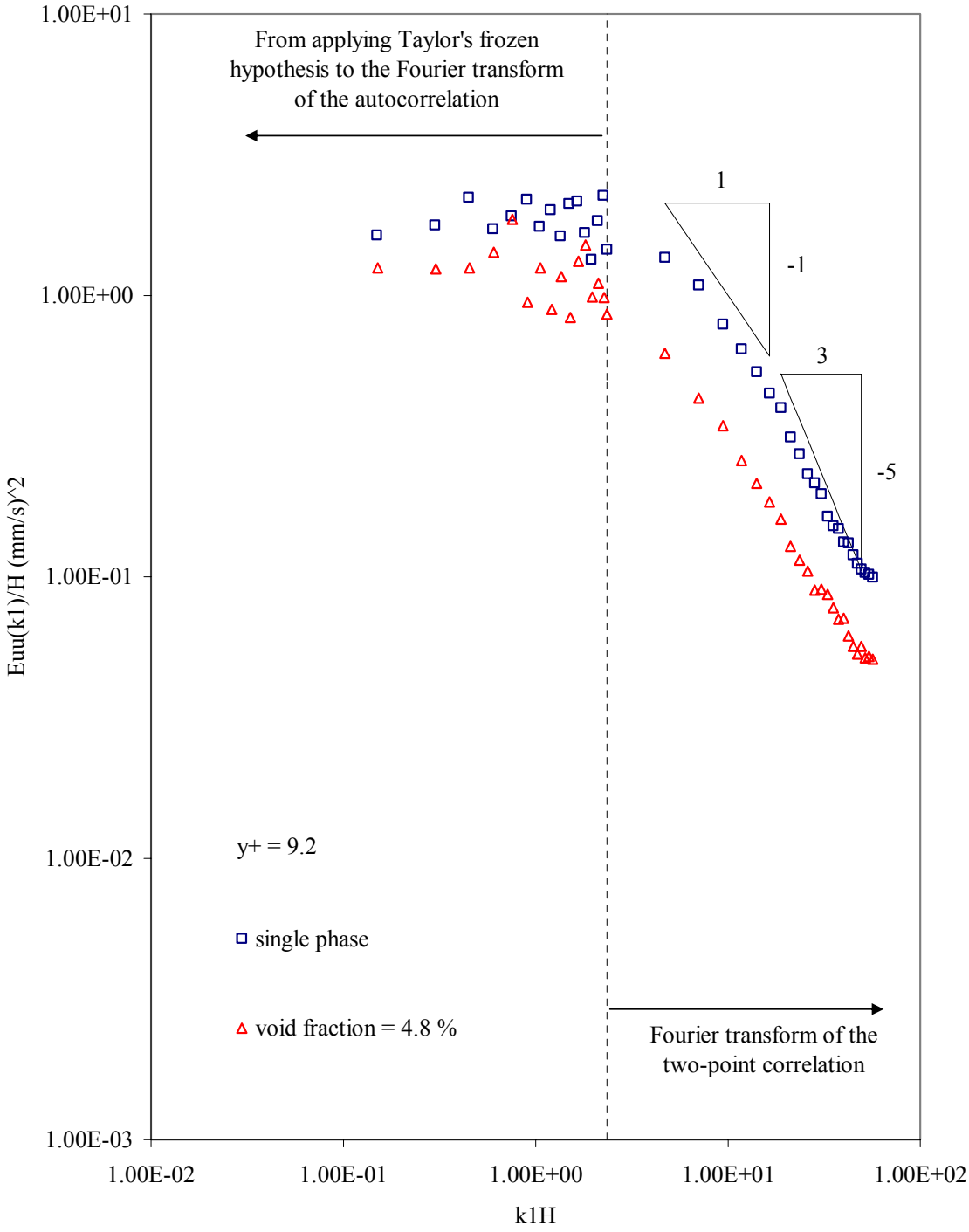

FIGURE 21. Dimensional streamwise spectra versus non-dimensional wavenumber at y/H = 0.027.

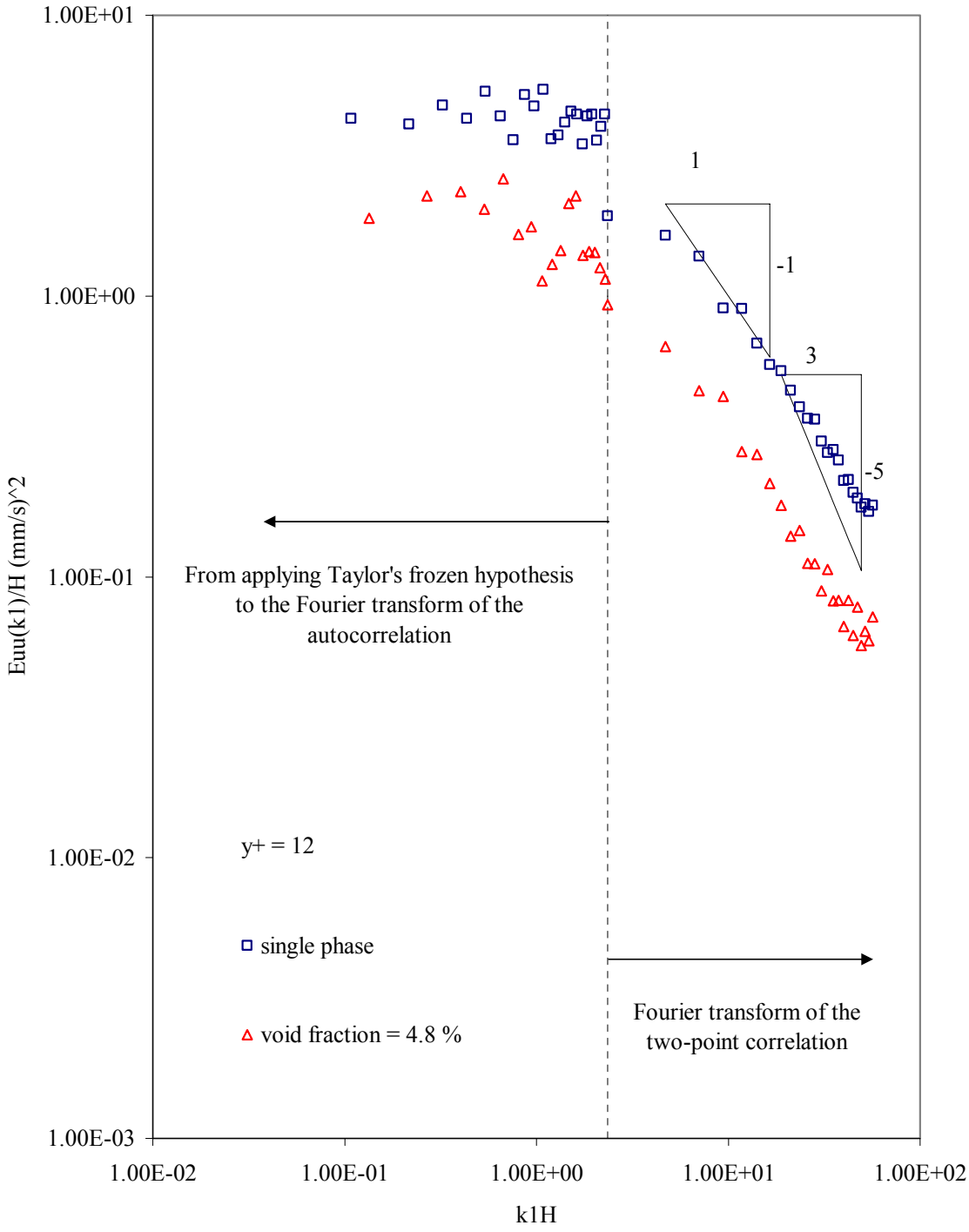

FIGURE 22. Dimensional streamwise spectra versus non-dimensional wavenumber at y/H = 0.036.

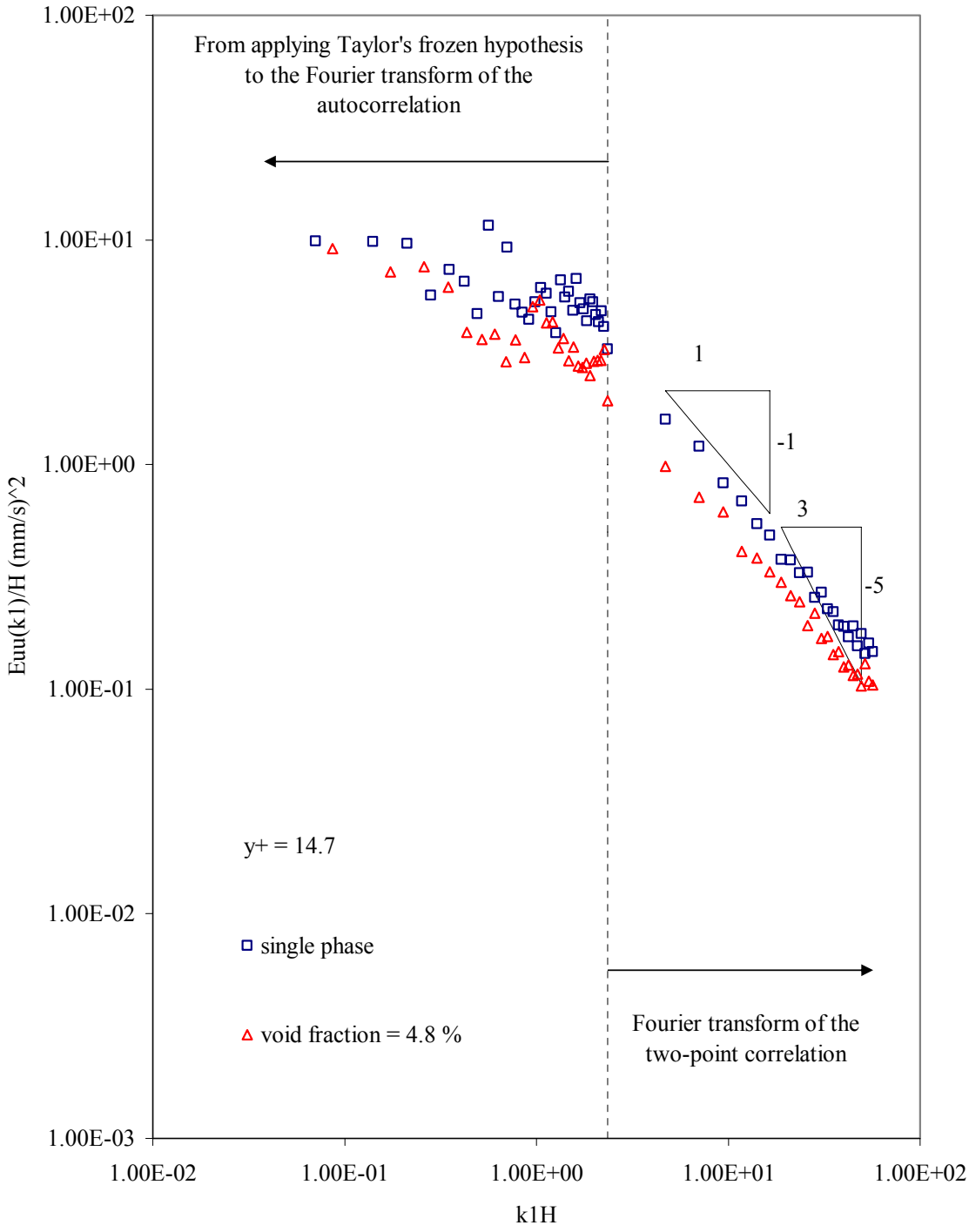

FIGURE 23. Dimensional streamwise spectra versus non-dimensional wavenumber at y/H = 0.044.

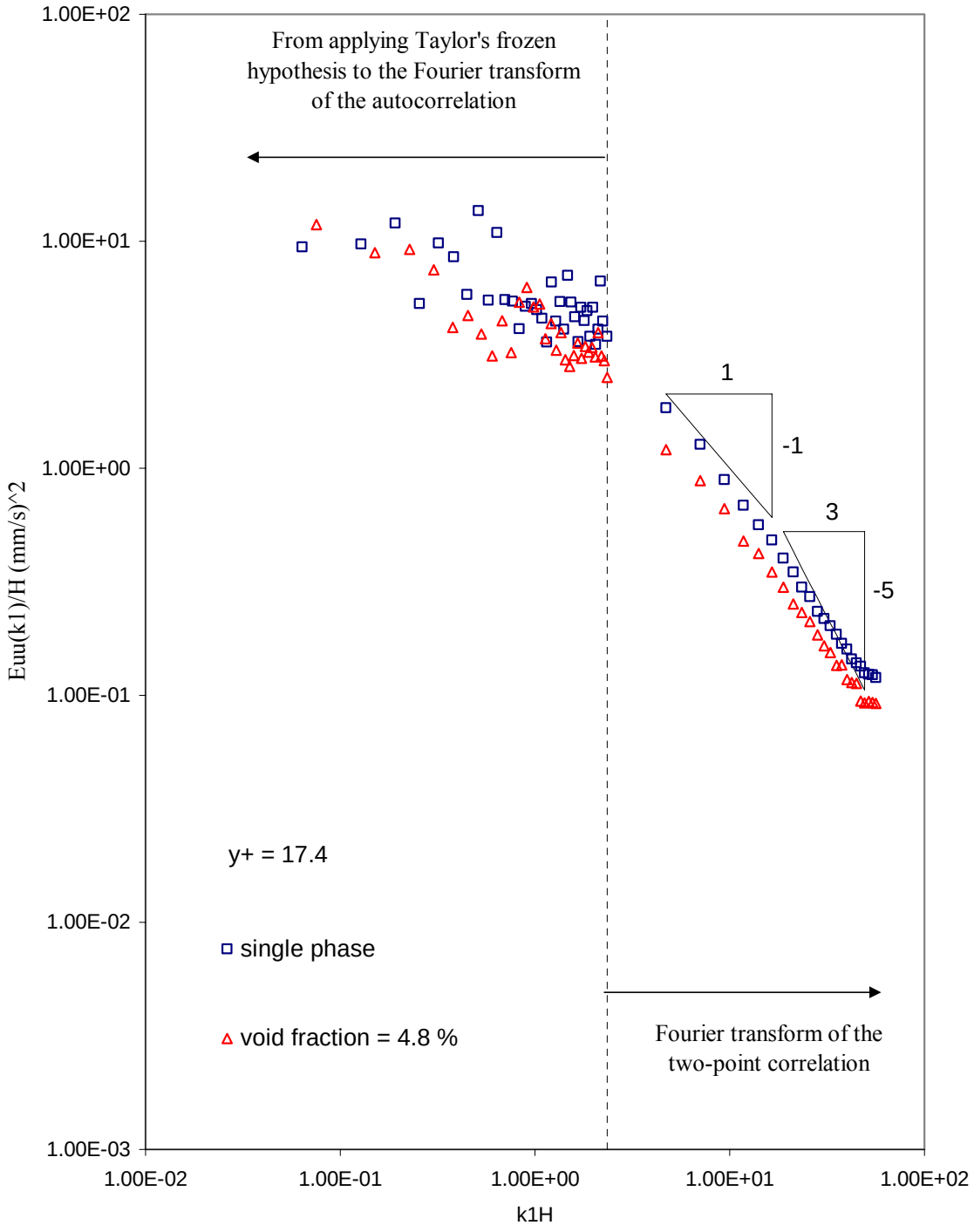

FIGURE 24. Dimensional streamwise spectra versus non-dimensional wavenumber at y/H = 0.052.

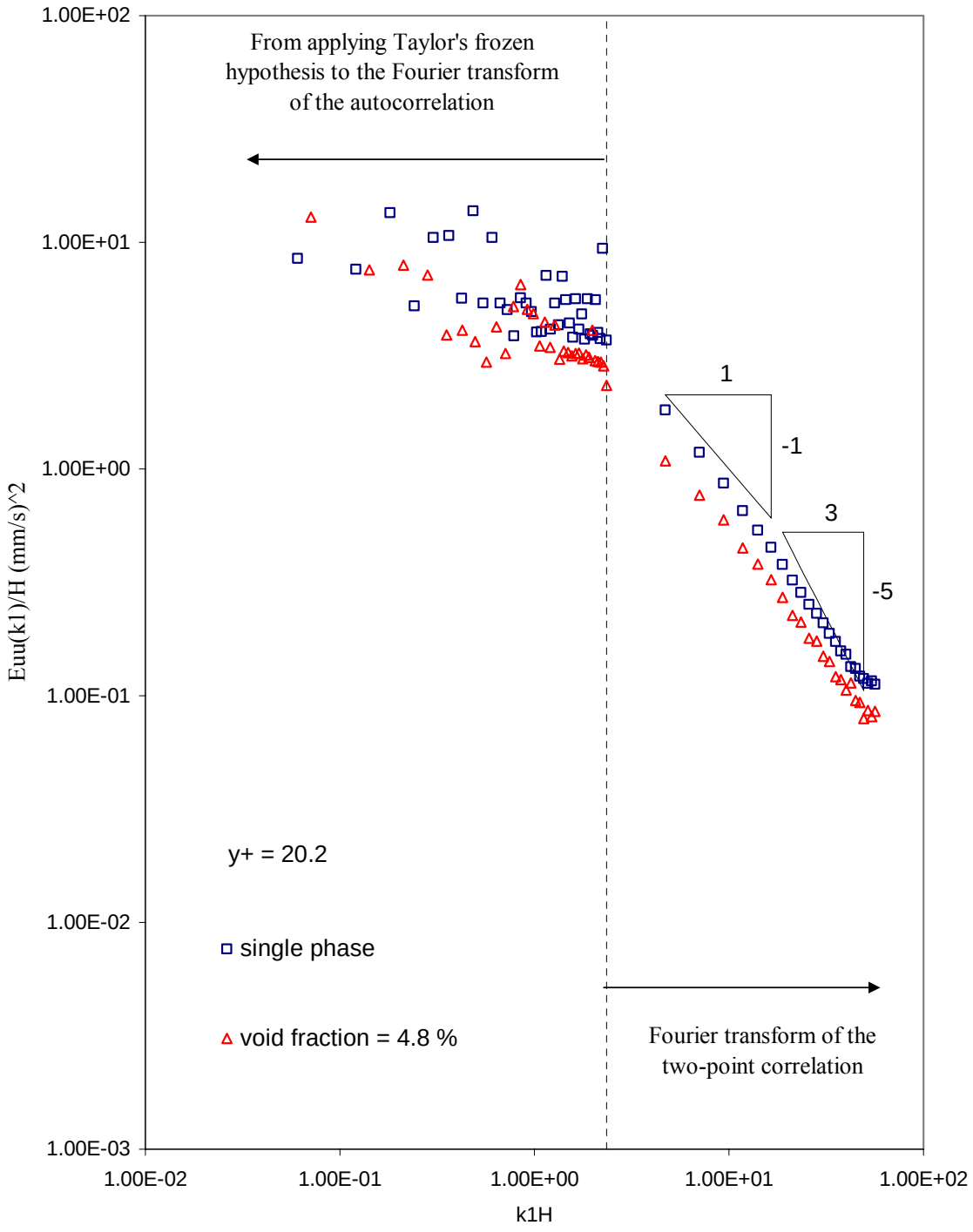

FIGURE 25. Dimensional streamwise spectra versus non-dimensional wavenumber at y/H = 0.06.

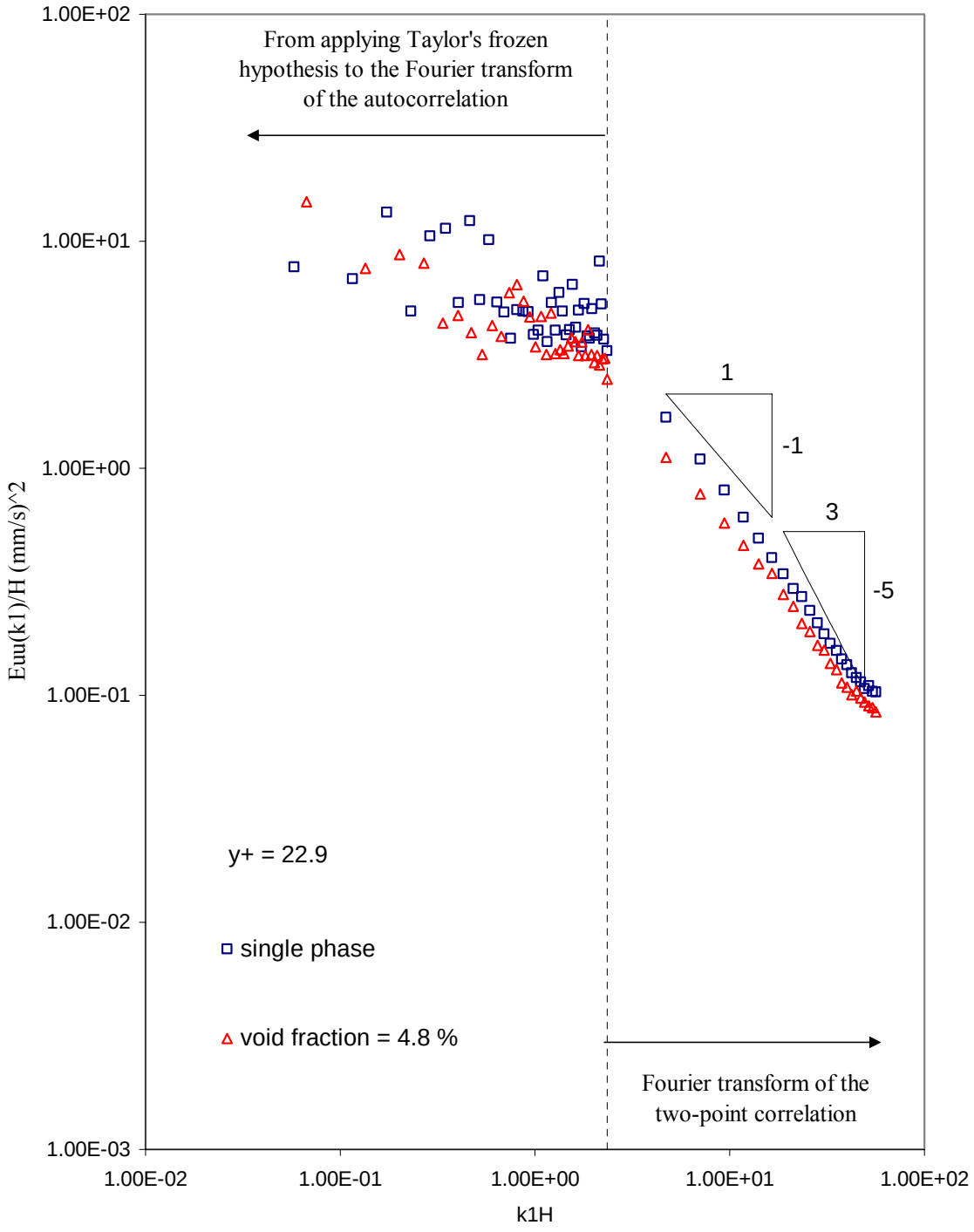

FIGURE 26. Dimensional streamwise spectra versus non-dimensional wavenumber at y/H = 0.069.

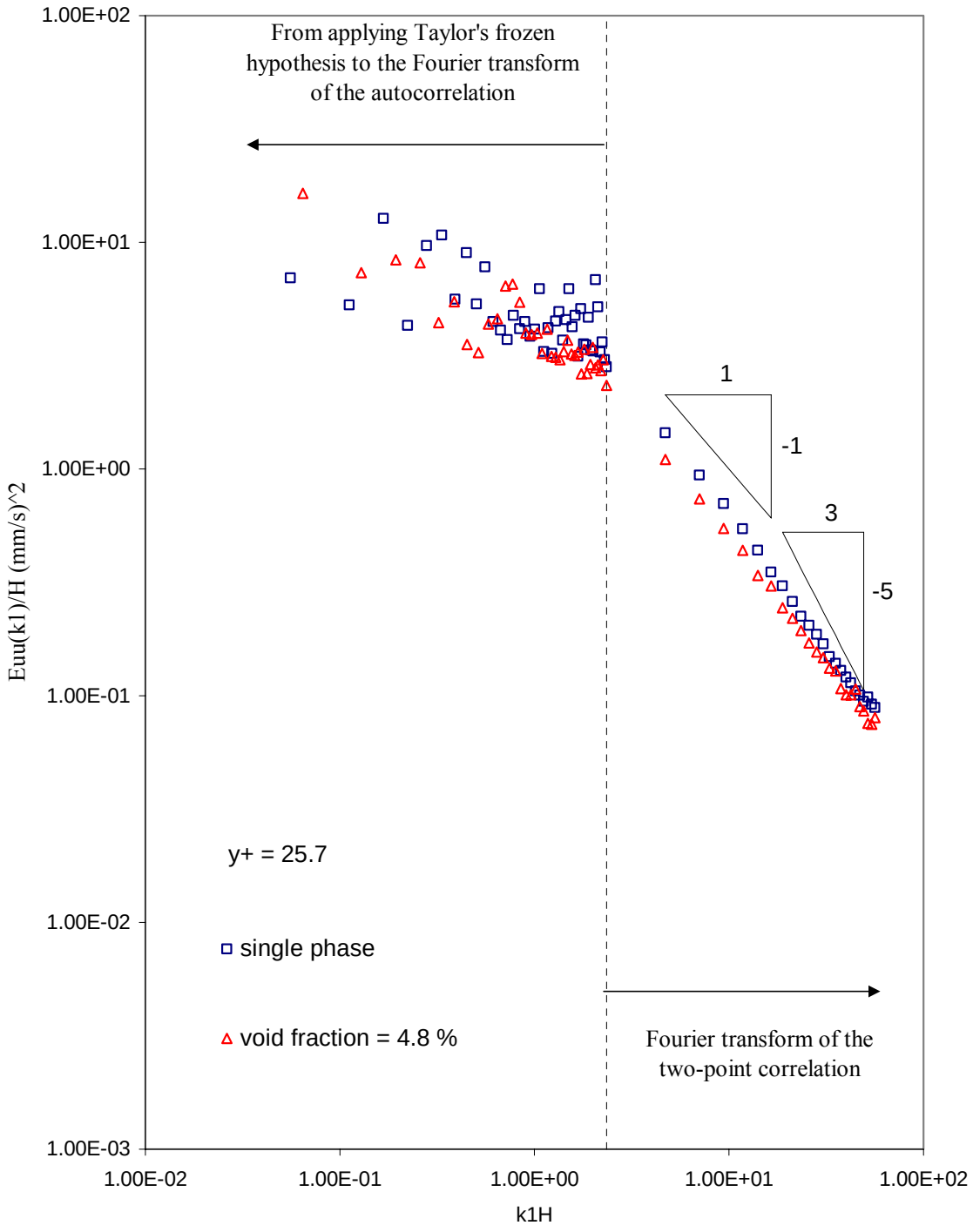

FIGURE 27. Dimensional streamwise spectra versus non-dimensional wavenumber at y/H = 0.077.

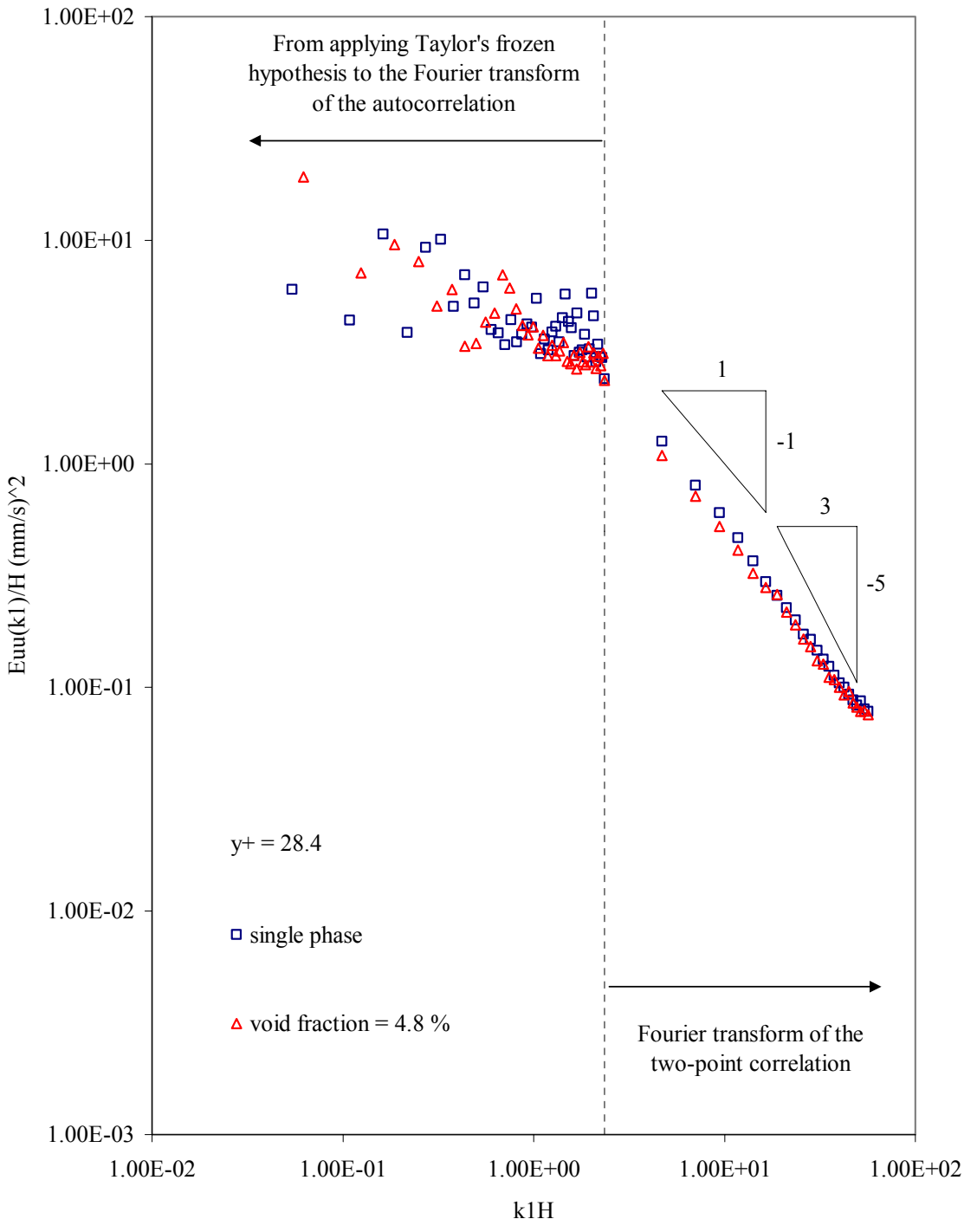

FIGURE 28. Dimensional streamwise spectra versus non-dimensional wavenumber at y/H = 0.085.

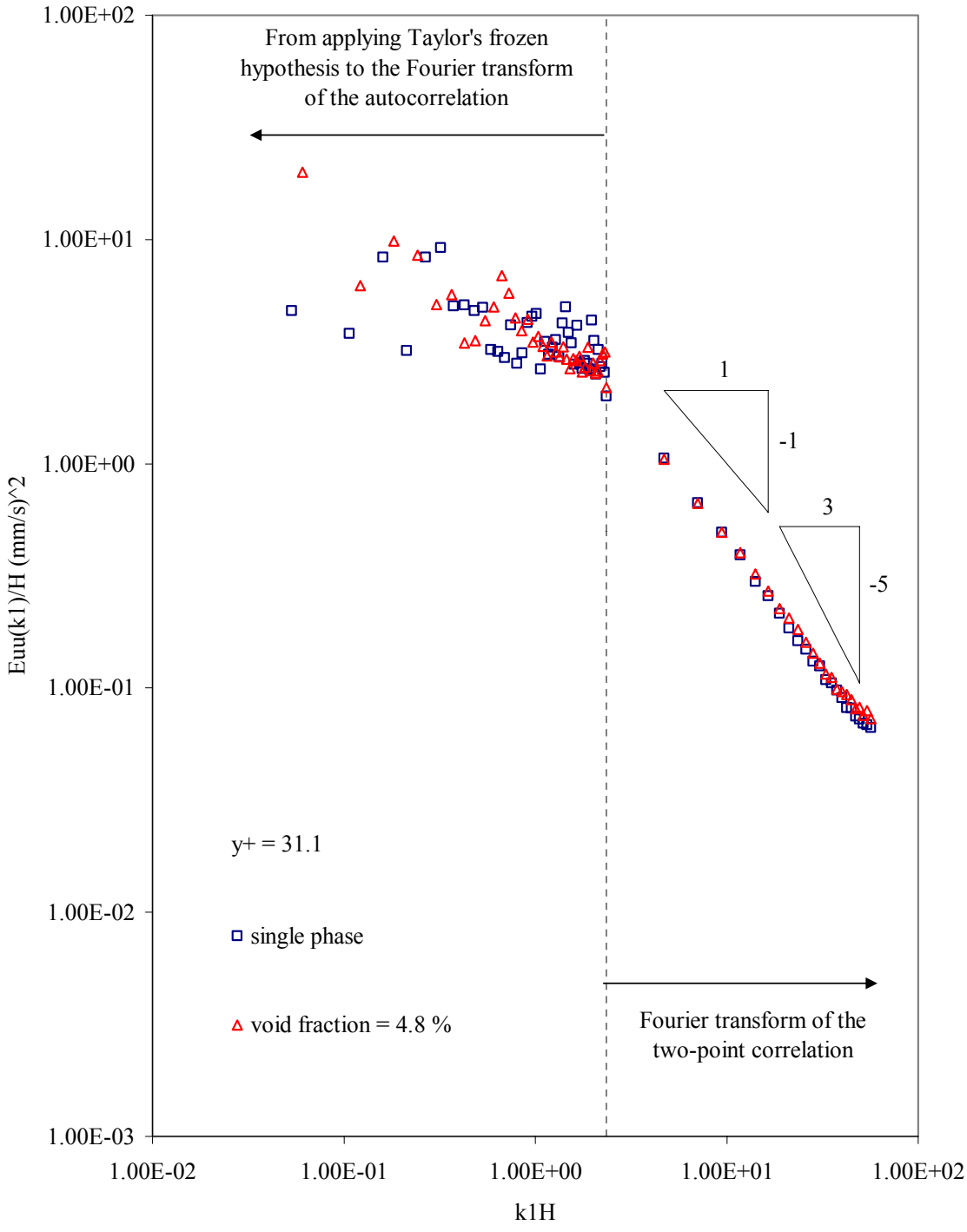

FIGURE 29. Dimensional streamwise spectra versus non-dimensional wavenumber at y/H = 0.094.

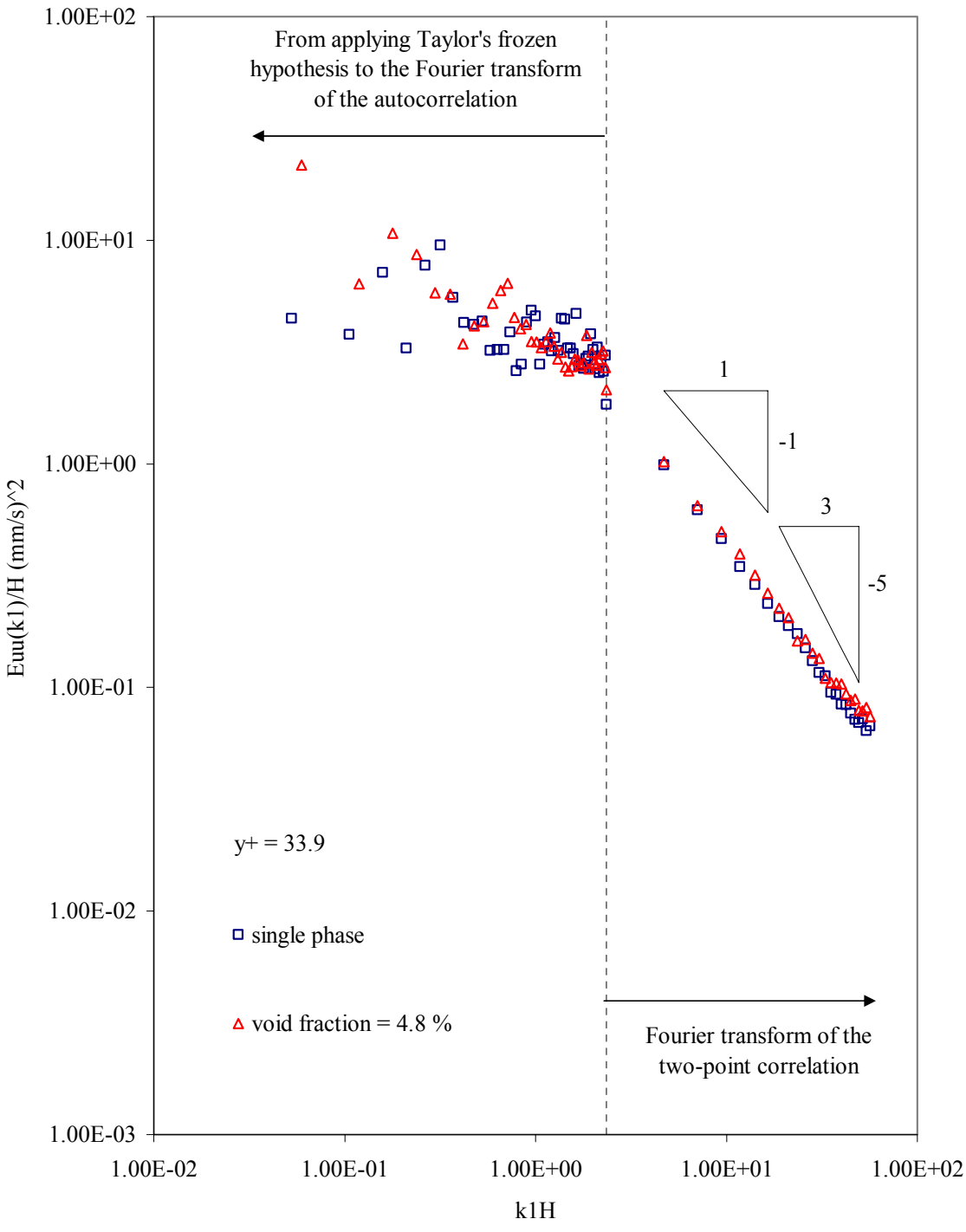

FIGURE 30. Dimensional streamwise spectra versus non-dimensional wavenumber at y/H = 0.10.

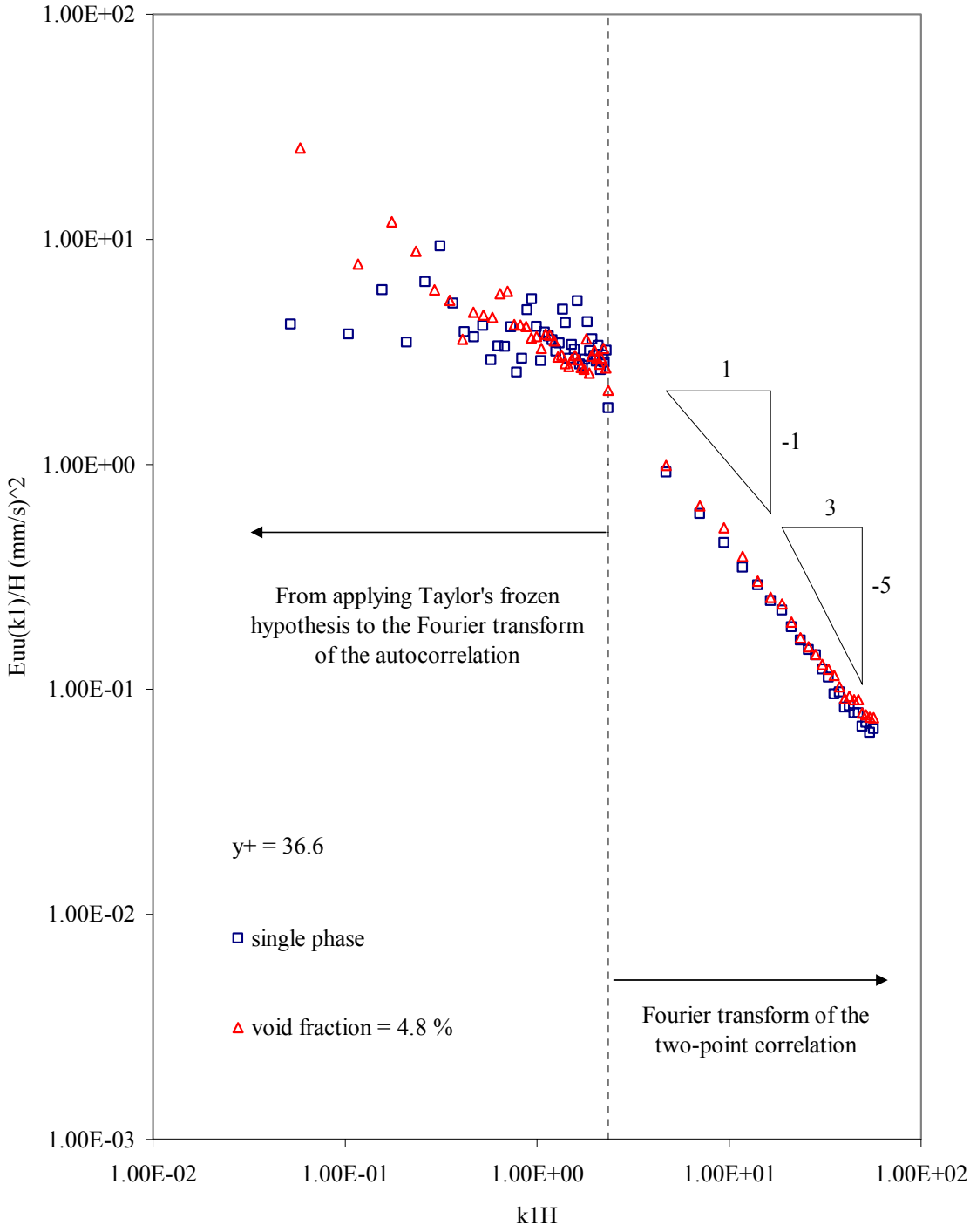

FIGURE 31. Dimensional streamwise spectra versus non-dimensional wavenumber at y/H = 0.11.

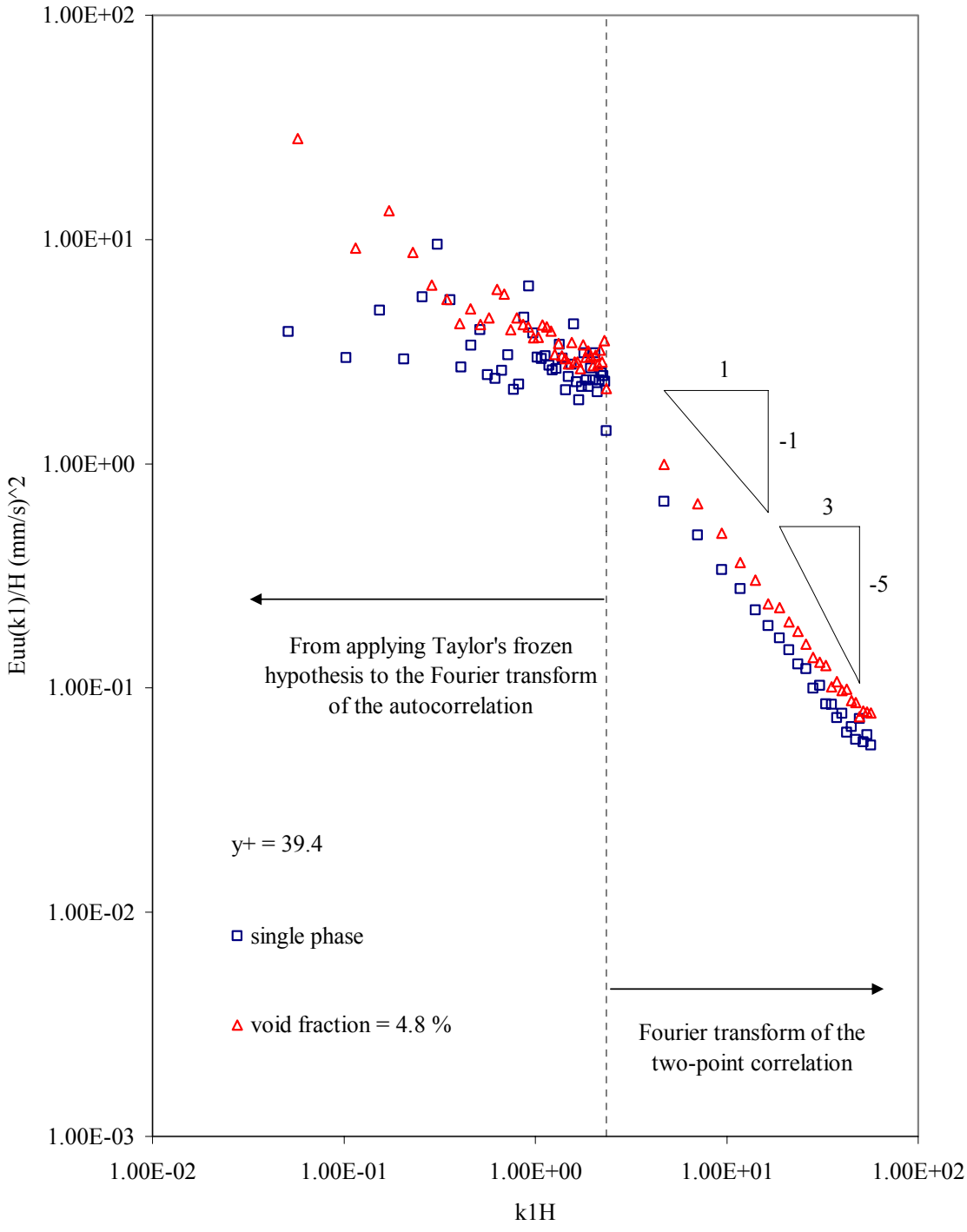

FIGURE 32. Dimensional streamwise spectra versus non-dimensional wavenumber at y/H = 0.118.

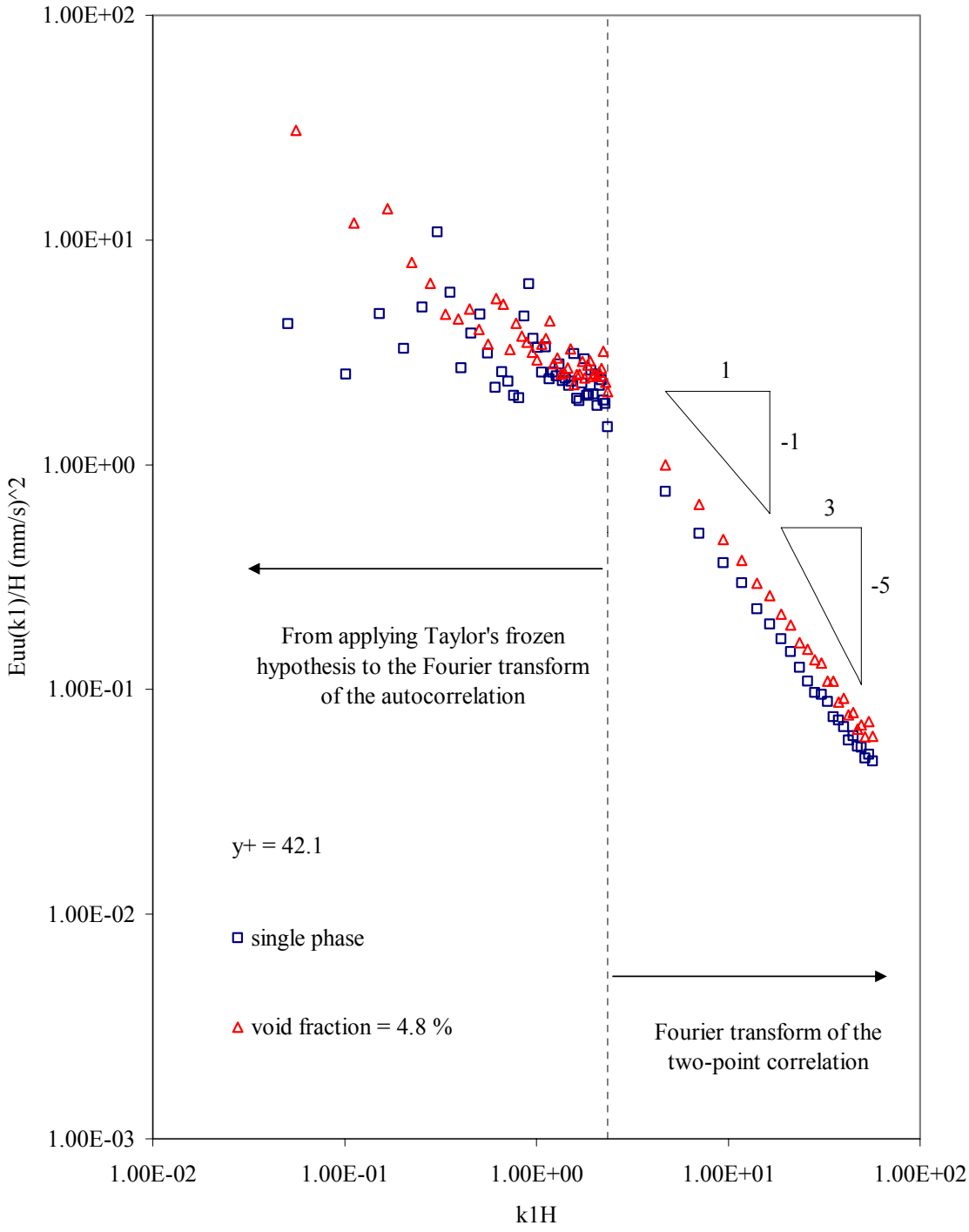

FIGURE 33. Dimensional streamwise spectra versus non-dimensional wavenumber at y/H = 0.127.

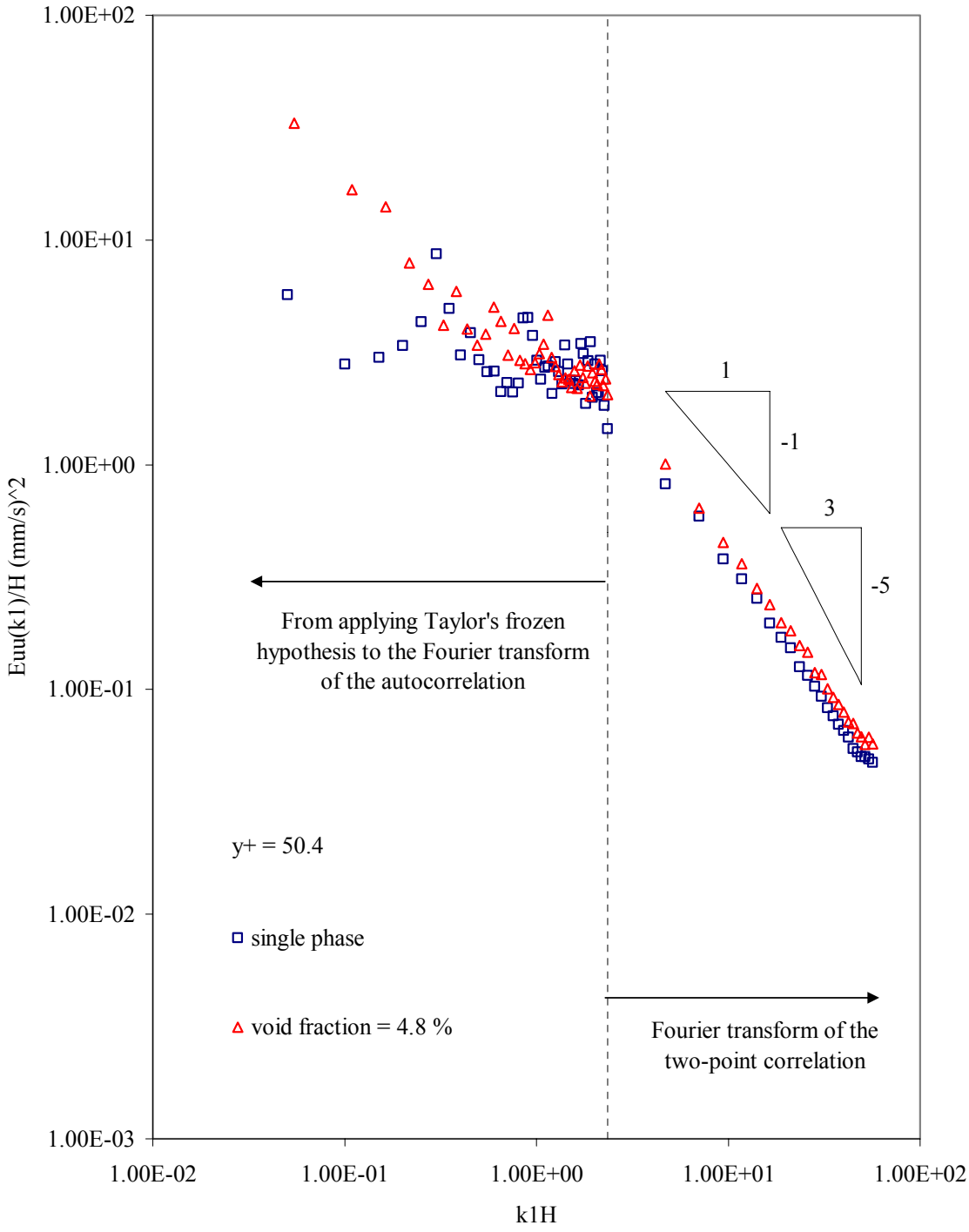

FIGURE 34. Dimensional streamwise spectra versus non-dimensional wavenumber at y/H = 0.15.

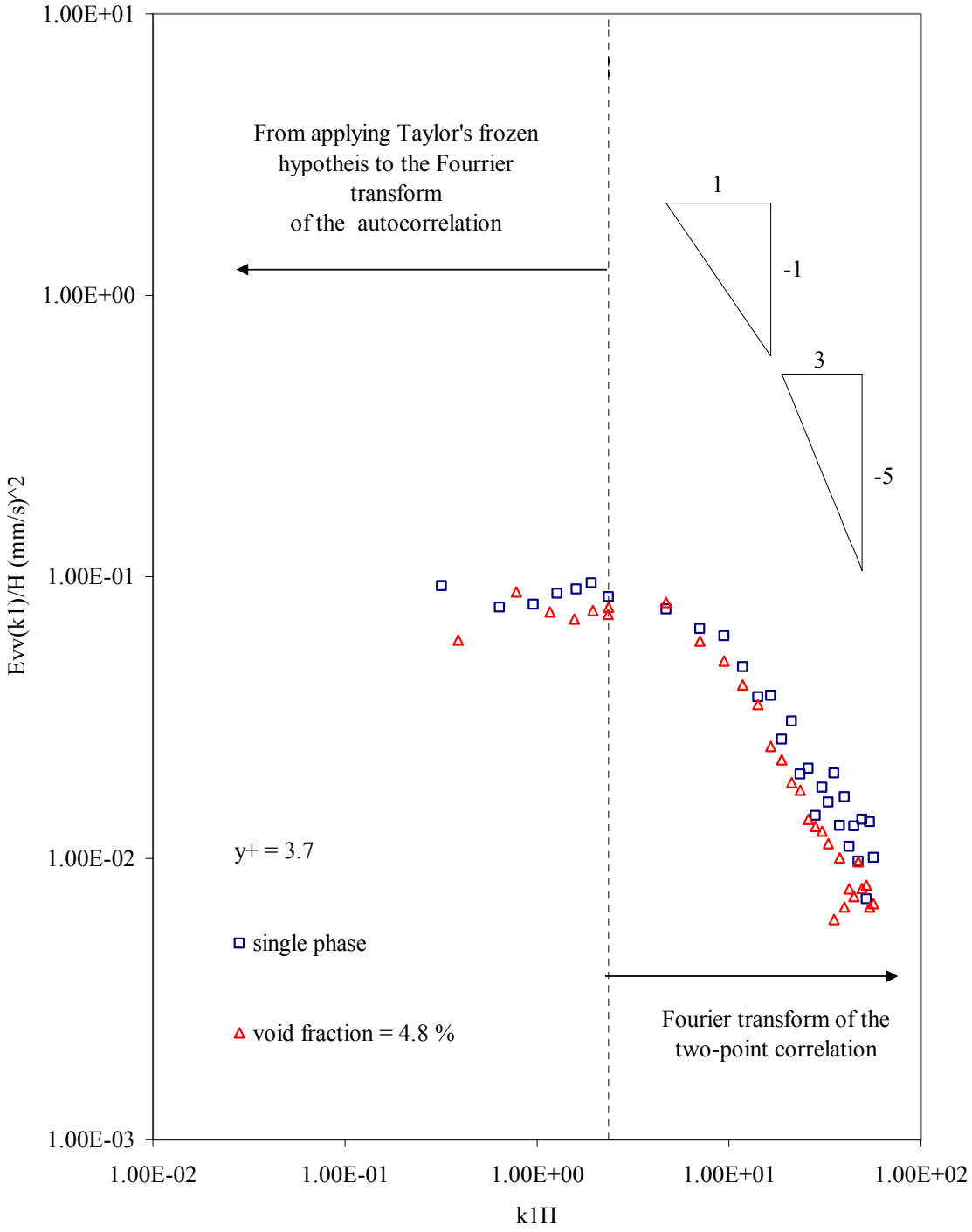

FIGURE 35. Dimensional normal spectra versus non-dimensional wavenumber at y/H = 0.011.

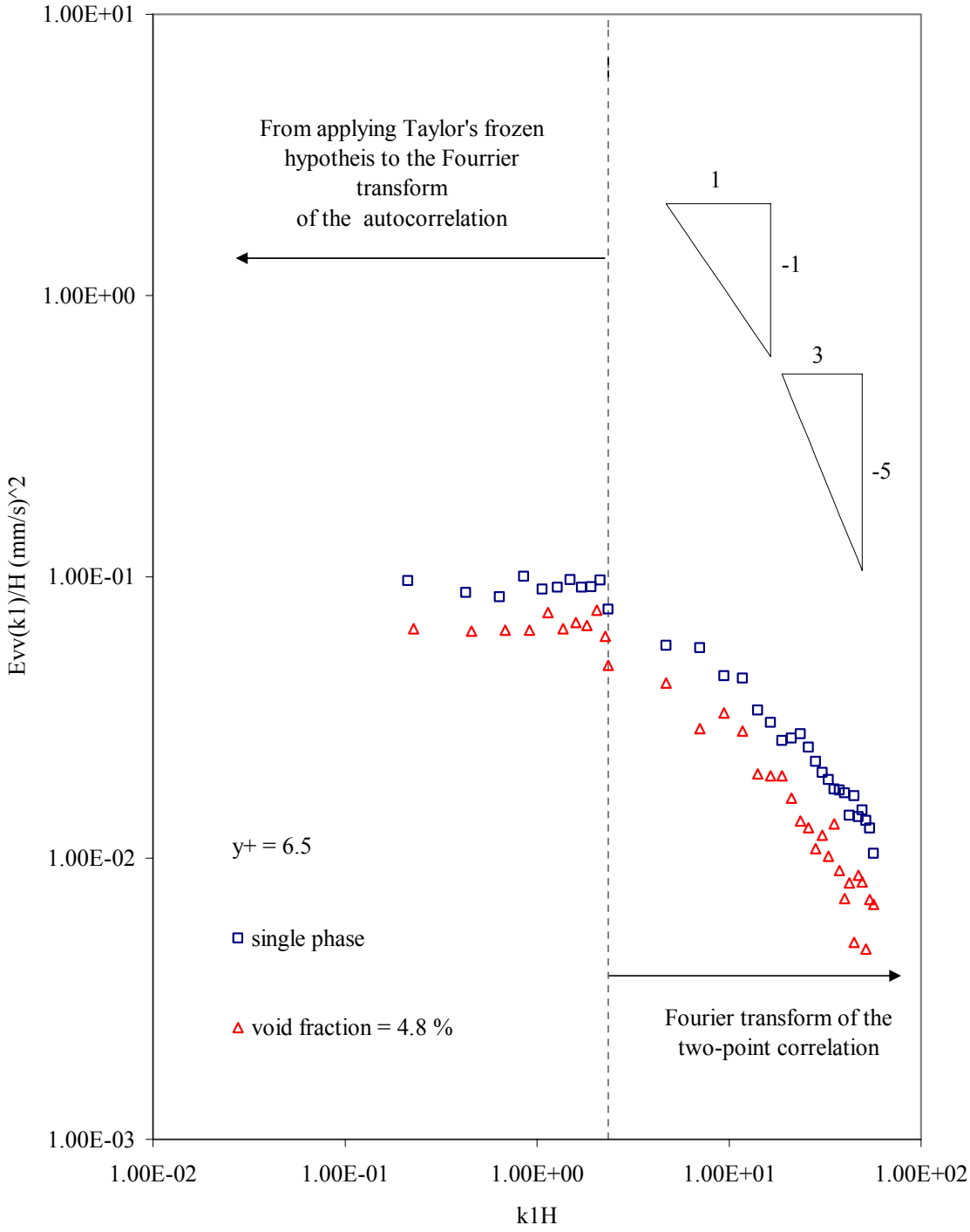

FIGURE 36. Dimensional normal spectra versus non-dimensional wavenumber at y/H = 0.019.

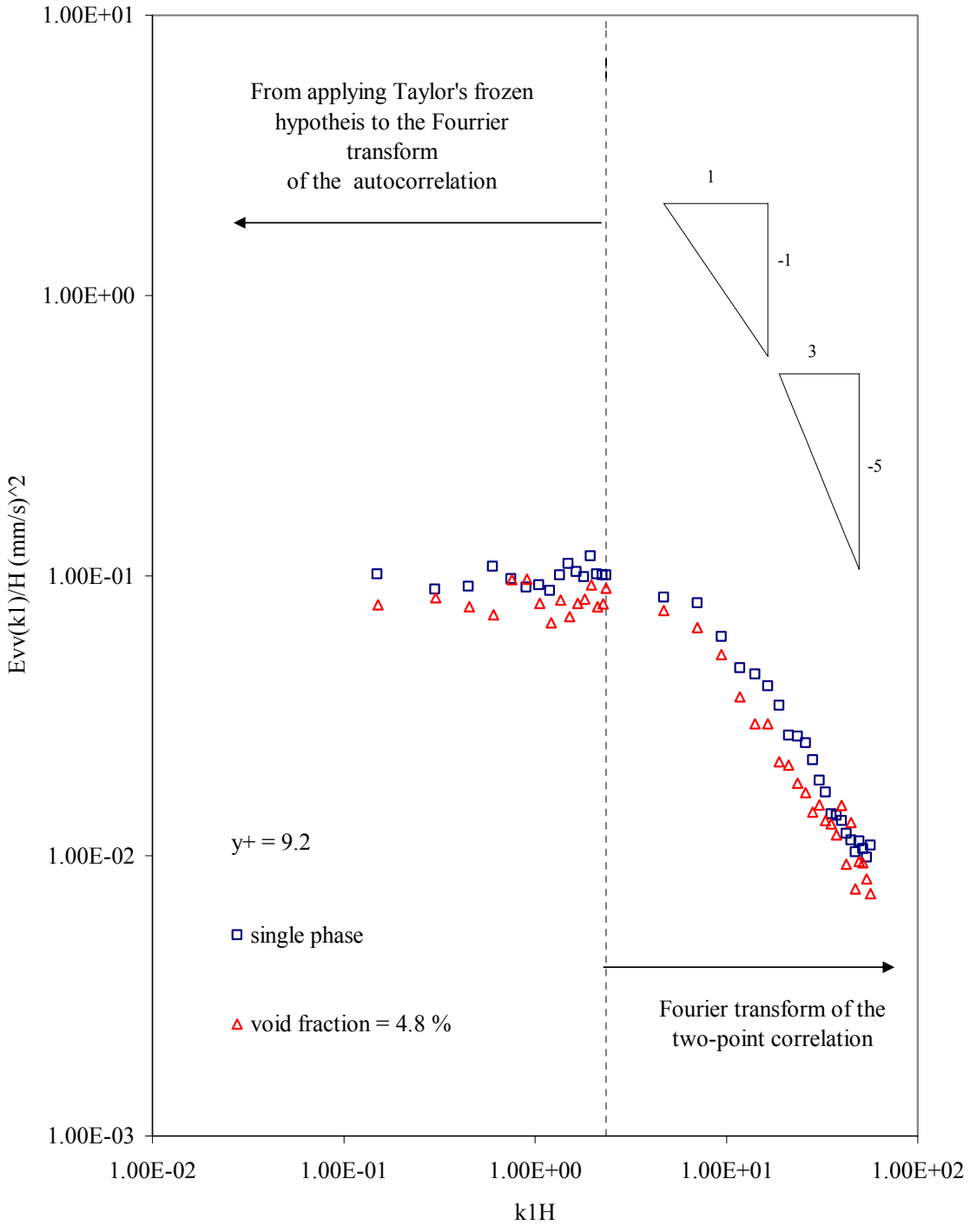

FIGURE 37. Dimensional normal spectra versus non-dimensional wavenumber at y/H = 0.027.

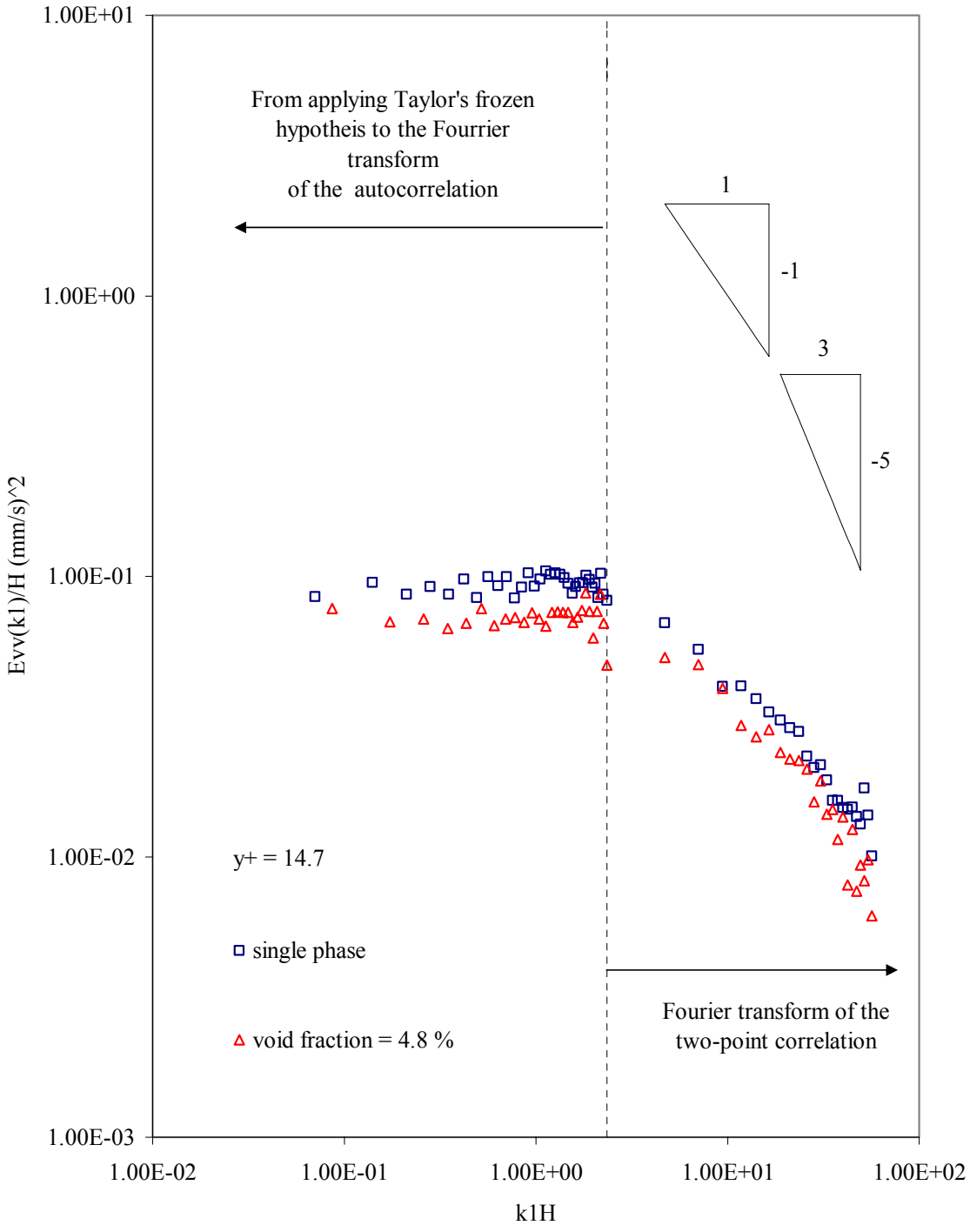

FIGURE 38. Dimensional normal spectra versus non-dimensional wavenumber at y/H = 0.044.

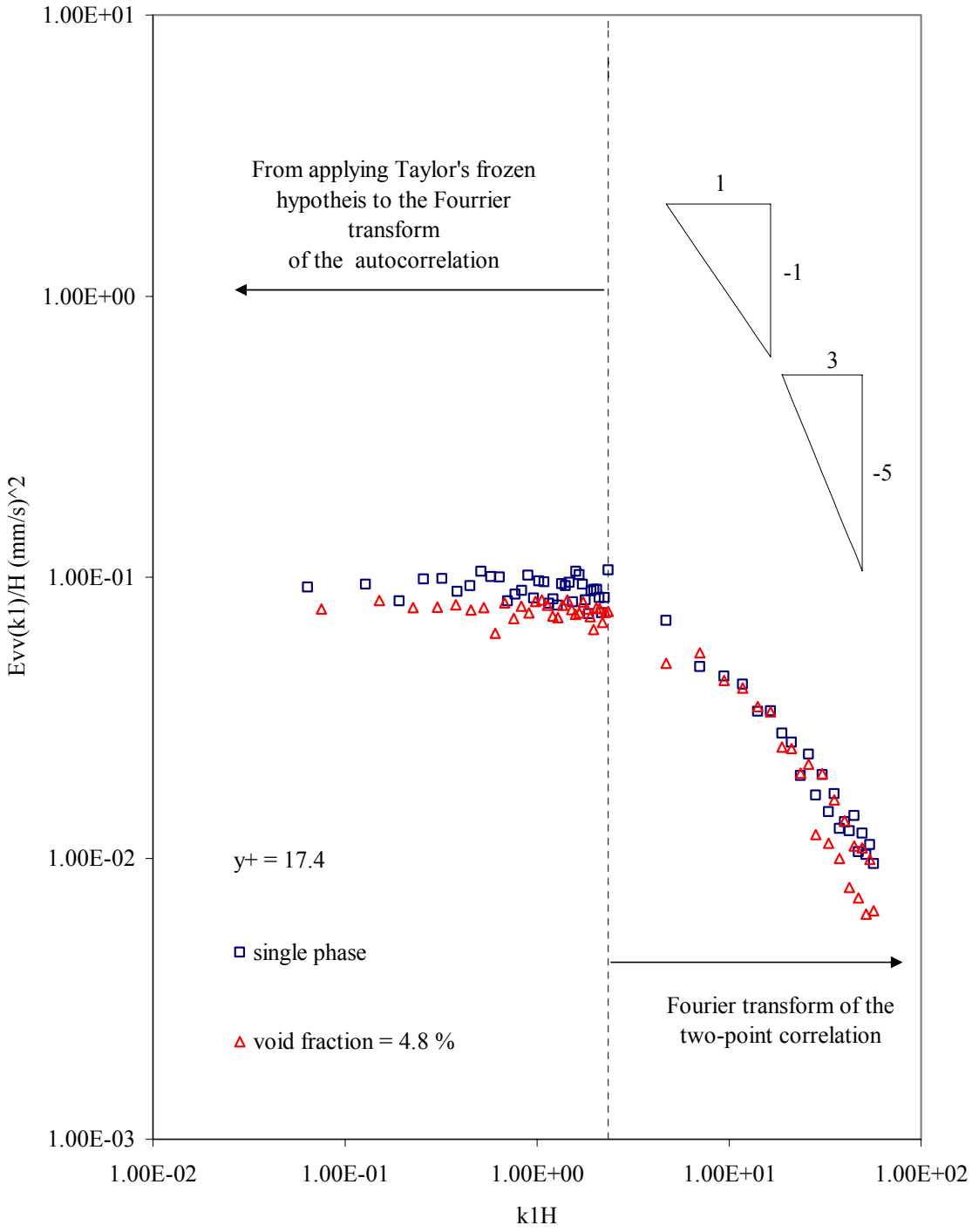

FIGURE 39. Dimensional normal spectra versus non-dimensional wavenumber at y/H = 0.052.

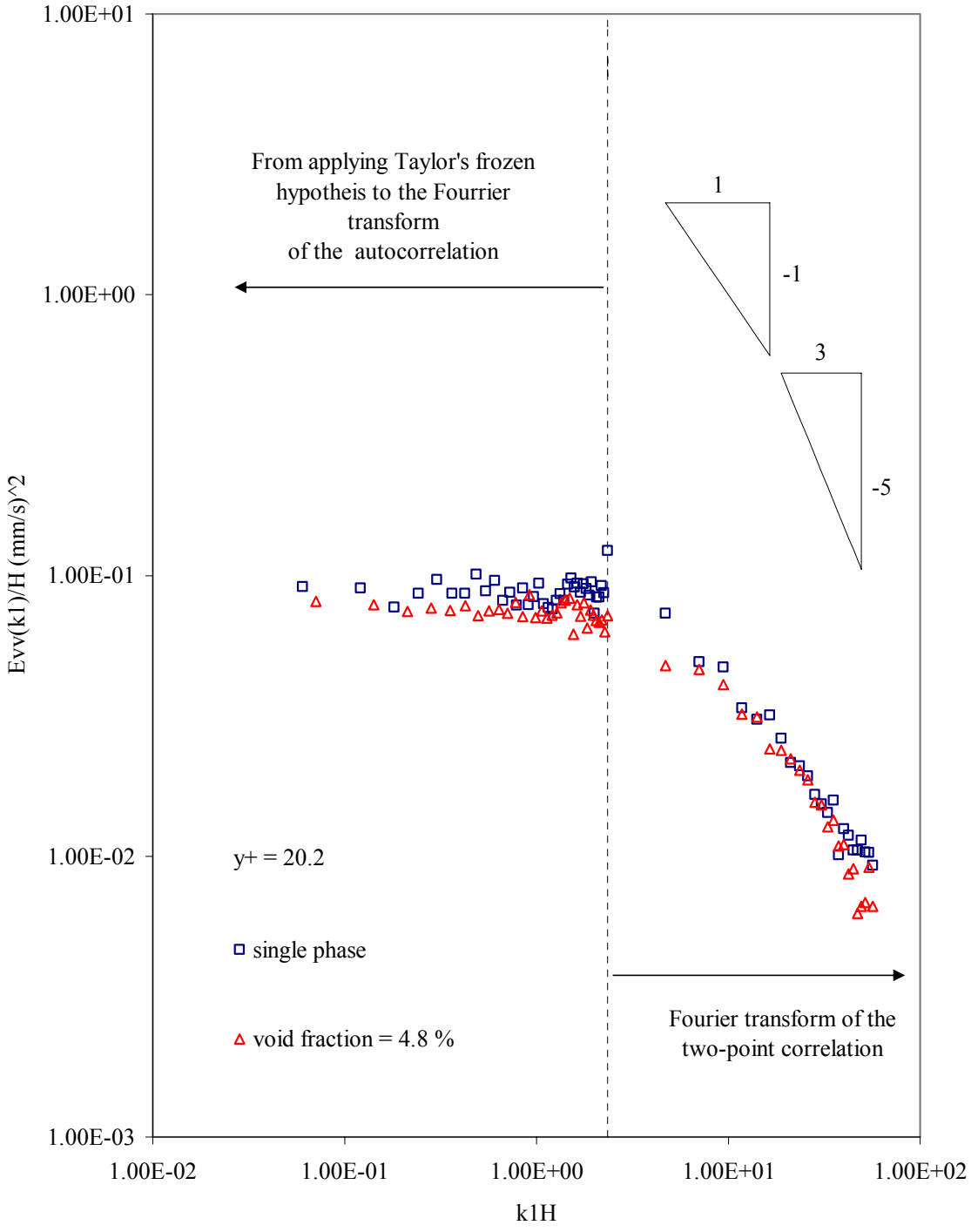

FIGURE 40. Dimensional normal spectra versus non-dimensional wavenumber at y/H = 0.06.

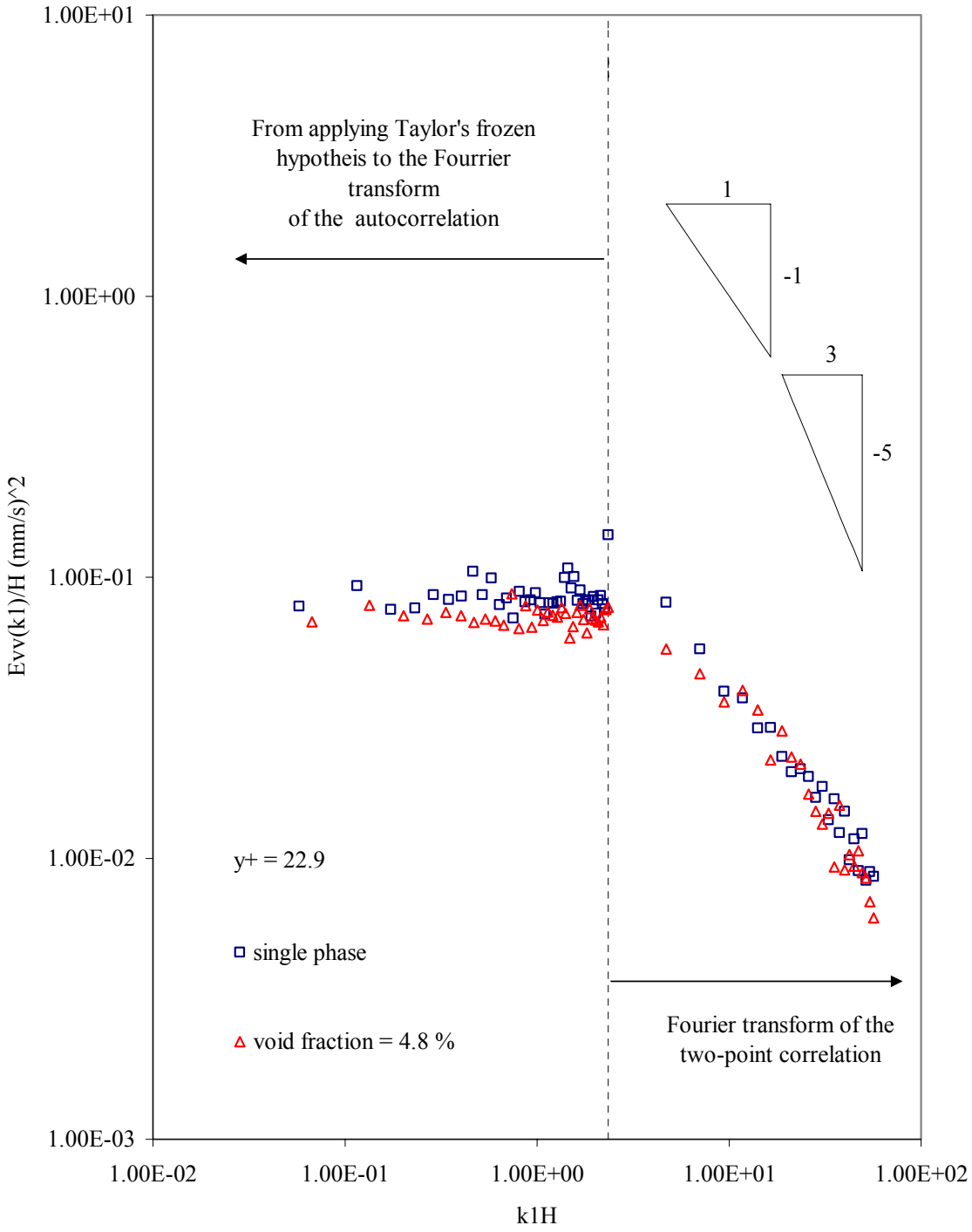

FIGURE 41. Dimensional normal spectra versus non-dimensional wavenumber at y/H = 0.069.

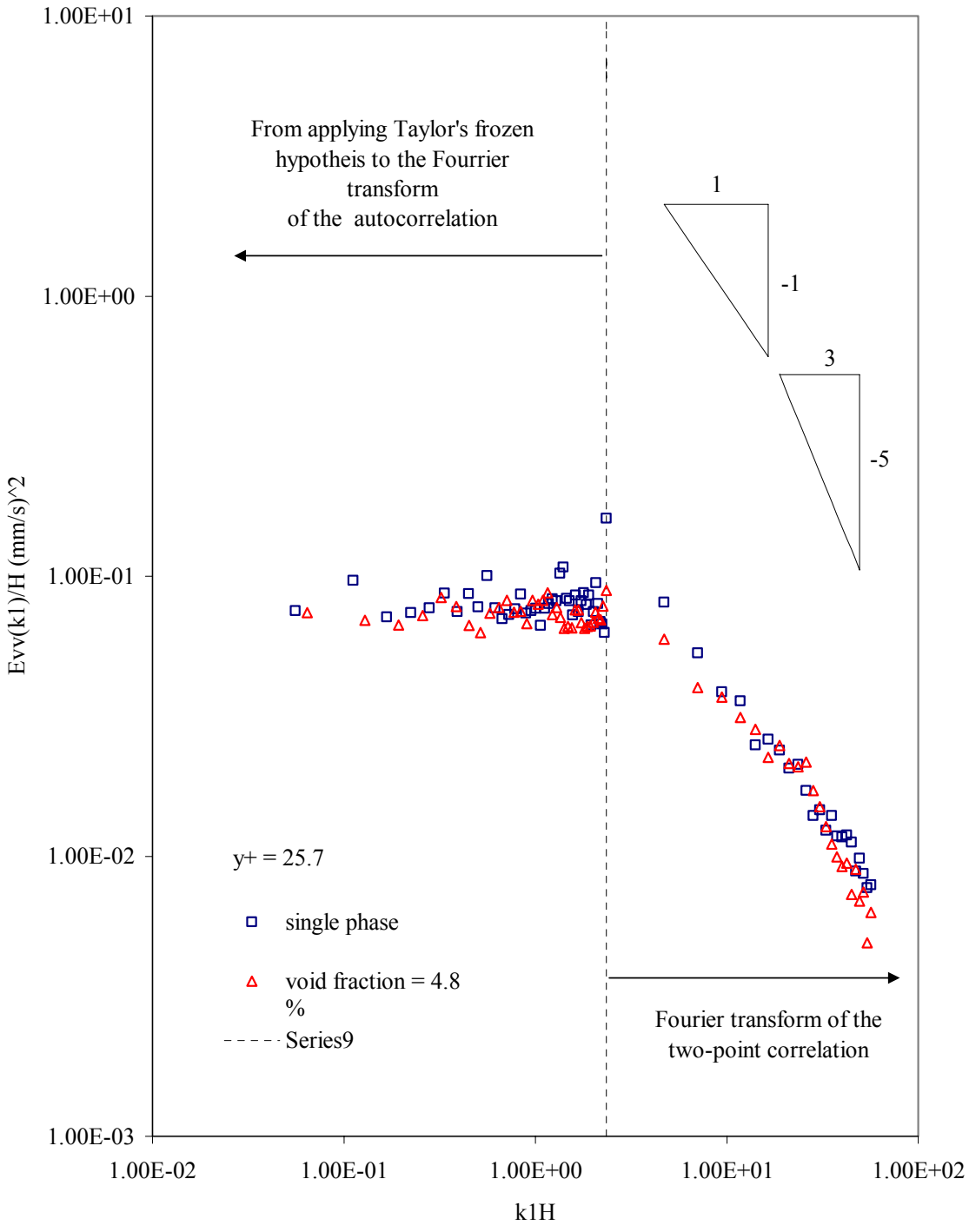

FIGURE 42. Dimensional normal spectra versus non-dimensional wavenumber at y/H = 0.077.

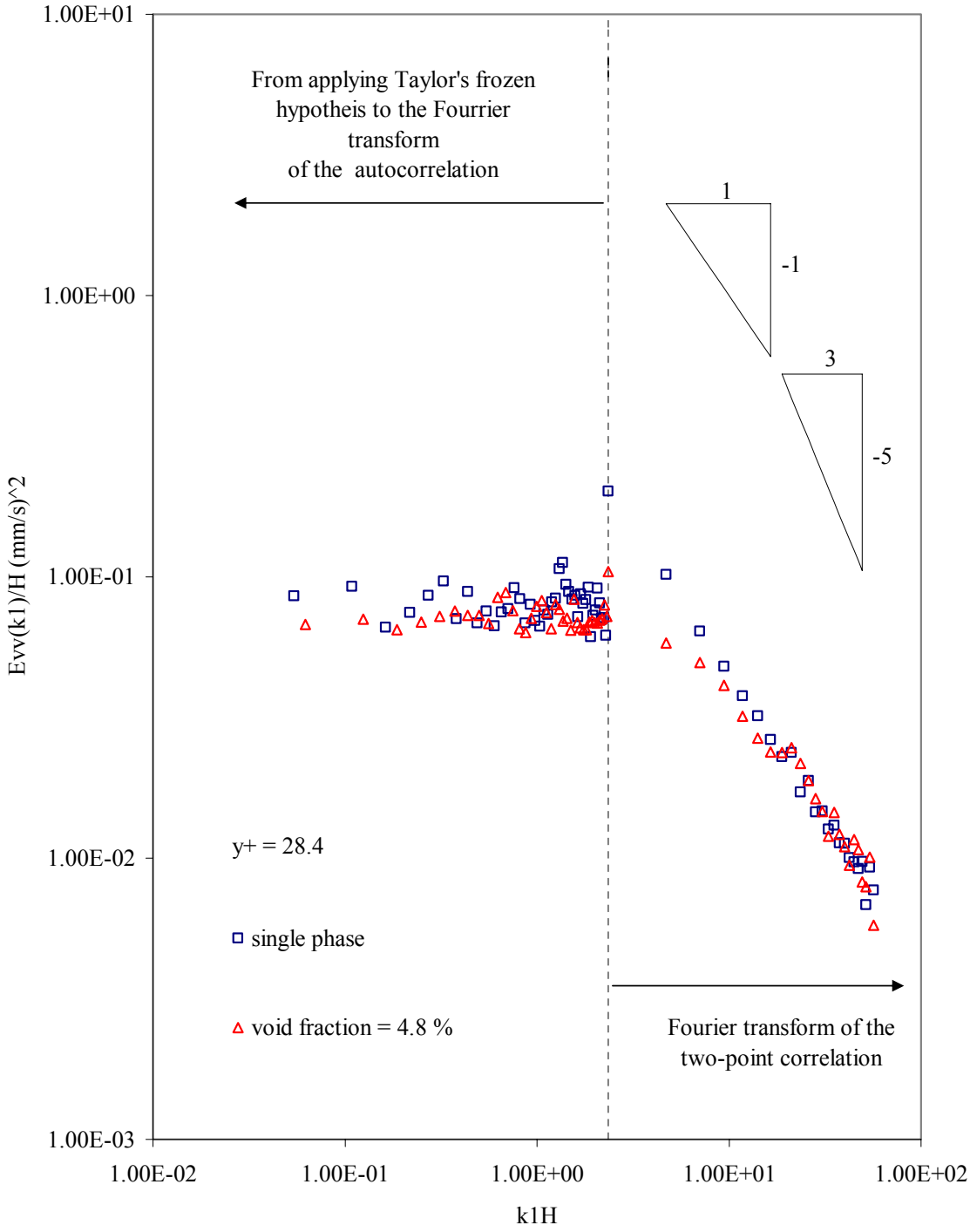

FIGURE 43. Dimensional normal spectra versus non-dimensional wavenumber at y/H = 0.085.

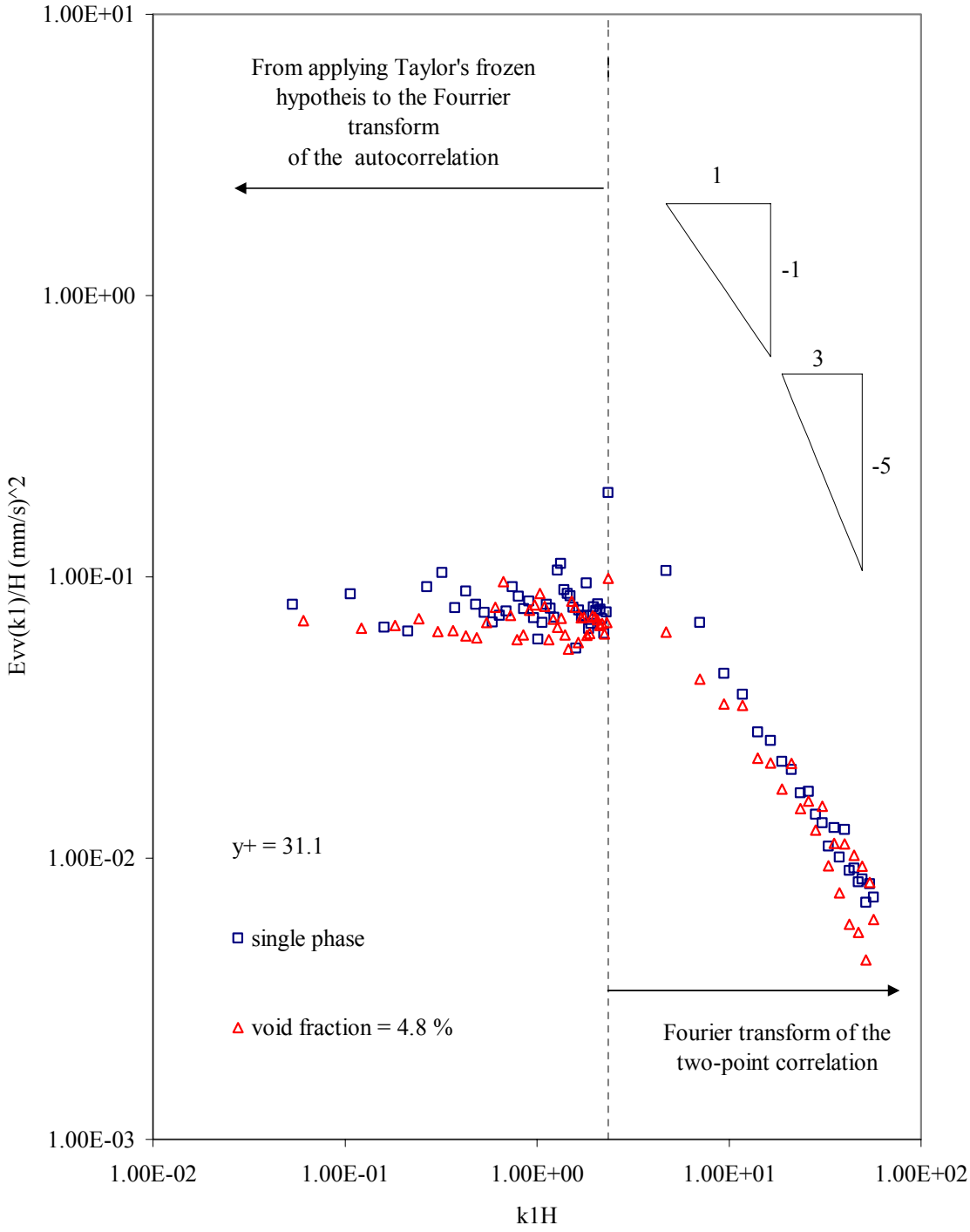

FIGURE 44. Dimensional normal spectra versus non-dimensional wavenumber at y/H = 0.094.

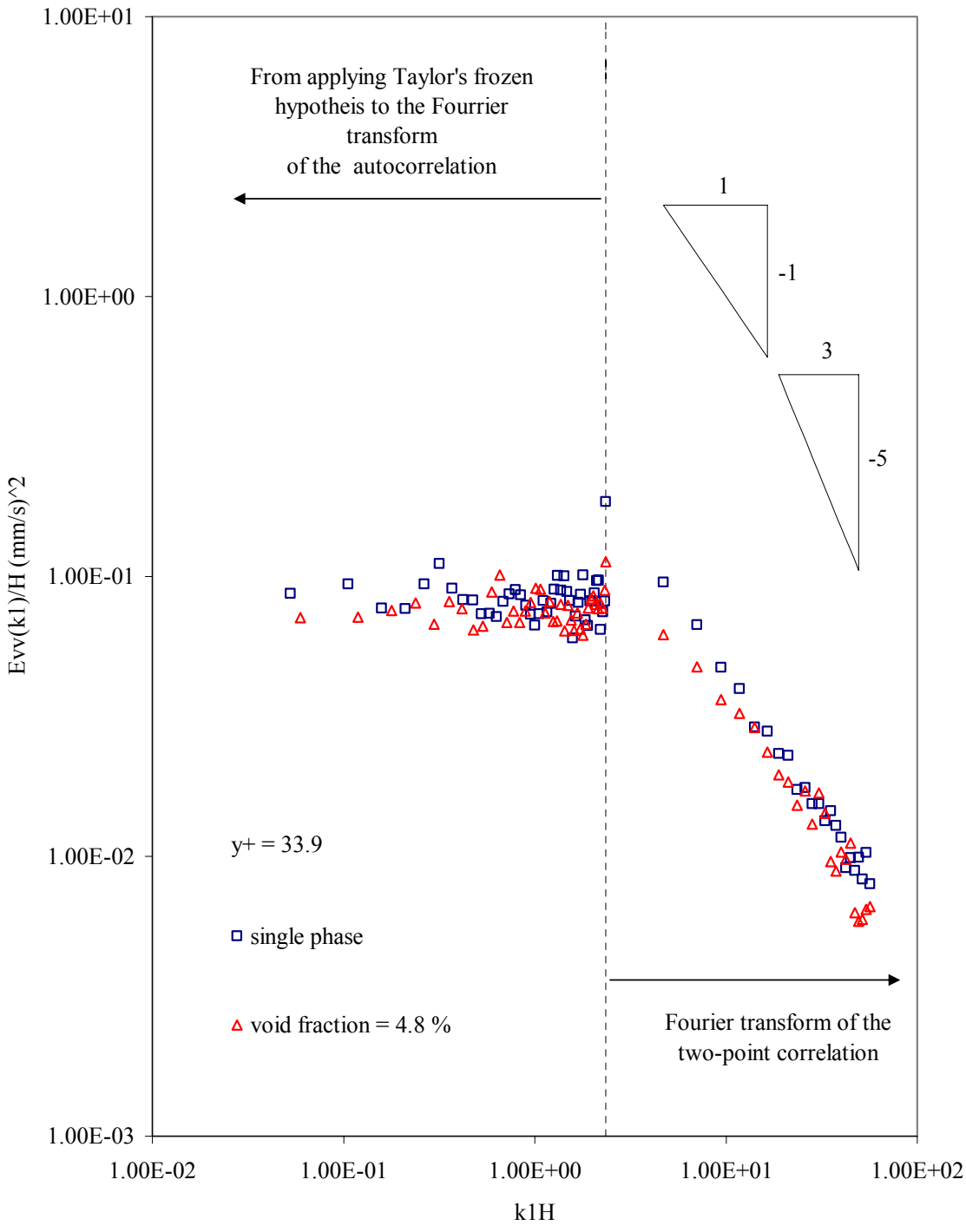

FIGURE 45. Dimensional normal spectra versus non-dimensional wavenumber at y/H = 0.10.

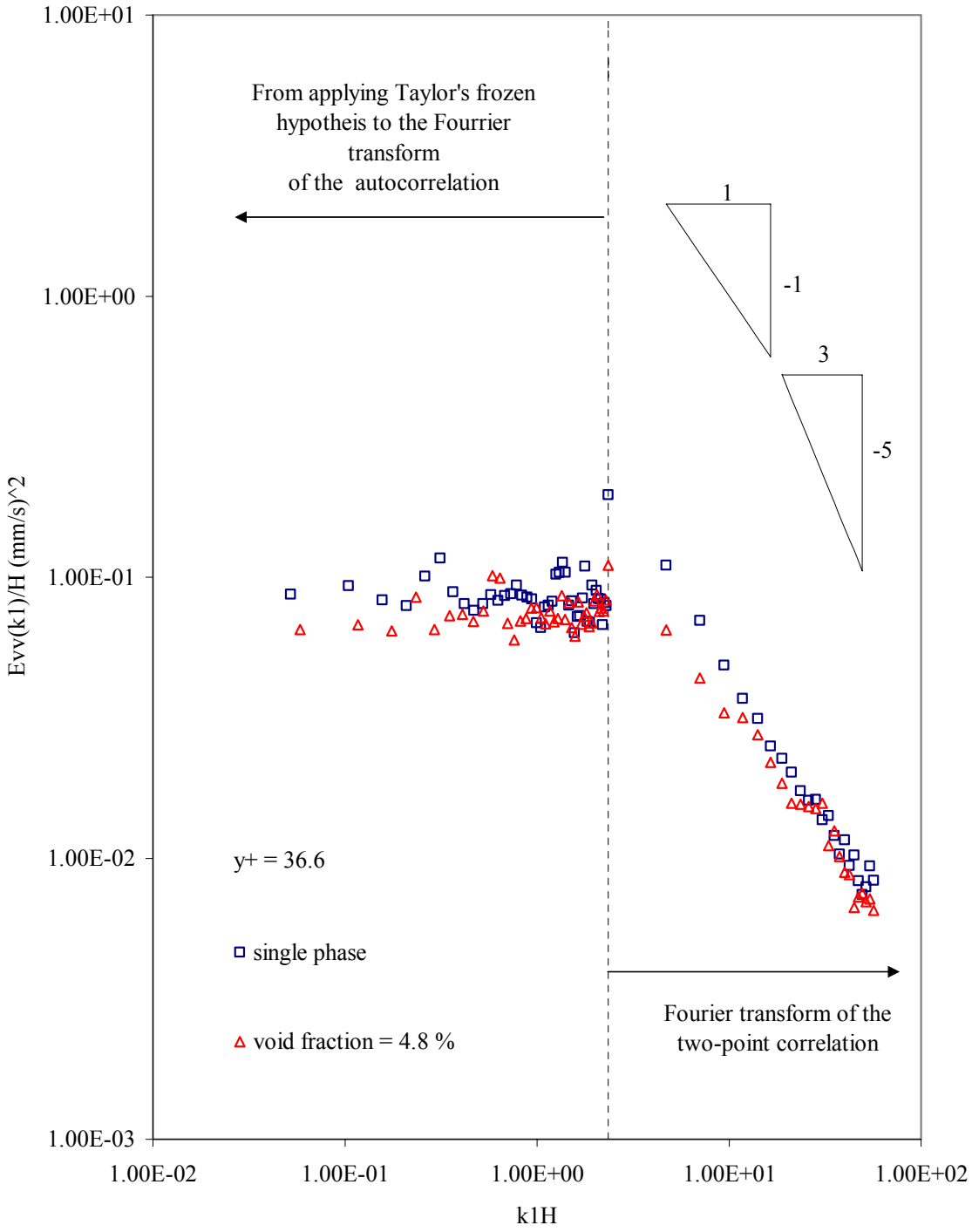

FIGURE 46. Dimensional normal spectra versus non-dimensional wavenumber at y/H = 0.11.

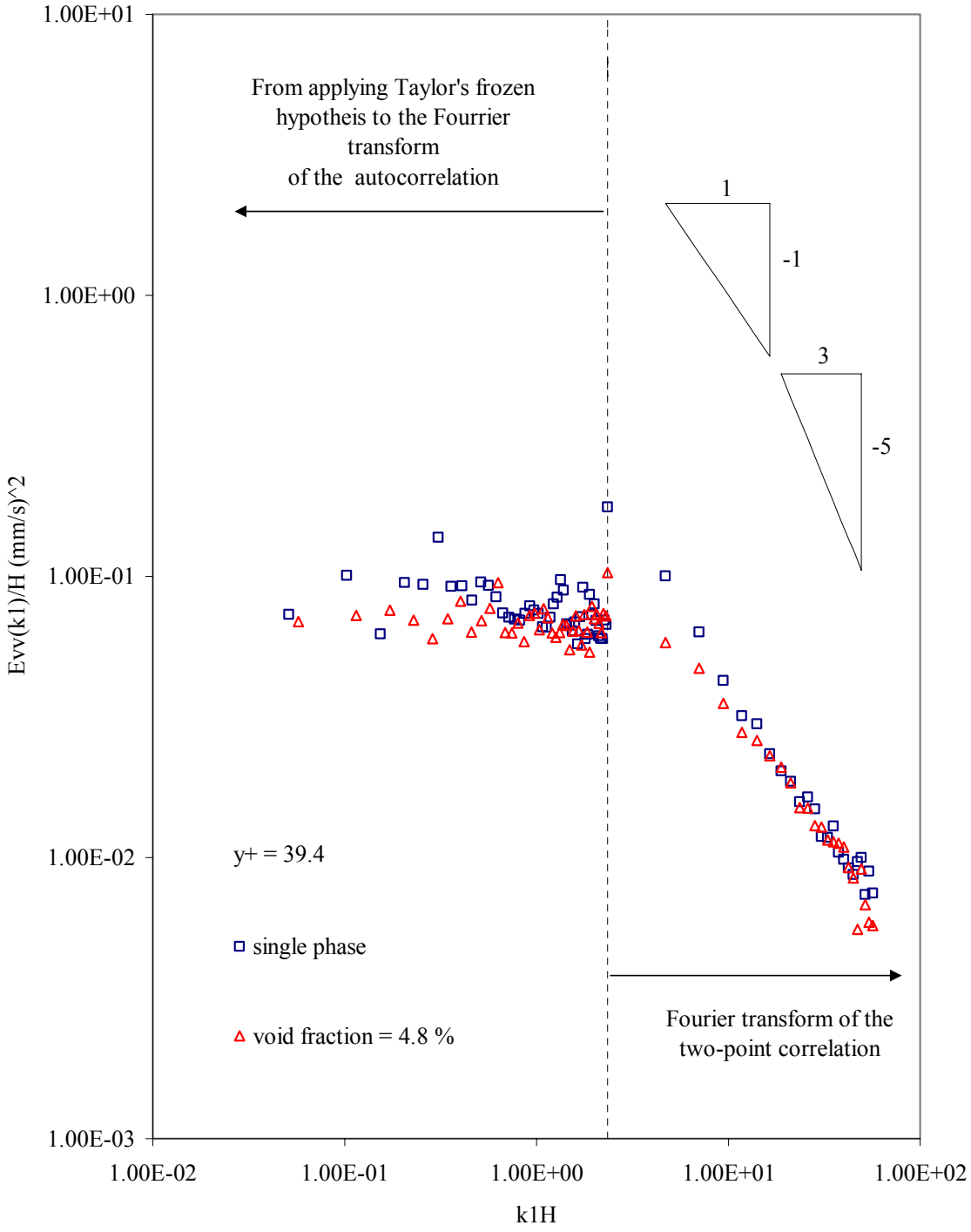

FIGURE 47. Dimensional normal spectra versus non-dimensional wavenumber at y/H = 0.118.

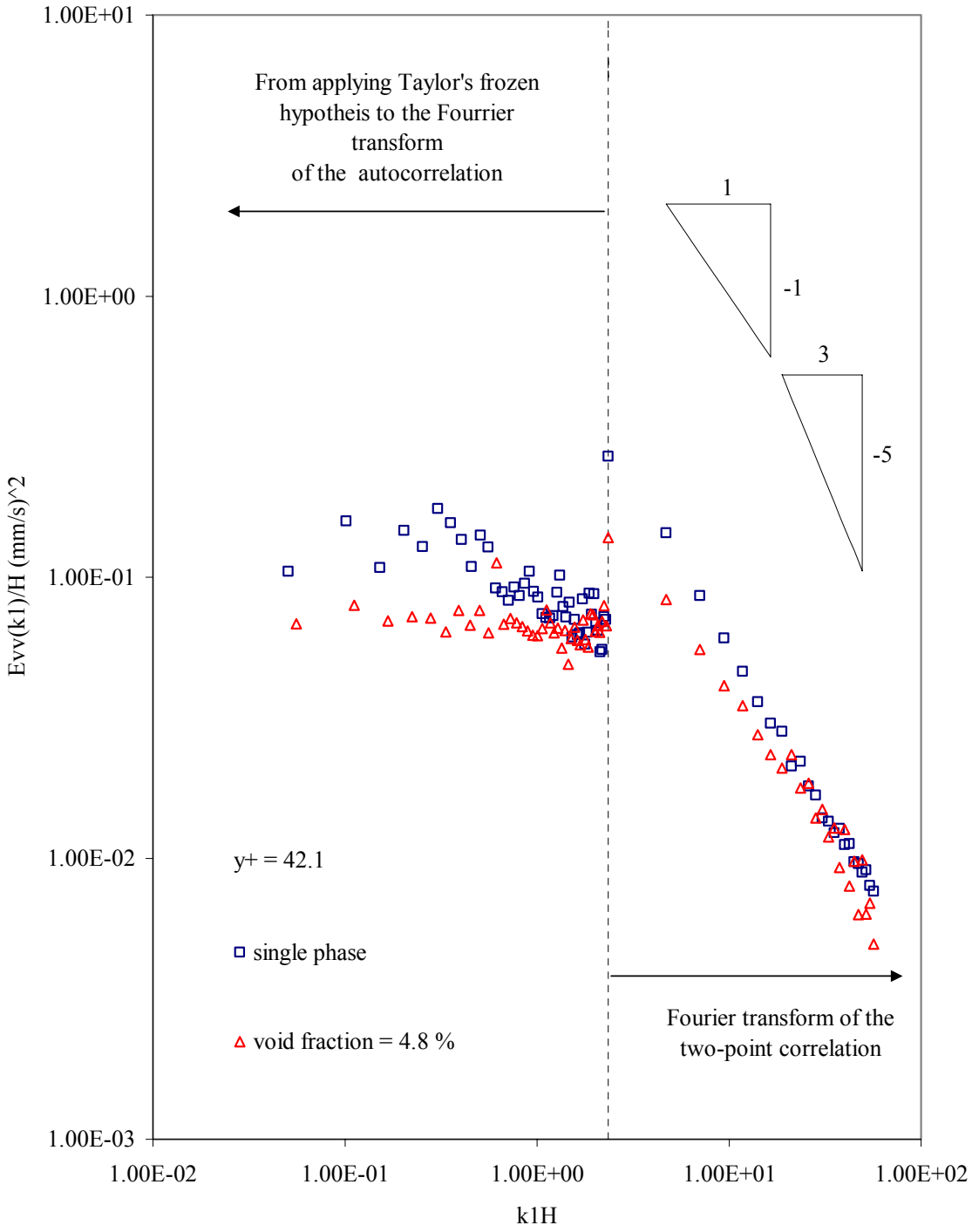

FIGURE 48. Dimensional normal spectra versus non-dimensional wavenumber at y/H = 0.127.

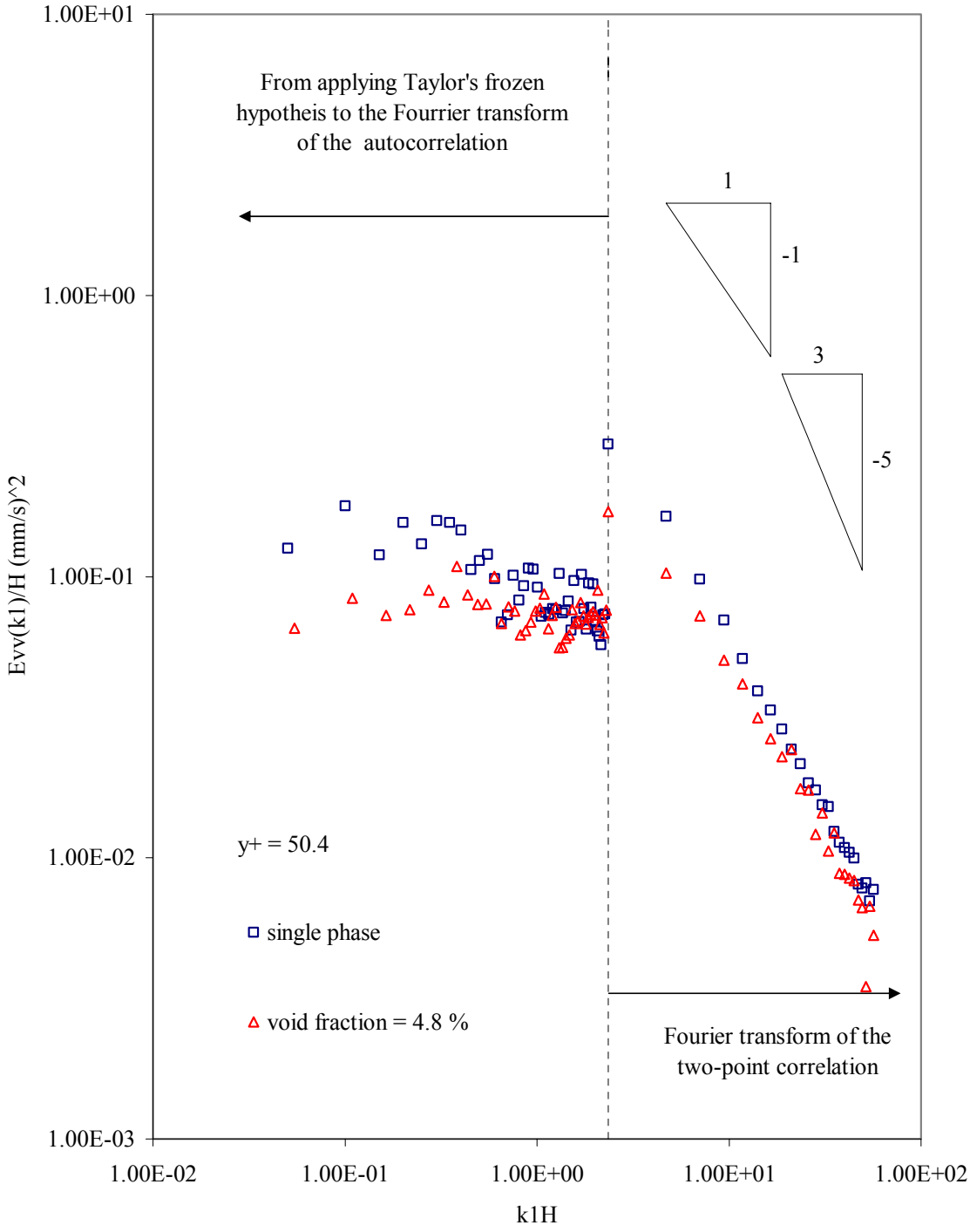

FIGURE 49. Dimensional normal spectra versus non-dimensional wavenumber at y/H = 0.15.

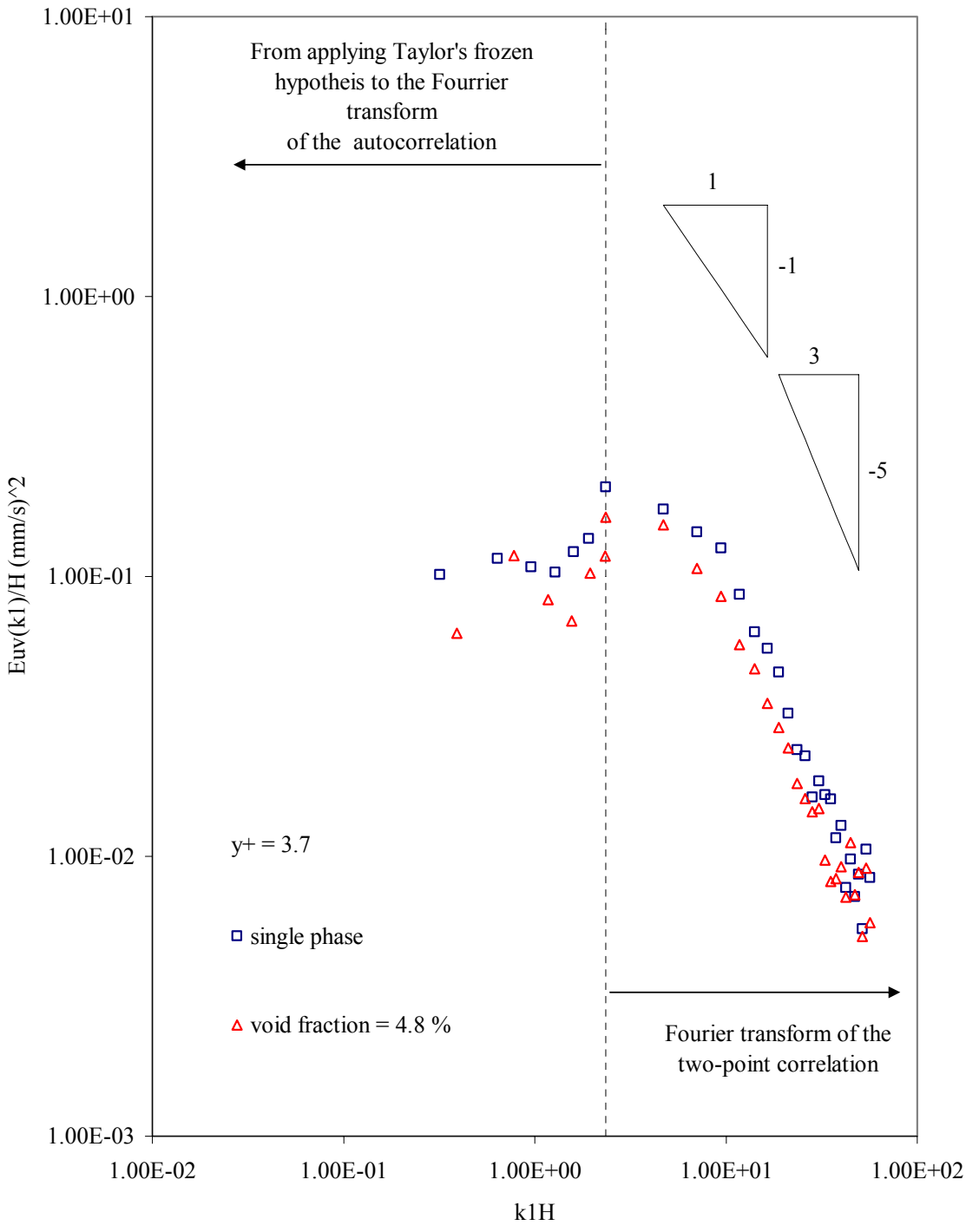

FIGURE 50. Dimensional $E_{uv}(k_1)$ spectra versus non-dimensional wavenumber at y/H = 0.01.

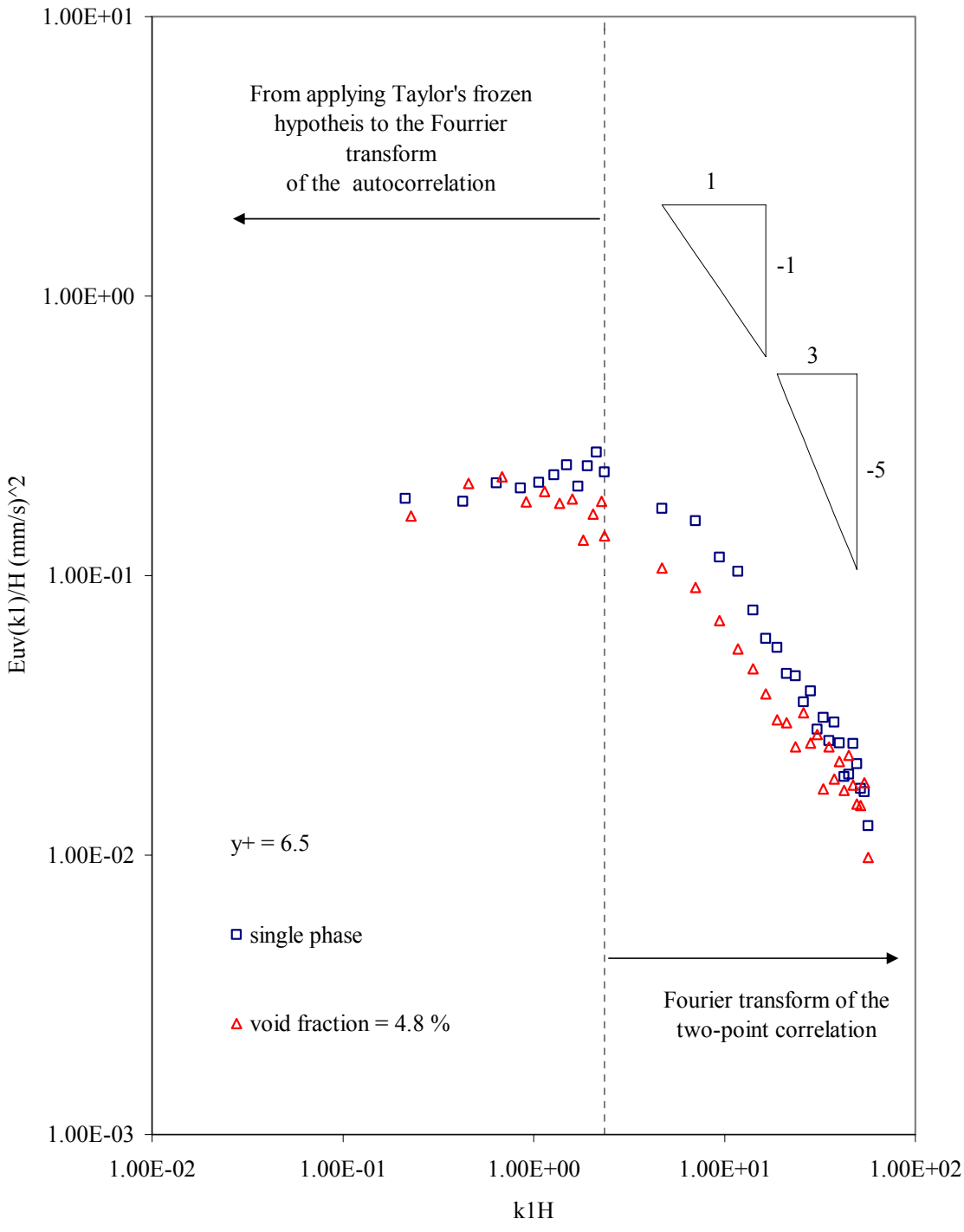

FIGURE 51. Dimensional $E_{uv}(k_1)$ spectra versus non-dimensional wavenumber at y/H = 0.019.

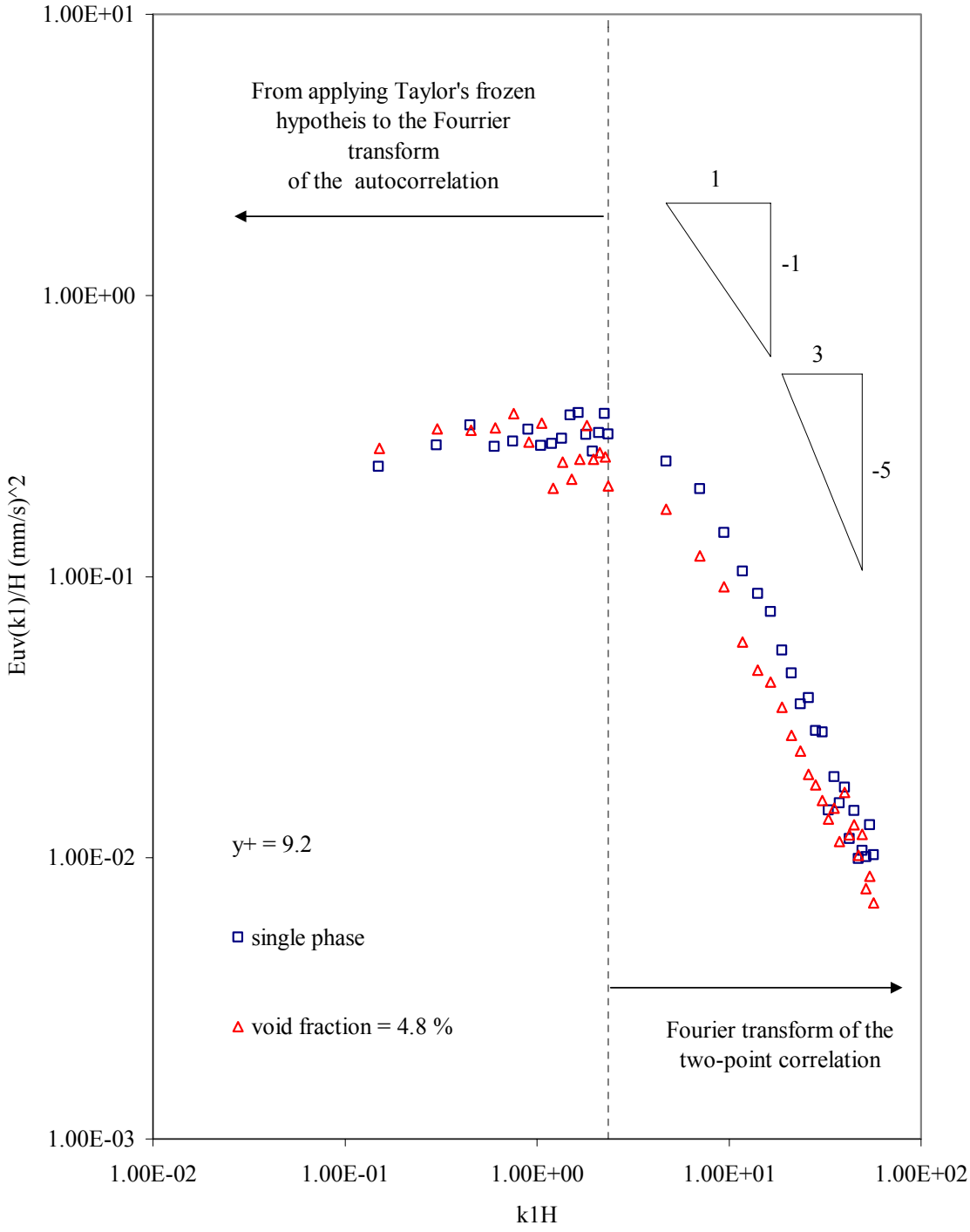

FIGURE 52. Dimensional $E_{uv}(k_1)$ spectra versus non-dimensional wavenumber at y/H = 0.027.

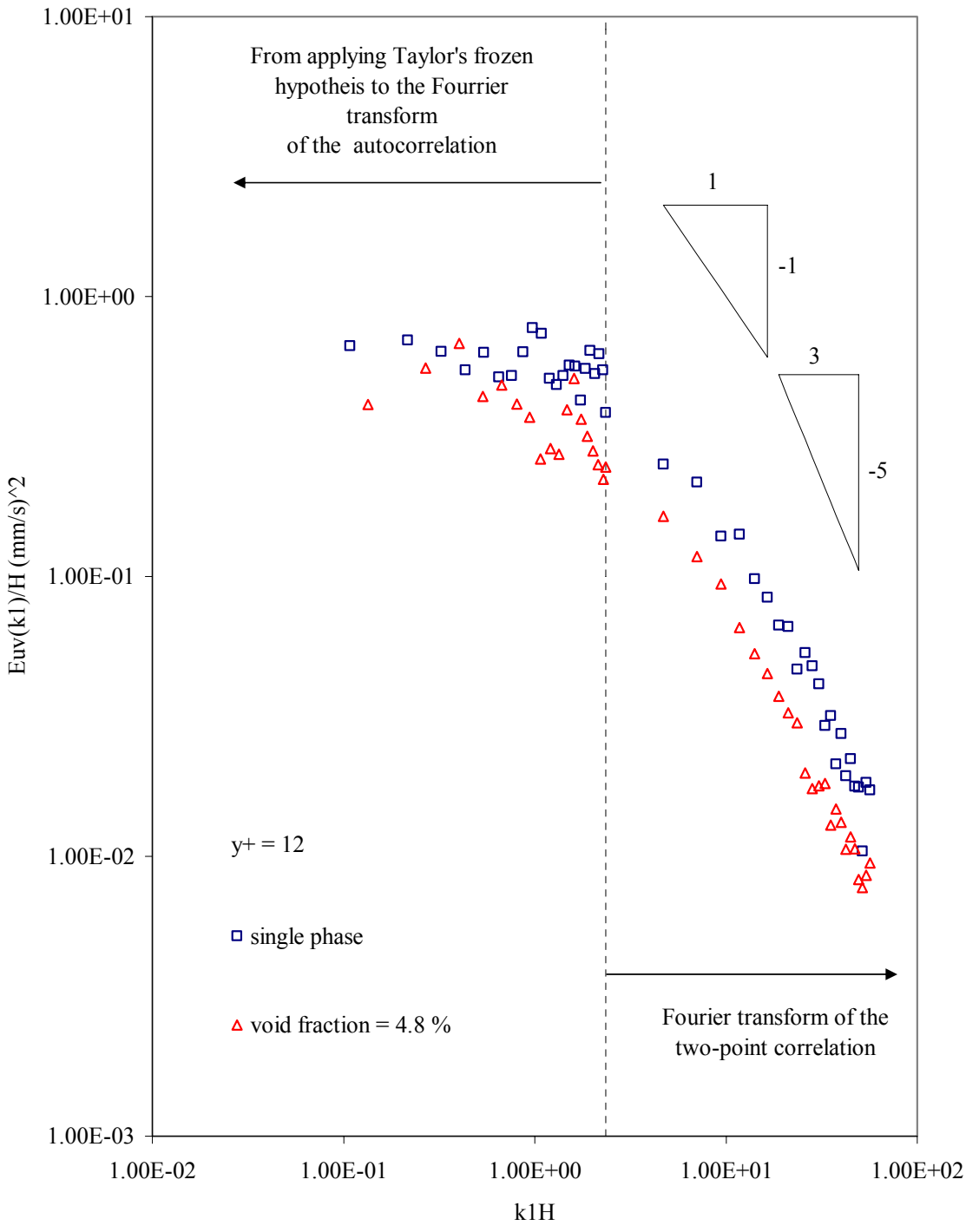

FIGURE 53. Dimensional $E_{uv}(k_1)$ spectra versus non-dimensional wavenumber at y/H = 0.036.

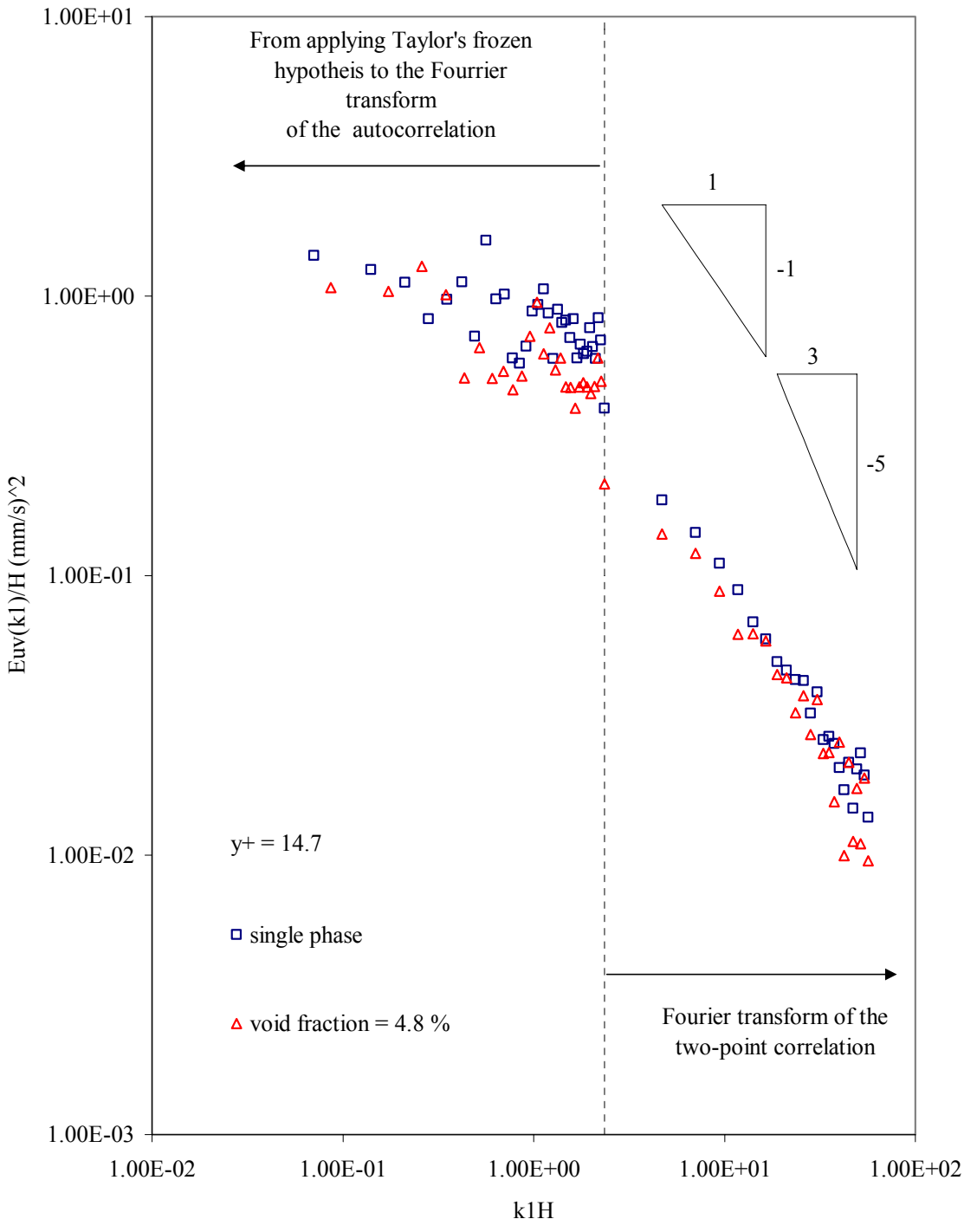

FIGURE 54. Dimensional $E_{uv}(k_1)$ spectra versus non-dimensional wavenumber at y/H = 0.044.

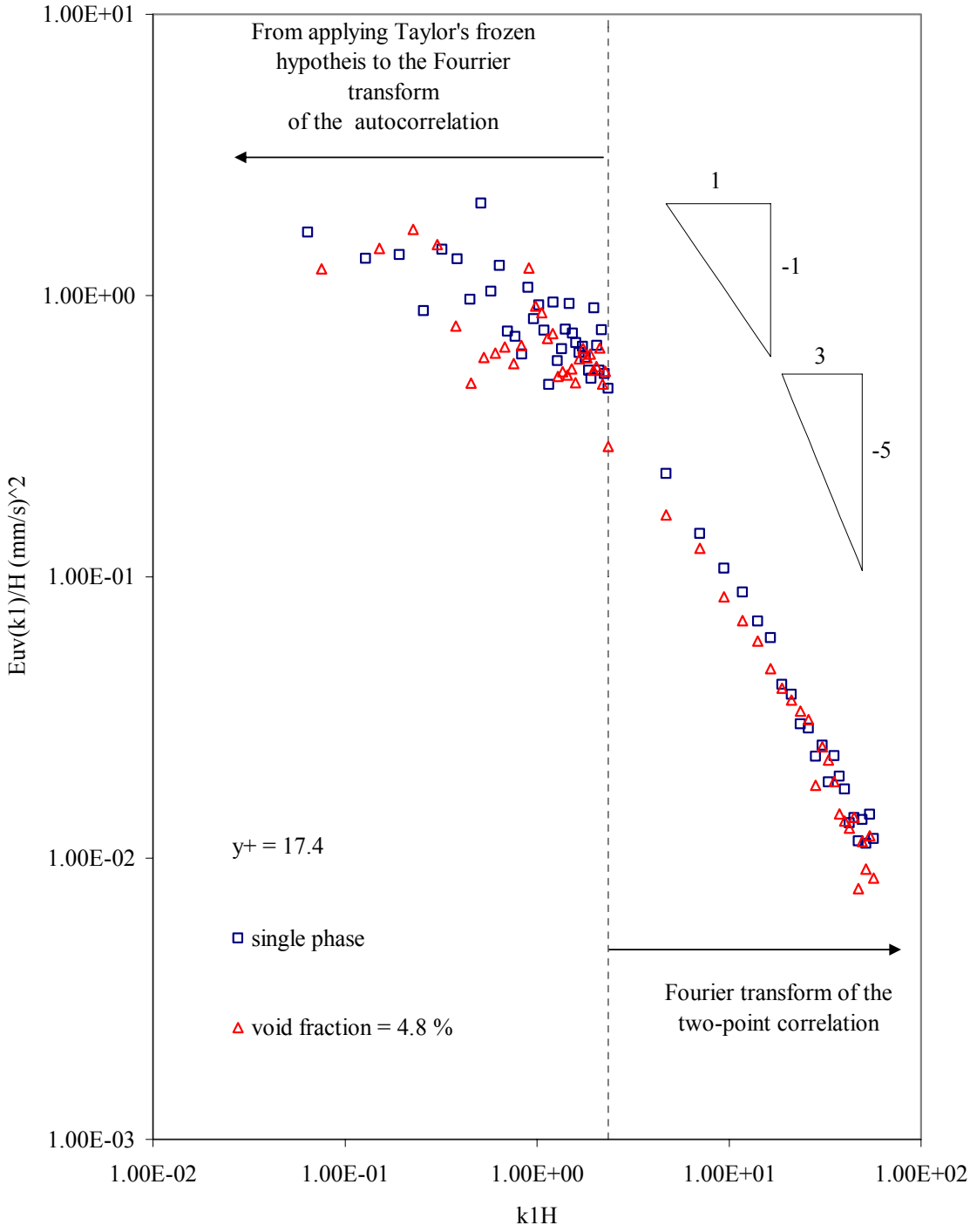

FIGURE 55. Dimensional $E_{uv}(k_1)$ spectra versus non-dimensional wavenumber at y/H = 0.052.

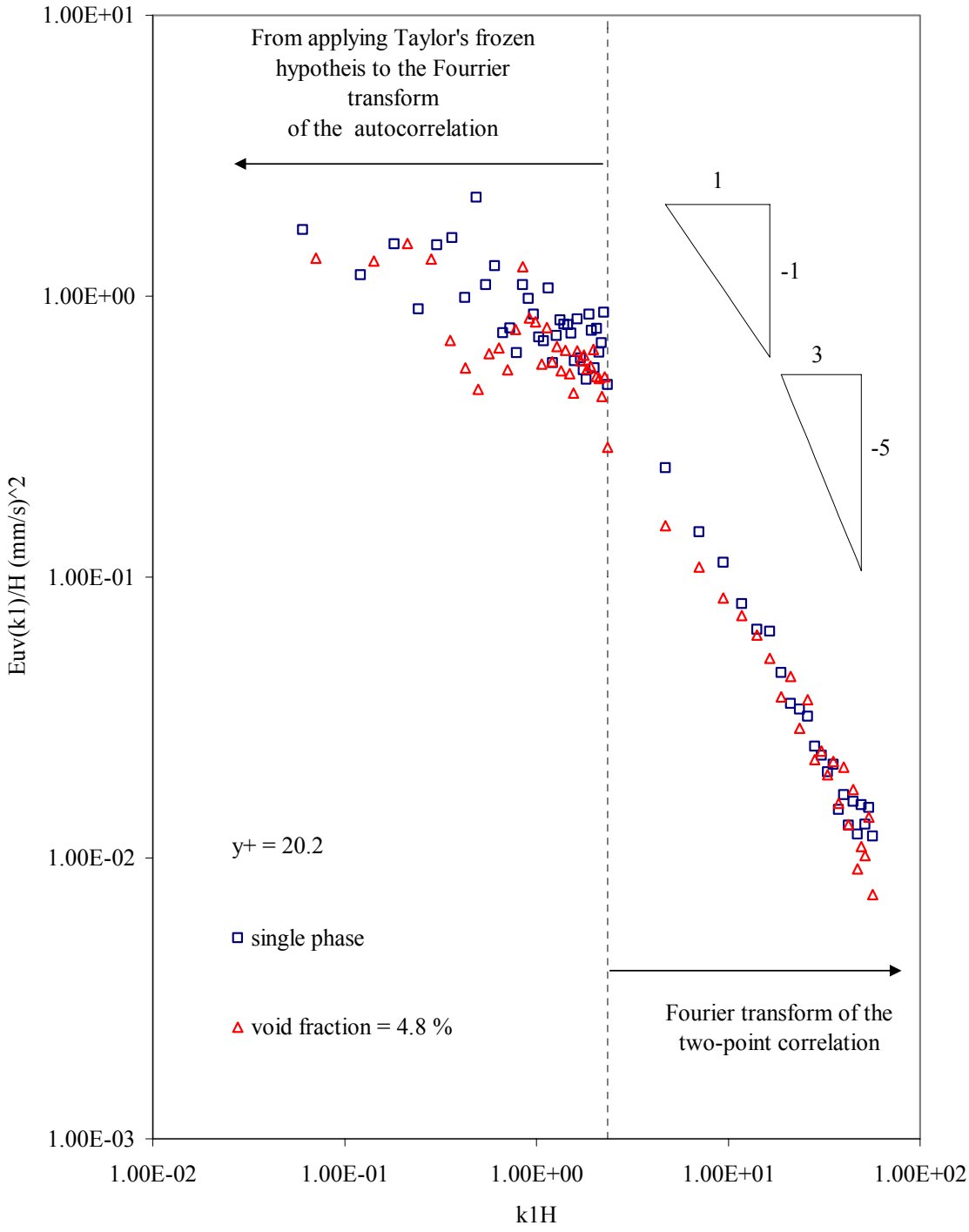

FIGURE 56. Dimensional $E_{uv}(k_1)$ spectra versus non-dimensional wavenumber at y/H = 0.06.

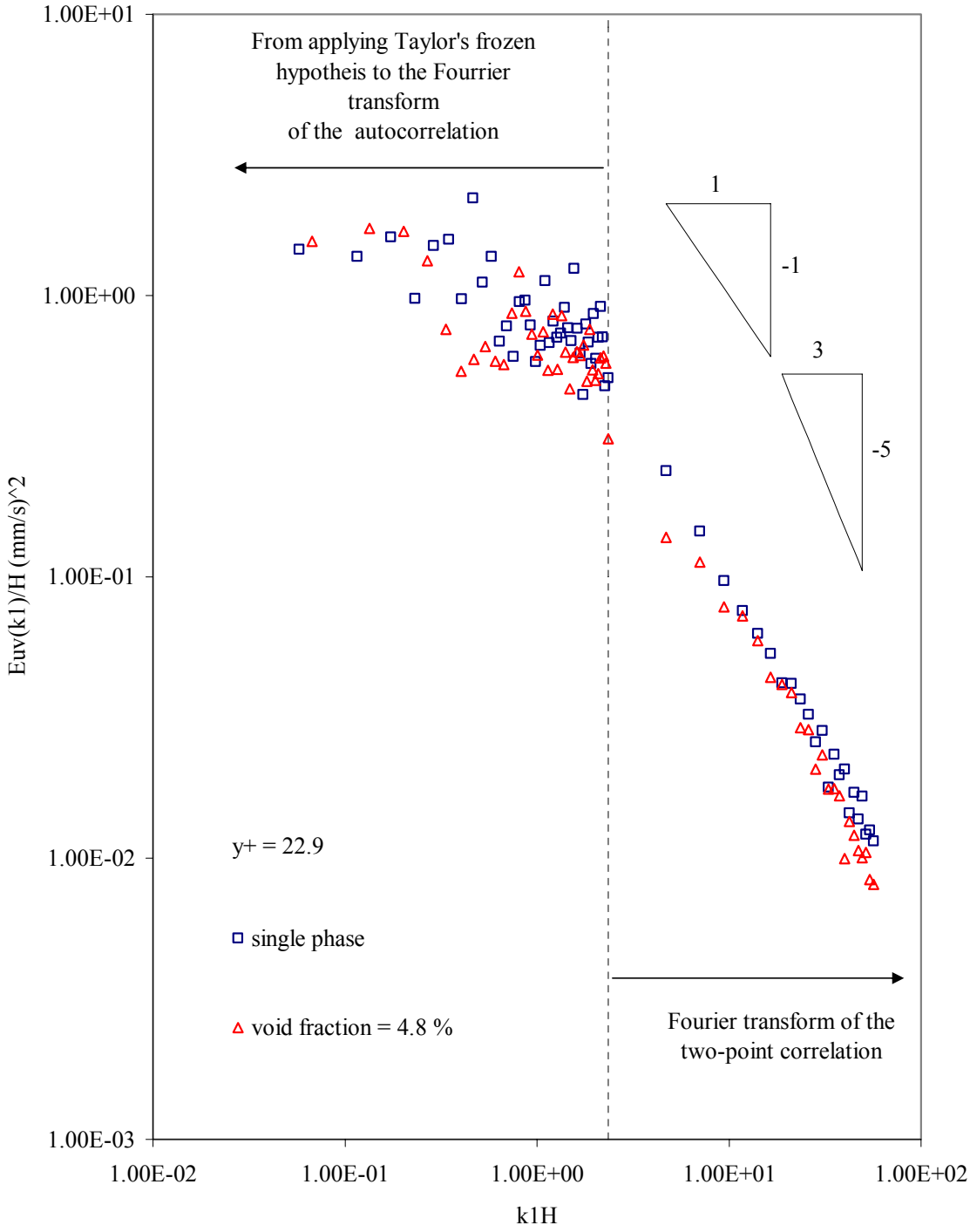

FIGURE 57. Dimensional $E_{uv}(k_1)$ spectra versus non-dimensional wavenumber at y/H = 0.069.

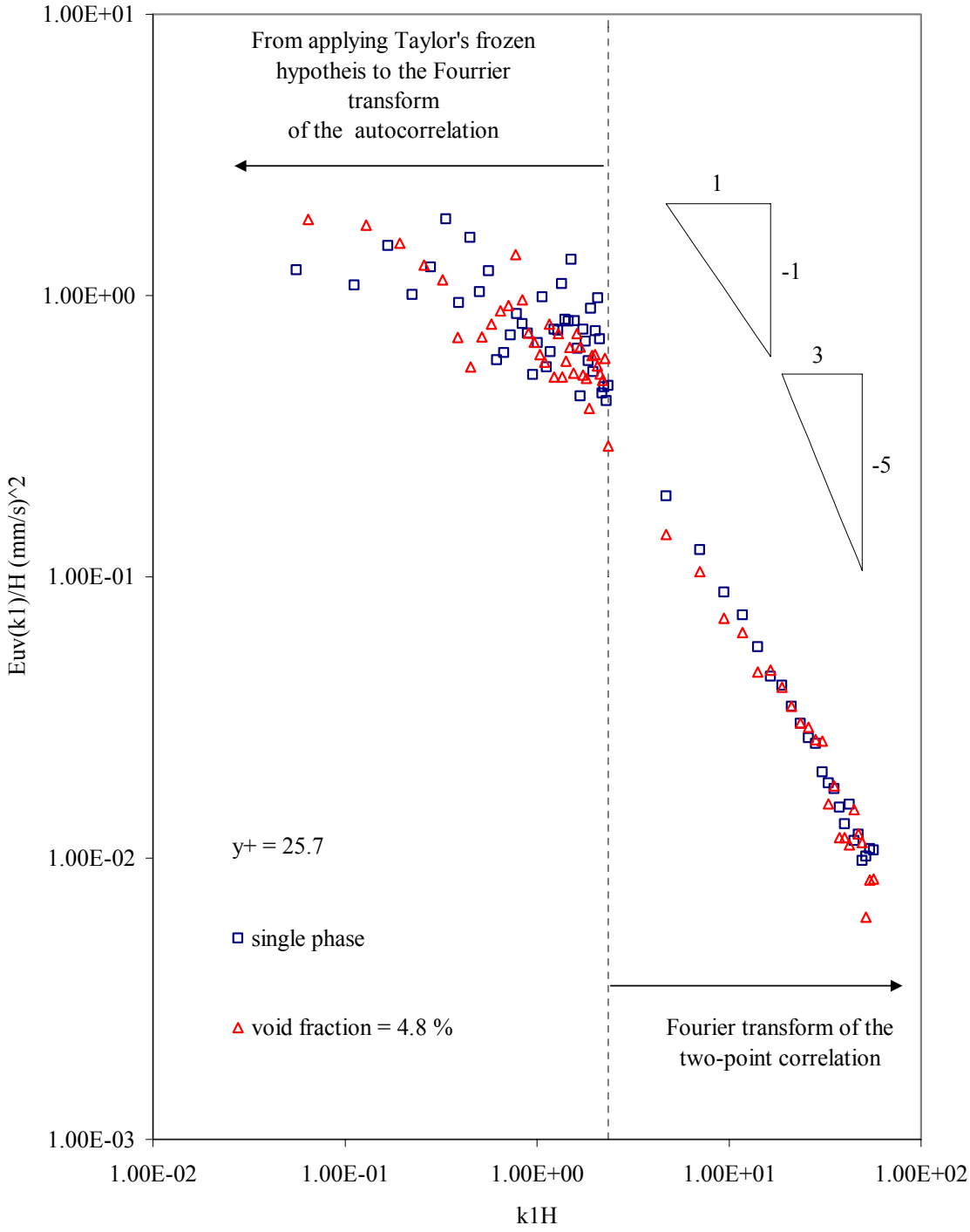

FIGURE 58. Dimensional $E_{uv}(k_1)$ spectra versus non-dimensional wavenumber at y/H = 0.077.

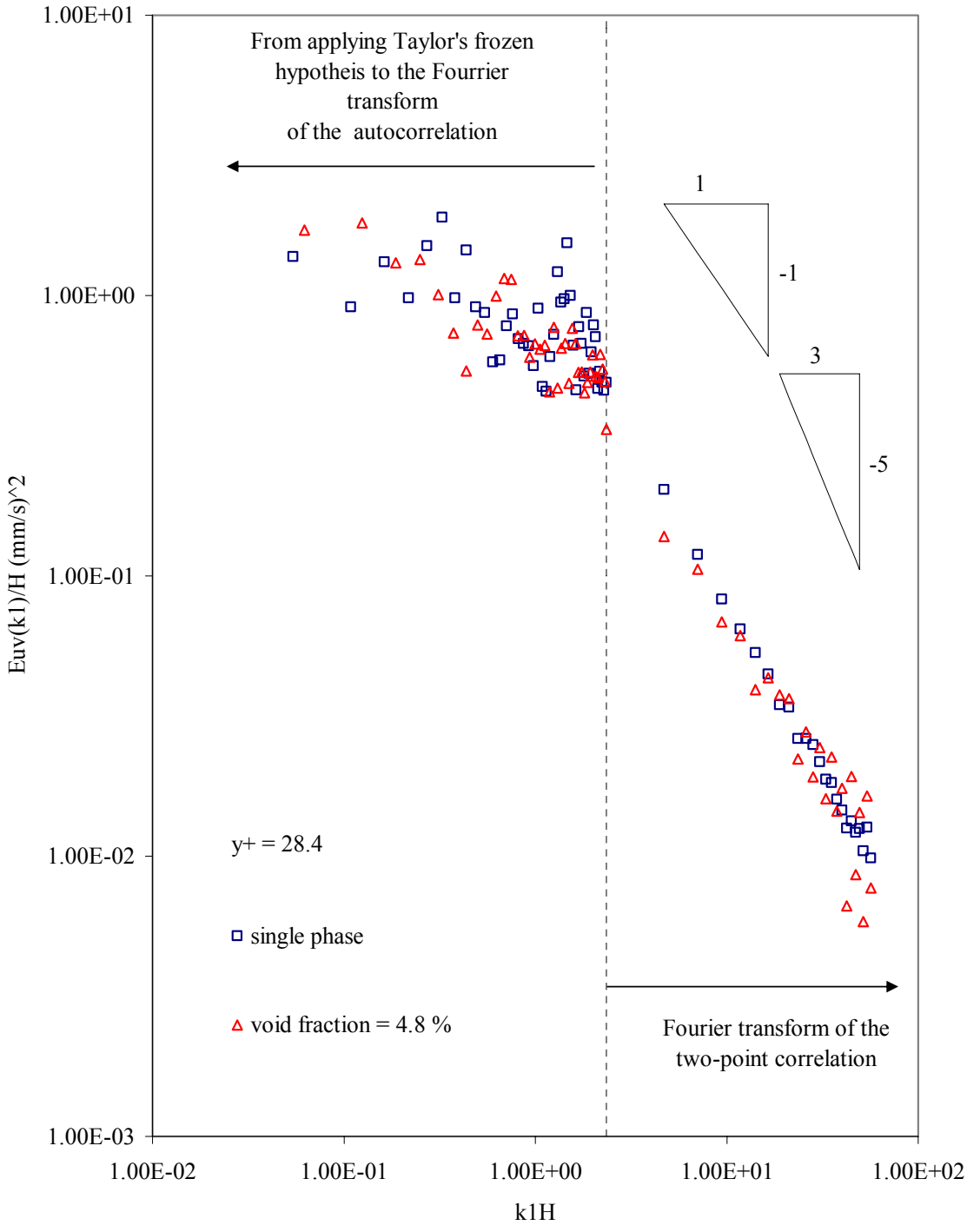

FIGURE 59. Dimensional $E_{uv}(k_1)$ spectra versus non-dimensional wavenumber at y/H = 0.085.

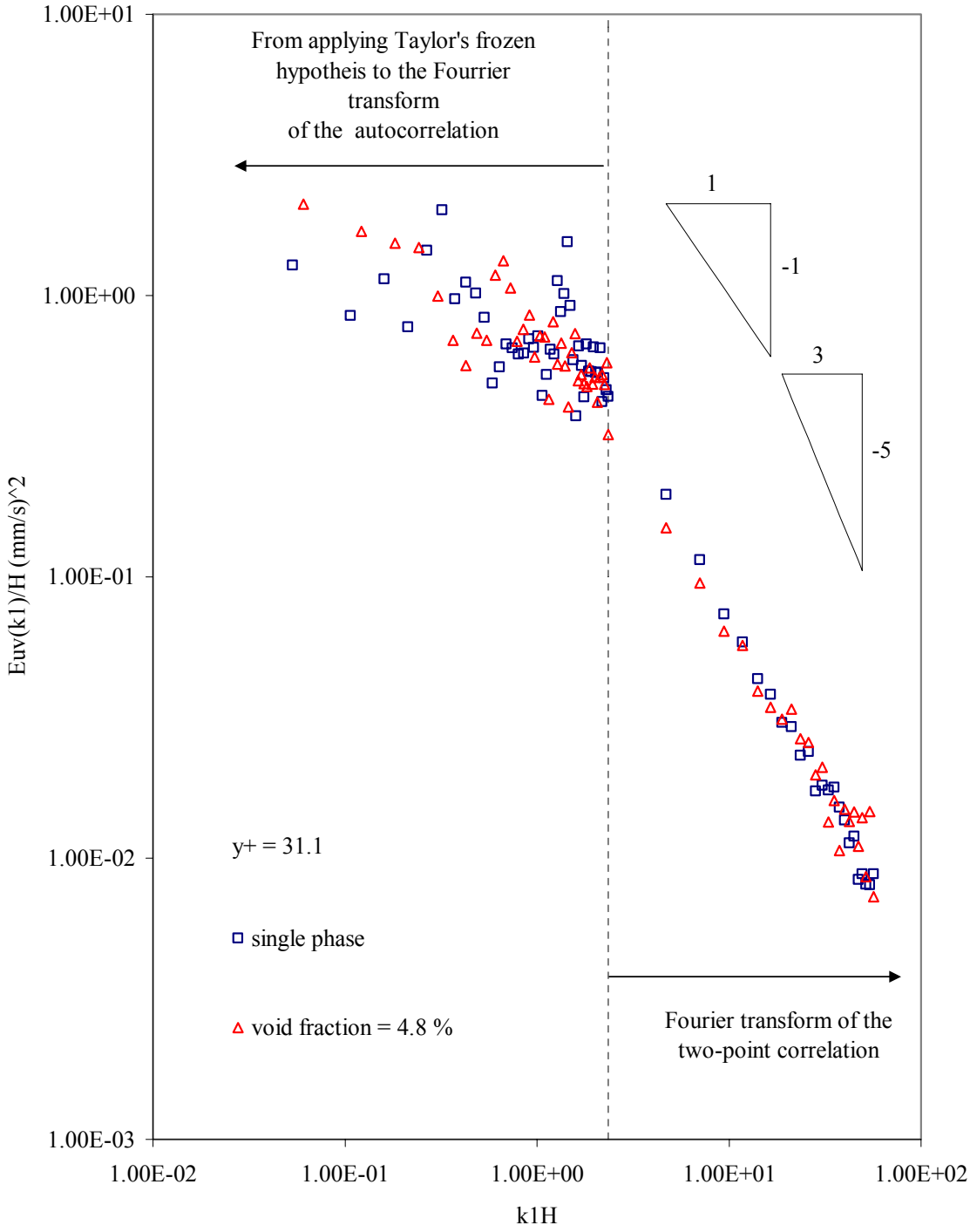

FIGURE 60. Dimensional $E_{uv}(k_1)$ spectra versus non-dimensional wavenumber at y/H = 0.094.

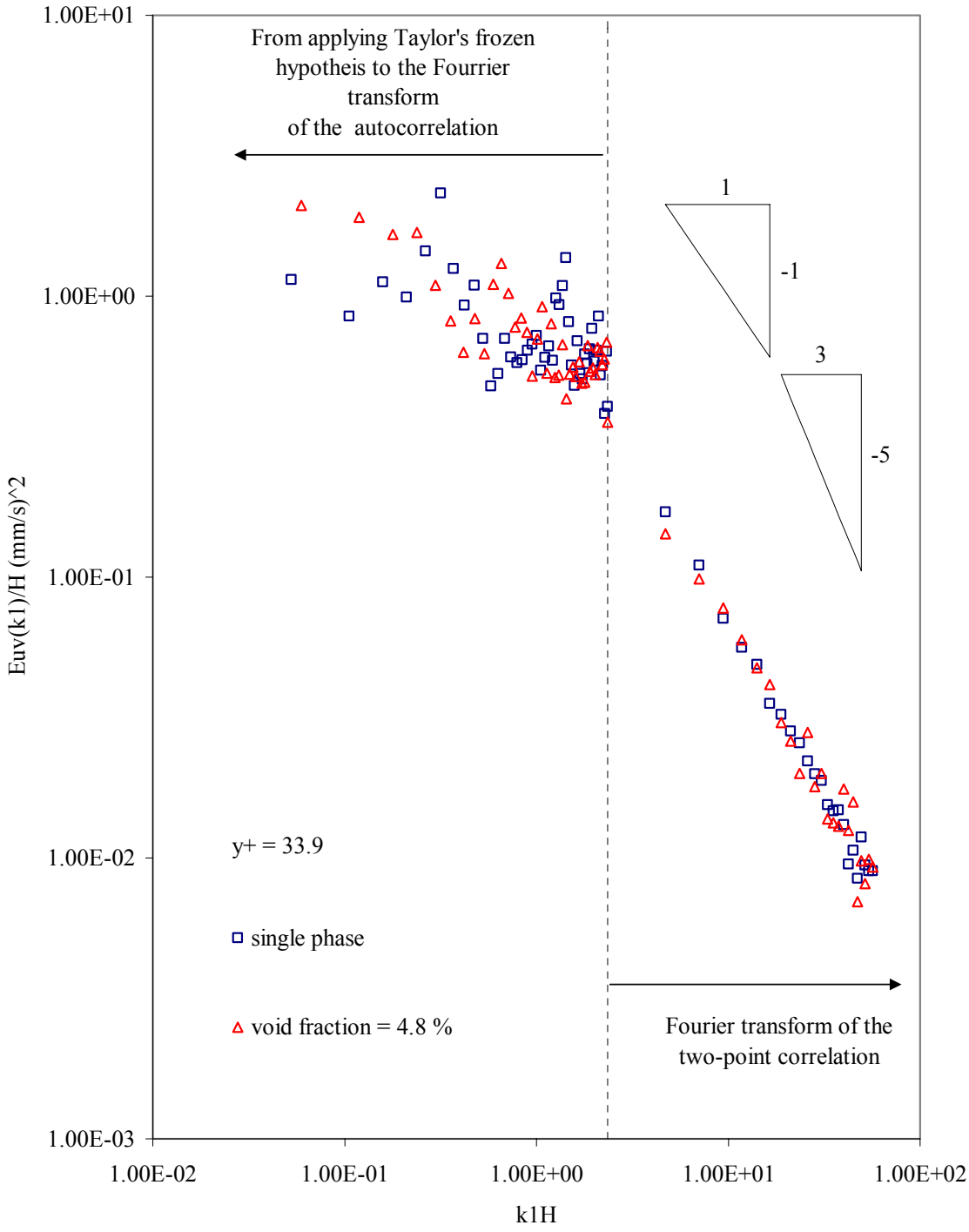

FIGURE 61. Dimensional $E_{uv}(k_1)$ spectra versus non-dimensional wavenumber at y/H = 0.1.

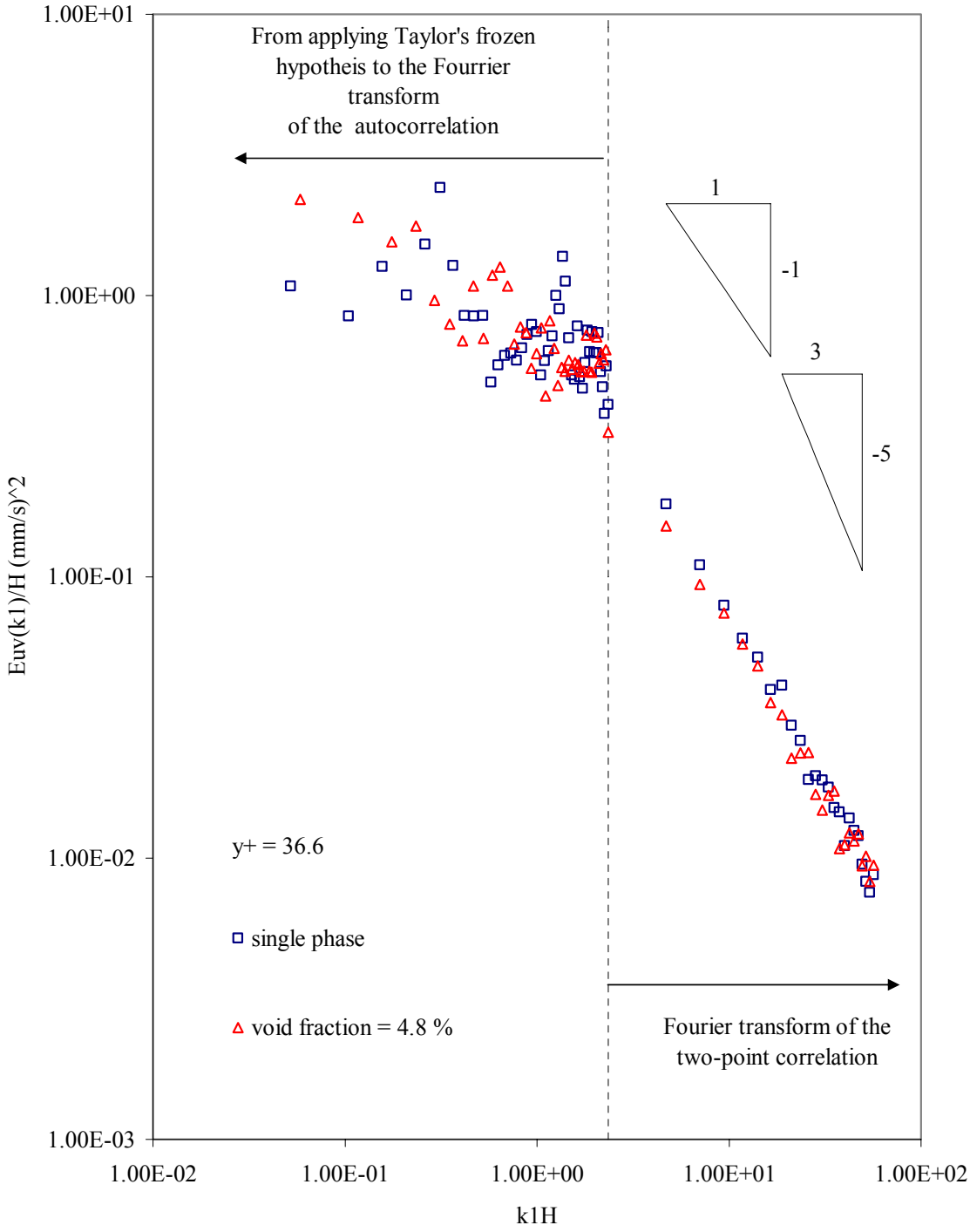

FIGURE 62. Dimensional $E_{uv}(k_1)$ spectra versus non-dimensional wavenumber at y/H = 0.11.

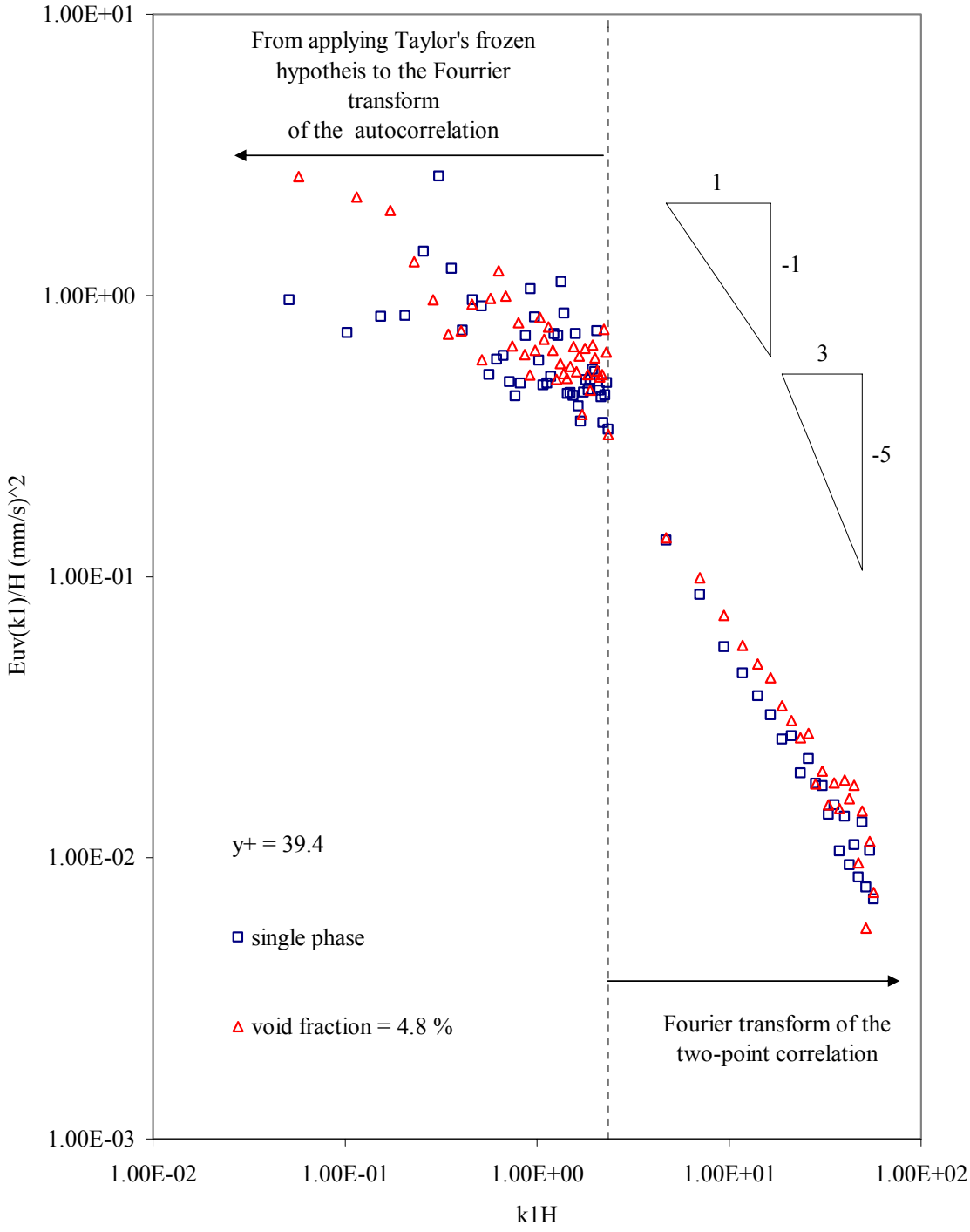

FIGURE 63. Dimensional $E_{uv}(k_1)$ spectra versus non-dimensional wavenumber at y/H = 0.118.

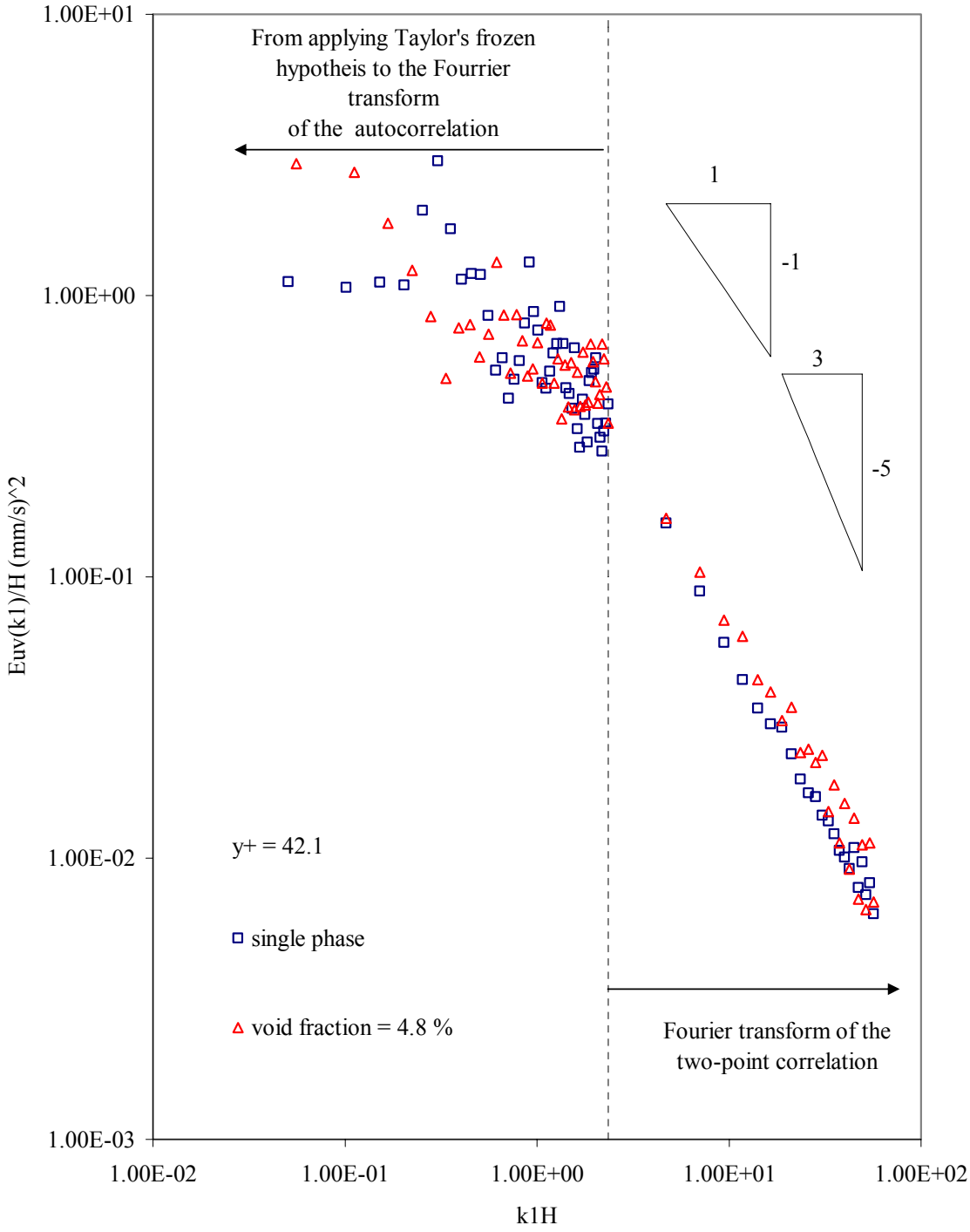

FIGURE 64. Dimensional $E_{uv}(k_1)$ spectra versus non-dimensional wavenumber at y/H = 0.127.

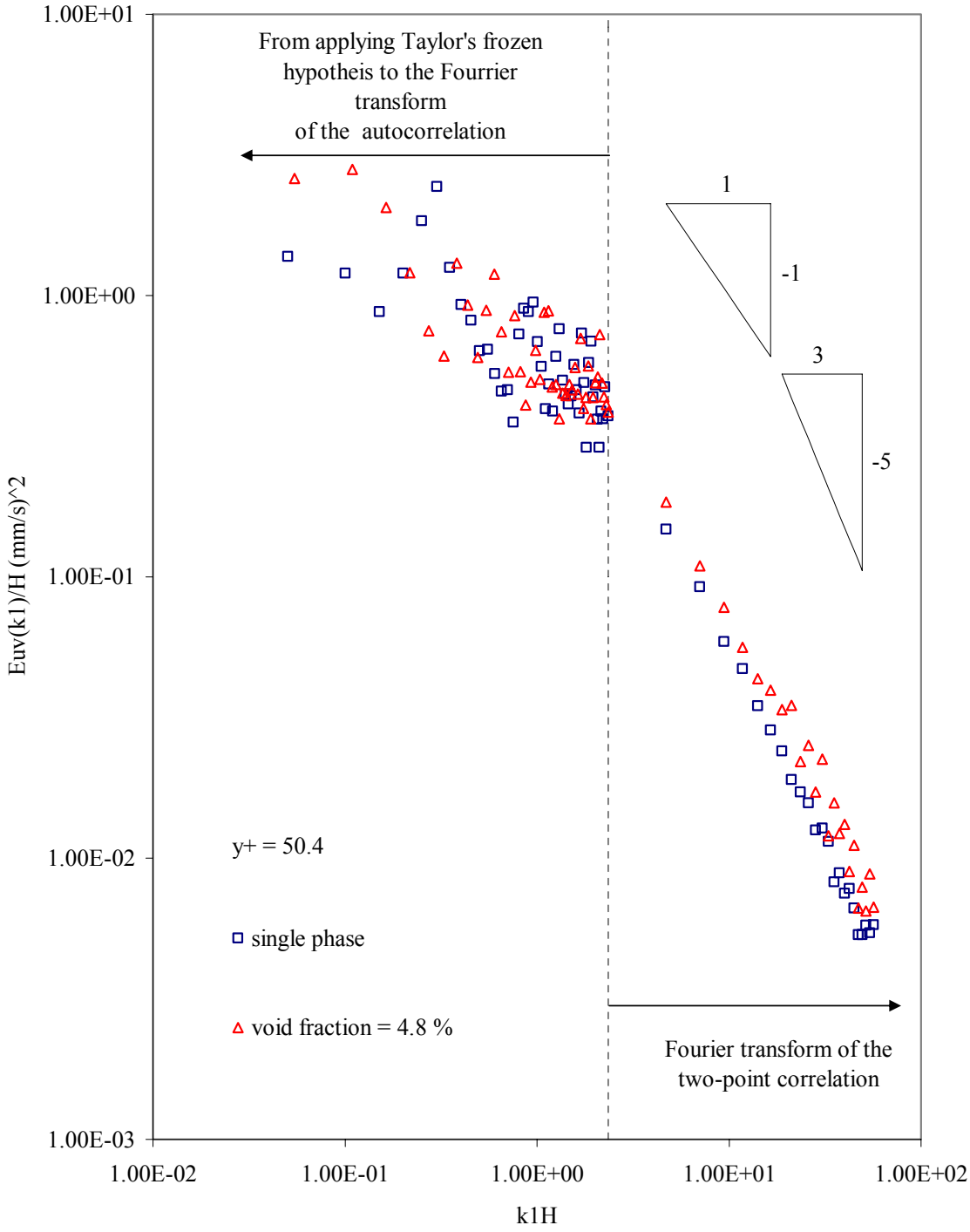

FIGURE 65. Dimensional $E_{uv}(k_1)$ spectra versus non-dimensional wavenumber at y/H = 0.15.

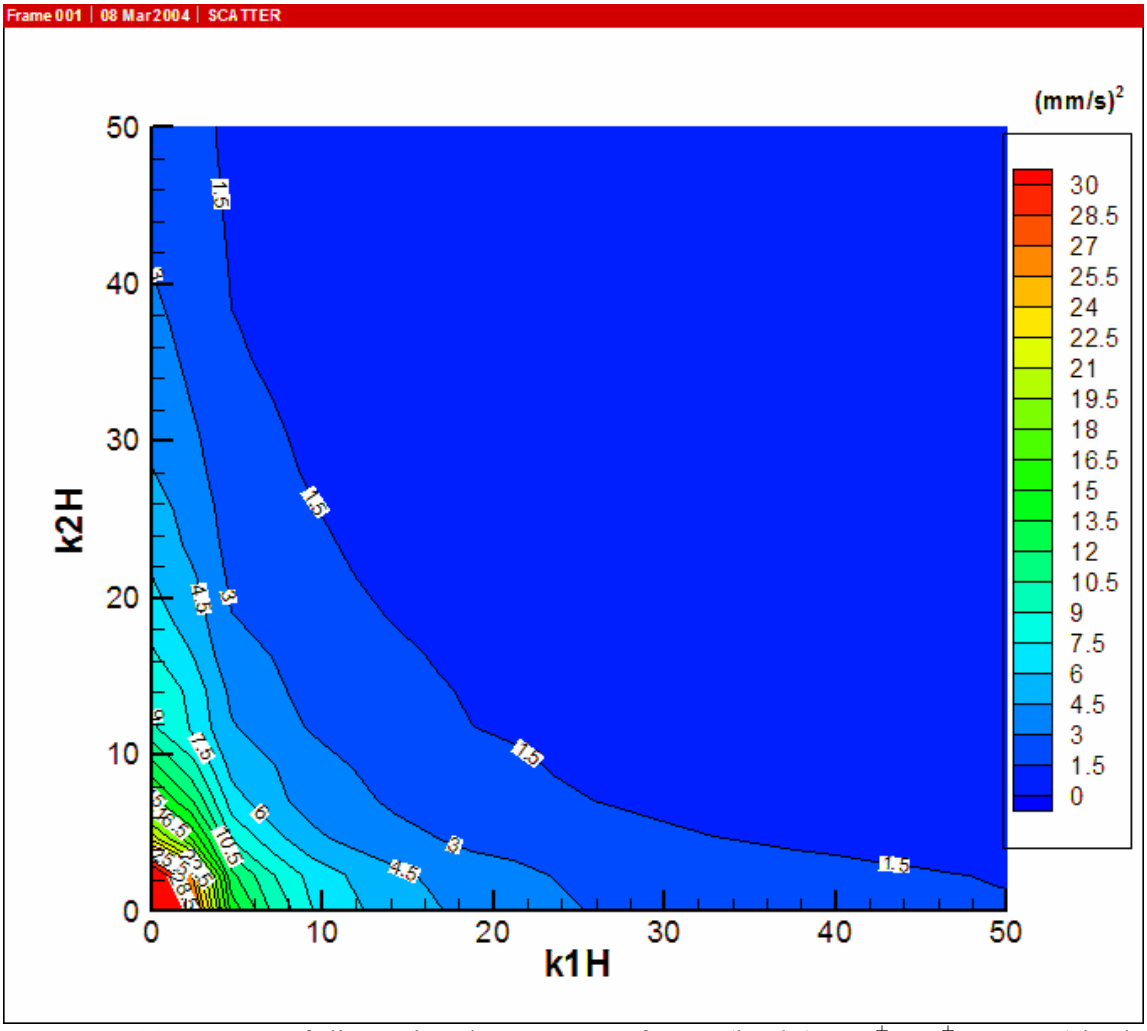

FIGURE 66.Contour of dimensional 2D spectra for $E_{uu}(k_1, k_2)$ at $y^+ = x^+ = 3.70$ (single phase).

can be attributed to the fact that normal fluctuations are aligned with the normal wavenumber (k_2). Therefore, the use of streamwise convection velocity for the Taylor's frozen hypothesis was not adequate and did not yield satisfactory results for the approach propose in this study. Then, the local value of the mean velocity at $y^+ = 3.7$ was used and produced better results in the buffer layer to reduce the discontinuity mentioned above as shown in figure 35 to figure 49.

The results for $E_{uv}(k_1)$ at different positions from the wall are shown in figure 50 to figure 65. The assumption of Taylor's frozen hypothesis performed very well in the overlapping region ($k_1H = 2.3$). These figures show that the beginning of the buffer layer there is a redistribution of the energy from larger to lower wavenumbers. However, the opposite trend is observed at the end and outside the buffer layer.

The results of one-dimensional spectra show that the wavenumber region of the spectra can be increased by using the temporal and spatial information of the PIV fluctuating velocity fields. The Taylor's frozen hypothesis has a good agreement for $E_{uu}(k_1)$ and $E_{uv}(k_1)$. However, it did not work very well in the near wall region for $E_{vv}(k_1)$.

The spatial information of PIV allowed the evaluation of the dimensional 2D spectra. This comparison for single phase and maximum drag reduction was important because the contributions of the streamwise wavenumber and normal wavenumber were taken into account at the same time. Figure 66 shows the contour of dimensional 2D spectra for $E_{uu}(k_1, k_2)$ at $y^+ = x^+ = 3.70$ (single phase) and figure 67 shows the contour of dimensional 2D spectra for $E_{uu}(k_1, k_2)$ at $y^+ = x^+ = 3.70$ for a DR = 38.45%. A shift of

energy from high wavenumbers to low wavenumbers was observed; this trend was also observed in the one-dimensional spectra. It illustrates that there is a reduction of the production of turbulence. Moreover, the microbubbles seem to have a bigger effect on the streamwise wavenumber.

Figure 68 shows the contour of dimensional 2D spectra for $E_{vv}(k_1, k_2)$ at $y^+ = x^+ = 3.70$ for single phase and figure 69 shows the dimensional 2D spectra for $E_{vv}(k_1, k_2)$ at $y^+ = x^+ = 3.70$ for a DR = 38.45%. The microbubbles produce a shift of energy from high wavenumbers to low wavenumbers. Furthermore, the microbubbles affect uniformly both the normal and streamwise wavenumber.

Figure 70 shows the contour of $E_{uv}(k_1, k_2)$ at $y^+ = x^+ = 3.70$ for single phase and figure 71 depicts the contour of $E_{uv}(k_1, k_2)$ at $y^+ = x^+ = 3.70$ for a DR = 38.45%. The energy is also shifted from high wavenumber to low wavenumber. Moreover, the microbubbles produced the same effect in both normal and streamwise wavenumber. It is plausible that the shift of energy observed on these results could be associated with a reduction of the Reynolds stresses.

Contours of dimensional 2D spectra for $E_{uu}(k_1, k_2)$, $E_{vv}(k_1, k_2)$, and $E_{uv}(k_1, k_2)$ at $y^+ = x^+ = 69.7$ for single phase and maximum drag reduction are shown from figure 72 to 77. These figures show clearly that there is also a redistribution of energy. However, in the lower wavenumber region the energy contain of single phase flow is lower that that of the DR = 38.45 %; this trend is contrary to that the spectra evaluated in the near wall region. It suggests that the phenomenon that occurs in the near wall region is different from the one occurring far from the wall.

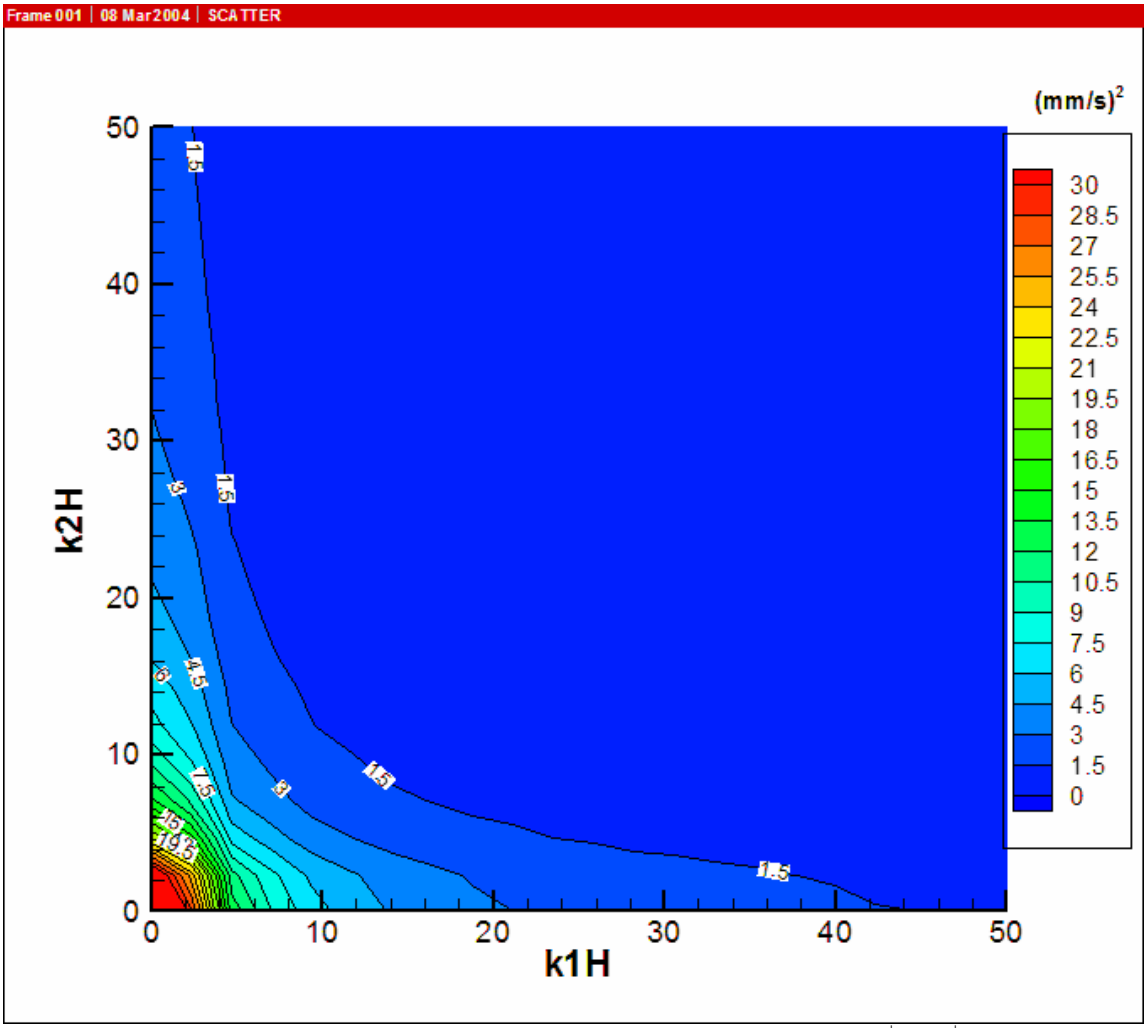

FIGURE 67. Contour of dimensional 2D spectra for $E_{uu}(k_1, k_2)$ at $y^+ = x^+ = 3.70$ (DR = 38.45 %).

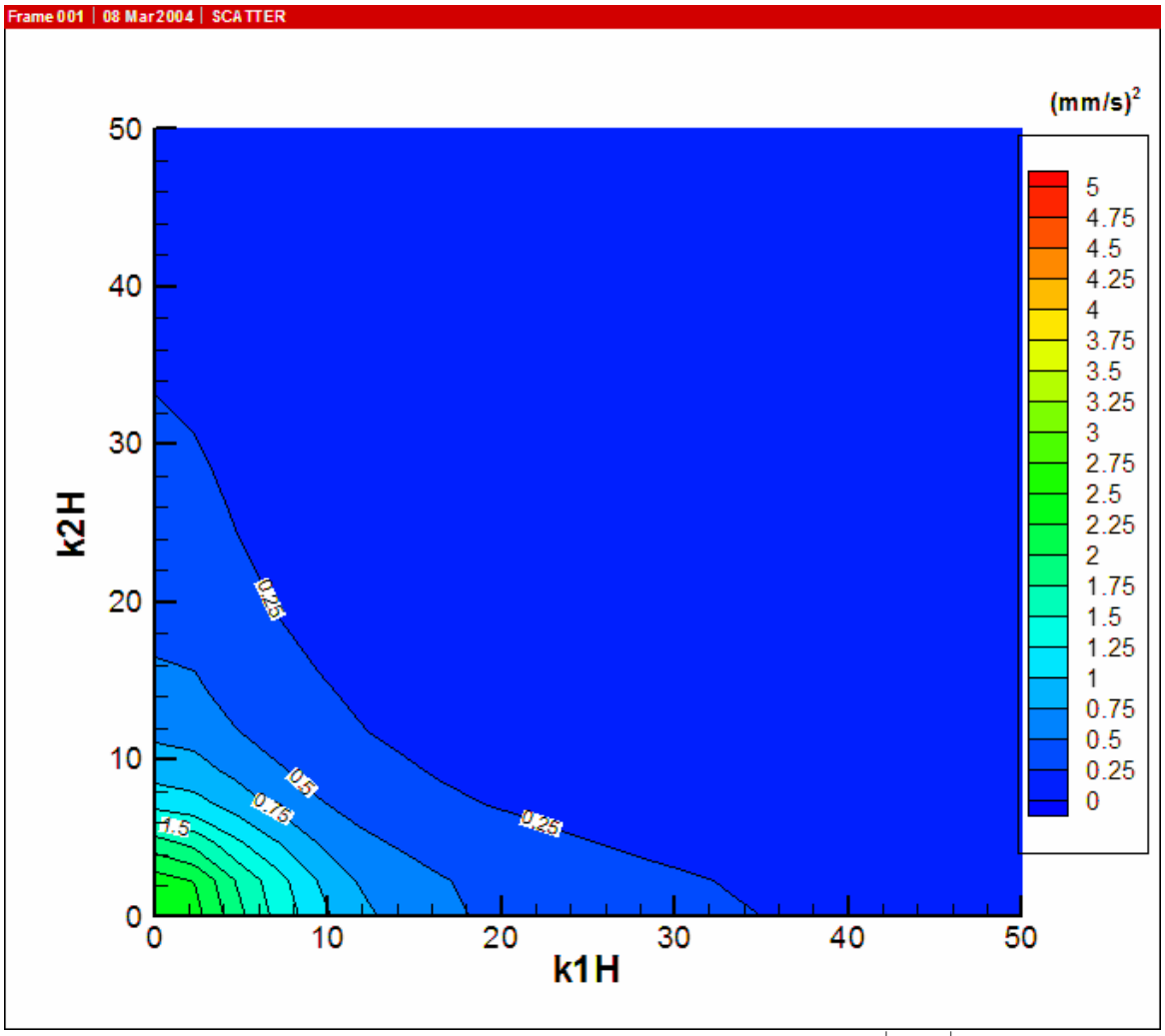

FIGURE 68. Contour of dimensional 2D spectra for $E_{vv}(k_1, k_2)$ at $y^+ = x^+ = 3.70$ (single phase).

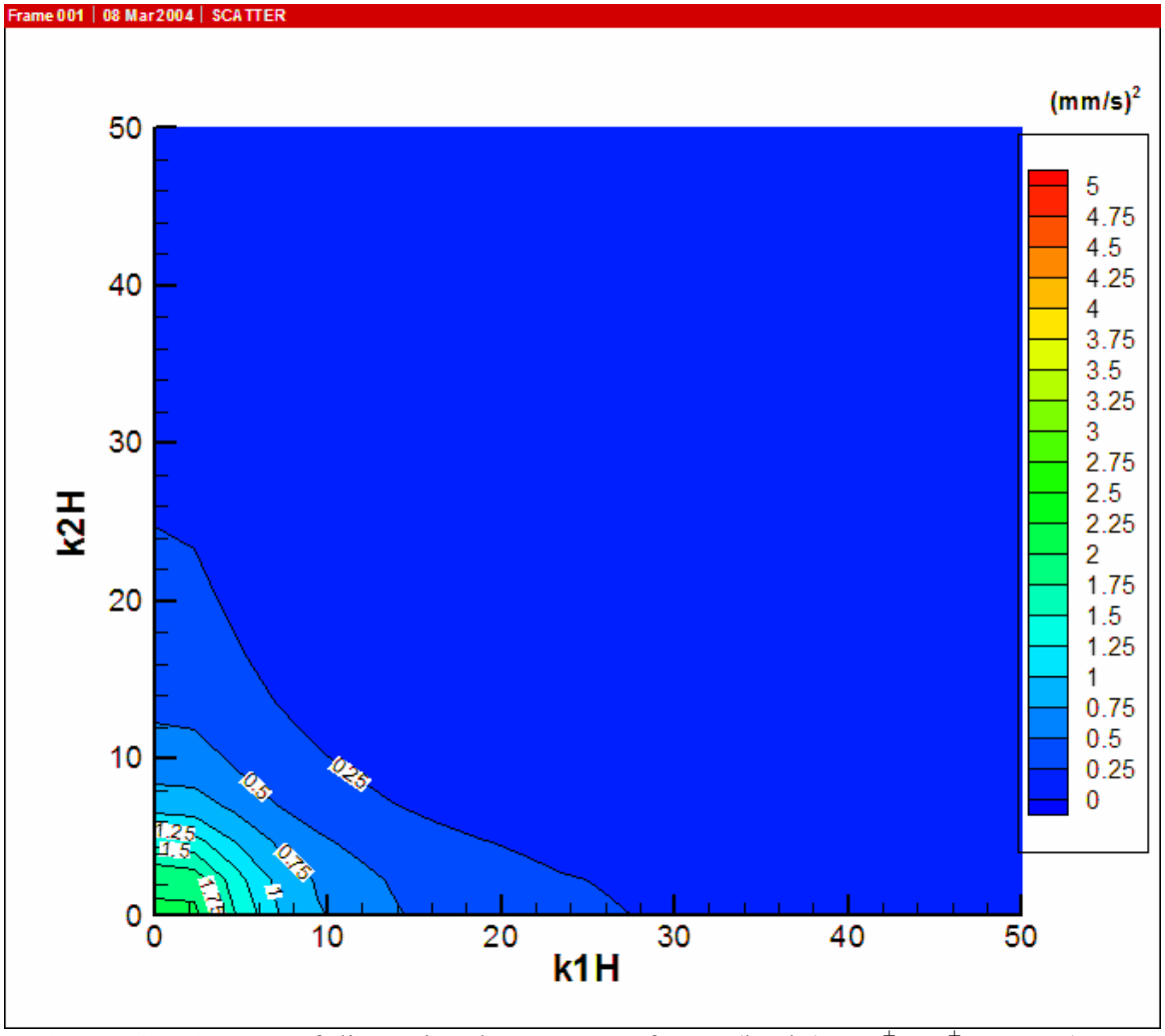

FIGURE 69. Contour of dimensional 2D spectra for $E_{vv}(k_1, k_2)$ at $y^+ = x^+ = 3.70$ (DR = 38.45 %).

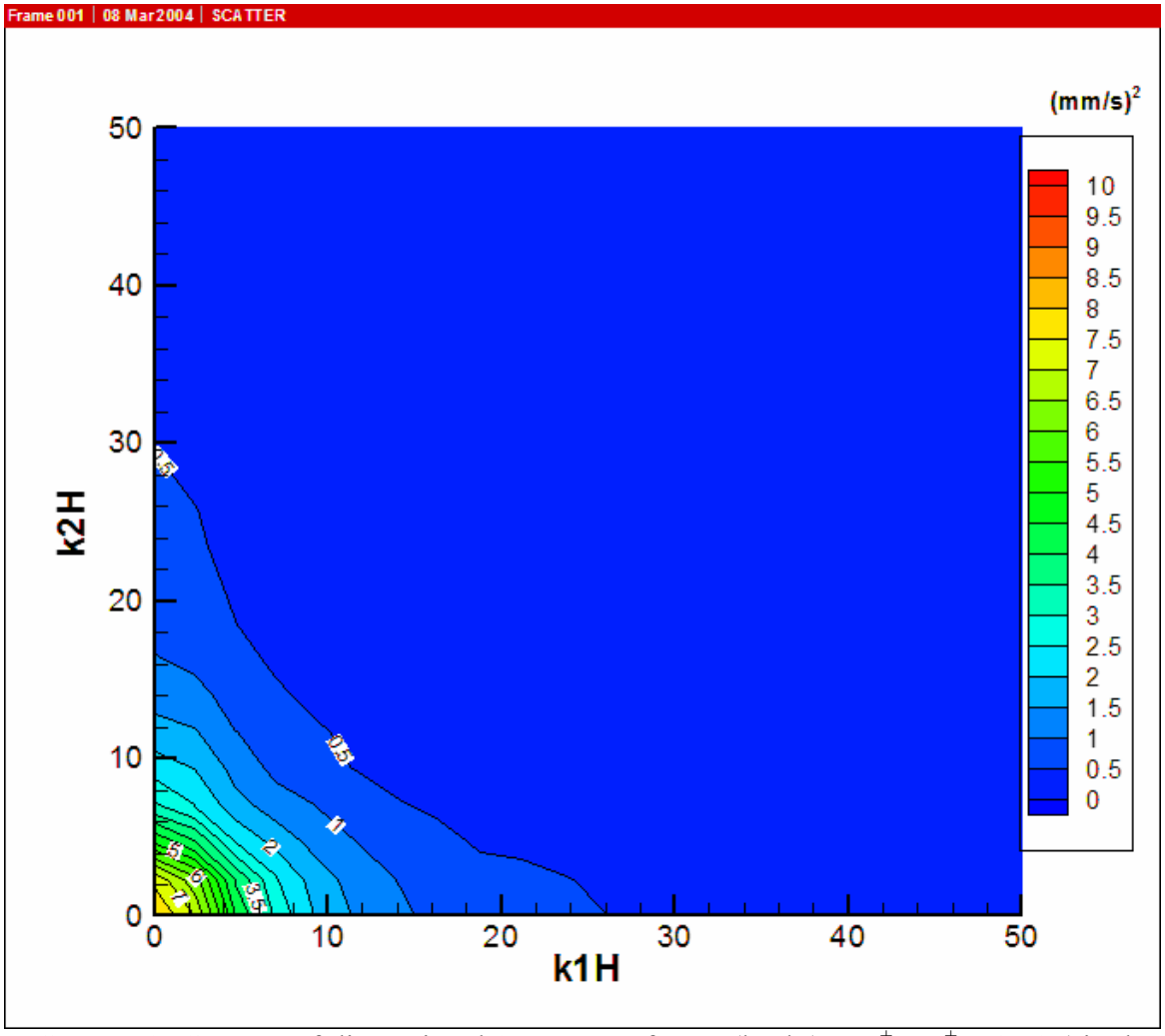

FIGURE 70. Contour of dimensional 2D spectra for $E_{uv}(k_1, k_2)$ at $y^+ = x^+ = 3.70$ (single phase).

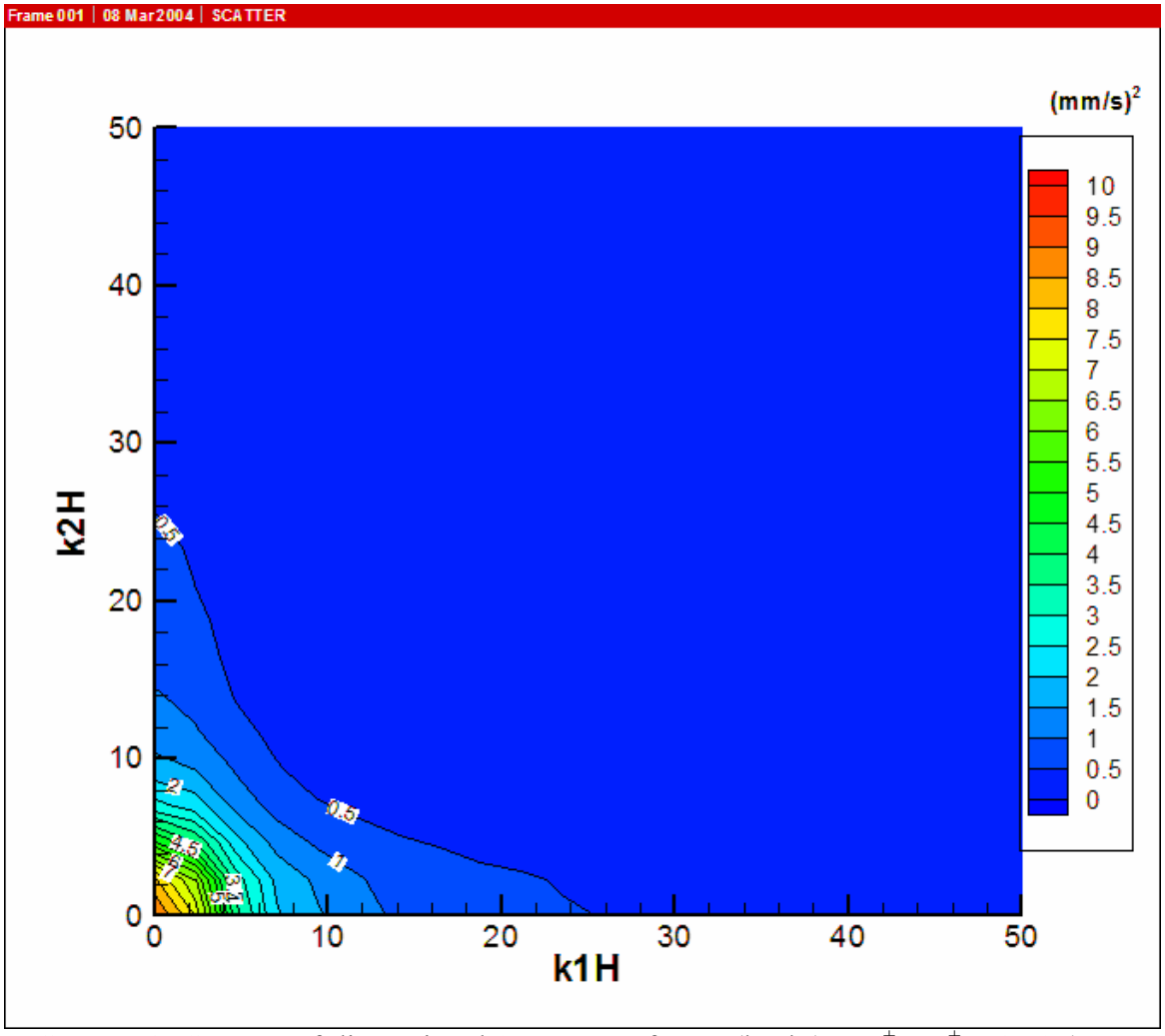

FIGURE 71. Contour of dimensional 2D spectra for $E_{uv}(k_1, k_2)$ at $y^+ = x^+ = 3.70$ (DR = 38.45 %).

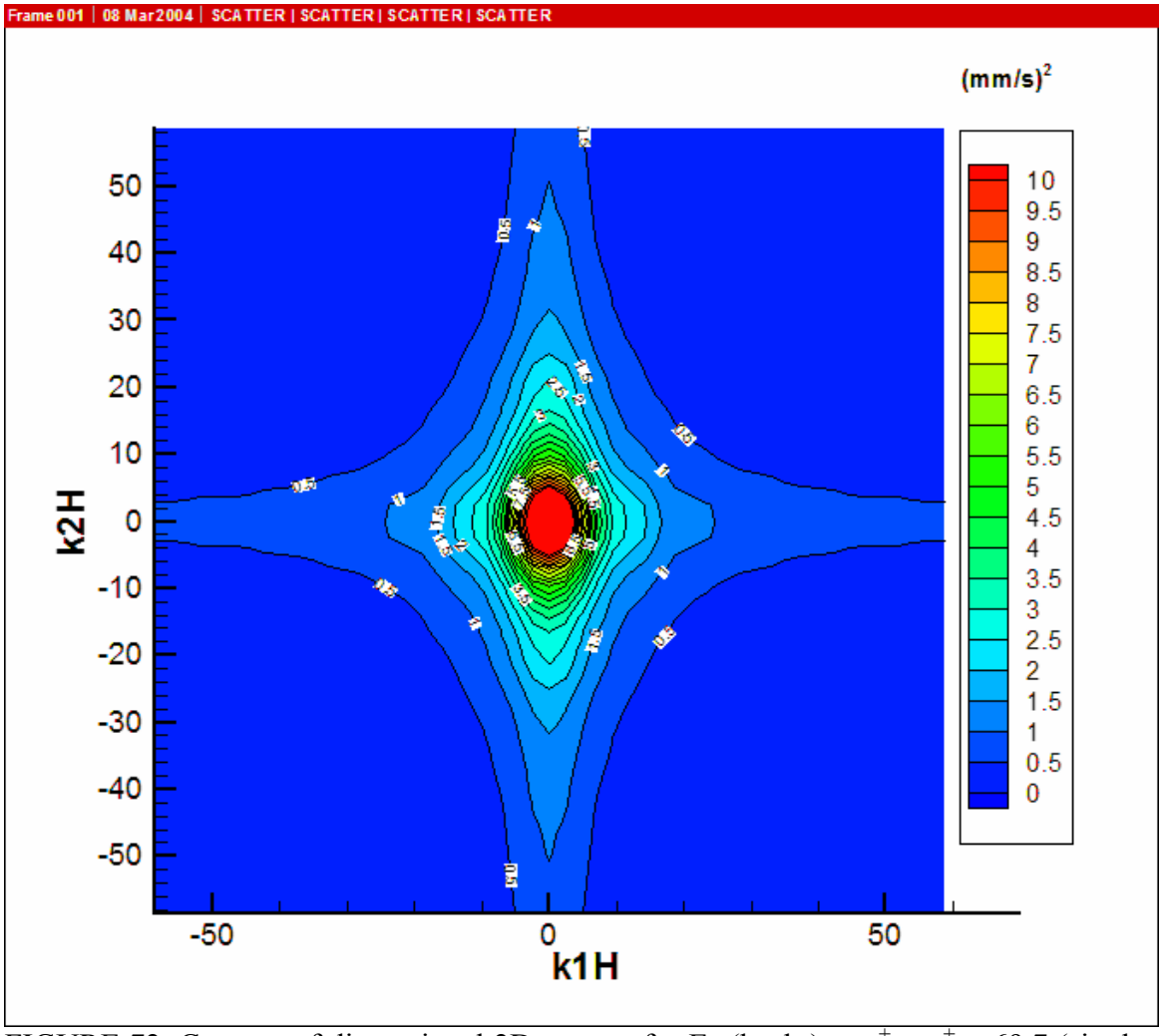

FIGURE 72. Contour of dimensional 2D spectra for $E_{uu}(k_1, k_2)$ at $y^+ = x^+ = 69.7$ (single phase).

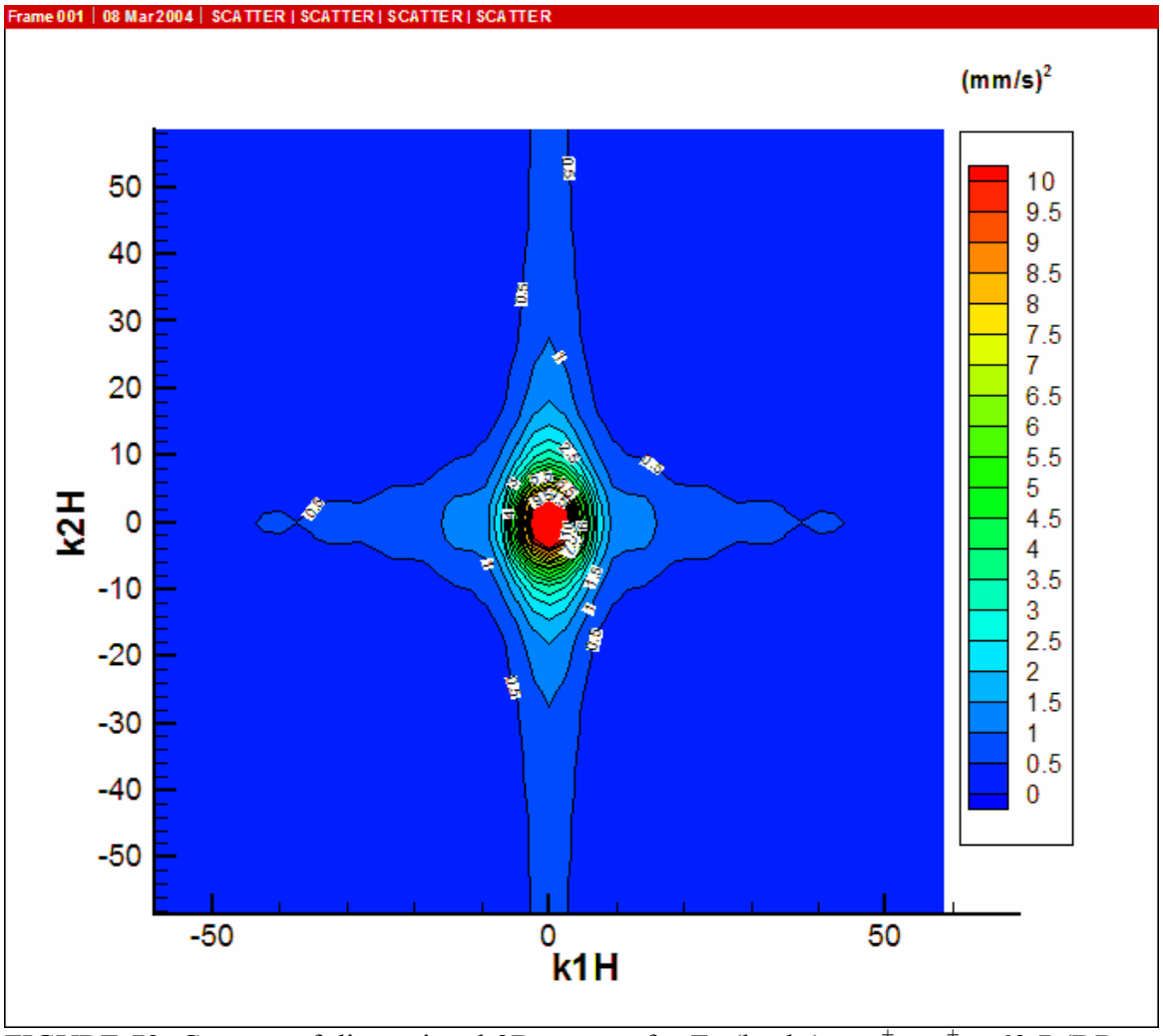

FIGURE 73. Contour of dimensional 2D spectra for $E_{uu}(k_1, k_2)$ at $y^+ = x^+ = 69.7$ (DR = 38.45%).

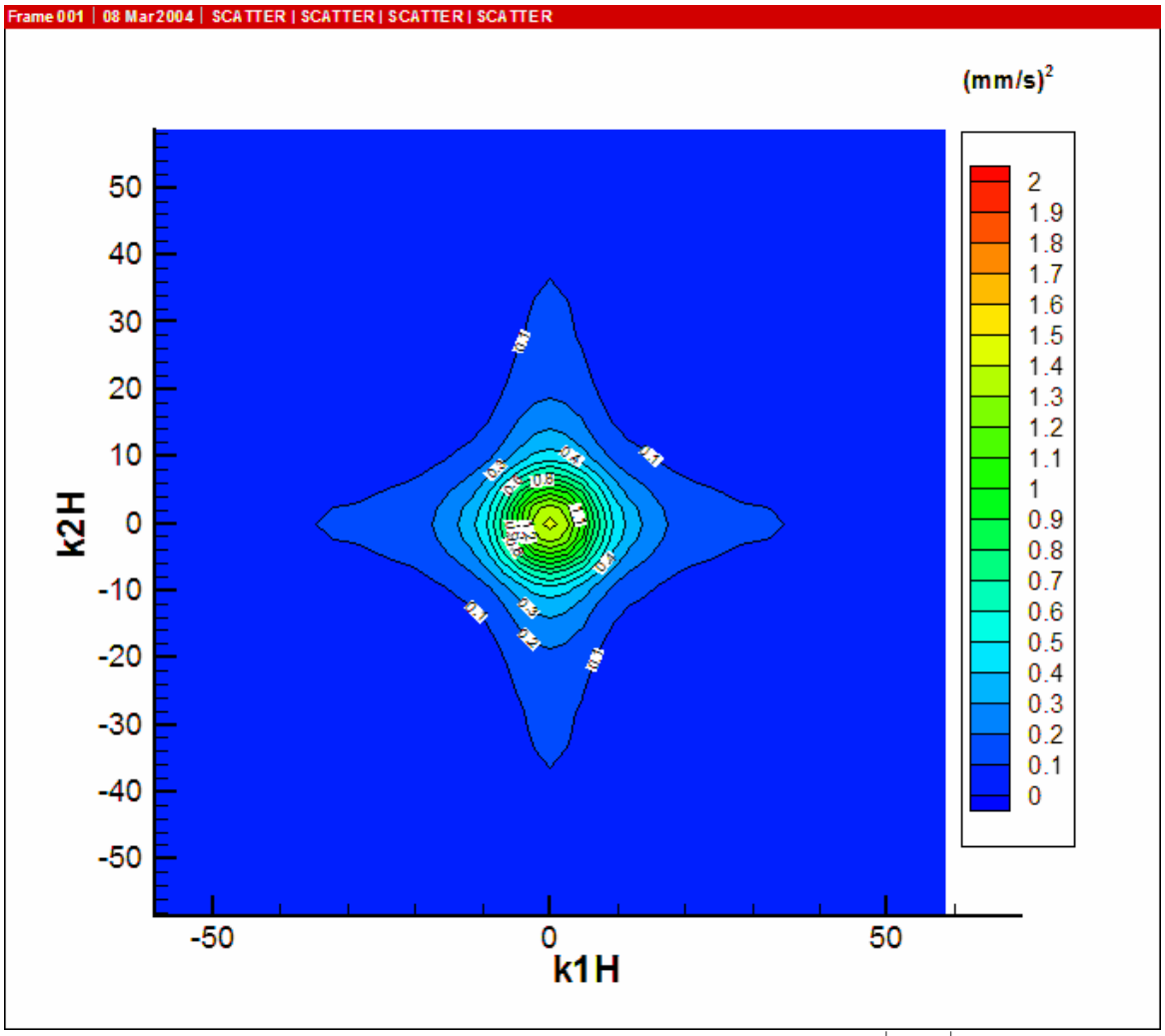

FIGURE 74. Contour of dimensional 2D spectra for $E_{vv}(k_1, k_2)$ at $y^+ = x^+ = 69.7$ (single phase).

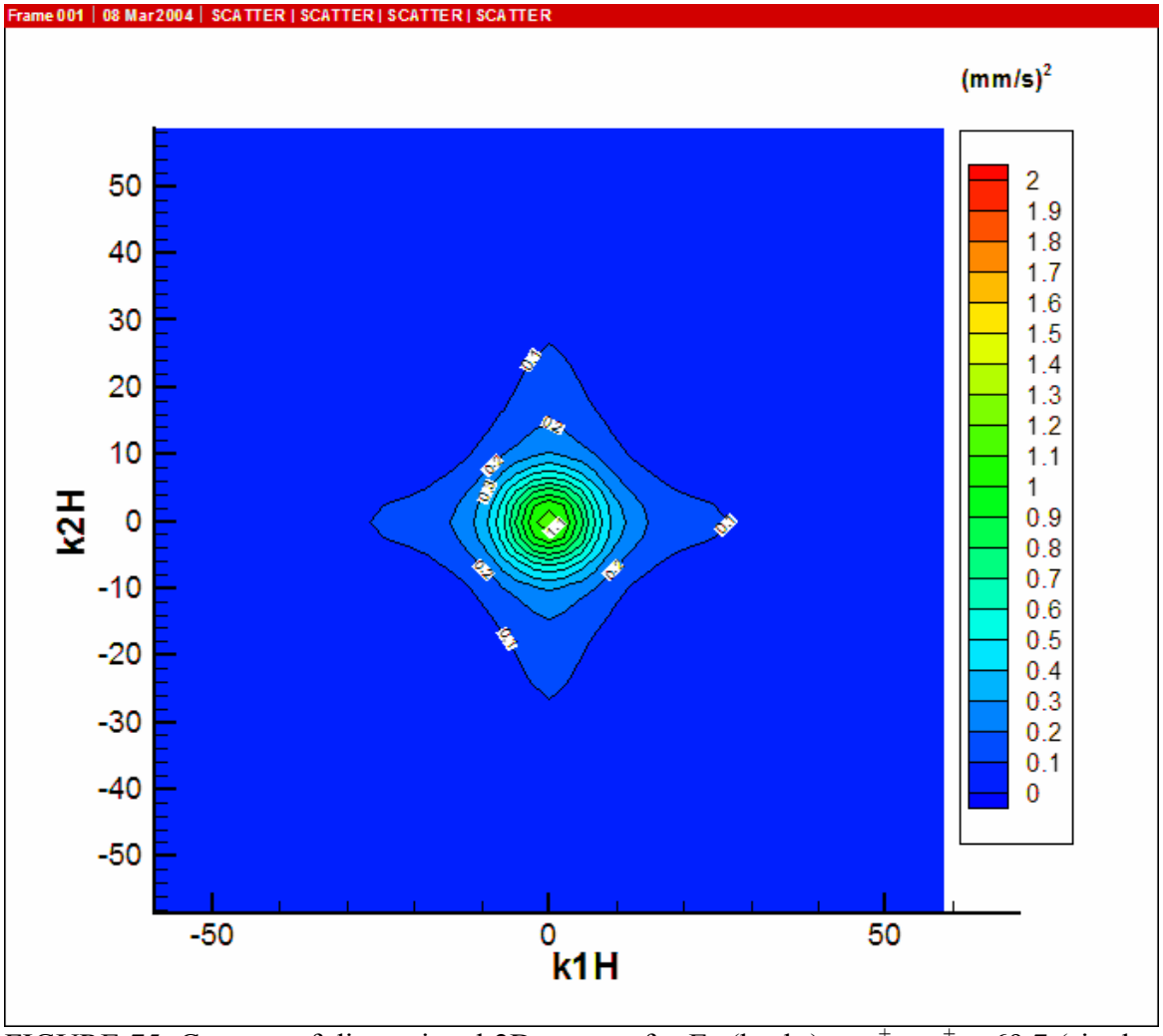

FIGURE 75. Contour of dimensional 2D spectra for $E_{vv}(k_1, k_2)$ at $y^+ = x^+ = 69.7$ (single phase).

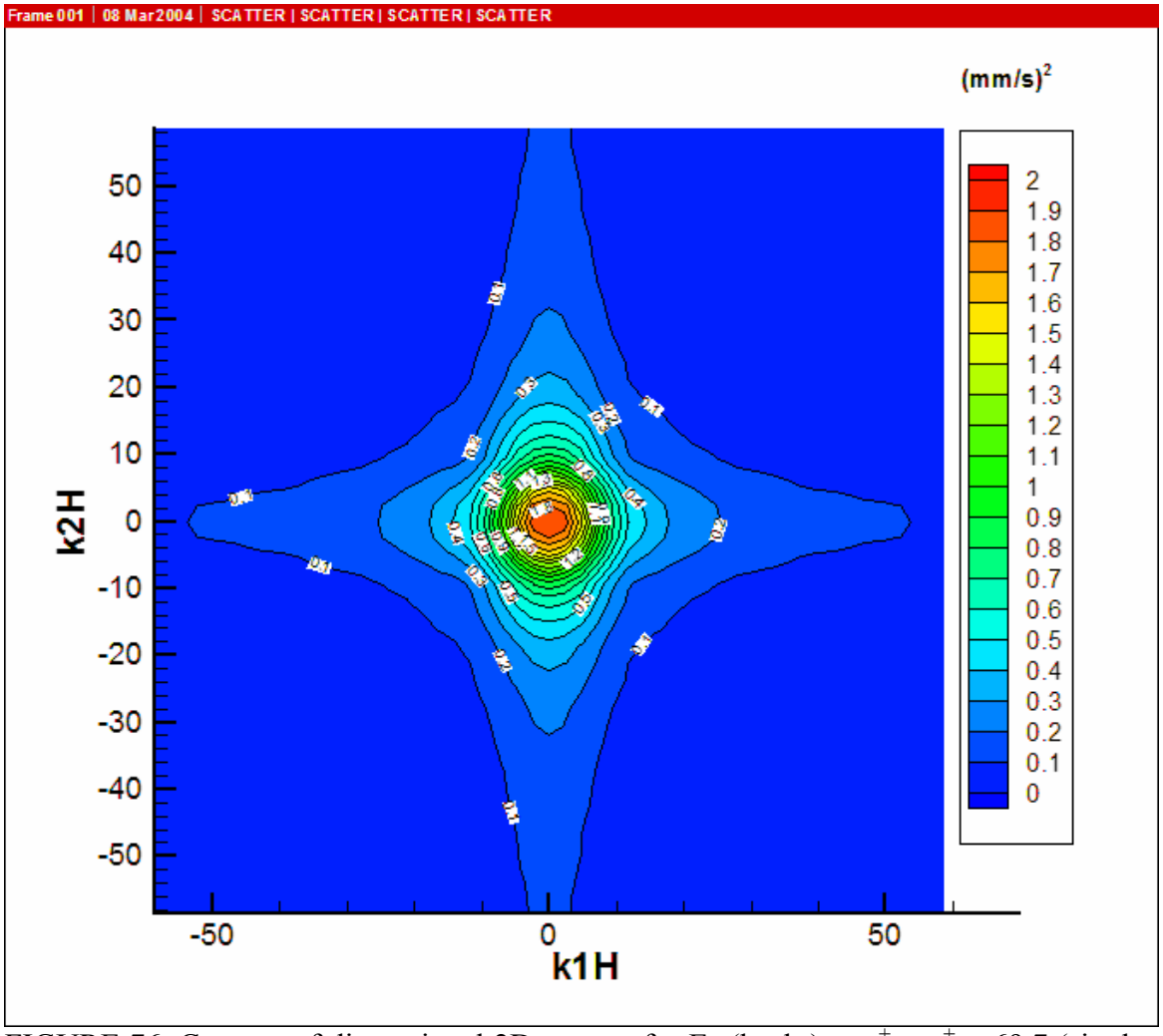

FIGURE 76. Contour of dimensional 2D spectra for $E_{uv}(k_1, k_2)$ at $y^+ = x^+ = 69.7$ (single phase).

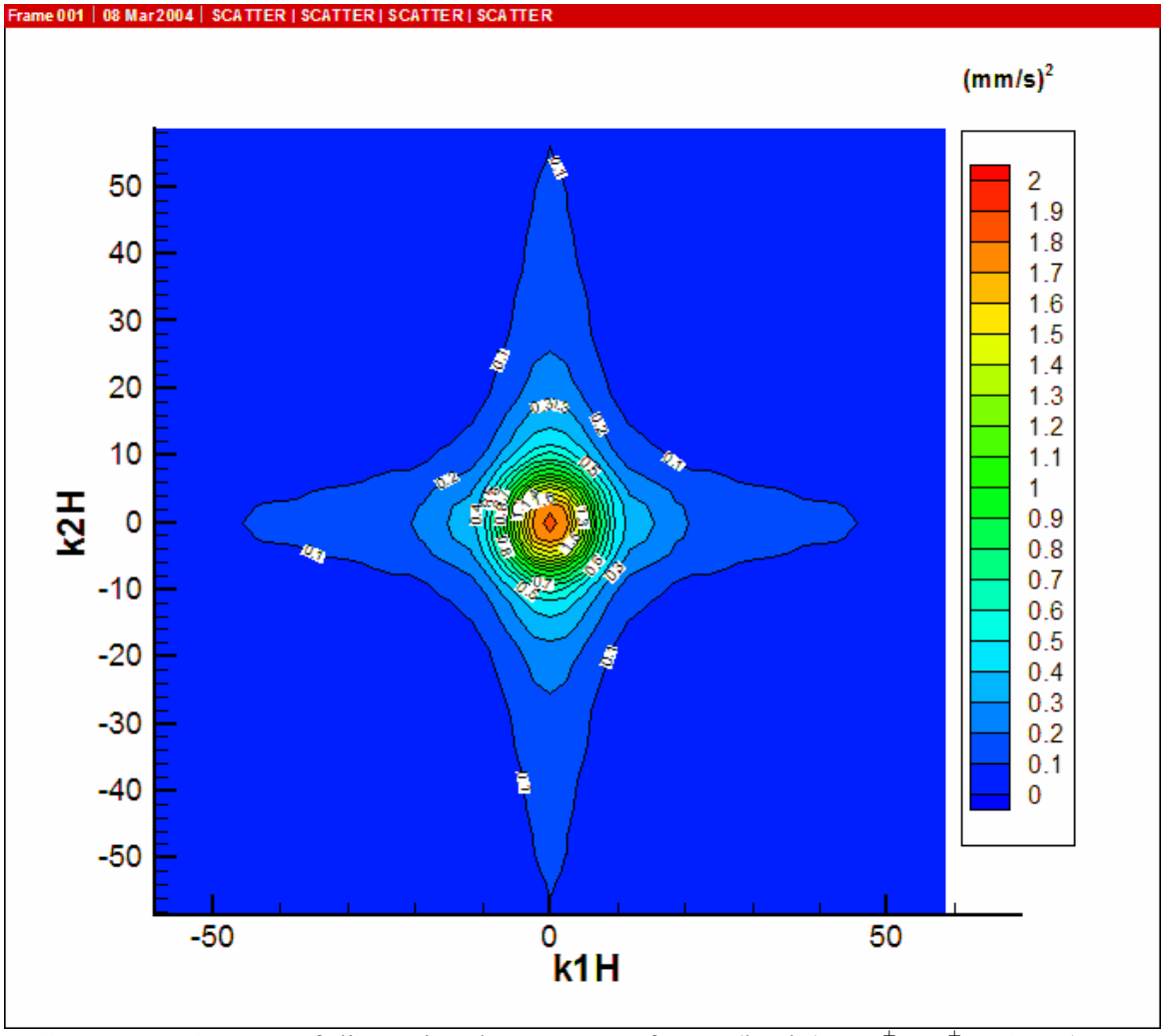

FIGURE 77. Contour of dimensional 2D spectra for $E_{uv}(k_1, k_2)$ at $y^+ = x^+ = 69.7$ (DR = 38.45 %).

The joint probability density function of the streamwise and normal fluctuating components of the velocity JPDF(u,v) was evaluated for single phase flow and for a maximum drag reduction case of 38.45 % at several distances from the wall (y^+ = 10, 15, 25, 35, 50 and 100); the JPDF(u,v) is constant along the contour lines. These results are reported in figure 78 to figure 91.

The evaluation of the JPDF in the region of maximum energy production (y^+ = 10-15) illustrates contour regions that are predominantly x-direction oriented. This behavior means the appearing of high values of the streamwise velocity fluctuating with relatively small normal velocity fluctuations.

The presence of microbubbles within the boundary layer produces a decrease in the values of the joint PDF. This indicates a reduction of the correlation of the u and v velocity fluctuations which leads directly to a decrease in the Reynolds stresses and consequently a reduction in drag.

As the distance from the wall increases, the shape of the joint probability density function for single phase flow corresponds to an enhanced negative correlation (Tennekes & Lumley 1972) and enlarged Reynolds stresses $-\rho\overline{uv}$.

Similar results of the JPDF were presented by Gampert & Yong (1989). They showed the JPDF for pure water and for a polymer drag-reducing solution. The changes in the shape of the JPDF for the polymer solution were more palpable on their comparison than in the comparison presented on this drag reduction by microbubble injection study. However, the tendency of decrease in a negative correlation and therefore a decrease in the Reynolds stresses can be observed in both cases. The lack of data in the literature

related to the values of the JPDF for microbubble injection does not allow a complete comparison between the behavior of polymers and microbubbles in drag reduction phenomena.

Gyr & Bewersdorff (1989) presented joint PDF results of a comparison between the effects of polymers and solvents in the drag reduction phenomena. Although both solutions produce a drag reducing effect, the shape of the joint PDF results are quite different between both of them and also differ from the results presented in this investigation. Again, the lack of data about the values of the joint PDF makes impossible a quantitative comparison, but it seems to be evident that the agent used to produce the desired drag reduction effect has an influence in the modification of the behavior of the joint PDF of u and v in turbulent flows under drag reduction effects.

The inner product of the vorticity is the enstrophy. The evaluation of this parameter is fundamental because it can allow the location of stronger structures in the near wall region. While the vorticity save the sign information enstrophy does not. It is a good indicator of the vortical structures and regions with high shear stress. In figures 92, 93 and 94 the instantaneous enstrophy is evaluated. It is shown that there is a reduction of the intensity of the structures near the wall for the cases with drag reduction when they are compared with the single phase case. It implies that the microbubbles reduce and modify the regions of high shear that are close the wall.

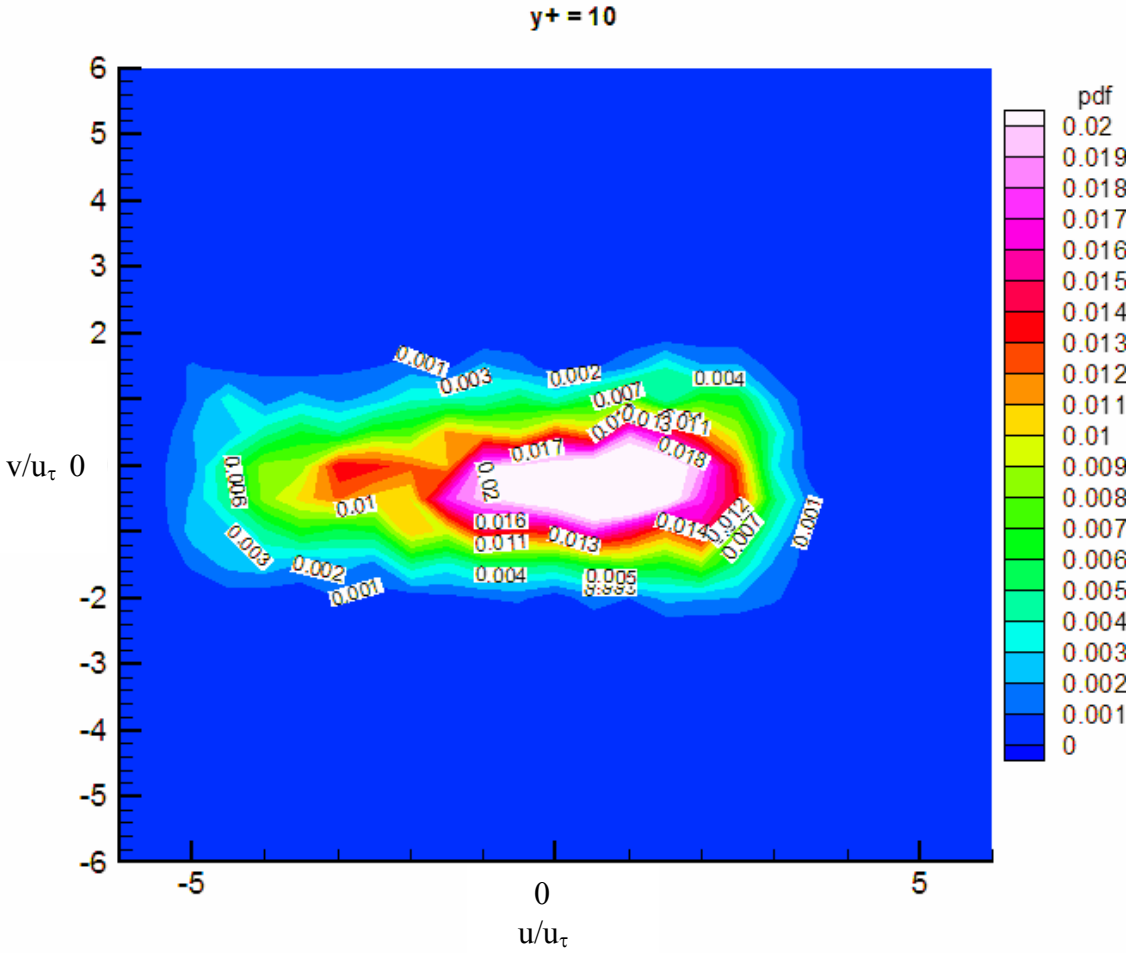

FIGURE 78. JPDF at $y^+ = 10$ (single phase).

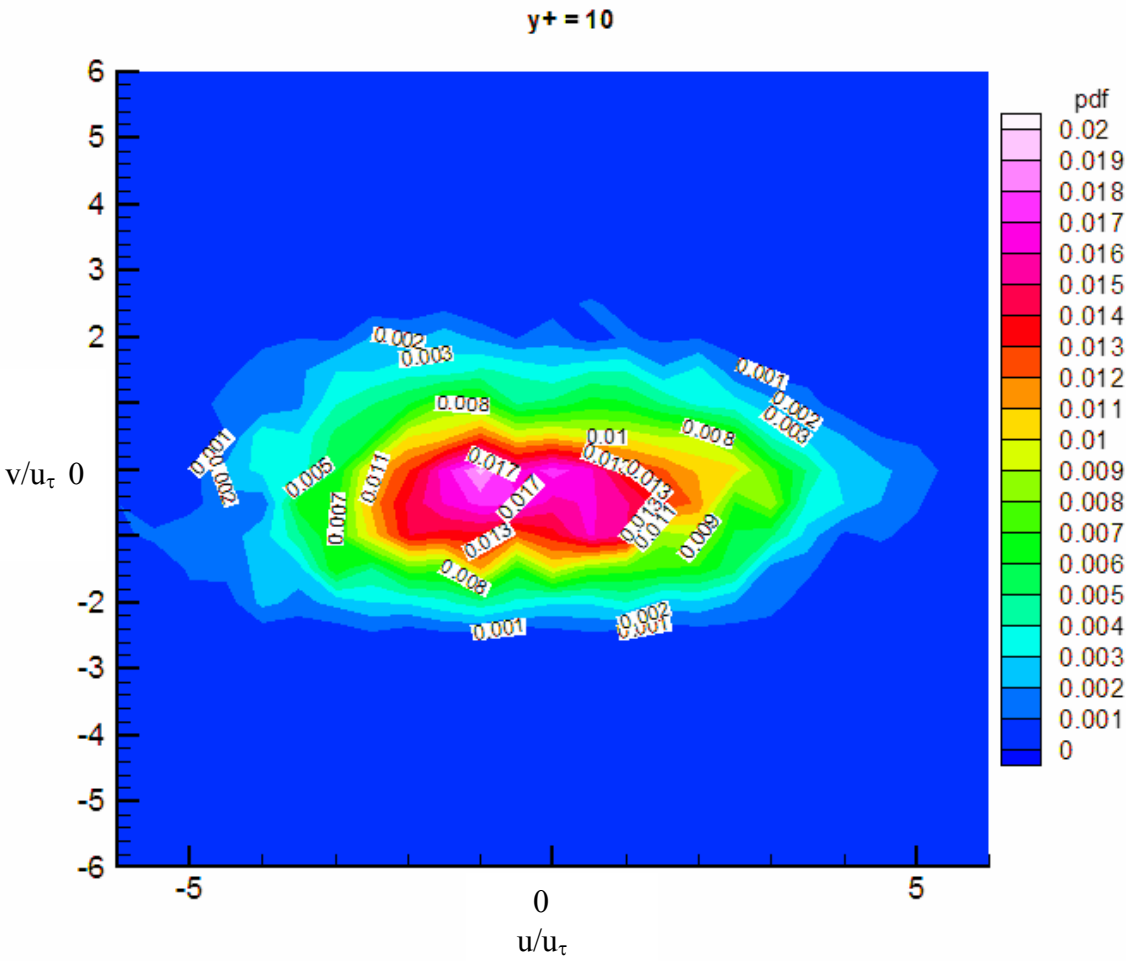

FIGURE 79. JPDF at $y^+ = 10$ (DR = 38.45 %).

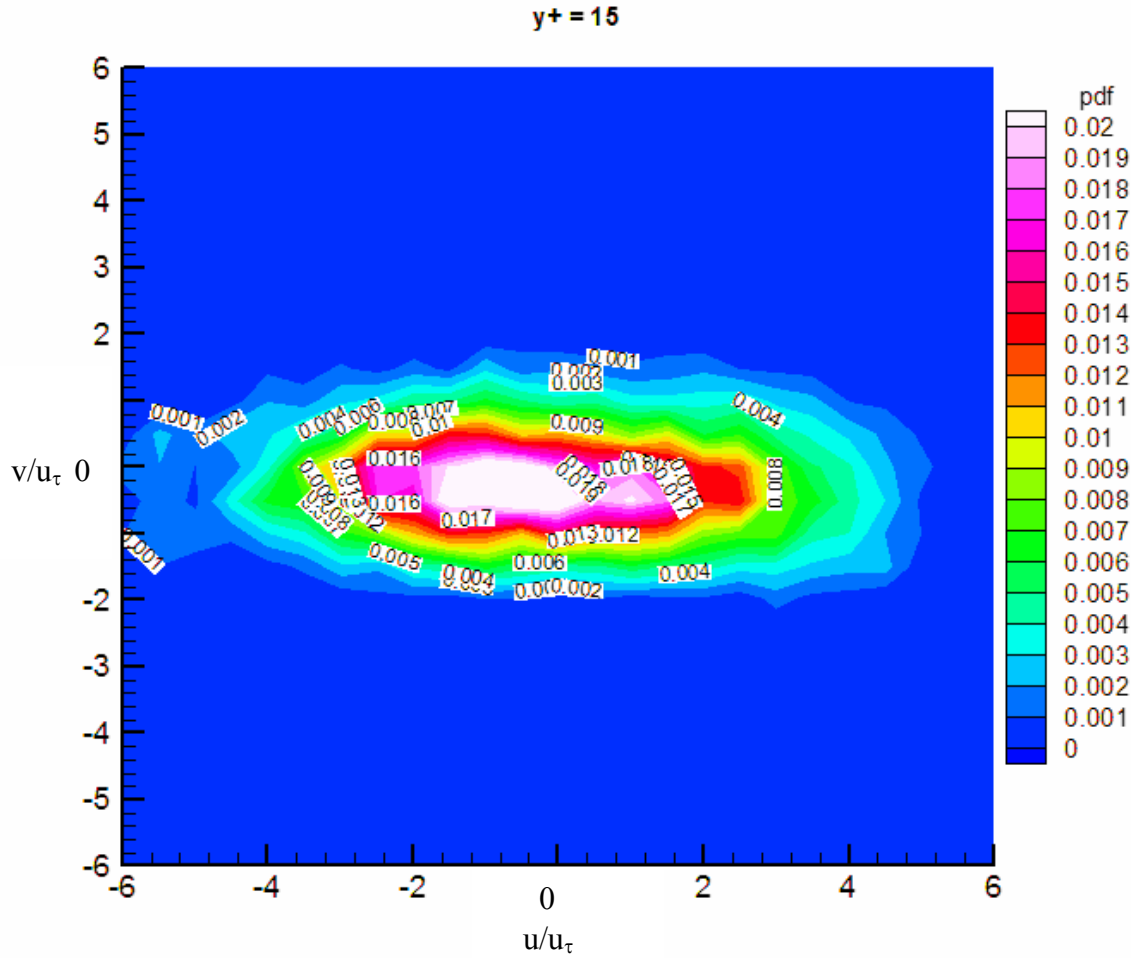

FIGURE 80. JPDF at $y^+ = 15$ (single phase).

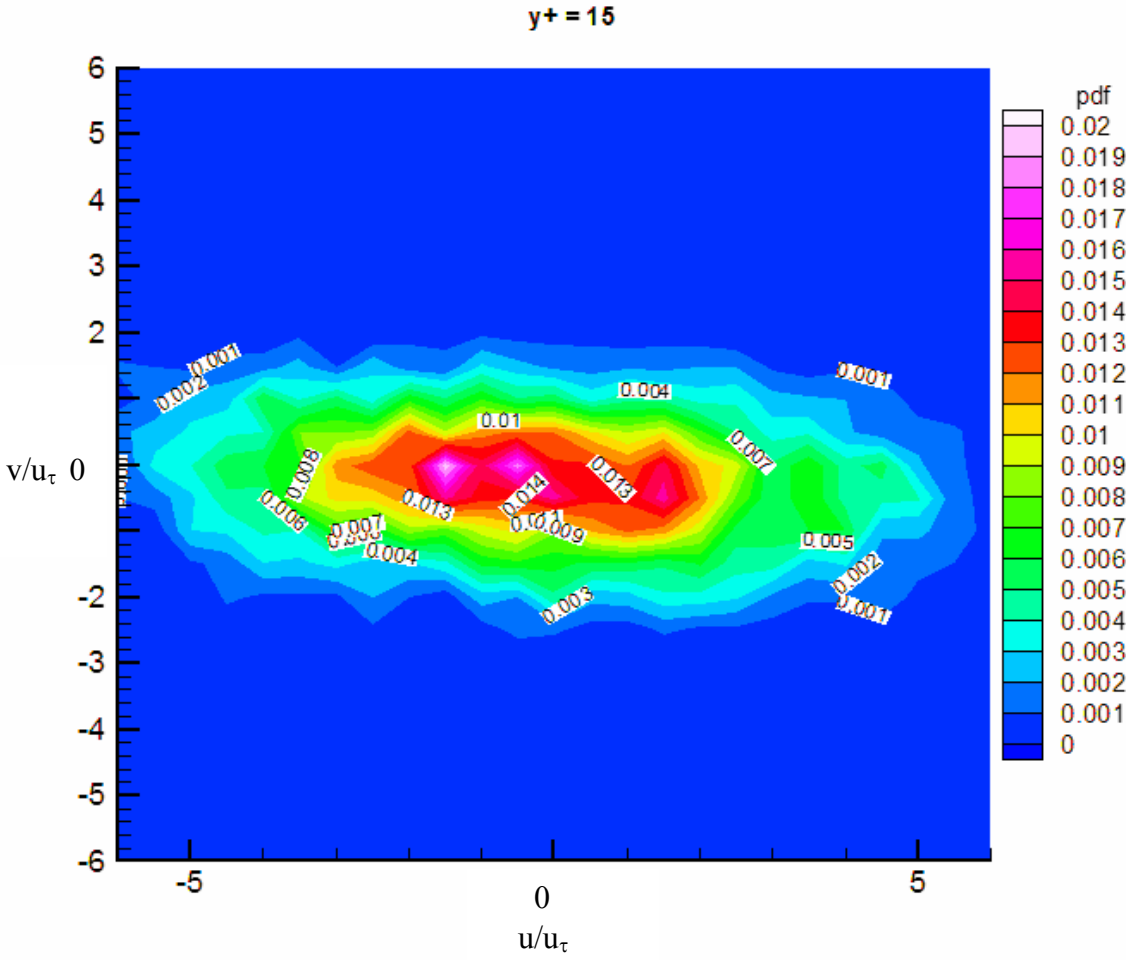

FIGURE 81. JPDF at $y^+ = 15$ (DR = 38.45 %).

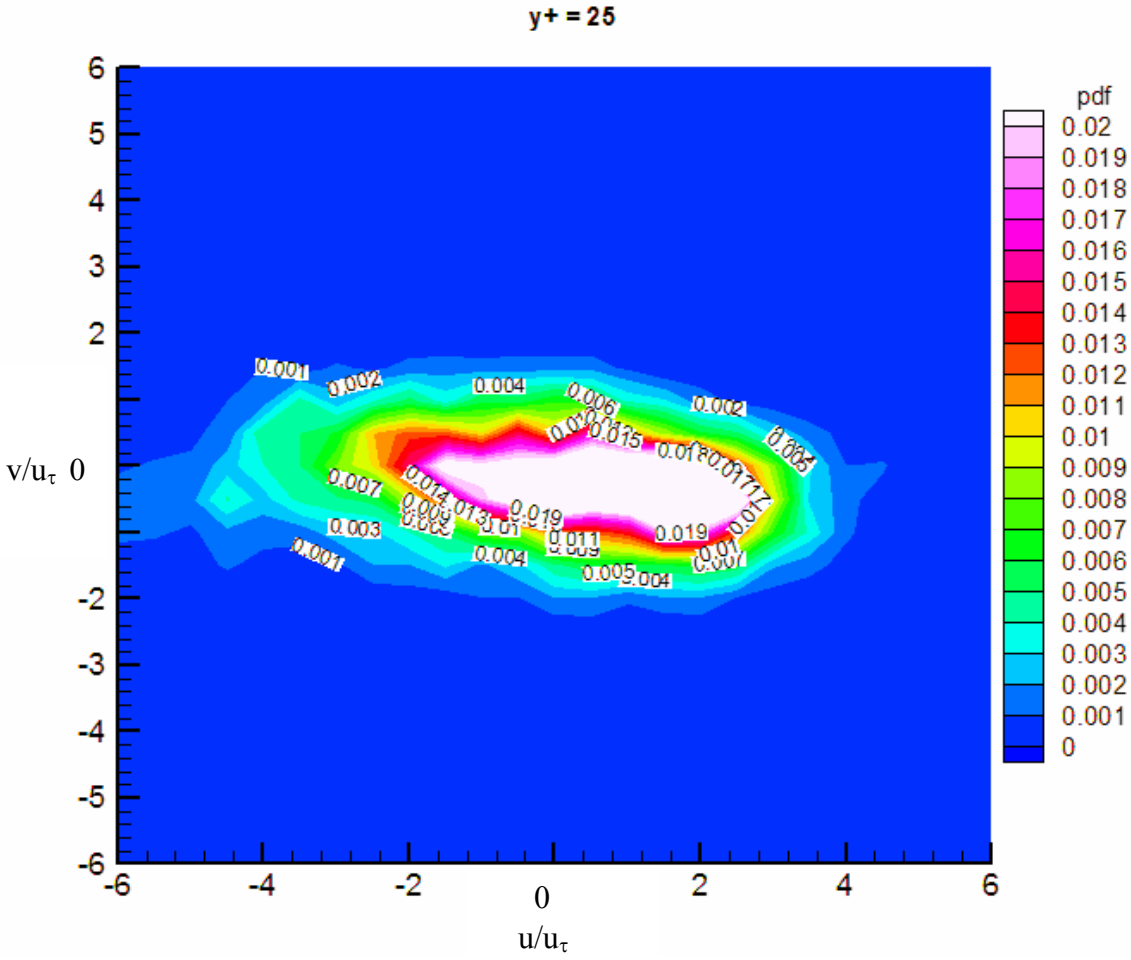

FIGURE 82. JPDF at $y^+ = 25$ (single phase).

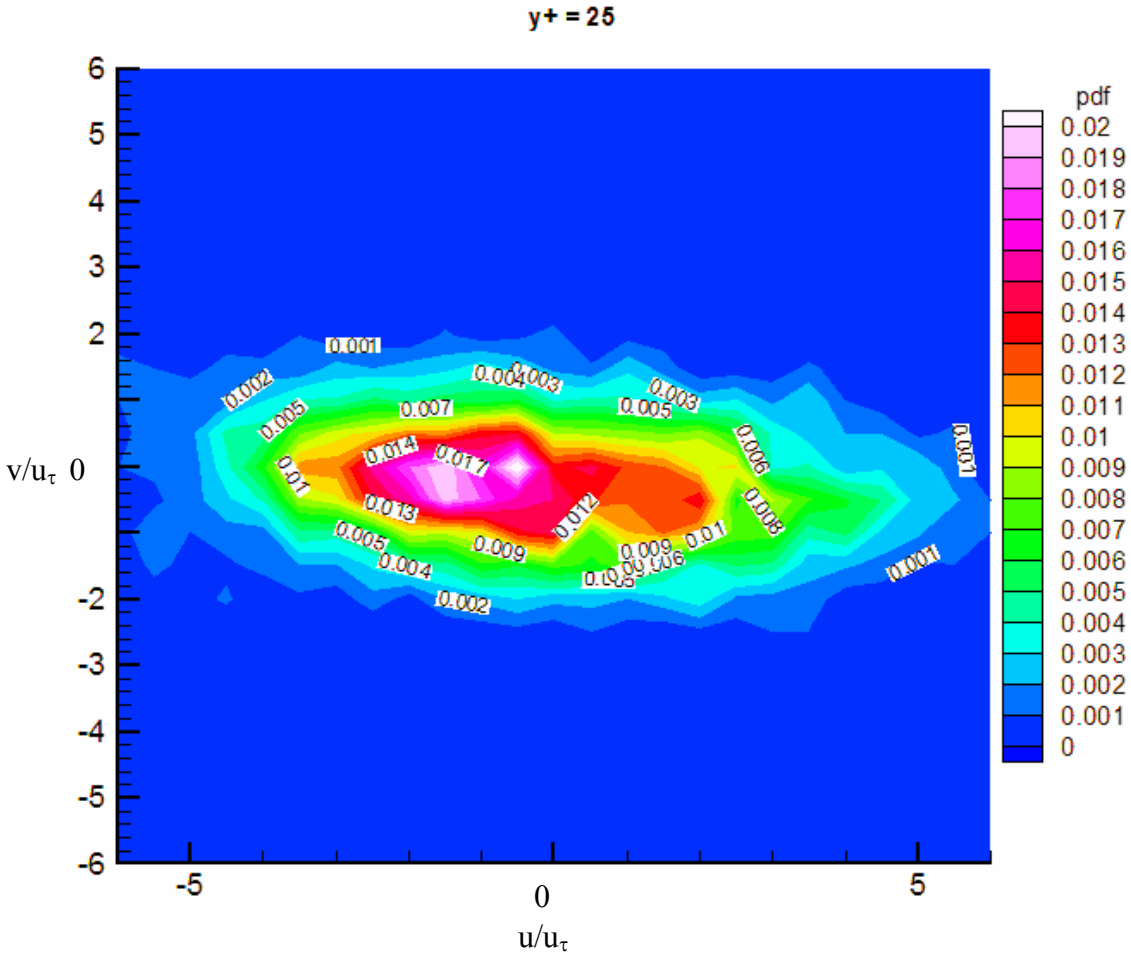

FIGURE 83. JPDF at $y^+ = 25$ (DR = 38.45 %).

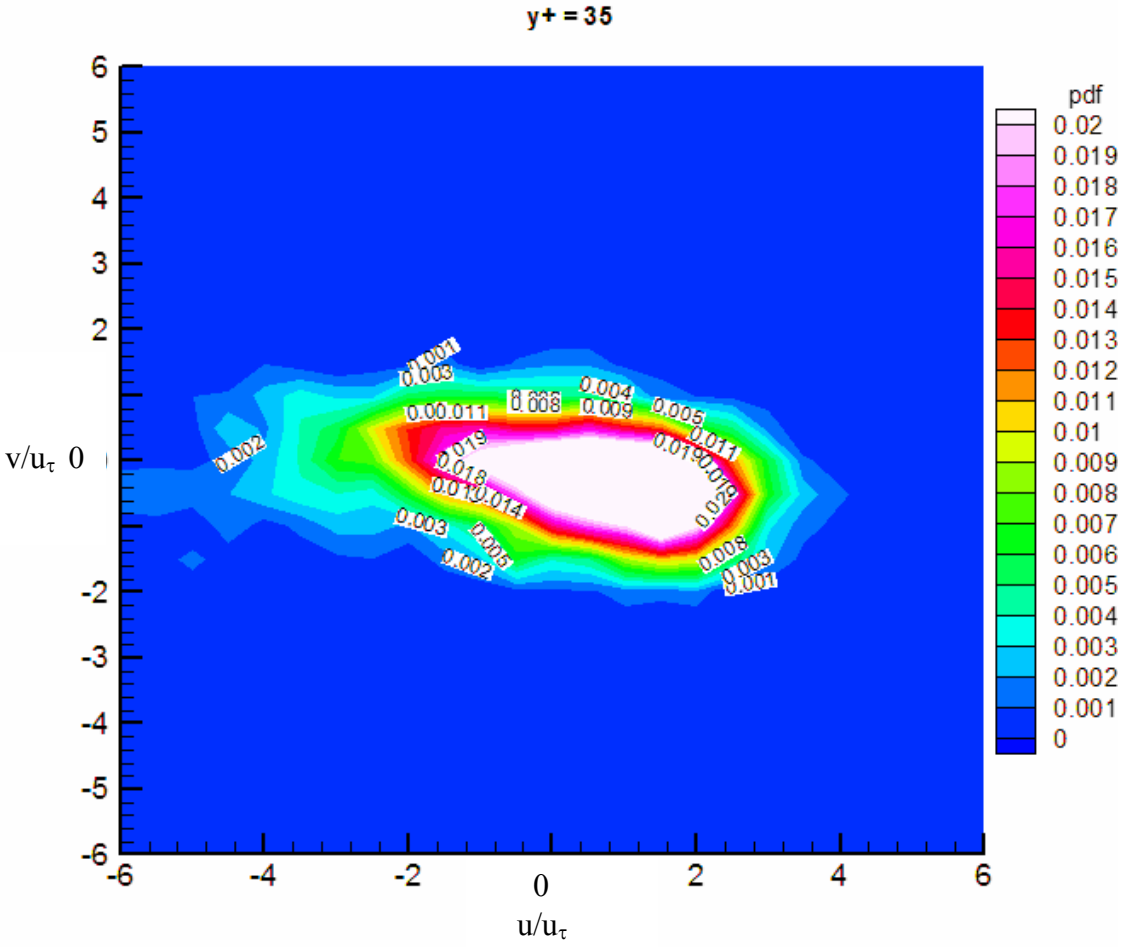

FIGURE 84. JPDF at $y^+ = 35$ (single phase).

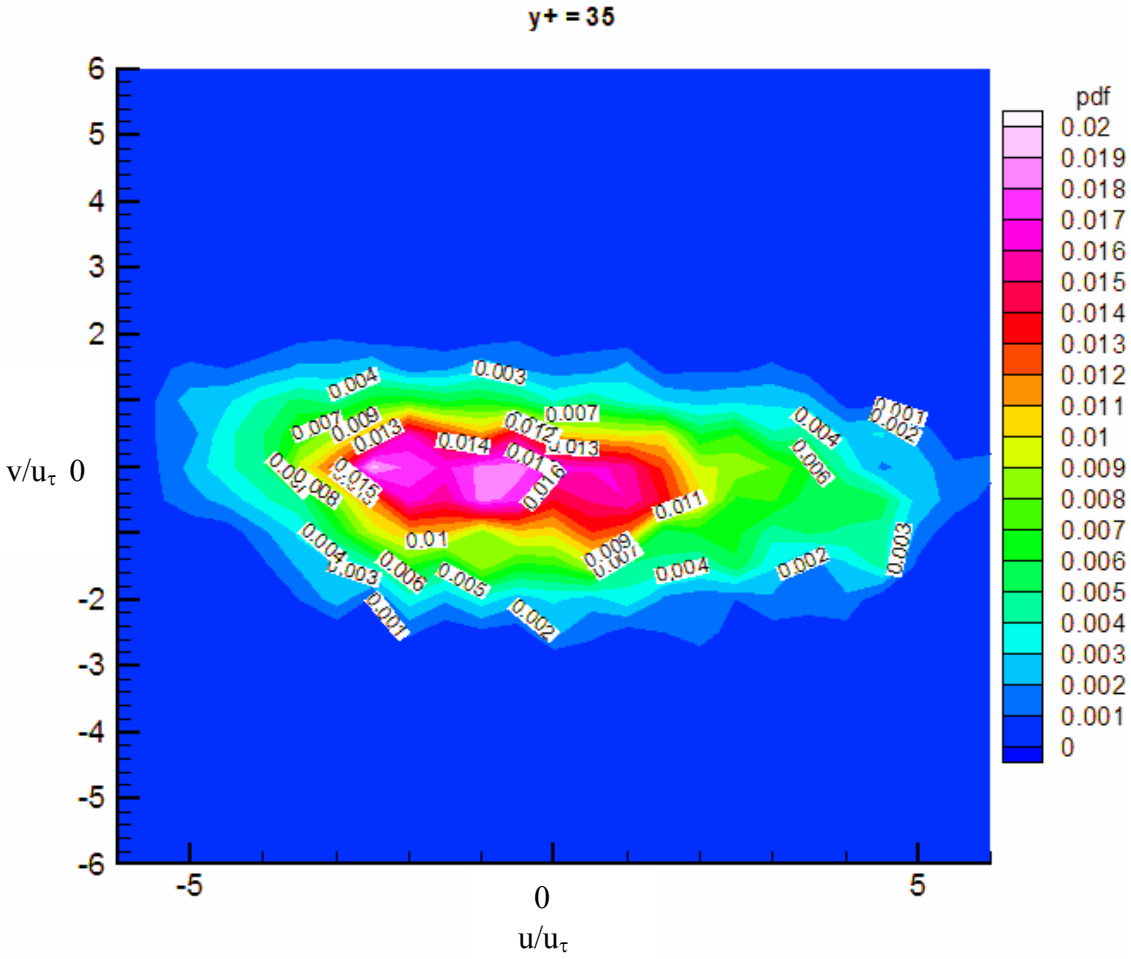

FIGURE 85. JPDF at $y^+ = 35$ (DR = 38.45 %).

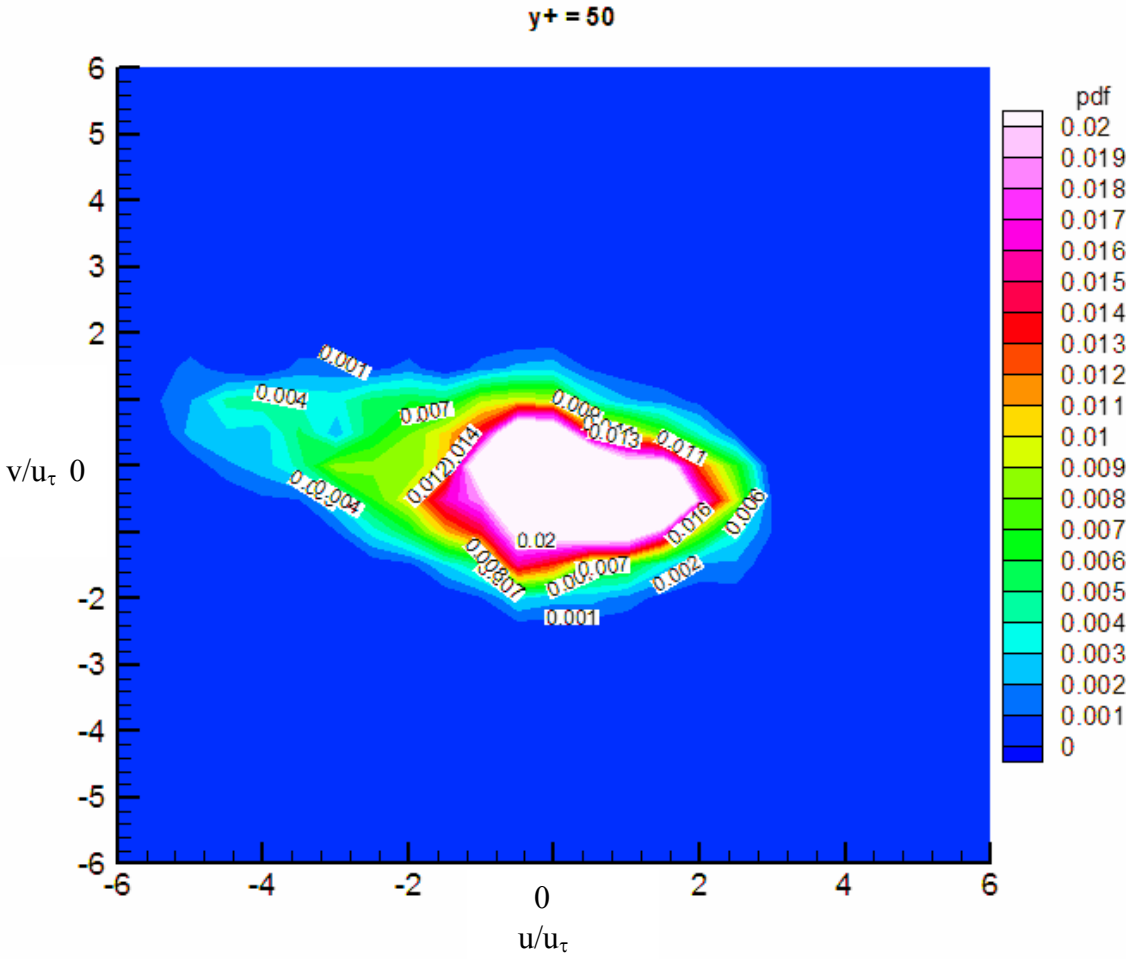

FIGURE 86. JPDF at $y^+ = 50$ (single phase).

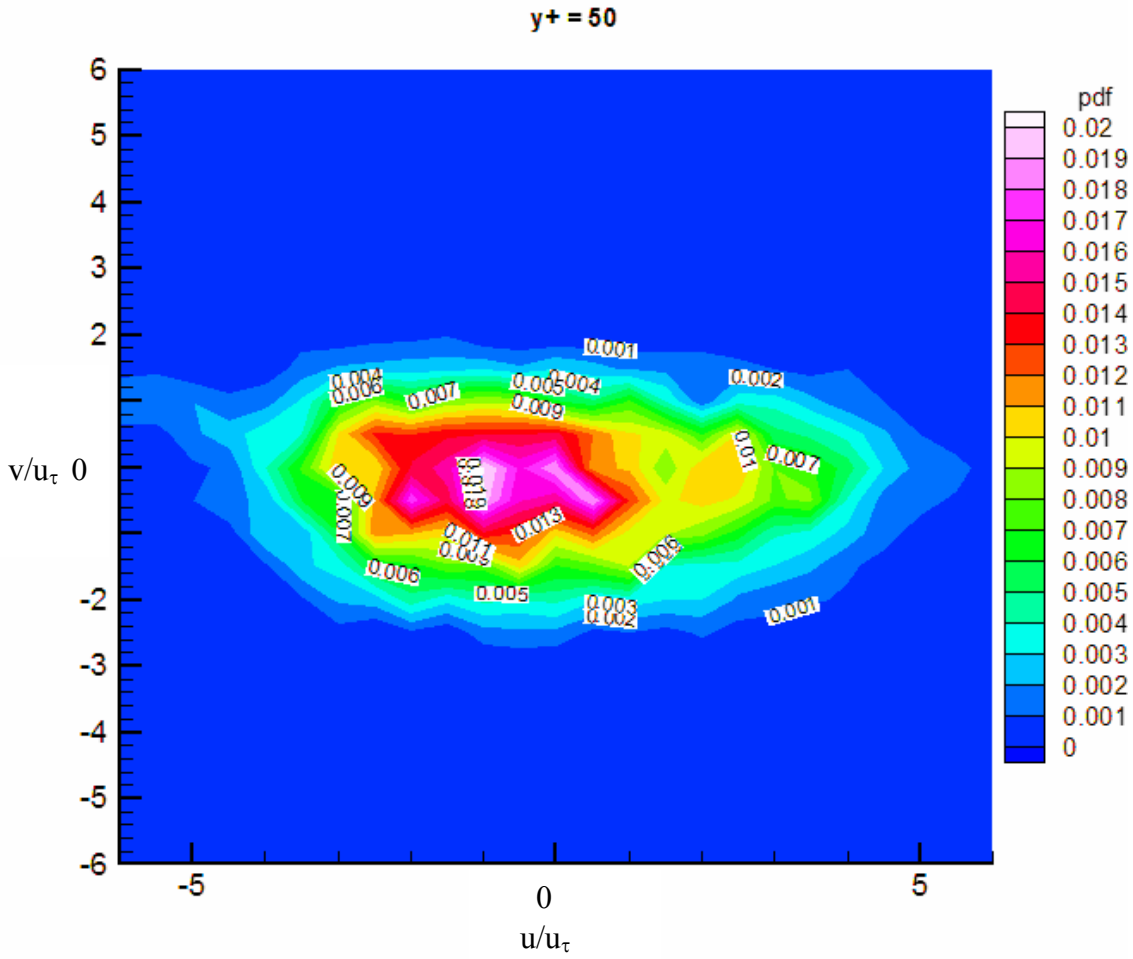

FIGURE 87. JPDF at $y^+ = 50$ (DR = 38.45 %).

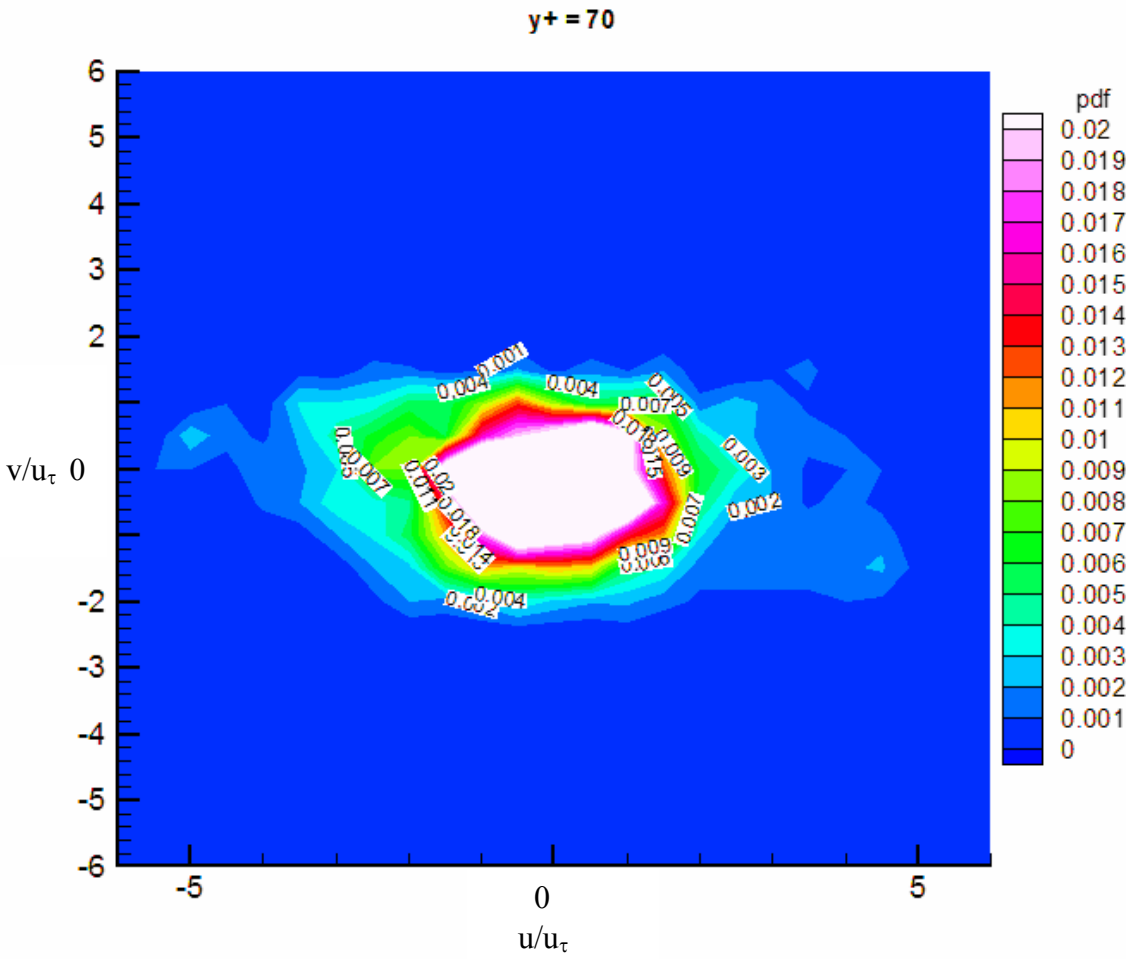

FIGURE 88. JPDF at $y^+ = 70$ (single phase).

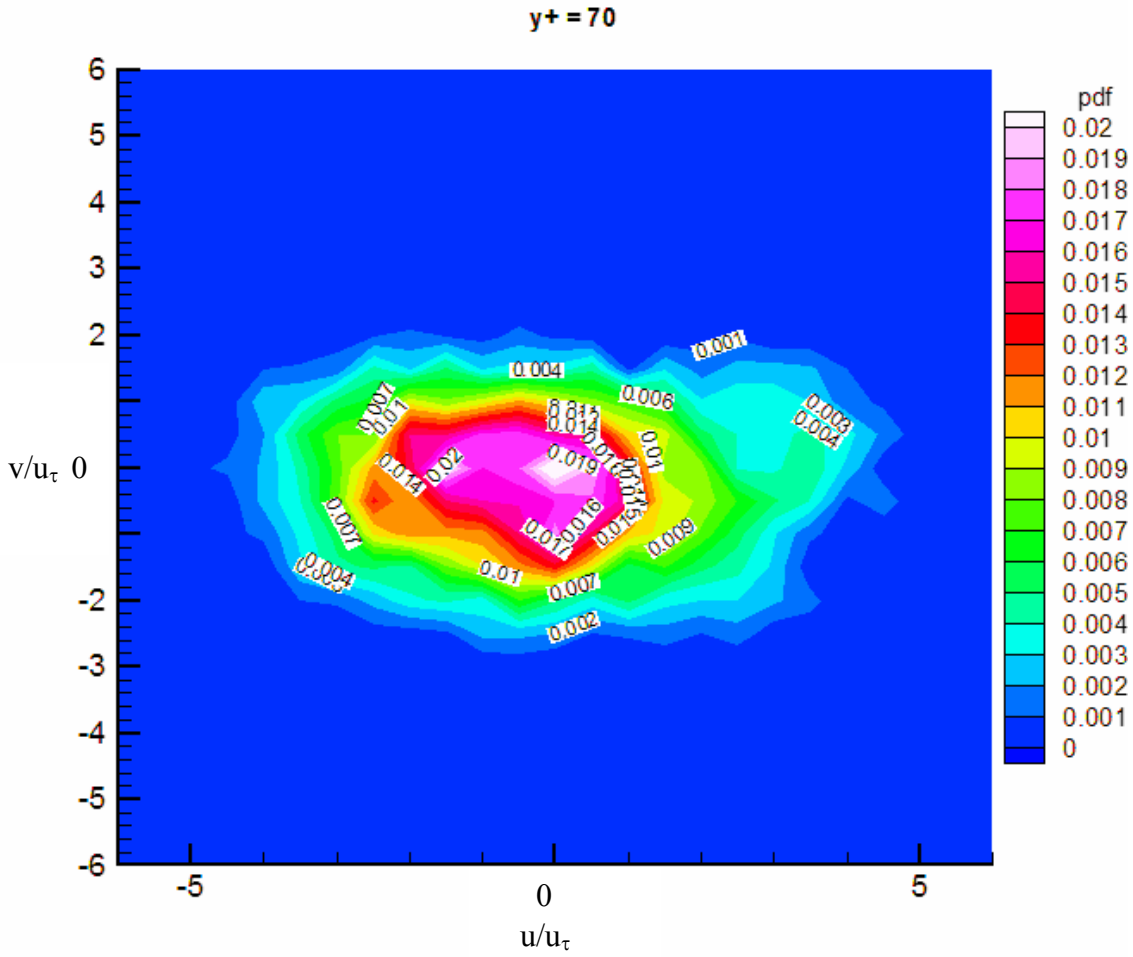

FIGURE 89. JPDF at $y^+ = 70$ (DR = 38.45 %).

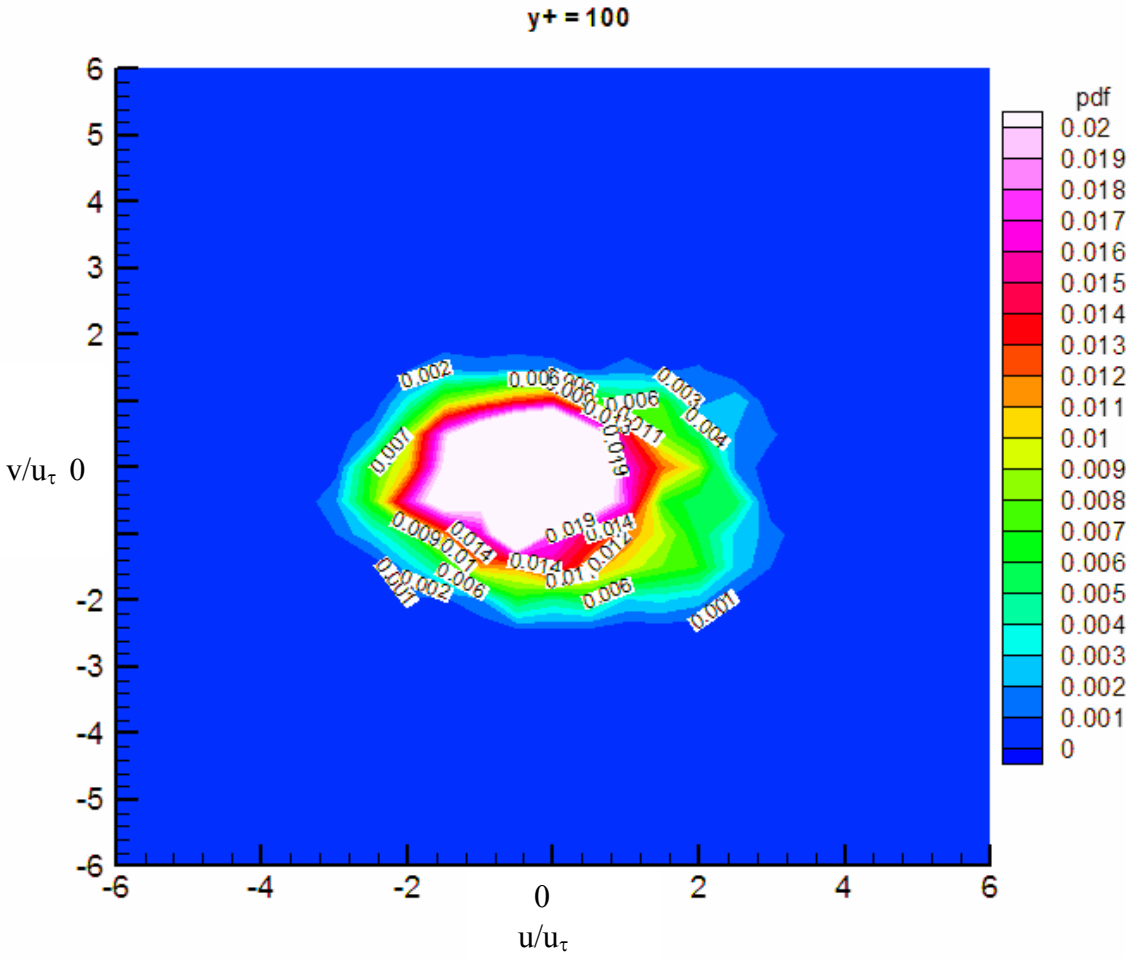

FIGURE 90. JPDF at $y^+ = 100$ (single phase).

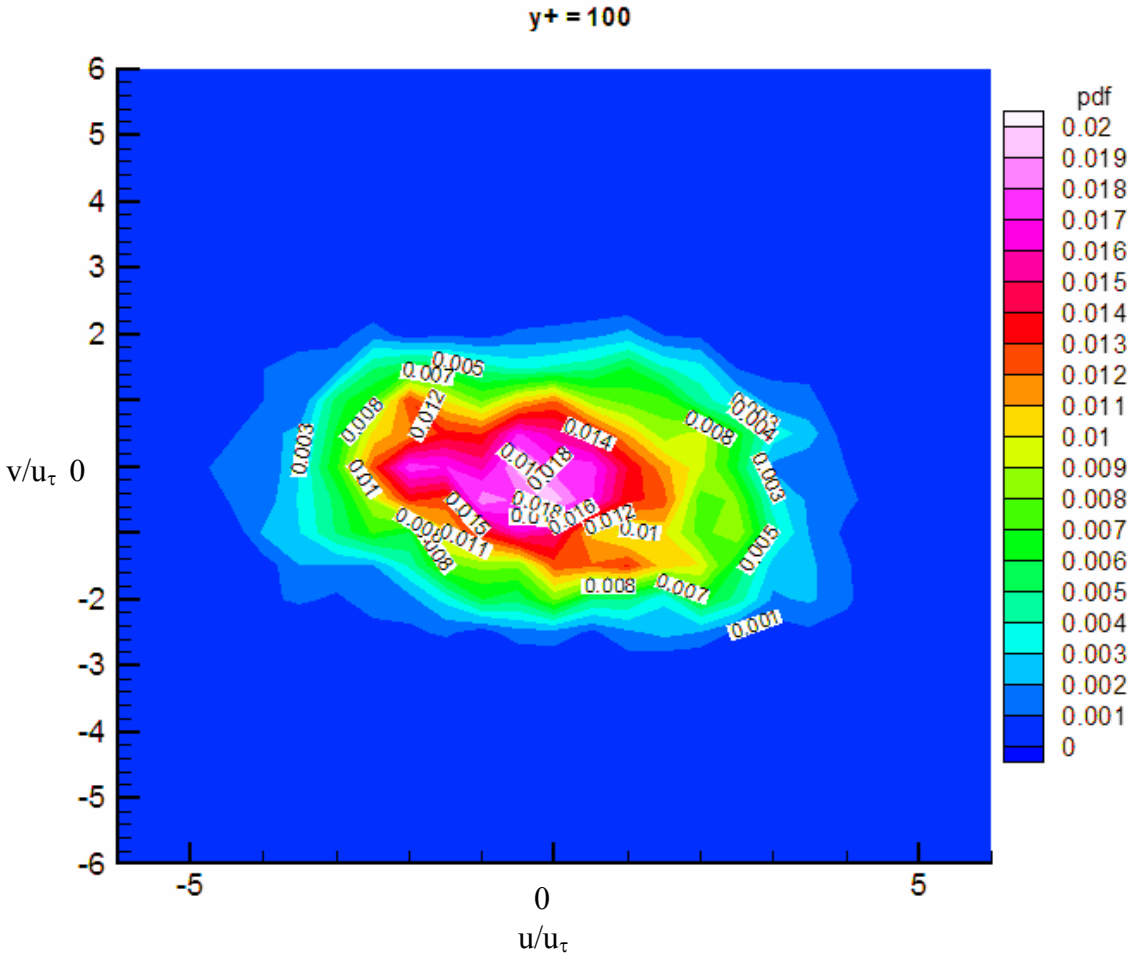

FIGURE 91. JPDF at $y^{+} = 100$ (DR = 38.45 %).

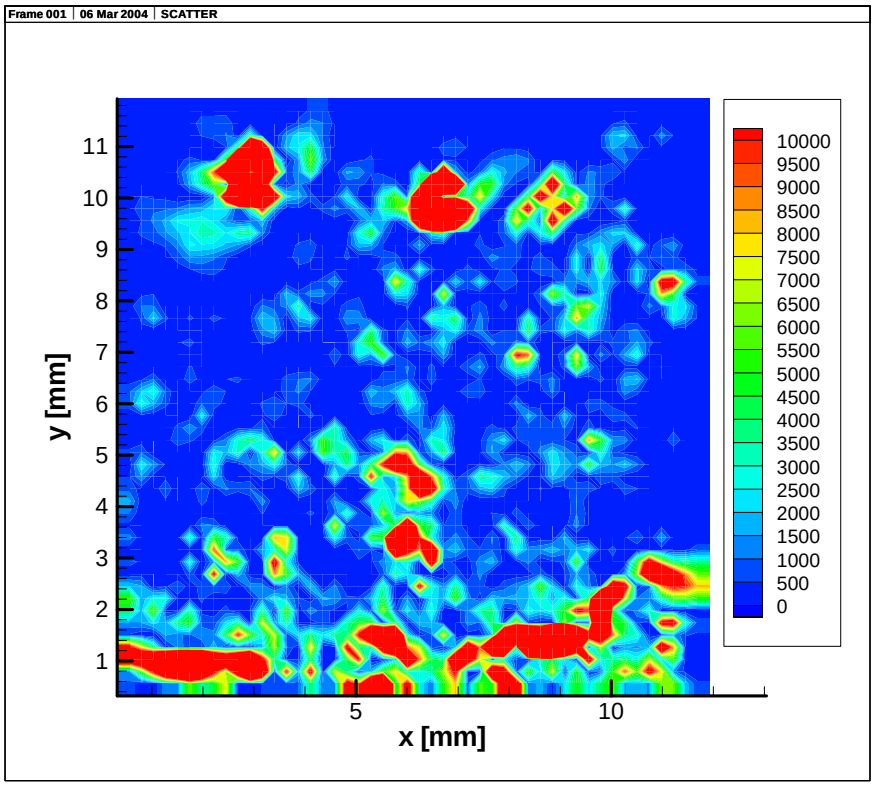

a)

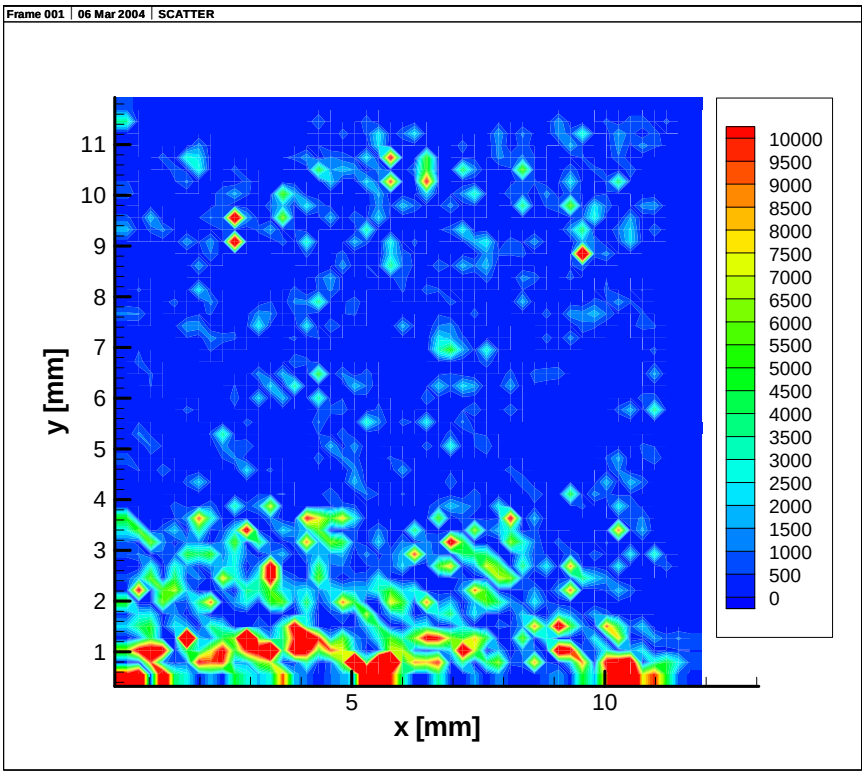

b)

FIGURE 92. Instantaneous enstrophy for a) single phase, b) DR = 12.06 %.

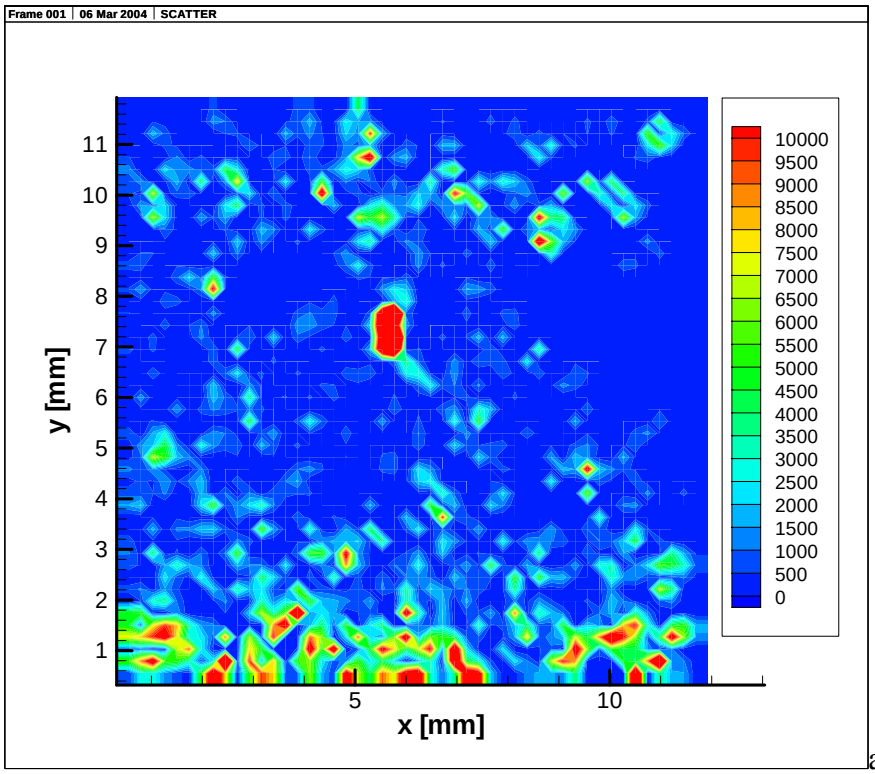

a)

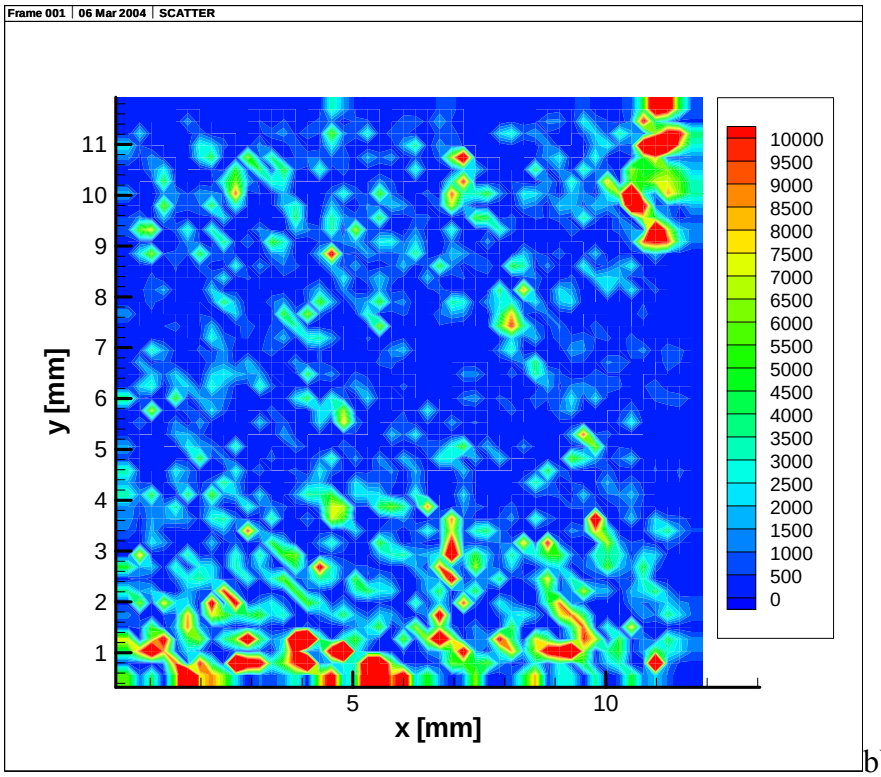

b)

FIGURE 93. Instantaneous enstrophy for a) DR = 16.62 %, b) DR = 29.81 %.

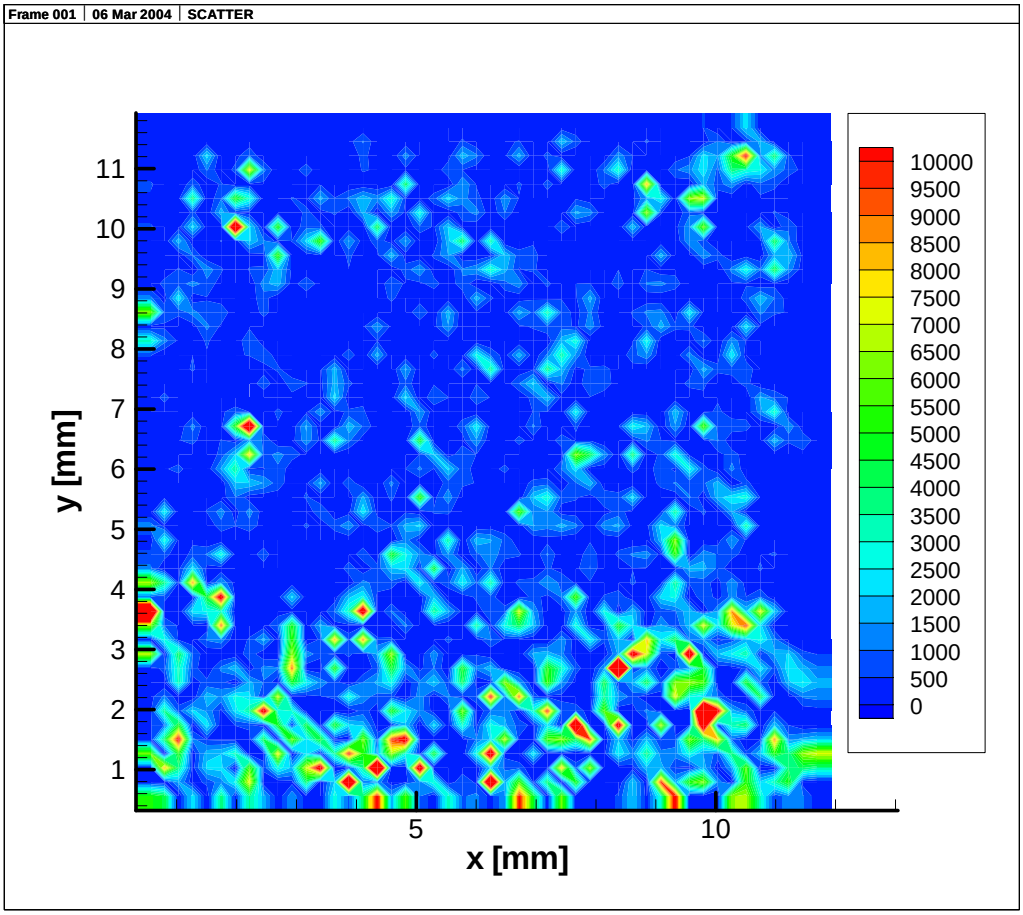

FIGURE 94. Instantaneous enstrophy for DR = 38.45 %.

CHAPTER V

CONCLUSIONS

Drag reduction is a complex process that can produce great savings of energy and money in different engineering applications. An experimental study in the near upper wall of a rectangular channel was carried out. Microbubbles with an average diameter of 30 μm, were produced by electrolysis and injected in the near wall region to reduce the drag. Particle Image Velocimetry (PIV) measurement technique was used to measure instantaneous x-y velocity fields. Qualitative and quantitative information was obtained from the statistical parameters that were evaluated.

A maximum drag reduction of 38.45 % was obtained for a local void fraction of 4.8 %. It indicates that local low concentrations of microbubbles produce a significant reduction of the drag. The results also show that microbubbles reduce the intermittency of the streamwise fluctuating velocity. However, a slight increase of the intermittency is present in the region close to the wall for the normal fluctuating component. When the spectra was evaluated in the region near the wall (inside the buffer layer), a shift of energy from high to low wavenumbers was observed for the maximum drag reduction results; it would indicate that then dissipation of turbulent energy would be reduced. On the other hand, the opposite trend was observed outside the buffer layer. It illustrates that two different phenomena are present. It is plausible that the transfer of momentum in the wall direction is altered by the presence of the microbubbles.

The new approach of using the spatial and the temporal information of PIV to evaluate the one dimensional wavenumber spectra results in obtaining more information about the distribution and interchange of turbulent fluctuating energy in wider wavenumber region.

It is necessary to point out that previous results of 2D spectra and JPDF evaluation for drag reduction by microbubbles injection were not found in the literature. The 2D spectra shows a shift of energy from high to low streamwise and normal wavenumbers. The JPDF results suggest that the correlation between u and v is decreased by the microbubbles; it mean that Reynolds stresses are suppressed where microbubbles are present.

The evaluation of the enstrophy shows a reduction of the high shear vortical structures near the wall region. Hence, it suggested that the microbubbles should be injected within the buffer layer to obtain better results.

It is suggested that there is an apparent interaction between the microbubbles and the smallest scales in the dissipation range; this interaction causes a reduction of the energy that is dissipated into internal energy of the fluid. These results suggest that there is a relationship between the Kolmogorov length scale and the diameter of the bubble d; it is plausible that when $d < \eta$ drag reduction occurs.

NOMENCLATURE

$E_{ij}(k_1)$	One dimensional spectra
$E_{ij}(k_1, k_2)$	Two dimensional spectra
$\dot{m}_H$	Hydrogen mass rate
CCD	Charge couple device
DR	Drag reduction
D	Diameter of the bubble
d^+	Diameter of the bubble in wall units
F	Flatness
F	frequency
H	Half height of the channel
H	Height of the riblet
I	Electrical current
JPDF(u, v)	Joint probability density function
k_1	Wavenumber in the streamwise direction
k_2	Wavenumber in the normal direction
N	Total number of samples
P	Static pressure
Re	Reynolds number
$R_{ij}(s)$	Spatial correlation
$R_{ij}(t')$	Temporal correlation

S	Skewness
s_x	Increment in the x-direction
s_y	Increment in the y-direction
S	Riblet space
s^+	Riblet space in wall units
U	Fluctuating streamwise velocity
U	Mean local velocity
u_τ	Friction velocity
u’	Turbulent intensity of the streamwise component
U_b	Bulk velocity
V	Vector velocity
V	Fluctuating normal velocity
v’	Turbulent intensity of the normal velocity
W	Atomic weight
X	Streamwise direction
Y	Normal direction
y^+	Distance from the wall in wall units
Z	Valence number
Z	Spanwise direction
Greek letter	
α	Void fraction
μ	Absolute water viscosity

μ'	Viscosity of liquid-bubble mixture
ν	Water Kinematic viscosity
ε_B	Bulk dissipation
ρ	Water density
τ	Shear stress
ω_z	Spanwise vorticity
ϕ	Bubble concentration in the boundary layer
η	Kolmogorov length scale
Δp	Pressure gradient
ρ_p	Seed particle's density
τ_w	Shear stress at the wall
τ_{tot}	Total shear stress
τ_{turb}	Turbulent stress

REFERENCES

BARON, A. & QUADRIO, M. 1993 Some preliminary results on the influence of riblets on the structure of a turbulent boundary layer. *Int. J. Heat and Fluid Flow* **14**, 223-230.

BECHERT, D. W., BRUSE, M., & HAGE, W. 2000 Experiments with three-dimensional riblets as an idealized model of shark skin. *Experiments in Fluids* **28**, 403-412.

BECHERT, D. W., BRUSE, M., HAGE, W., VAN DER HOEVEN, J. G. T., & HOPPE, G. 1997 Experiments on drag-reducing surfaces and their optimization with an adjustable geometry. *J. Fluid Mech.* **338**, 59-87.

BOGDEVICH, V. G., EVSEEV, A. R., MAYYUGA, A. G. & MIGIRENKO, G. S. 1977 Gas-saturation effect on near-wall turbulence characteristics. In *Proc. Second International Conference on Drag Reduction*, (ed. H.S. Stephens & J. A. Clark), pp. D2-25, Cambridge, England. BHRA Fluid Engineering.

BUSHNELL, D. M. & MOORE, K. J. 1991 Drag reduction in nature. *Annu. Rev. Fluid Mech.* **23**, 65-79.

CHOI, J., XU, C.X. & SUNG, H. J. 2002 Drag reduction by spanwise oscillation in wall-bounded turbulent flows. *AIAA Journal* **40**, 842-850.

CHOI, K. S. & ORCHARD, D. M. 1997 Turbulence management using riblets for heat and momentum transfer. *Experimental Thermal and Fluid Science* **15**, 109-124.

CHRISTENSEN, K. T. & ADRIAN, R. J. 2002 The velocity and acceleration signatures of small-scale vortices in turbulent channel flow. *Journal of Turbulence* **3**, 1-28.

DEUTSCH, S. & CASTANO, J. 1986 Microbubble skin friction on an axisymmetric body. *Phys. Fluids* **29**, 3590-3597.

FONTAINE, A. A., DEUTSCH, S., BRUNGART, T. A., PETRIE., H. L. & FENSTERMACKER, M. 1999 Drag reduction by coupled systems: microbubble injection with homogeneous polymer and surfactant solutions. *Experiments in Fluids* **26**, 397-403.

GAMPERT, B. & YONG, C. K. 1989 The influence of polymer additives on the coherent structure of turbulent channel flow. In *Proc. Structure of Turbulence and Drag Reduction IUATM Symposium,* (ed. A. Gyr), pp. 223-232, *Zurich, Switzerland*. Springer, New York.

GECKINLI, N. C. & YAVUZ, D. 1983 *Discret Fourier Transformation and Its Applications to Power Spectra Estimation*. Elsevier. Amsterdam, The Netherlands.

GUIN, M. M., KATO, H., YAMAGUCHI, H., MAEDA, M., & MIYANAGA, M. 1996 Reduction of skin friction by microbubbles and its relation with near wall concentration in a channel. *Journal of Marine Science and Technology*. **1**, 241-254.

GŰNTHER, A., PAPAVASSILIOU, D. V., WARHOLIC, M. D., & HANRATTY, T. J. 1998 Turbulent flow in a channel at low Reynolds number. *Experiments in Fluids.* **25**, 503-511.

GYR, A. & BEWERSDORFF, H. F. 1989 Chance of structures close to the wall of a turbulent flow in drag reducing fluids. In Proc. *Structure of Turbulence and Drag Reduction IUATM Symposium,* (ed. A. Gyr), pp. 215-222, *Zurich, Switzerland*. Springer, New York.

HASSAN, Y. A., BLANCHAT, T. K., & SEELEY Jr. C. H. 1992 PIV flow visualization using particle tracking techniques. *Measurements in Science and Technology* **3**, 633-642.

JIMENEZ, J. & PINELLI, A. 1997 Wall turbulence: how it works and how to damp it. *AIAA Paper* 97-2112, 1-9.

KANAI, A. & MIYATA, H. 2001 Direct numerical simulation of wall turbulent flows with microbubbles. *Int. J. Numer*. *Meth Fluids* **35,** 593-615.

KARNIADAKIS, G. E. & CHOI, K. S. 2003 Mechanisms on transverse motions in turbulent wall flows. *Annu. Rev. Fluid Mech.* **35**, 45-62.

KATO, H., MIYANAGA, M., HARAMOTO, Y., & GUIN, M. M. 1994 Frictional drag reduction by injecting bubbly water into turbulent boundary layer. In *Proc. 1994 Cavitation and Gas-Liquid Flow in Fluid Machinery and Devices ASME* **190**, 185-194.

KIM, J. 2003 Control of turbulent boundary layers. *Phys. Fluids* **15**, 1093-1105.

KODAMA, Y., KAKUGAWA, A., TAKAHASHI, T., & KAWASHIMA, H. 2000 Experimental study on microbubbles and their applicability to ships for skin friction reduction. *International Journal of Heat and Fluid Flow* **21**, 582-588.

KOELTZSCH, K., DINKEKACKER, A., & GRUNDMANN, R. 2002 Flow over convergent and divergent wall riblets. *Experiments in Fluids* **33**, 346-350.

LANCE, M. & BATAILLE, J. 1991 Turbulence in the liquid phase of a uniform bubbly air-water flow. *J. Fluid Mech.* ***222***, 95-118.

LATORRE, R. 1997 Ship hull drag reduction using bottom air injection. *Ocean Engng.* **24**, 161-175.

LEE, C. & KIM, J. 2002 Control of the viscous sublayer for drag reduction. *Phys. Fluids* **14**, 2523-2529.

LEE, S. J. & LEE, S. H. 2001 Flow field analysis of a turbulent boundary layer over a riblet surface. *Experiments in Fluids* **30**, 153-166.

LUMLEY, J. & BLOSSEY, P. 1998 Control of turbulence. *Annu. Rev. Fluid Mech.* **30,** 311-327.

LUMLEY, J. L. 1969 Drag reduction by additives. *Annu. Rev. Fluid Mech. 367-384.*

MADAVAN, N. K., DEUTSCH, S., & MERKLE, C. L. 1984 Reduction of turbulent skin friction by microbubbles. *Phys. Fluids* **27**, 356-363.

MADAVAN, N. K., MERKLE, C. L., & DEUTSCH, S. 1985 Numerical investigations into the mechanisms of microbubble drag reduction. *Journal of Fluids Engineering* **107**, 370-377.

McCOMB, W. D. 1990 *The Physics of Fluid Turbulence*. Oxford University Press, New York.

McCORMICK, M. E. & BHATTACHARYYA, R. 1973 Drag reduction of a submersible hull by electrolysis. *Naval Engineers Journal* **April**, 11-16.

MERKLE, C. L. & DEUTSCH, S. 1989 Microbubble drag reduction. In *Frontiers in Experimental Fluid Mechanics.* (ed. M. Gad-el-Hak), pp. 291-335. Springer, New York.

MURAI, Y., SONG, X., TAKAGI, T., ISHIKAWA, M., YAMAMOTO, & F., OHTA, J. 2000 Inverse energy cascade structure of turbulence in bubbly flow. *JSME International Journal Series* **. 43**, 188-196.

NELKIN, M. 1992 In what sense is turbulence an unsolved problem. *Science* **255**, 566-570.

PANTON, R. L. 1996 *Incompressible Flow*, 2nd ed. Wiley Interscience, New York.

POPE, S. B. 2000 *Turbulent Flows*. Cambridge University Press. Cambridge, UK.

SCHMIDL, W. D. 1999 Three-dimensional experimental investigation of the two-phase flow structure in a bubbly pipe flow. PhD dissertation, Department of Nuclear Engineering, Texas A&M University, College Station, Texas.

TENNEKES, H. & LUMLEY, J. L. 1972 *A First Course in Turbulence*. MIT Press, Cambridge, MA.

TOMS, B. A. 1977 On the early experiments on drag reduction by polymers. *Phys. Fluids* **20**, S3-S5.

TSINOBER, A. 2001 *An Informal Introduction to Turbulence*. Kluwer Academic Publishers. Dordrecht, The Netherlands.

WANG, J., LAN, S., & CHEN, G. 2000 Experimental study of the turbulent boundary layer flow over riblets surface. *Fluid Dynamics Research* **27**, 217-229.

WARHOLIC, M. D. 1997 Modification of turbulent channel flow by passive and additive devices. PhD dissertation, Department of Chemical Engineering, University of Illinois, Urbana.

WARHOLIC, M.D., HEIST, D.K., KATCHER, M. & HANRATTY, T.J. 2001 A study with particle-image velocimetry for the influence of drag-reducing polymers on the structure of turbulence. *Experiments in Fluids* **31**, 474-483.

WARHOLIC, M. D., MASSAH, H., & HANRATTY, T. J. 1999 Influence of drag-reducing polymers on turbulence: effects of Reynolds number, concentration and mixing. *Experiments in Fluids* **27**, 461-472.

WEI, T. & WILLMARTH, W., 1992 Modifying turbulent structure with drag-reducing polymer additives in turbulent channel flows. *J. Fluid Mech*. **245**, 619-641.

WHITE, A. & HEMMINGS, J. A. G., 1976 Drag reduction by additives review and bibliography. *BHRA Fluid Engineering*, 7-28.

WILKINSON, S. P., ANDERS, J. B., LAZOS, B. S., & BUNSHELL, D. M. 1988 Turbulent drag reduction research at NASA Langley: progress and plans. *Int. J. Heat and Fluid Flow* **9**, 266-277.

WOOD, R. M. 2003 Aerodynamic drag and drag reduction: energy and energy savings (invited). *AIAA Paper* 84-0174, 1-20.

YAMAMOTO, Y., UEMURA, T. & KADOTA, S. 2002 Accelerated super-resolution PIV based on successive abandonment method. In *Proceedings of 11th International Symposium on Applications of Laser Techniques to Fluid Mechanics*, paper 24-1. Lisbon.

APPENDIX A

This appendix shows fluctuating velocity fields for single phase flow at different times.

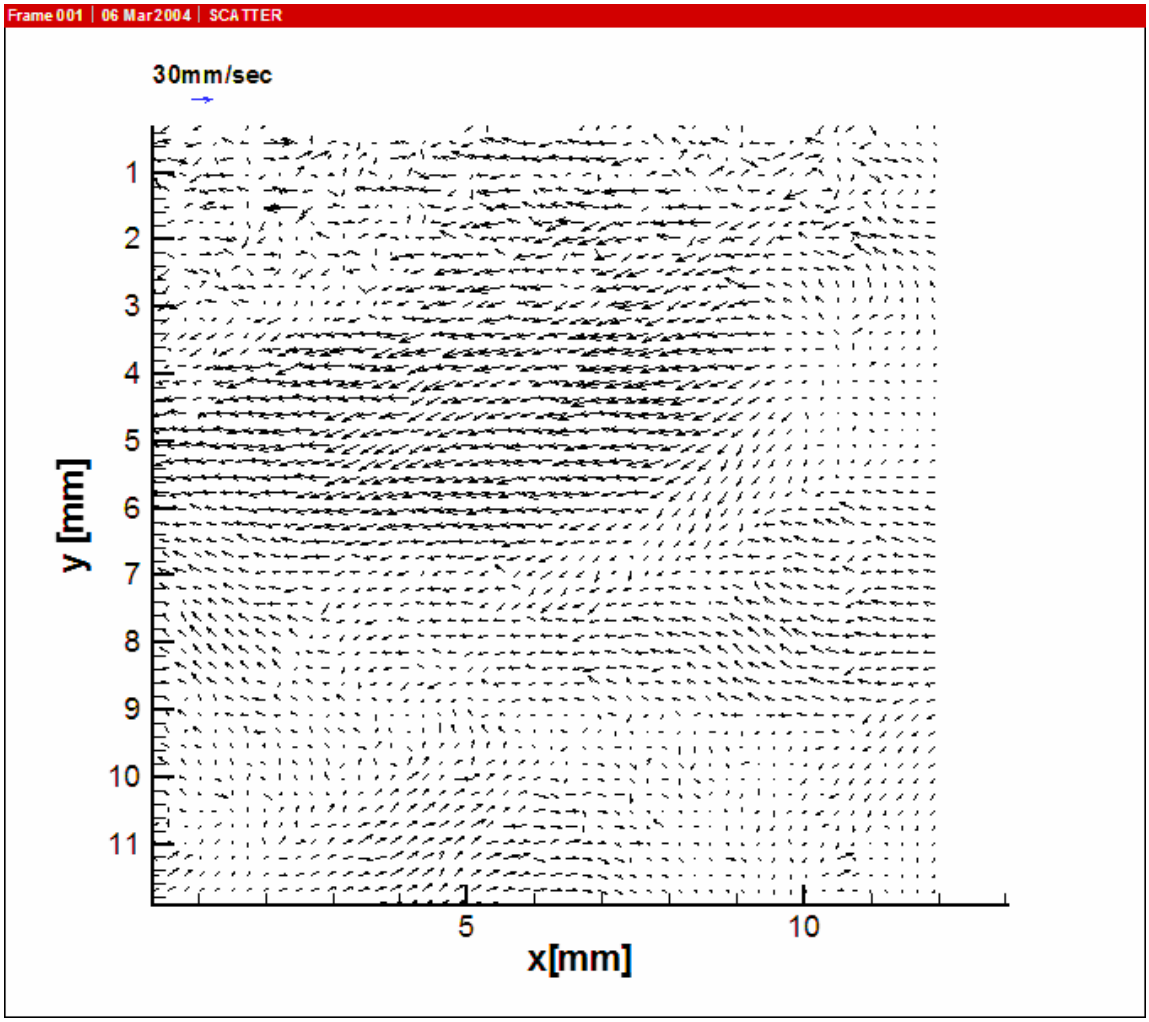

FIGURE A-1. Fluctuating velocity field at t =0.825 s (single phase).

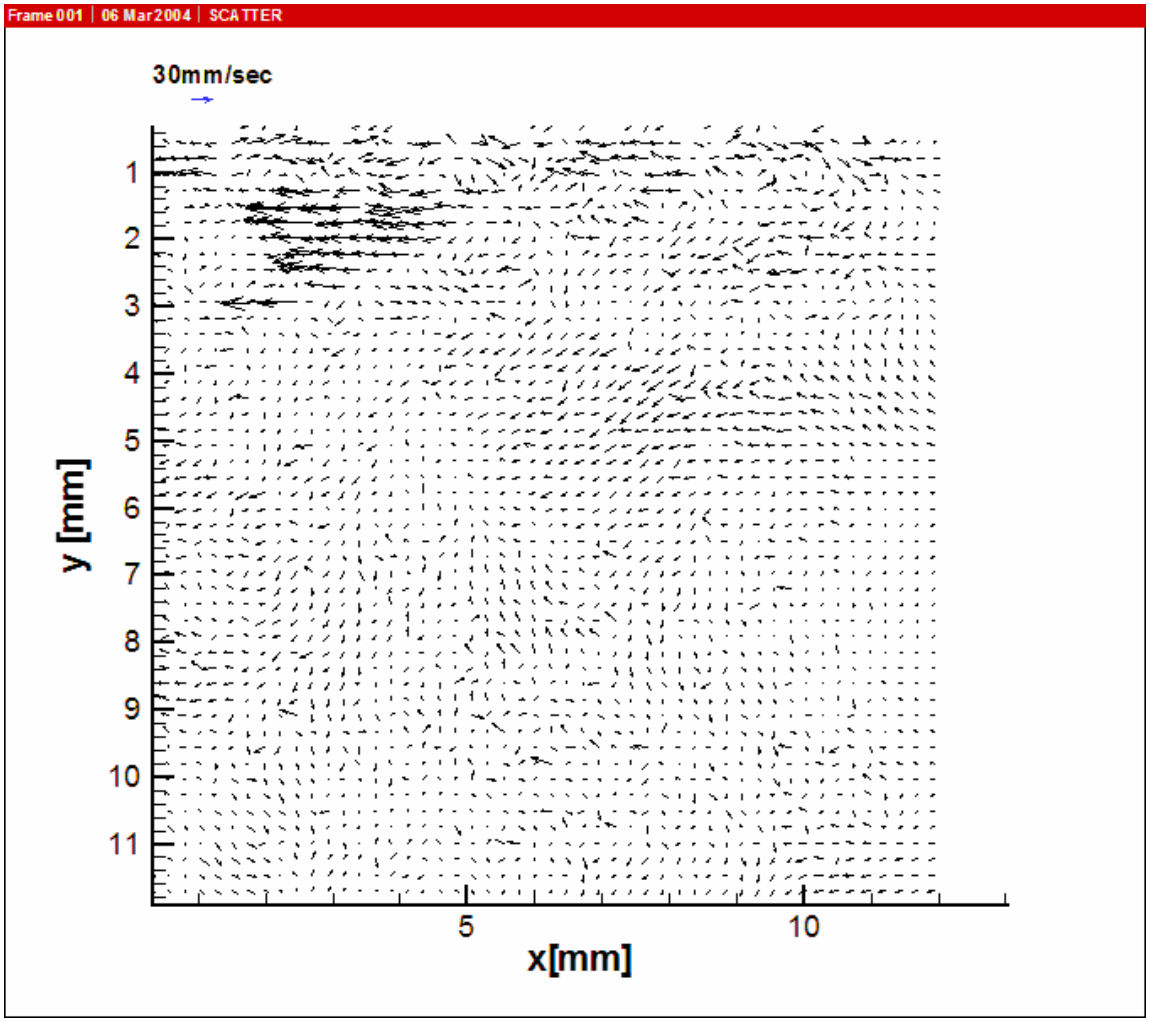

FIGURE A-2. Fluctuating velocity field at t = 0.891(single phase).

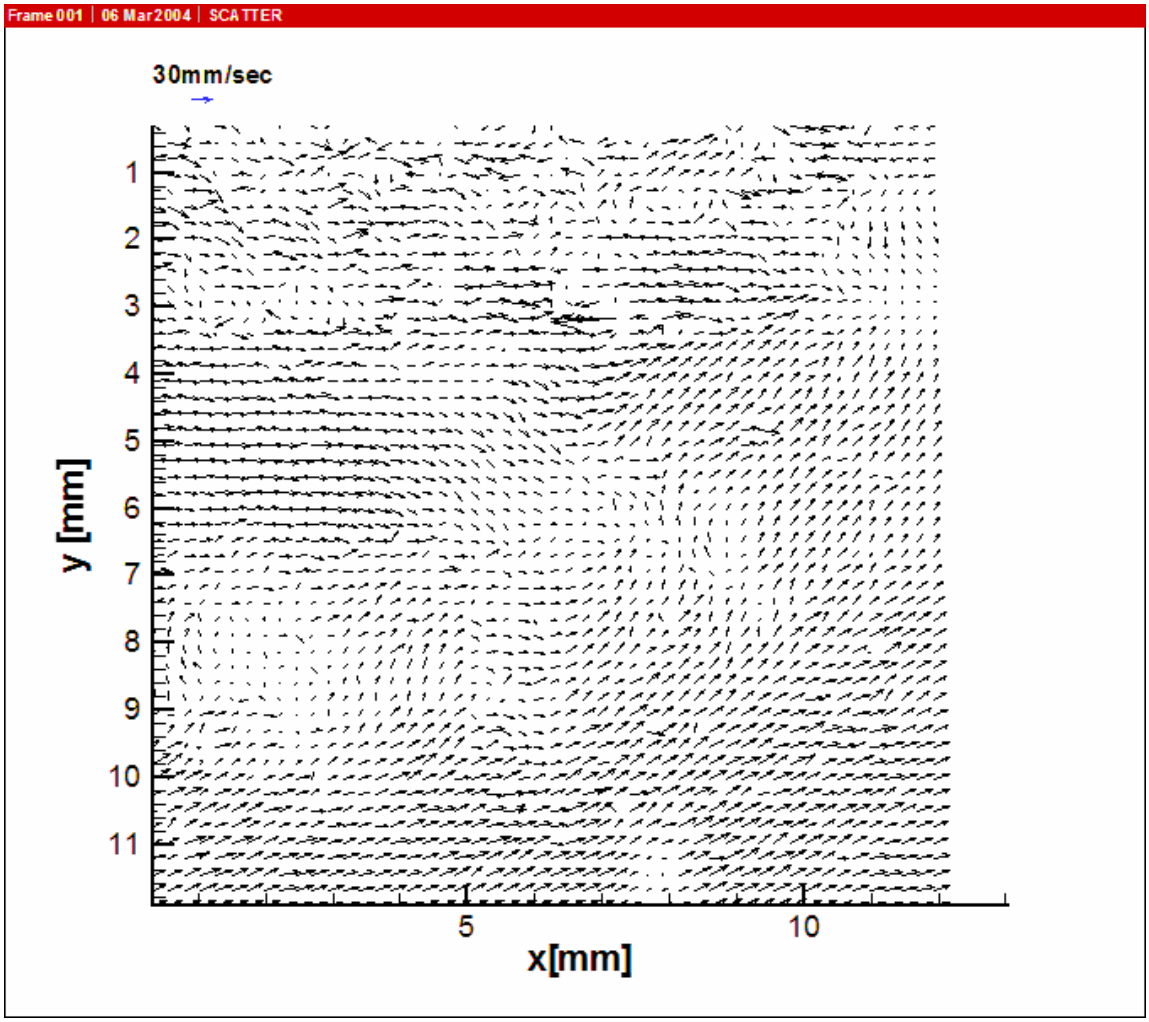

FIGURE A-3. Fluctuating velocity field at t =1.089 s (single phase).

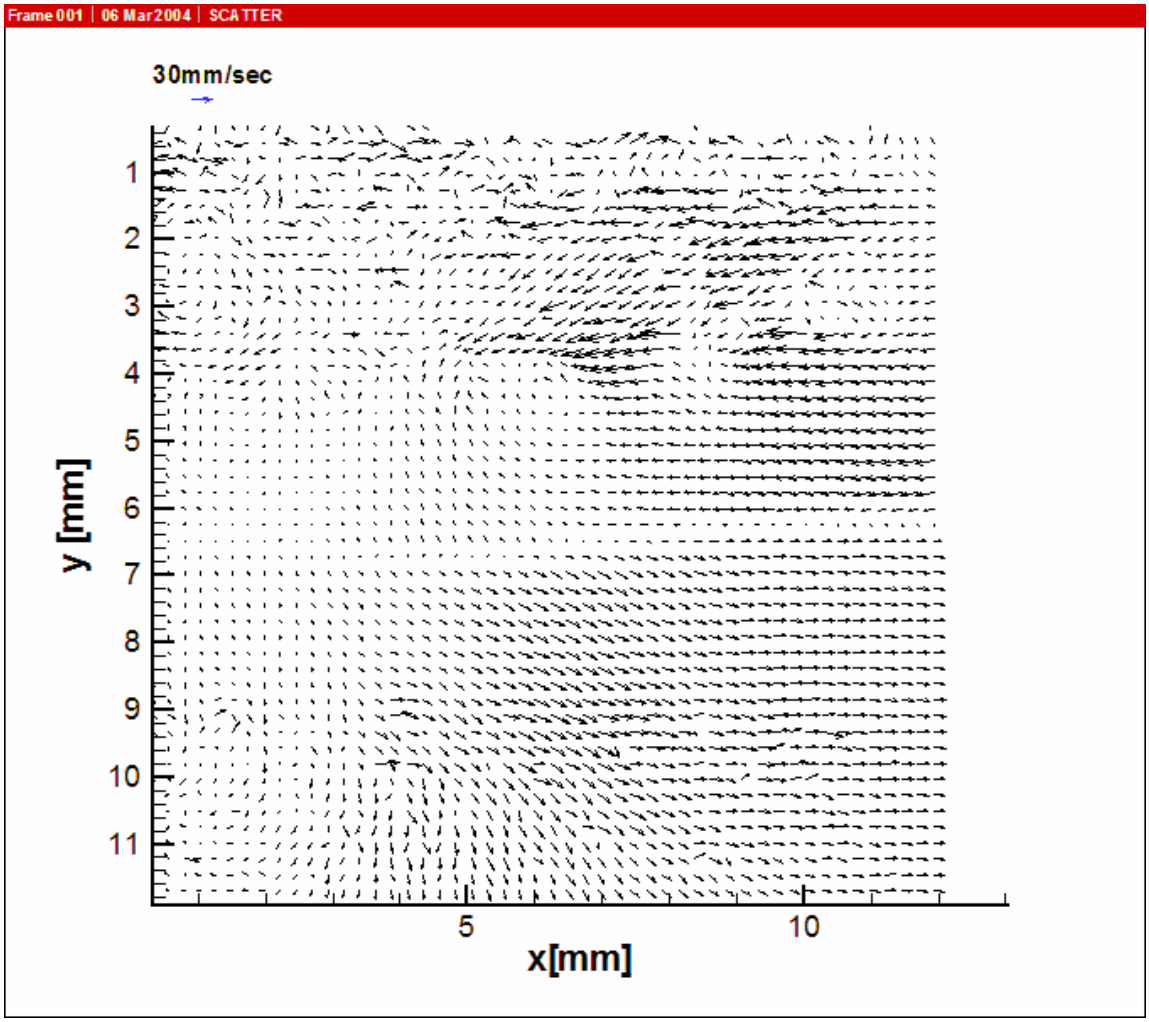

FIGURE A-4. Fluctuating velocity field at t =3.2 s (single phase).

APPENDIX B

This appendix shows the one dimensional spectra, E_{uu} (k_1) at different distance from the wall without any correction.

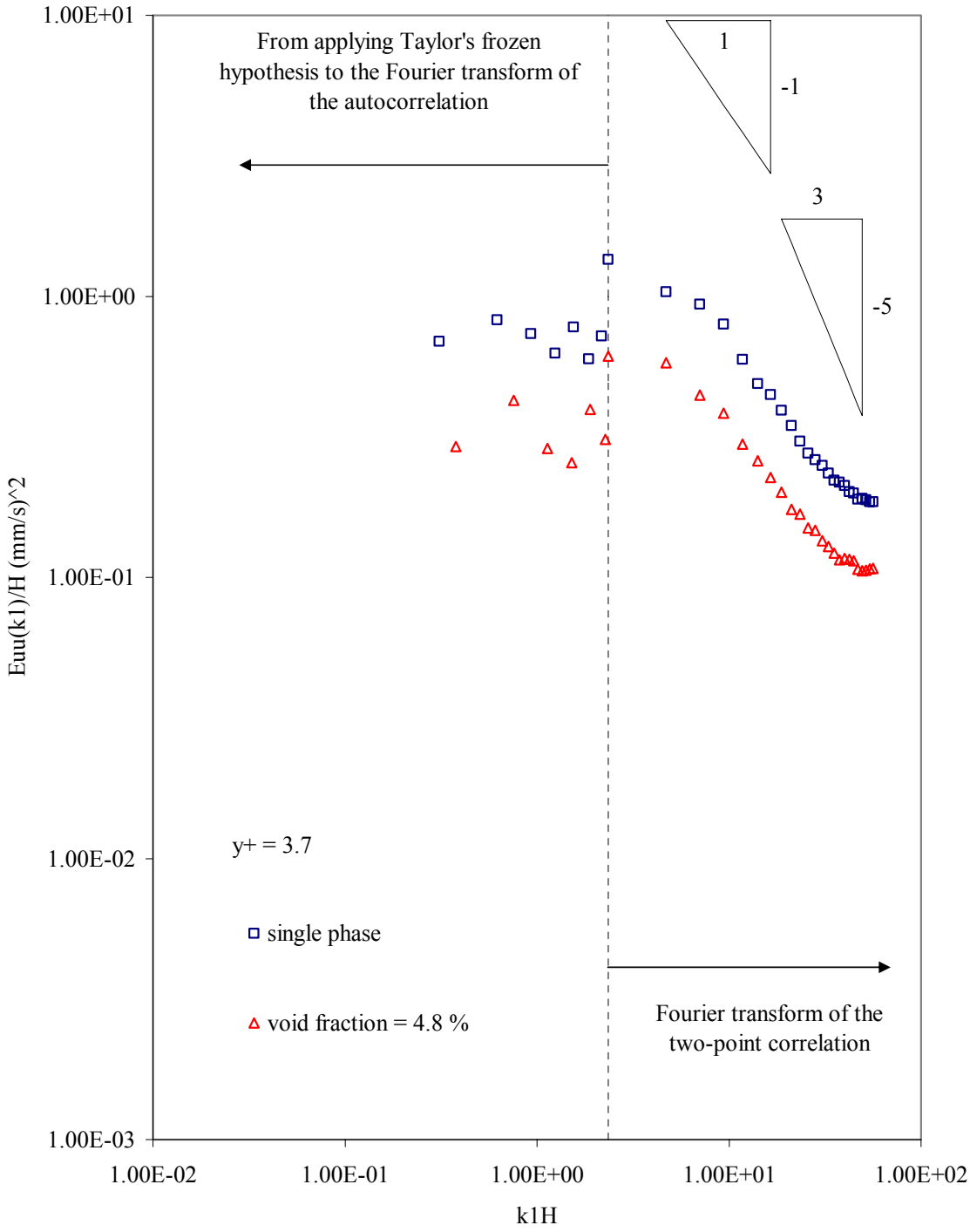

FIGURE B-1. Dimensional streamwise spectra versus non-dimensional wavenumber at y/H = 0.01 (without any correction).

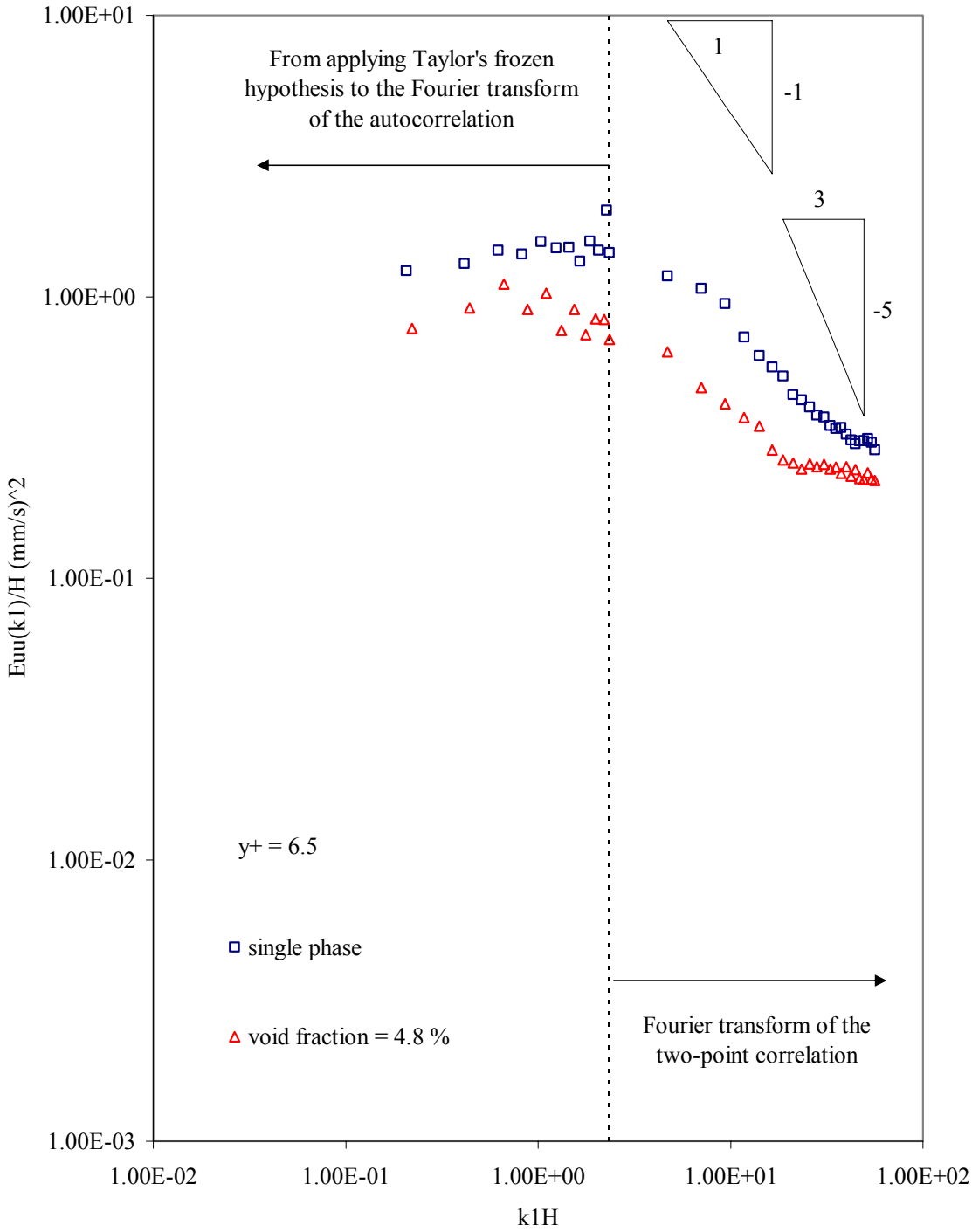

FIGURE B-2. Dimensional streamwise spectra versus non-dimensional wavenumber at y/H = 0.019 (without any correction).

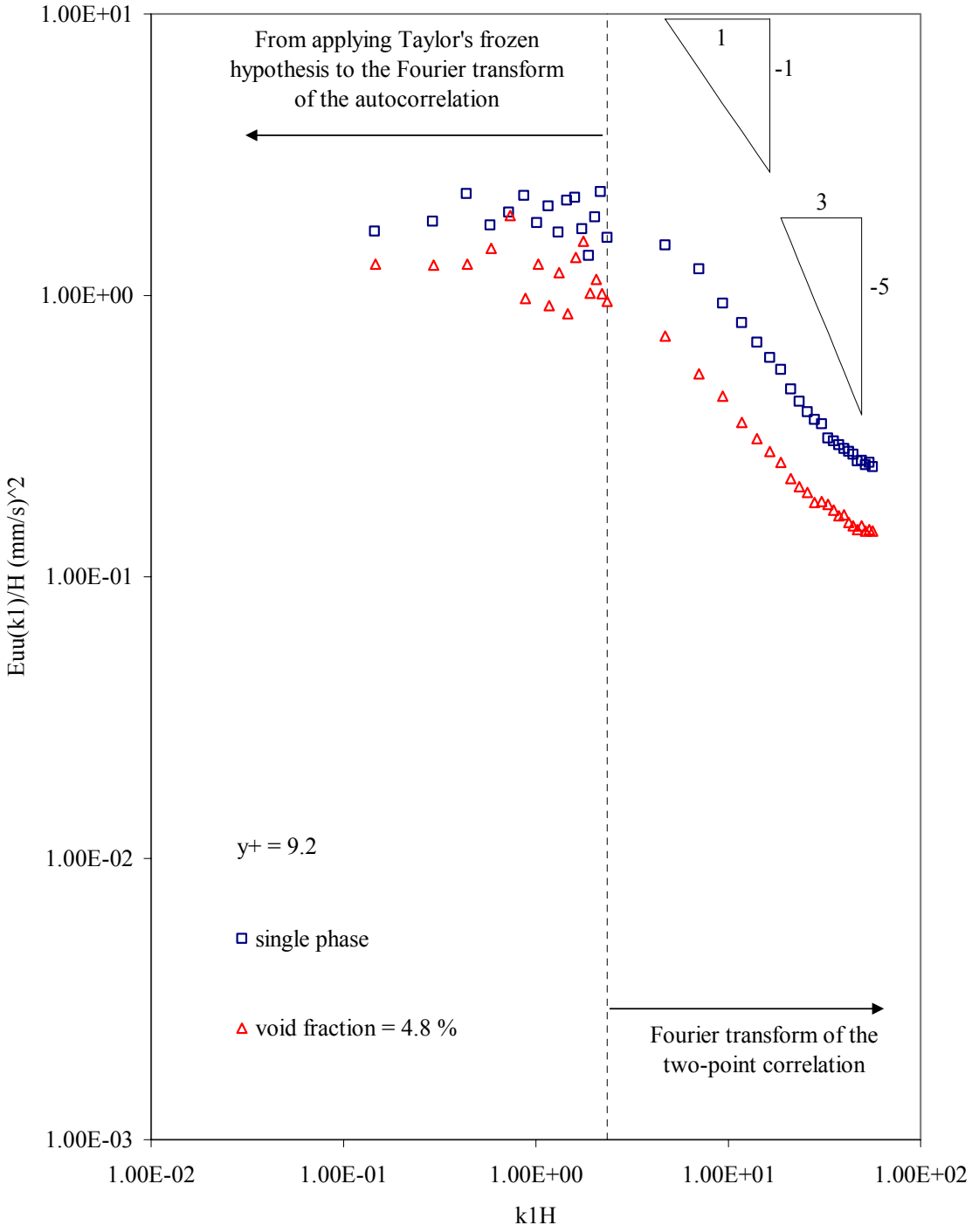

FIGURE B-3. Dimensional streamwise spectra versus non-dimensional wavenumber at y/H = 0.027 (without any correction).

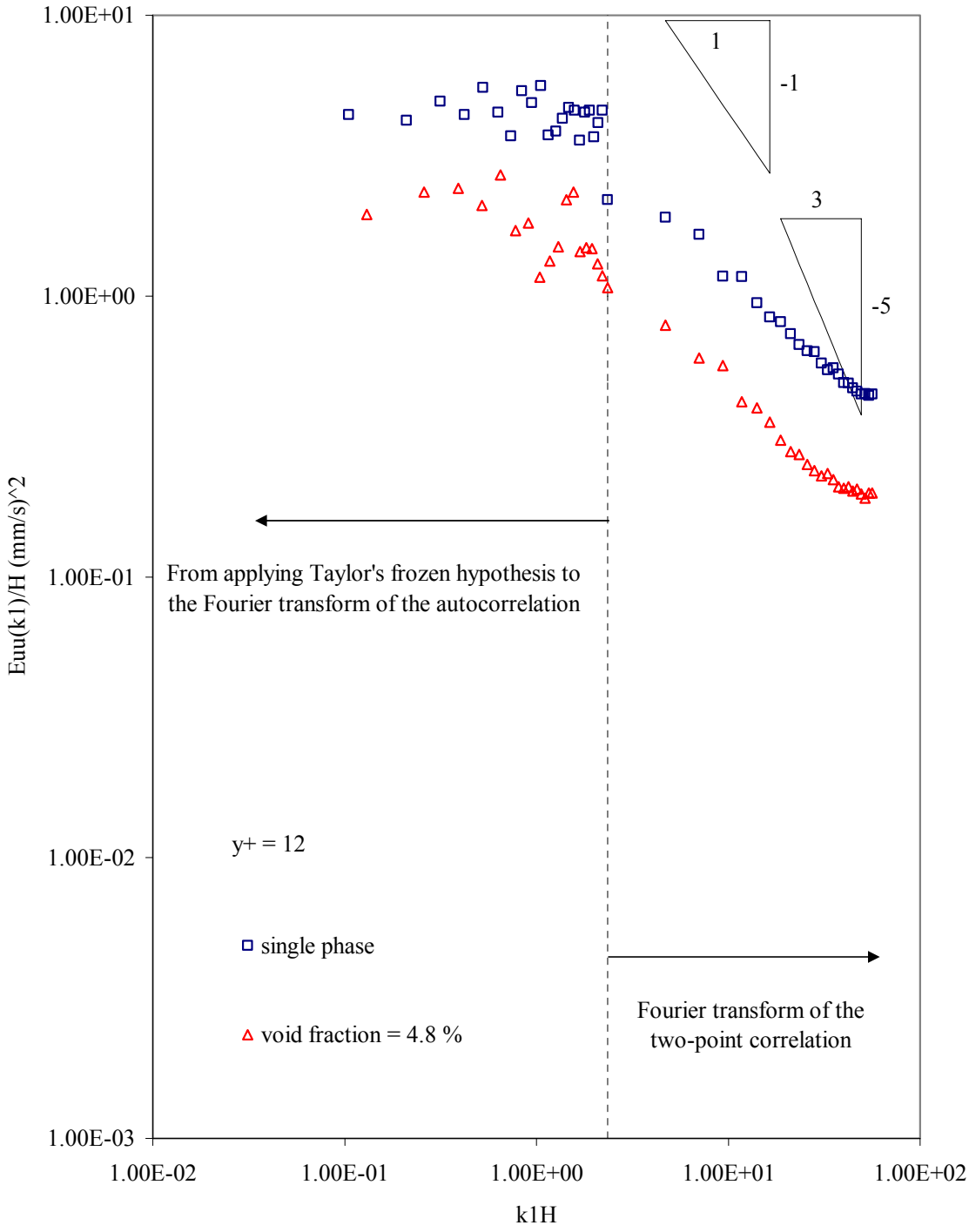

FIGURE B-4. Dimensional streamwise spectra versus non-dimensional wavenumber at y/H = 0.036 (without any correction).

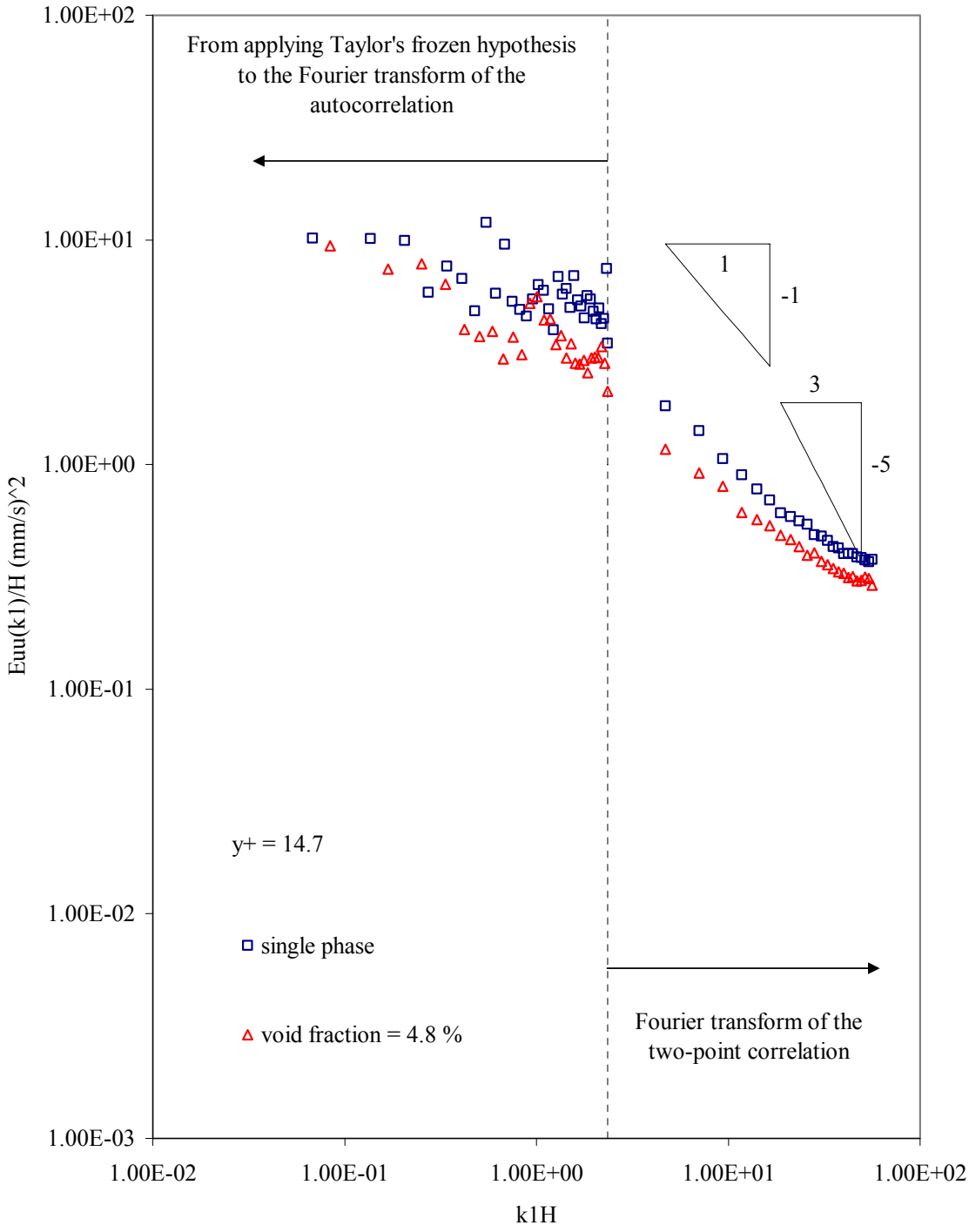

FIGURE B-5. Dimensional streamwise spectra versus non-dimensional wavenumber at y/H = 0.044 (without any correction).

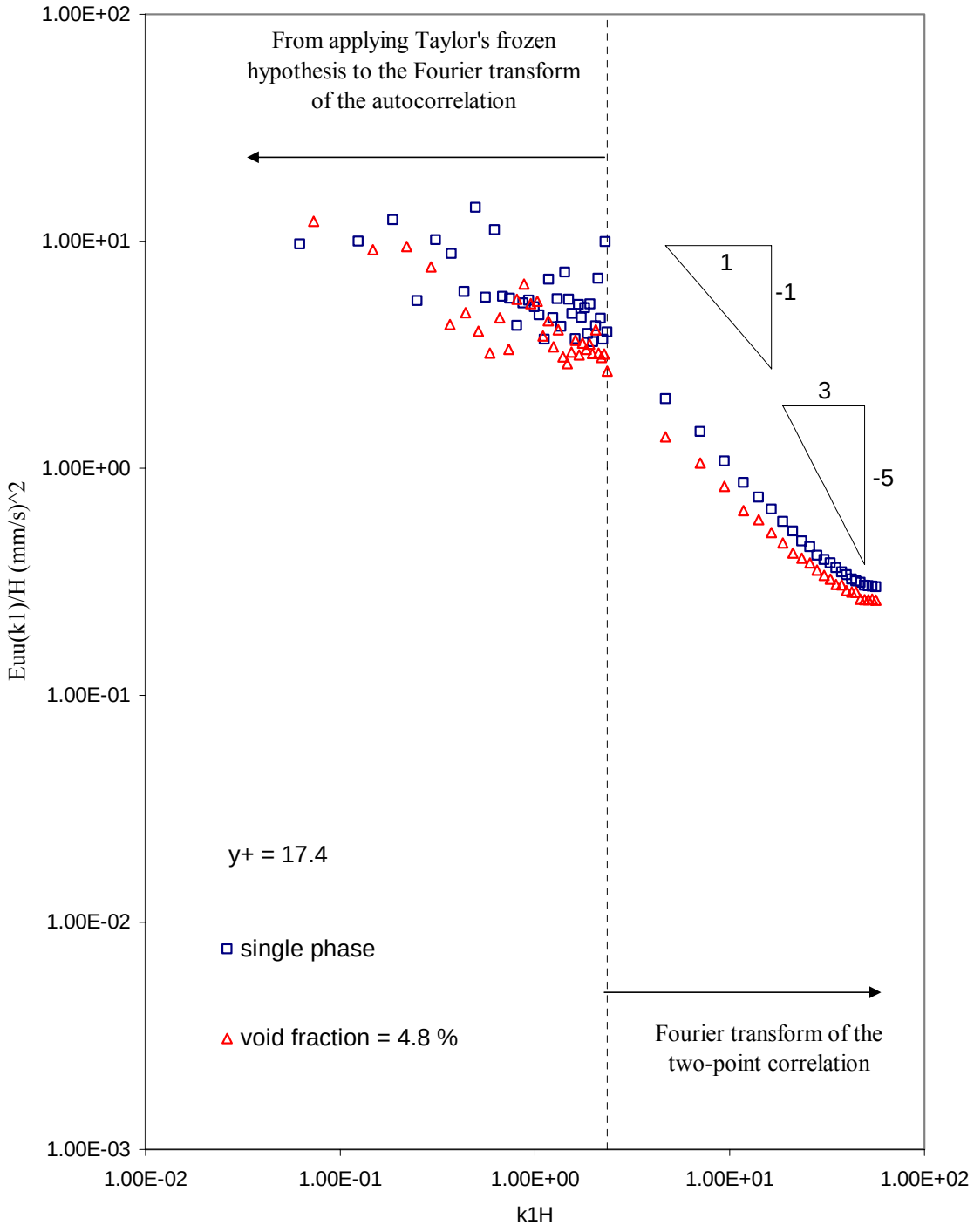

FIGURE B-6. Dimensional streamwise spectra versus non-dimensional wavenumber at y/H = 0.052 (without any correction).

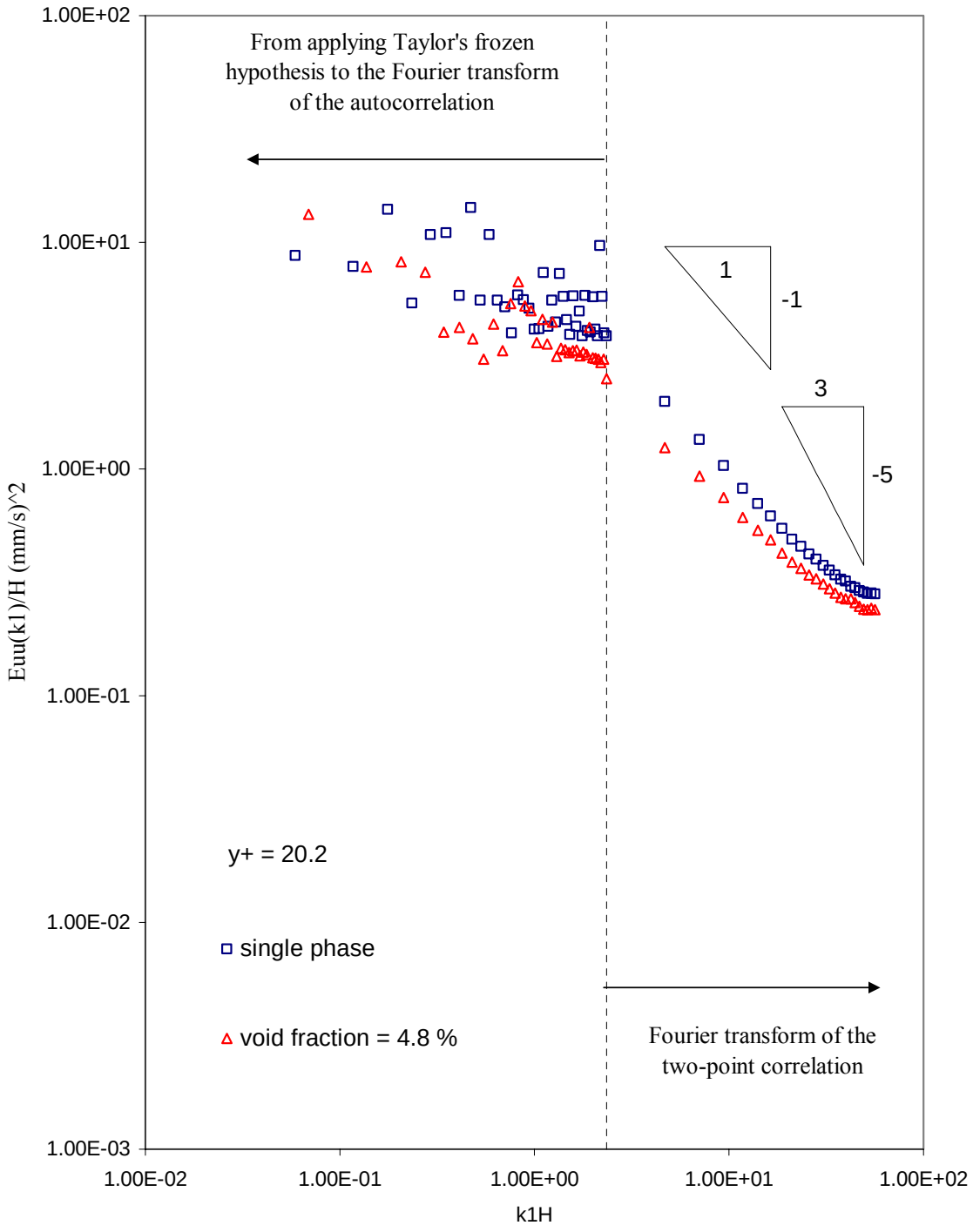

FIGURE B-7. Dimensional streamwise spectra versus non-dimensional wavenumber at y/H = 0.06 (without any correction).

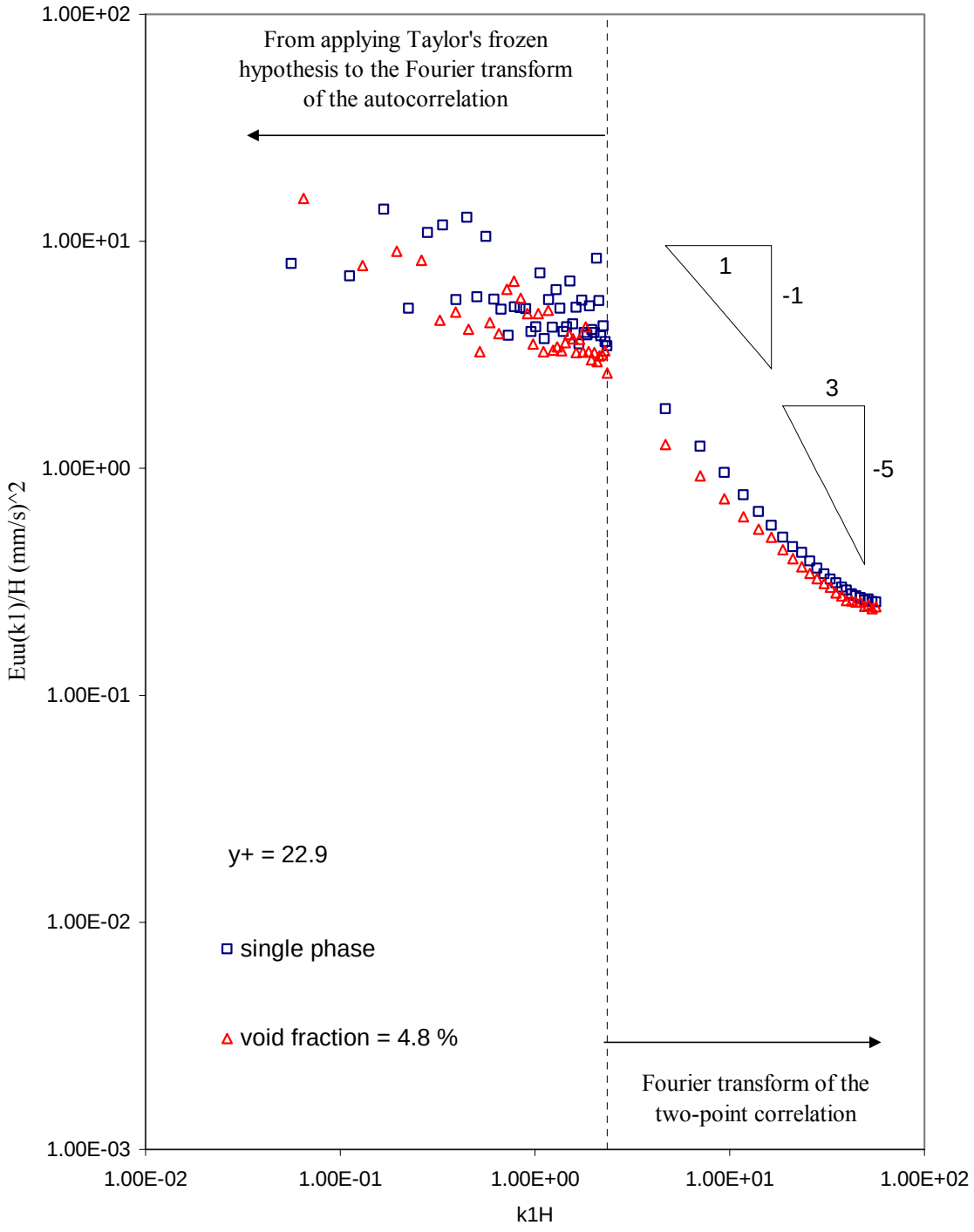

FIGURE B-8. Dimensional streamwise spectra versus non-dimensional wavenumber at y/H = 0.069 (without any correction).

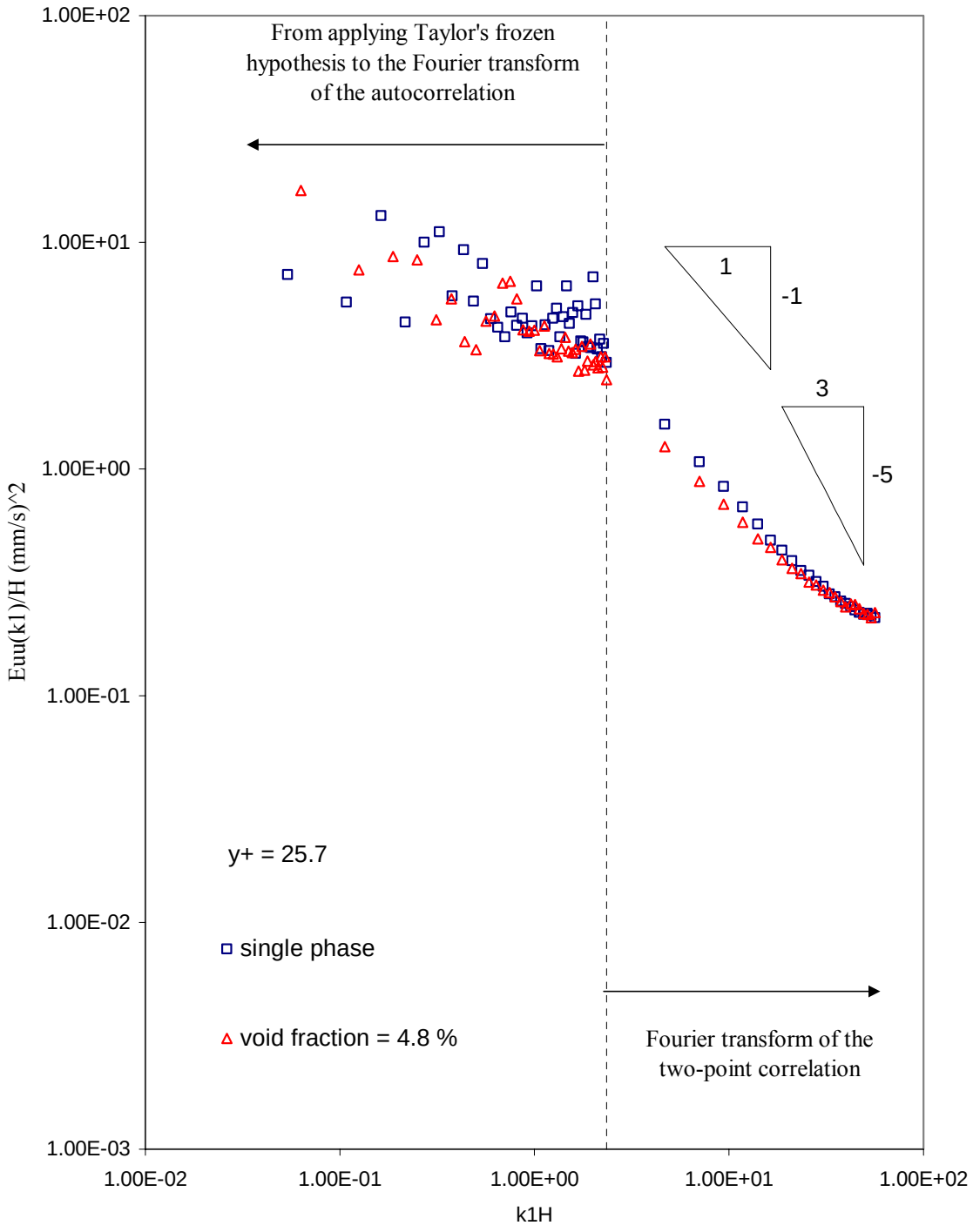

FIGURE B-9. Dimensional streamwise spectra versus non-dimensional wavenumber at y/H = 0.077 (without any correction).

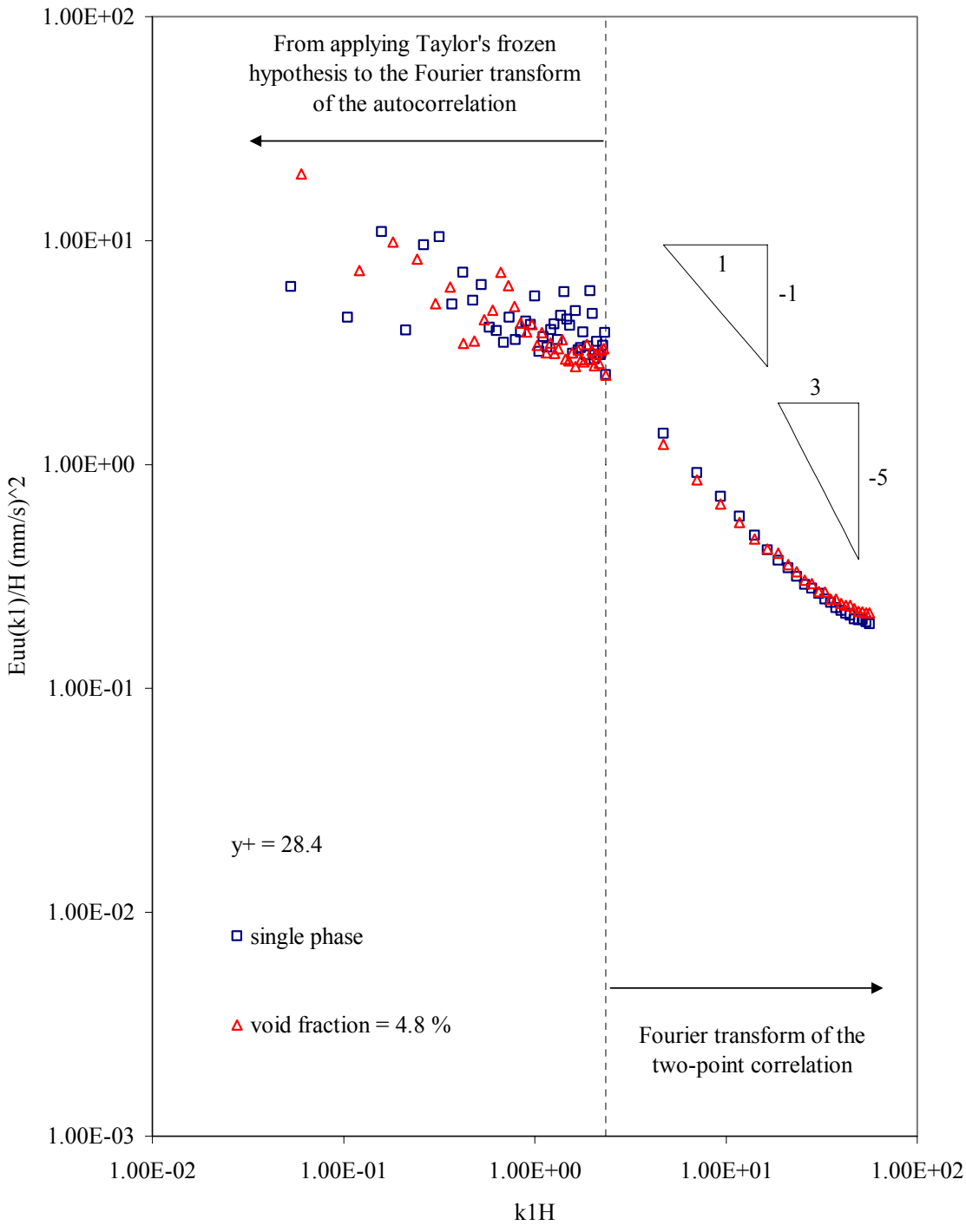

FIGURE B-10. Dimensional streamwise spectra versus non-dimensional wavenumber at y/H = 0.085 (without any correction).

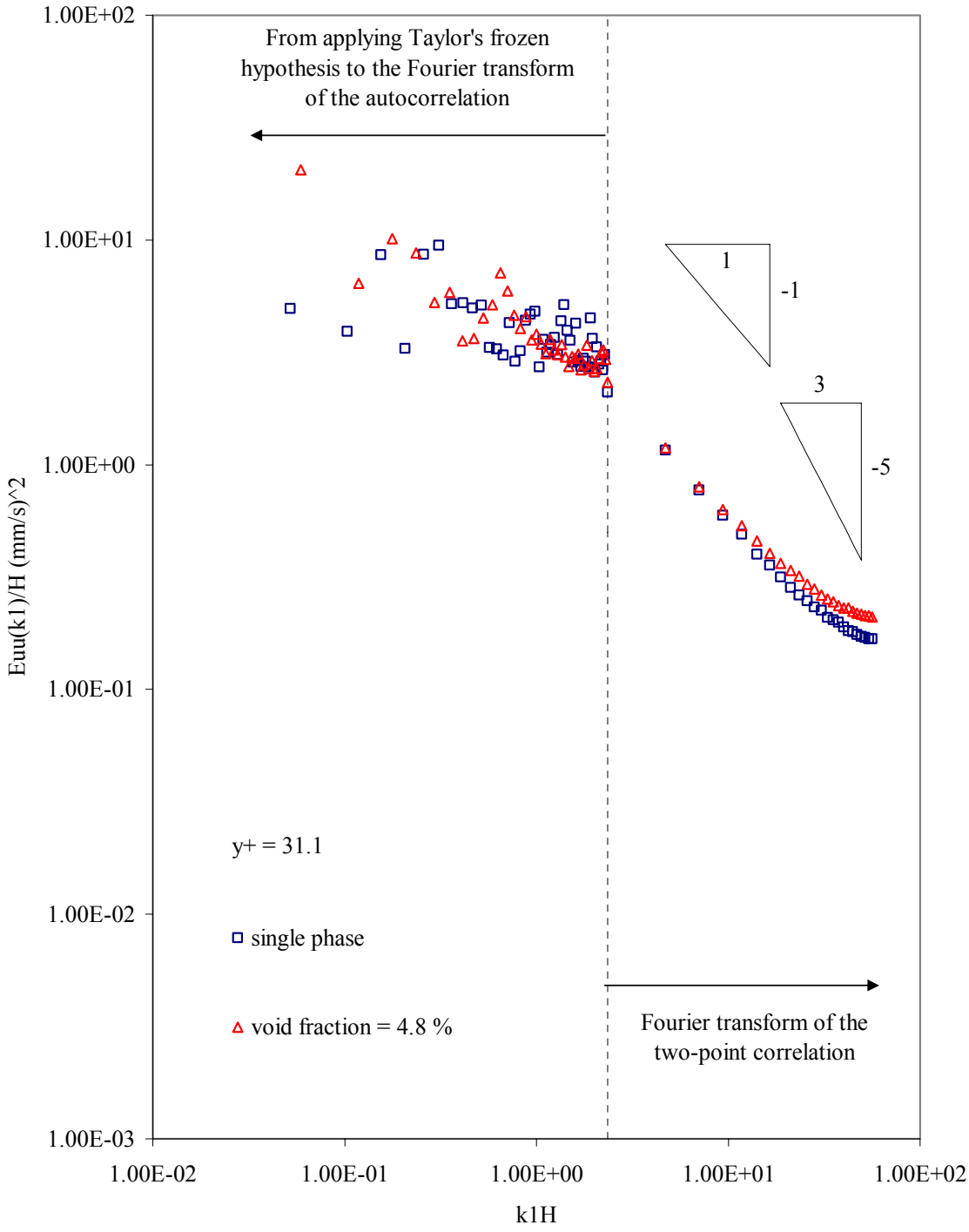

FIGURE B-11. Dimensional streamwise spectra versus non-dimensional wavenumber at y/H = 0.094 (without any correction).

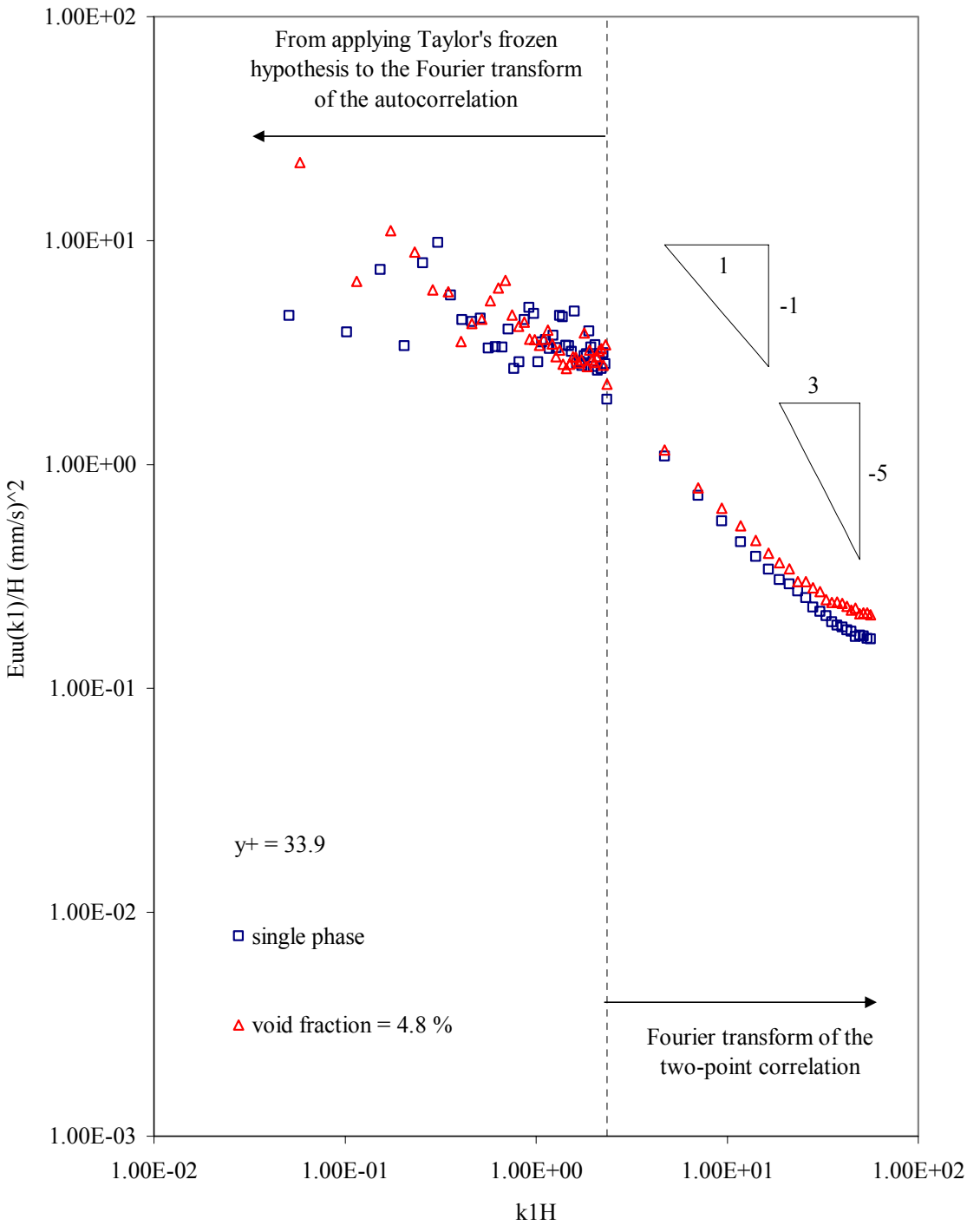

FIGURE B-12. Dimensional streamwise spectra versus non-dimensional wavenumber at y/H = 0.10 (without any correction).

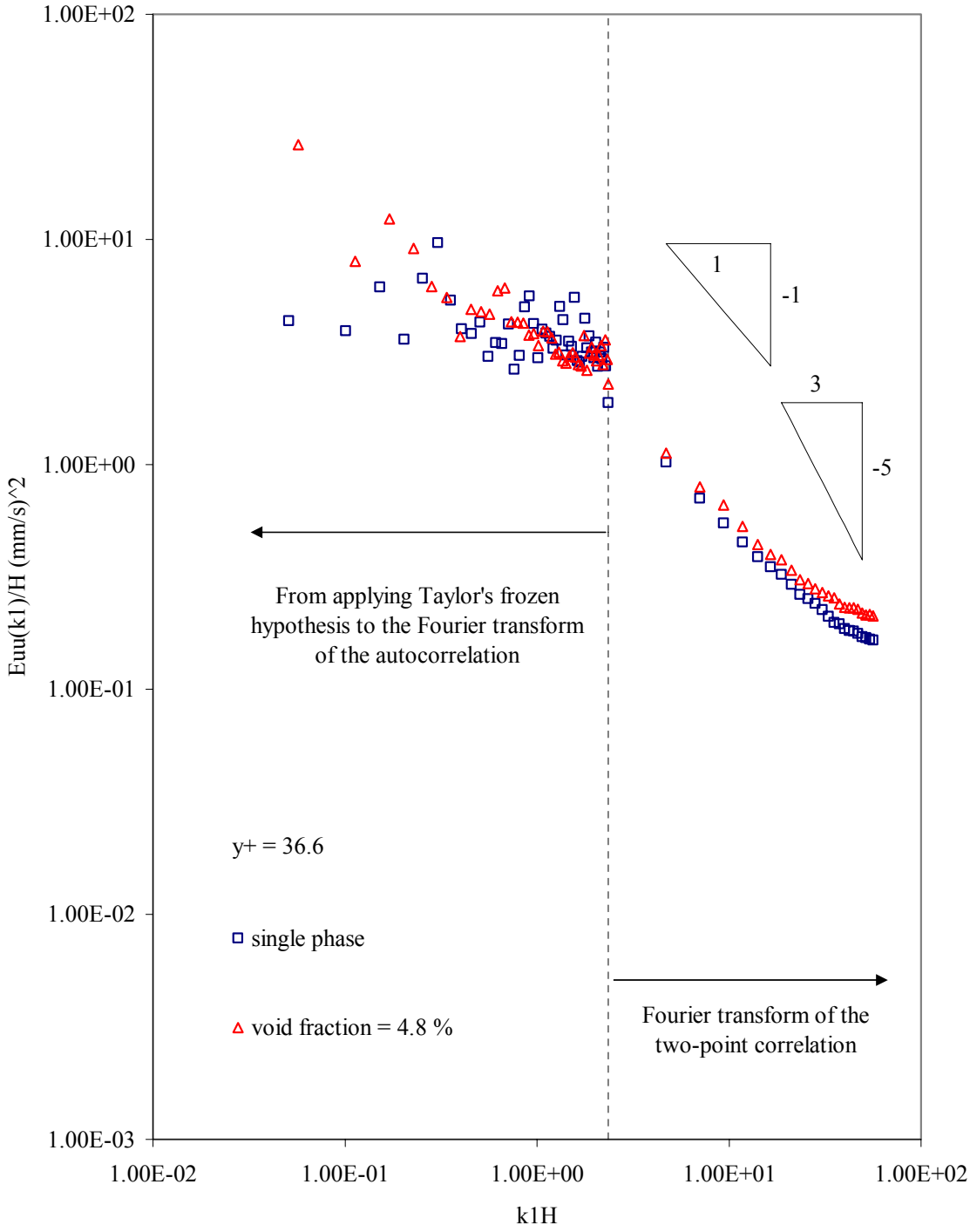

FIGURE B-13. Dimensional streamwise spectra versus non-dimensional wavenumber at y/H = 0.11 (without any correction).

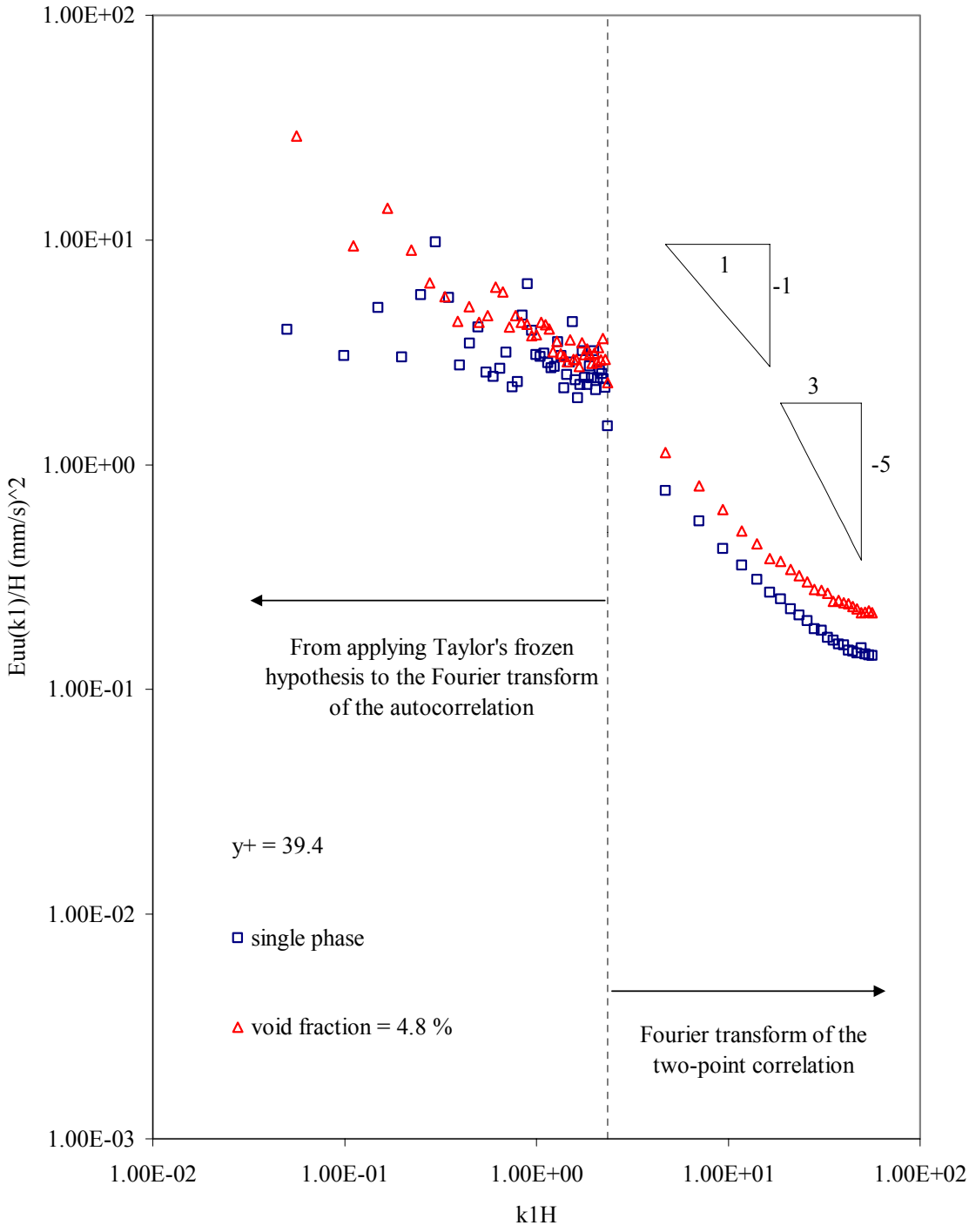

FIGURE B-14. Dimensional streamwise spectra versus non-dimensional wavenumber at y/H = 0.118 (without any correction).

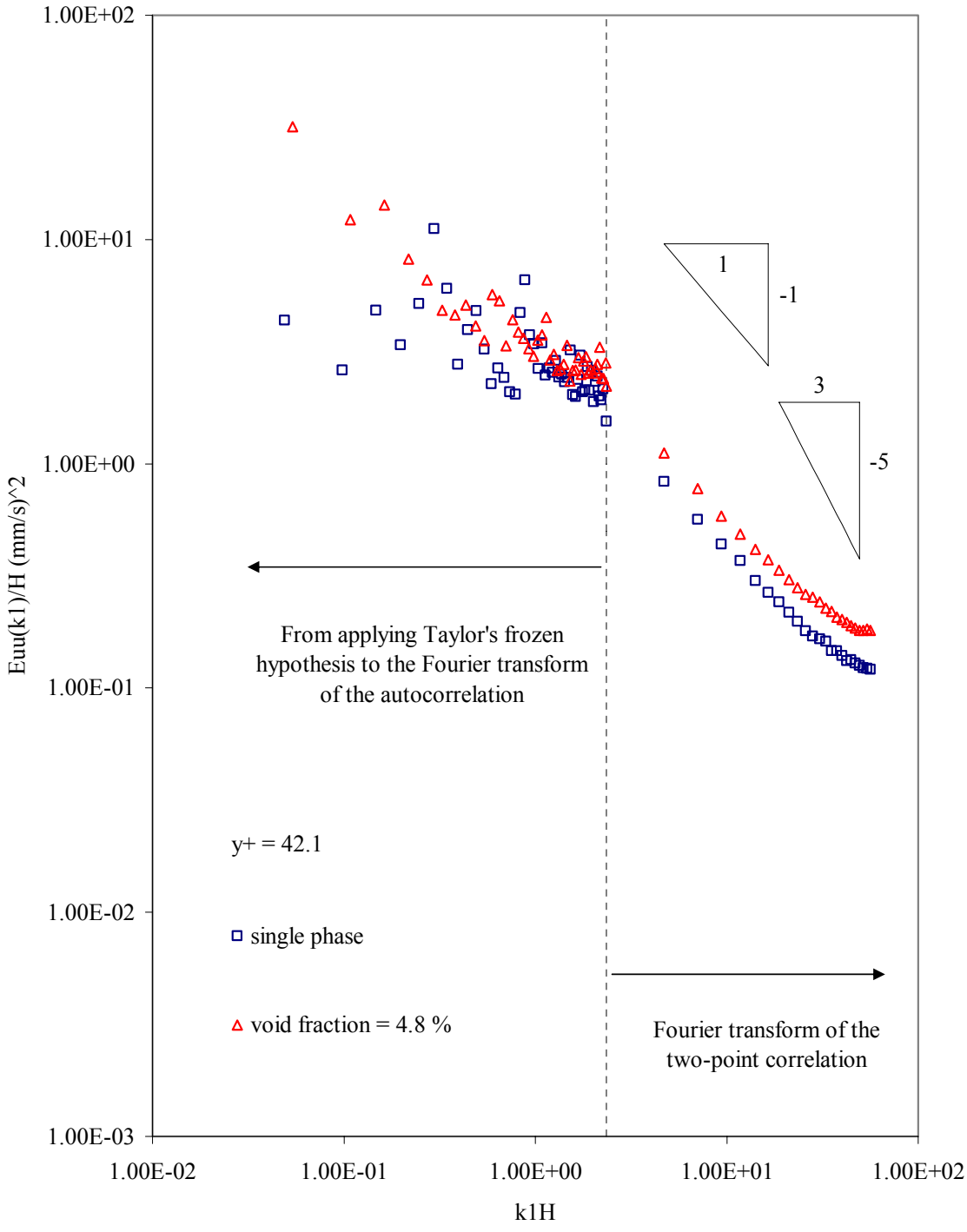

FIGURE B-15. Dimensional streamwise spectra versus non-dimensional wavenumber at y/H = 0.127 (without any correction).

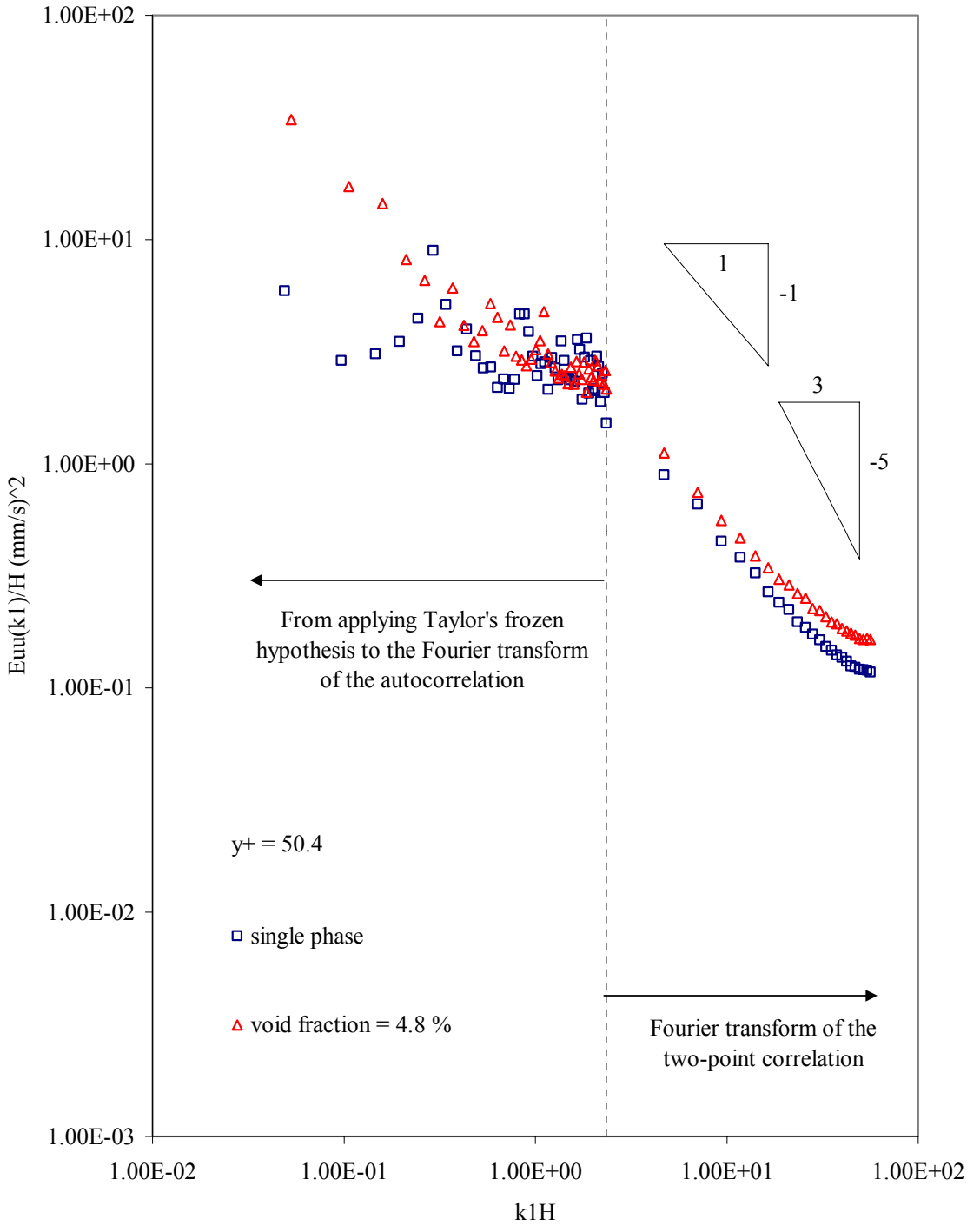

FIGURE B-16. Dimensional streamwise spectra versus non-dimensional wavenumber at y/H = 0.15 (without any correction).

APPENDIX C

This appendix shows the one dimensional spectra, E_{vv} (k_1) at different distance from the wall without any correction. The discontinuities at $k_1H = 2.3$ are produced by Taylor's frozen hypothesis.

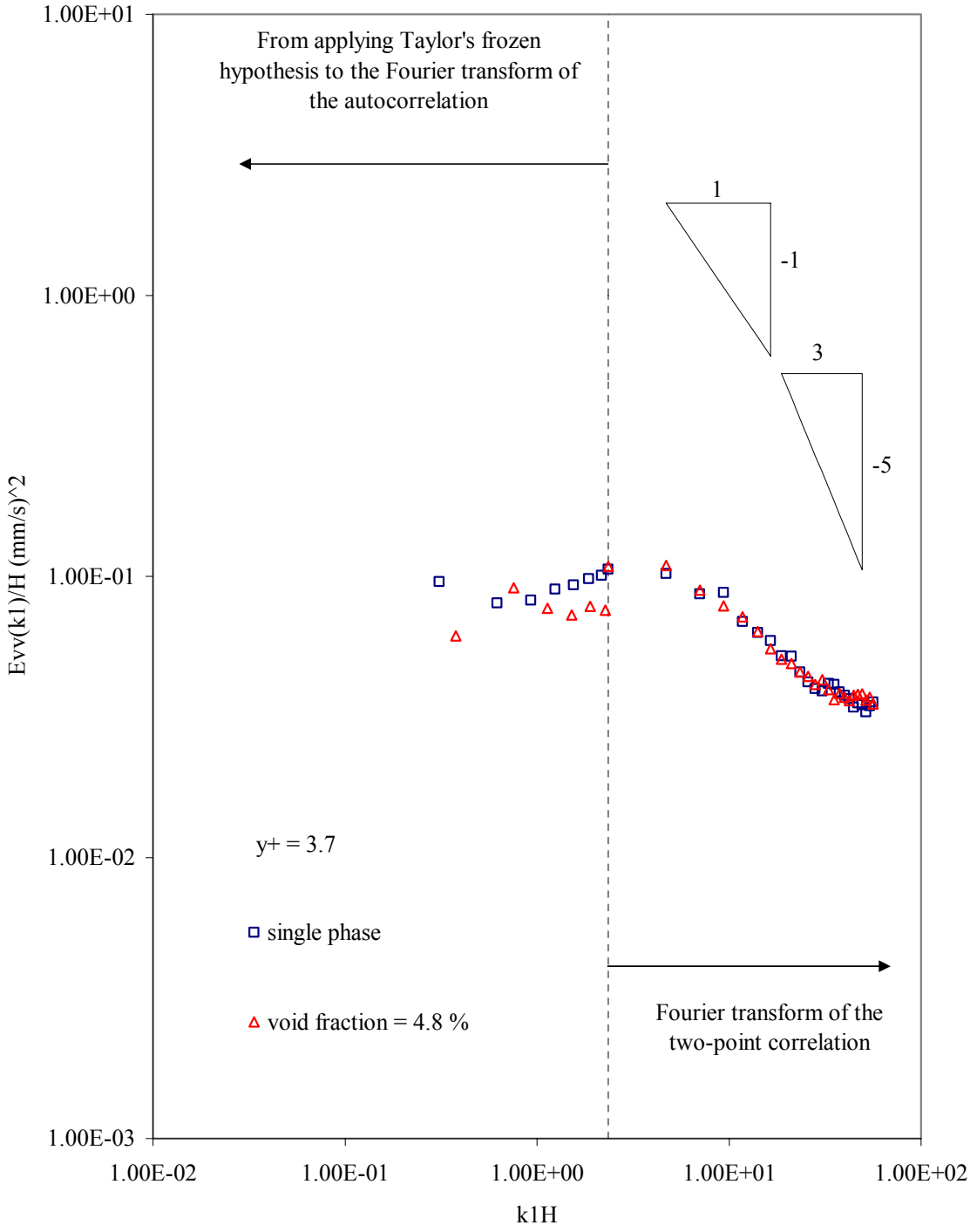

FIGURE C-1. Dimensional normal spectra versus non-dimensional wavenumber at y/H = 0.011 (without any correction).

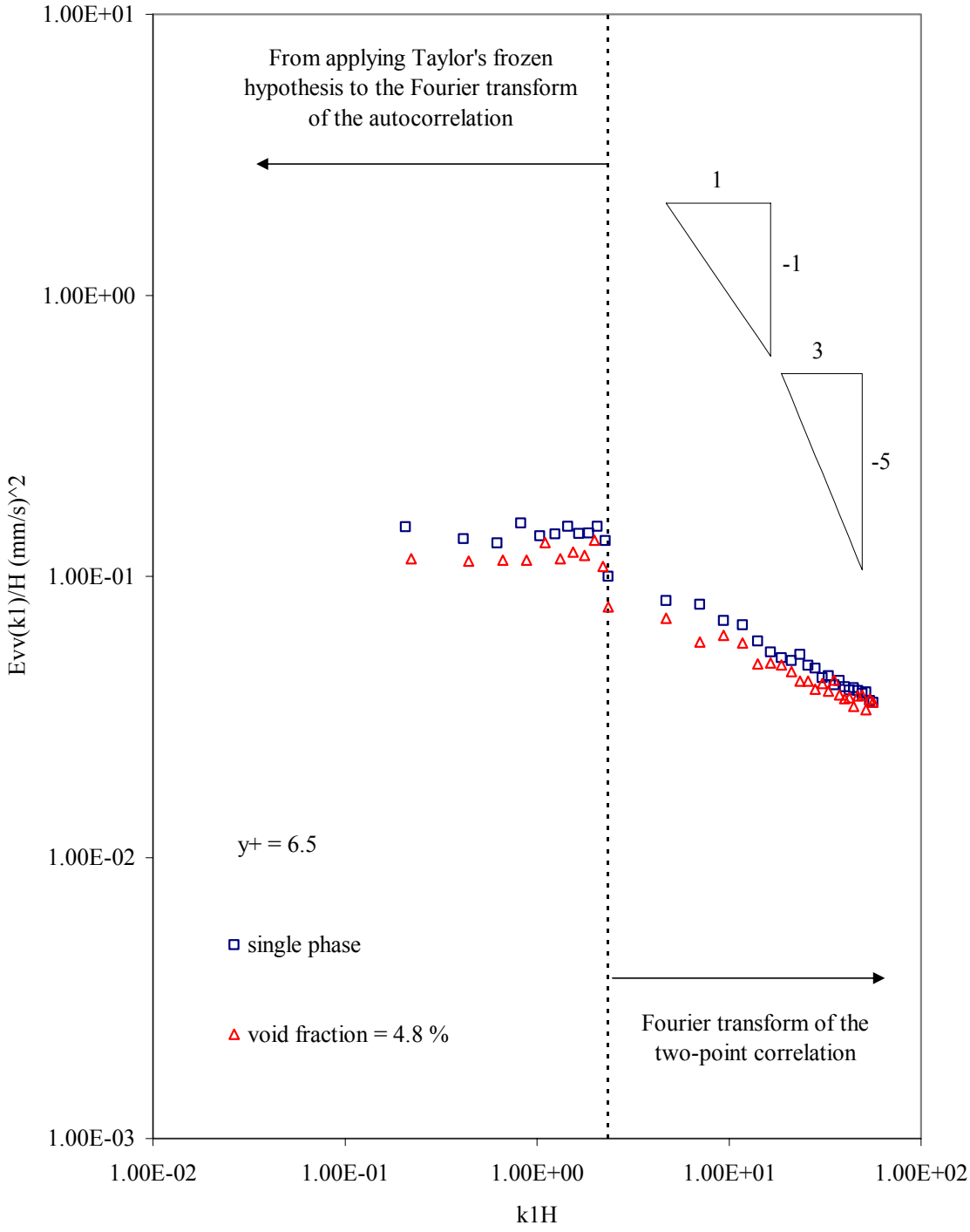

FIGURE C-2. Dimensional normal spectra versus non-dimensional wavenumber at y/H = 0.019 (without any correction).

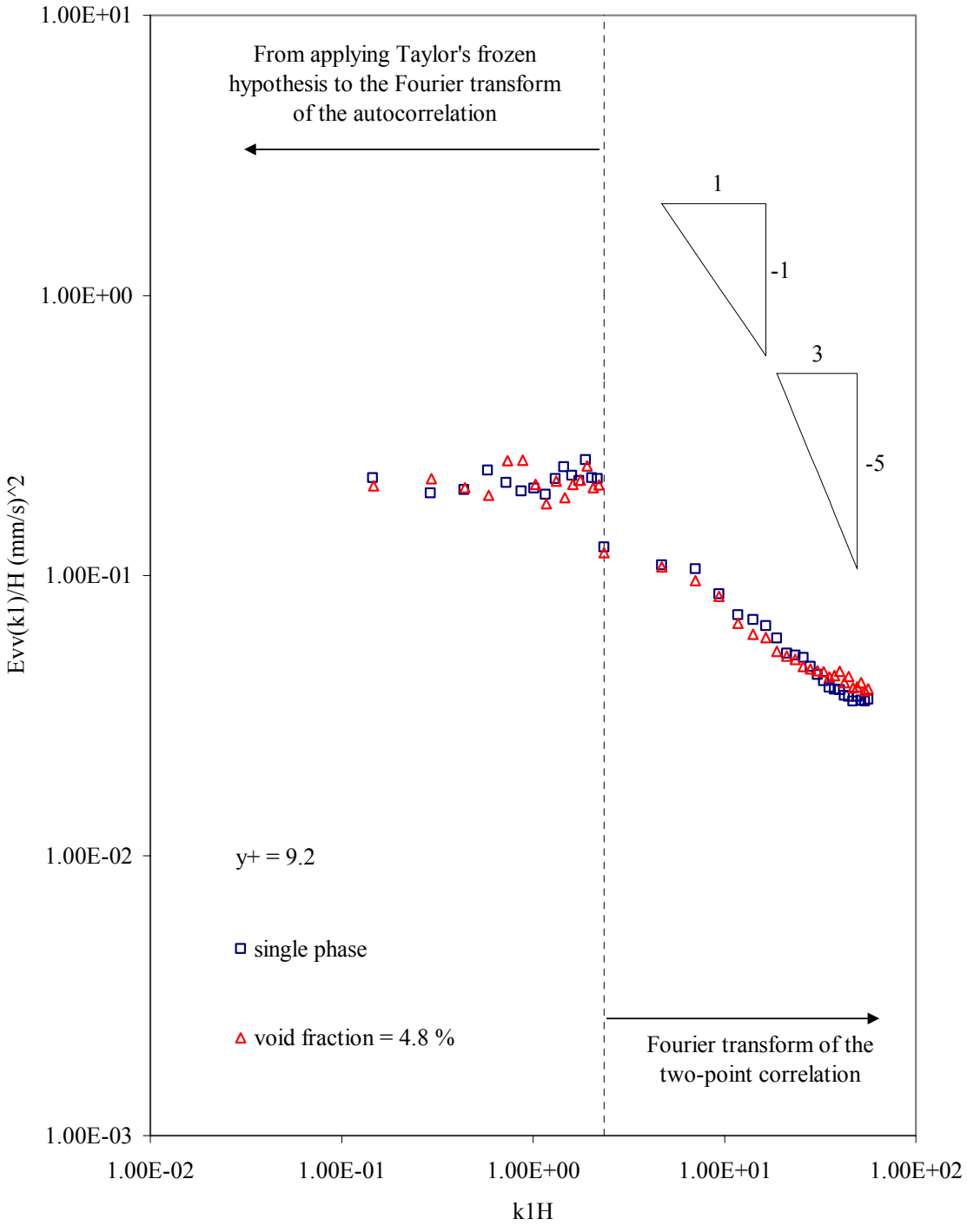

FIGURE C-3. Dimensional normal spectra versus non-dimensional wavenumber at y/H = 0.027 (without any correction).

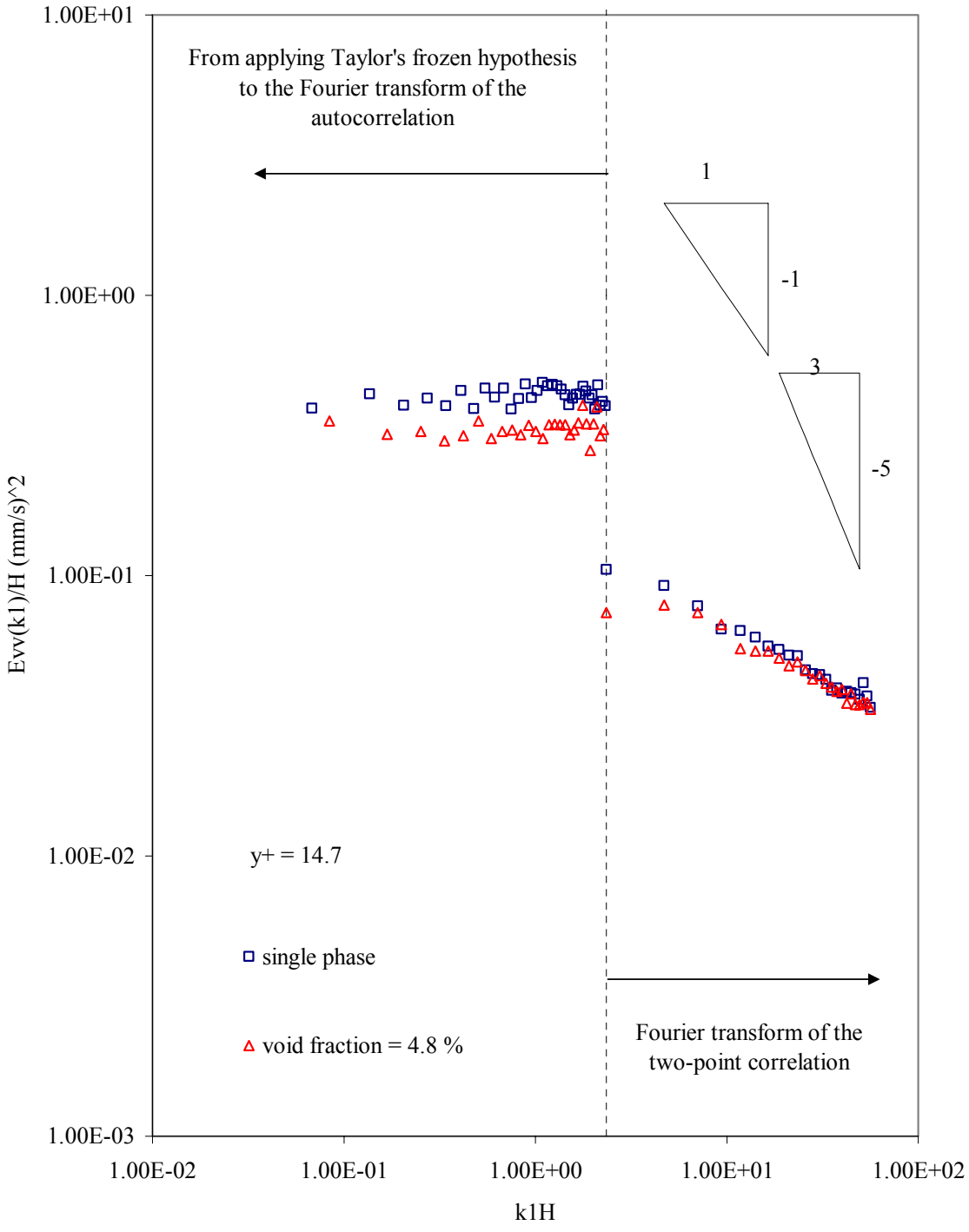

FIGURE C-4. Dimensional normal spectra versus non-dimensional wavenumber at y/H = 0.044 (without any correction).

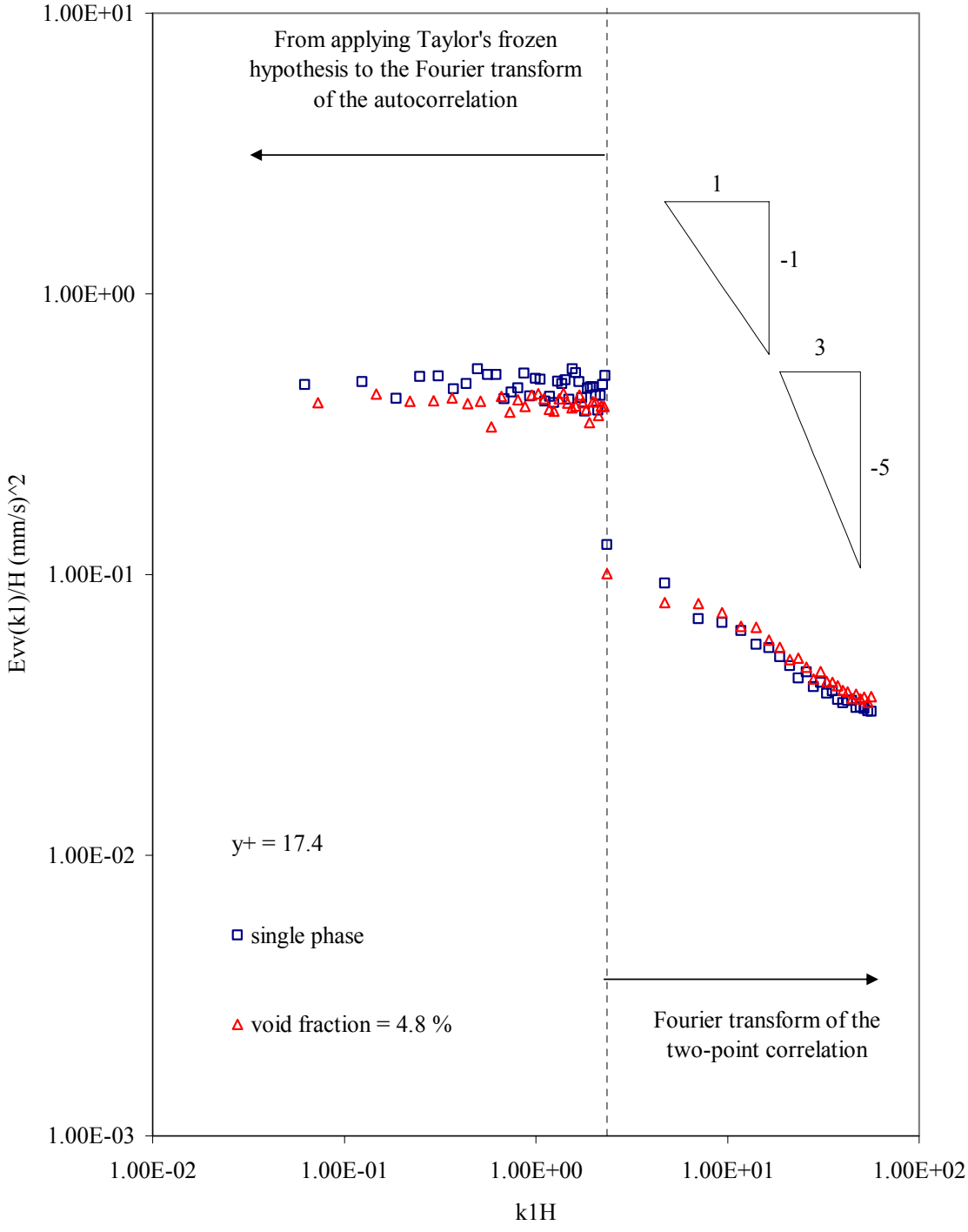

FIGURE C-5. Dimensional normal spectra versus non-dimensional wavenumber at y/H = 0.052 (without any correction).

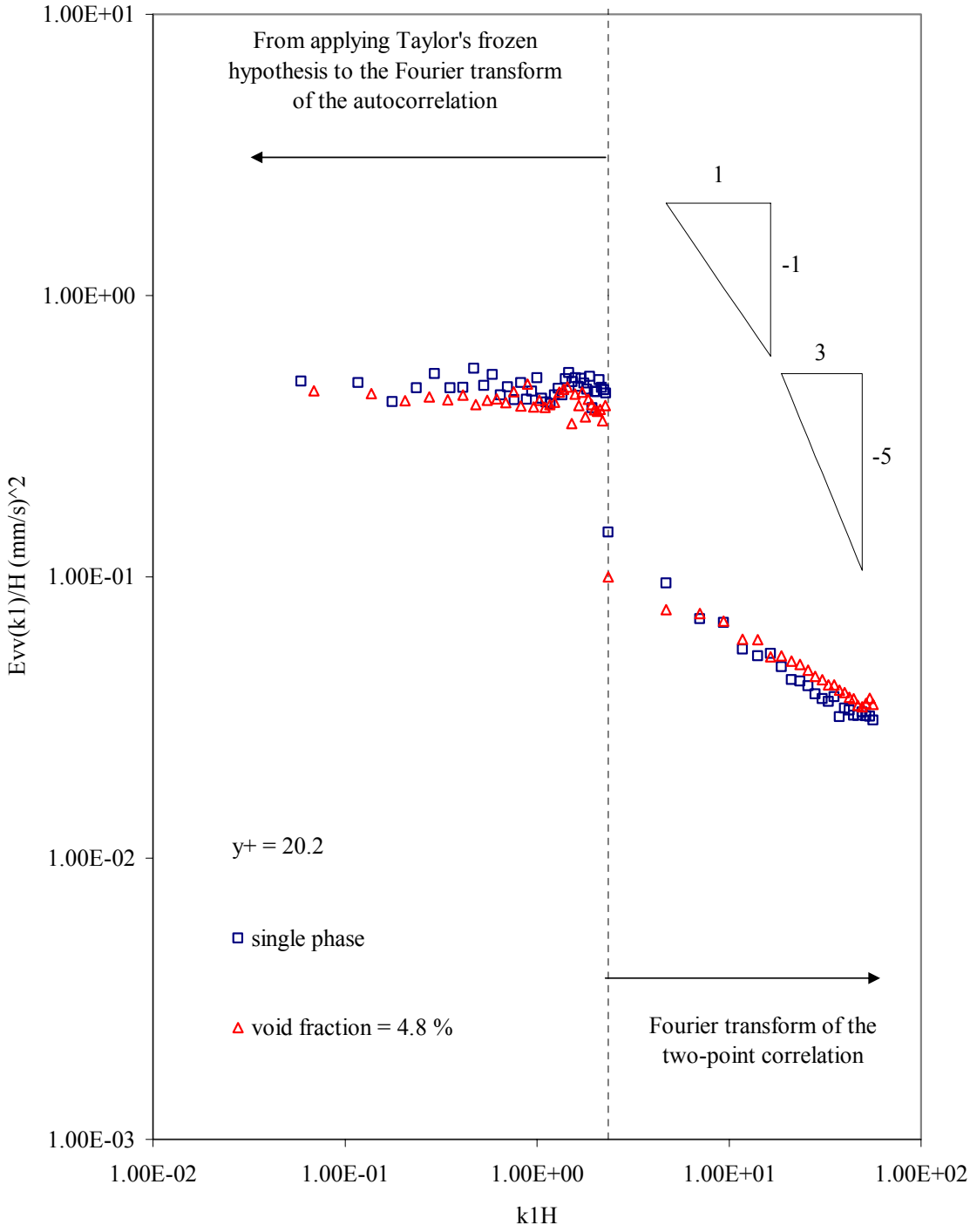

FIGURE C-6. Dimensional normal spectra versus non-dimensional wavenumber at y/H = 0.06 (without any correction).

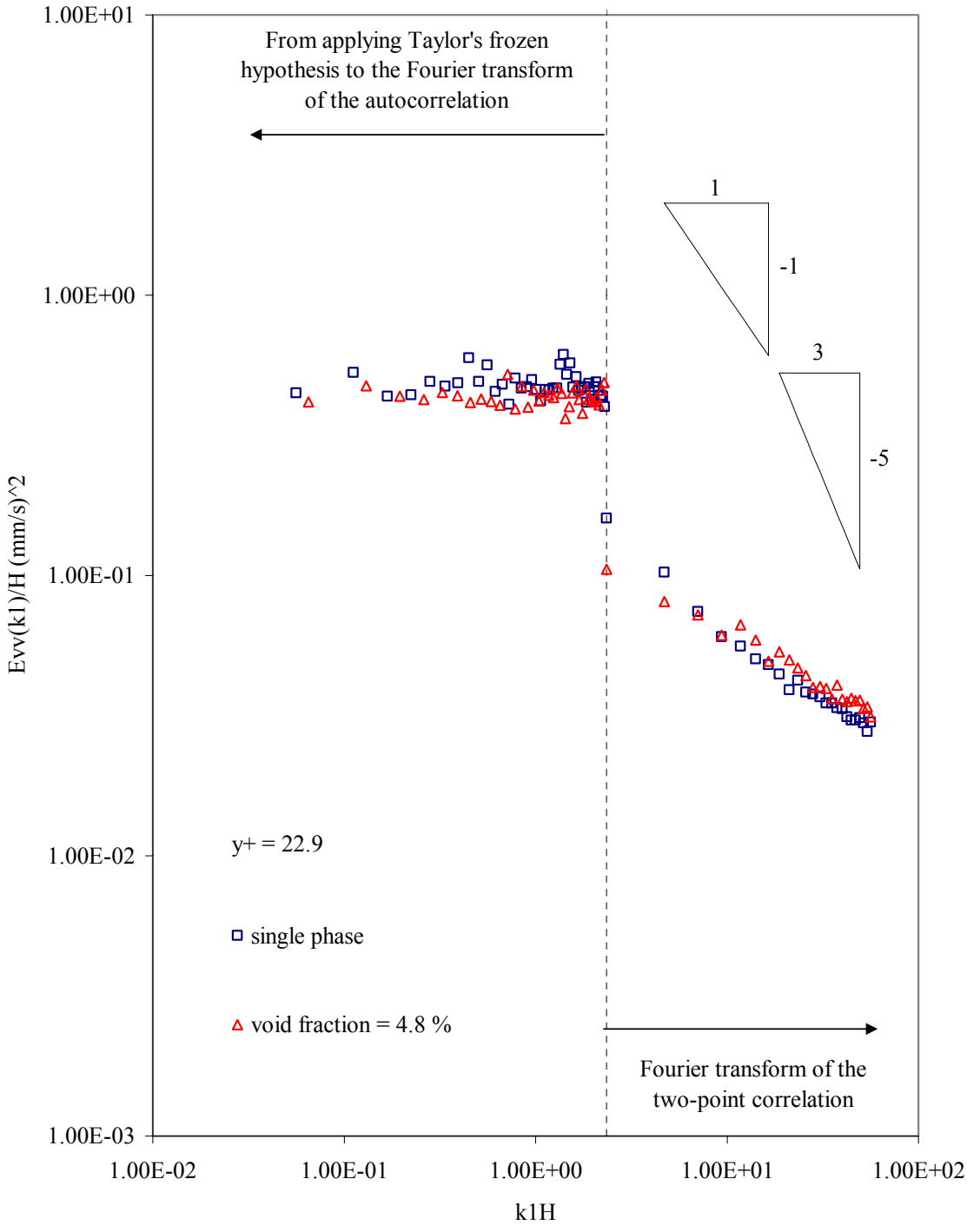

FIGURE C-7. Dimensional normal spectra versus non-dimensional wavenumber at y/H = 0.069 (without any correction).

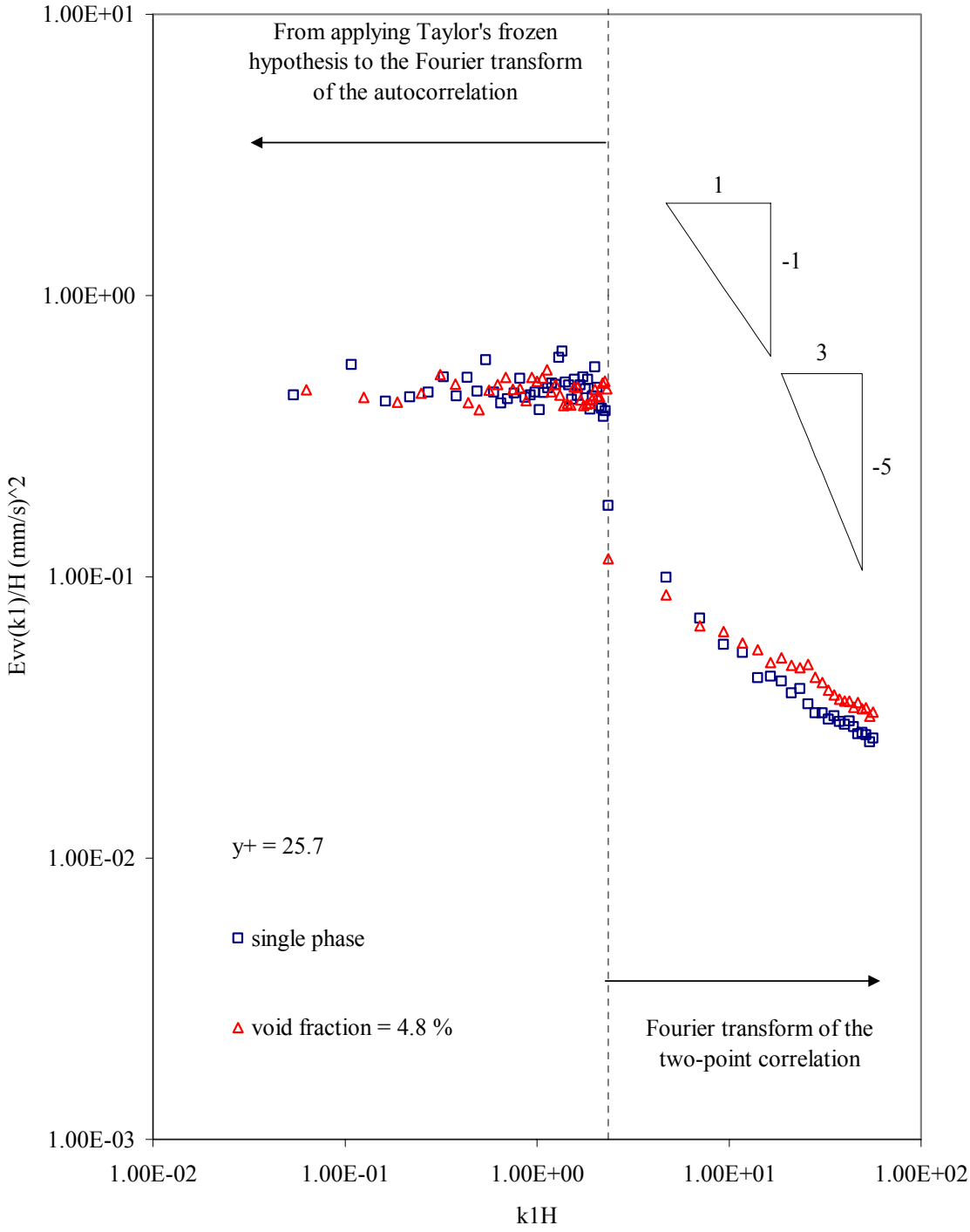

FIGURE C-8. Dimensional normal spectra versus non-dimensional wavenumber at y/H = 0.077 (without any correction).

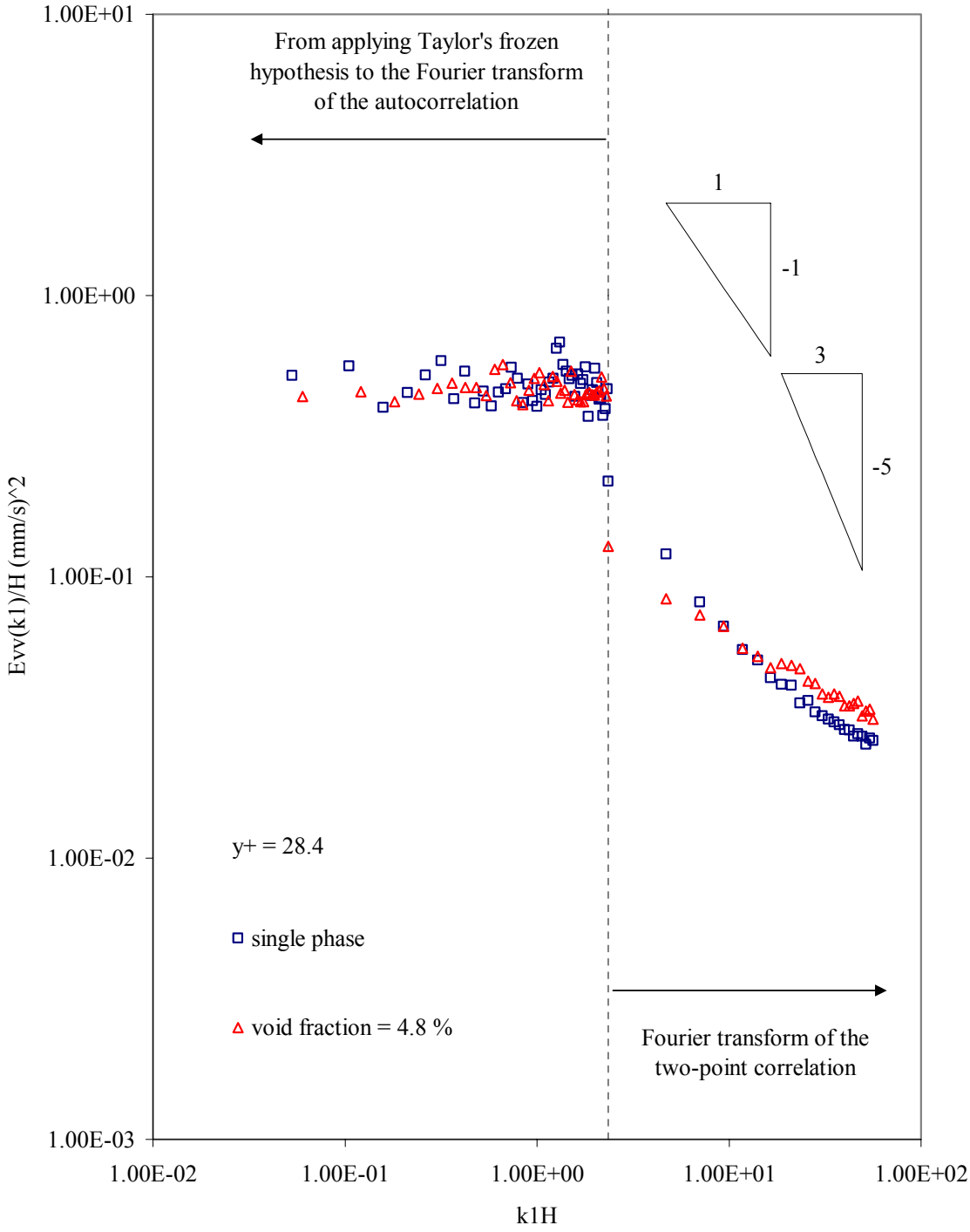

FIGURE C-9. Dimensional normal spectra versus non-dimensional wavenumber at y/H = 0.085 (without any correction).

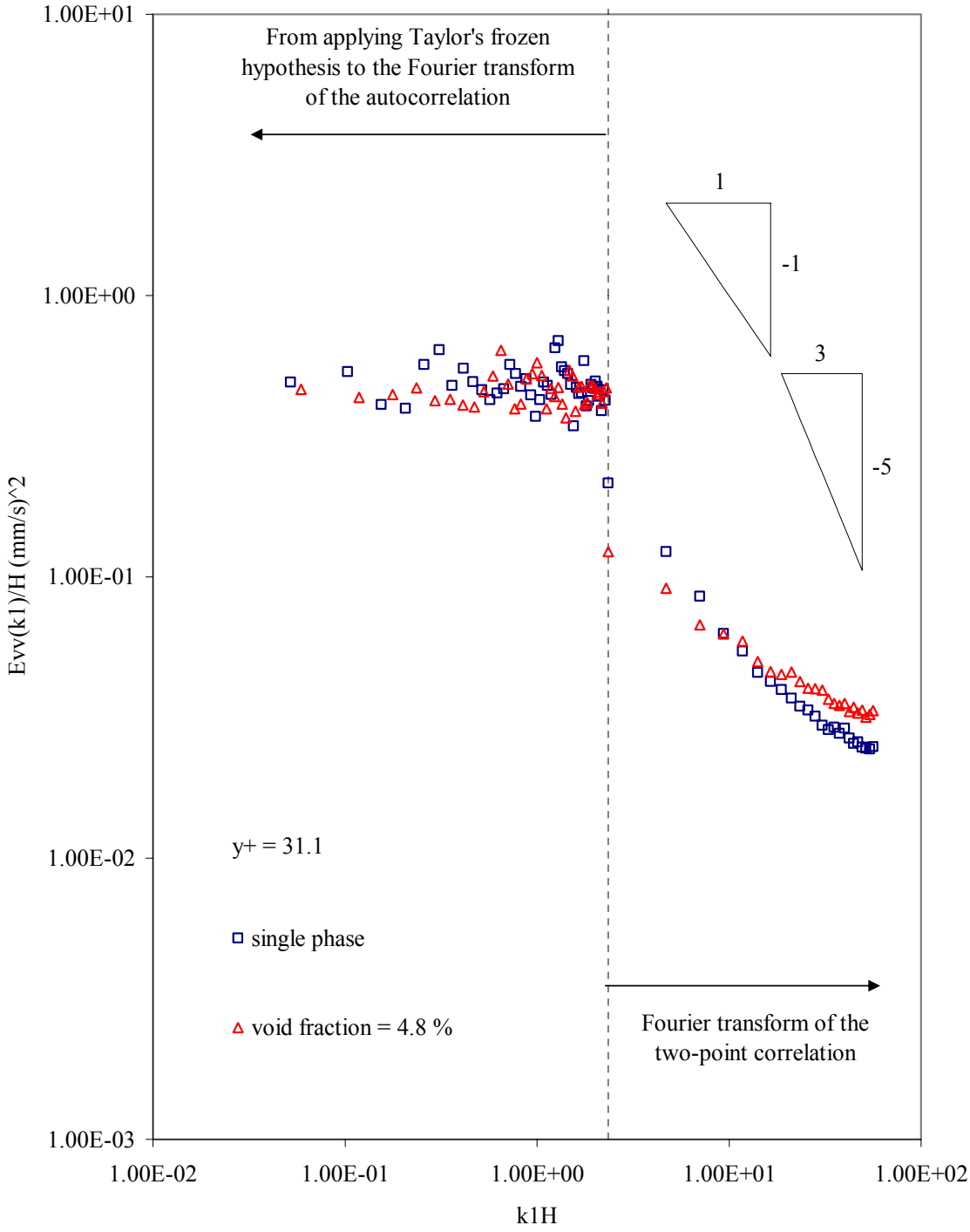

FIGURE C-10. Dimensional normal spectra versus non-dimensional wavenumber at y/H = 0.094 (without any correction).

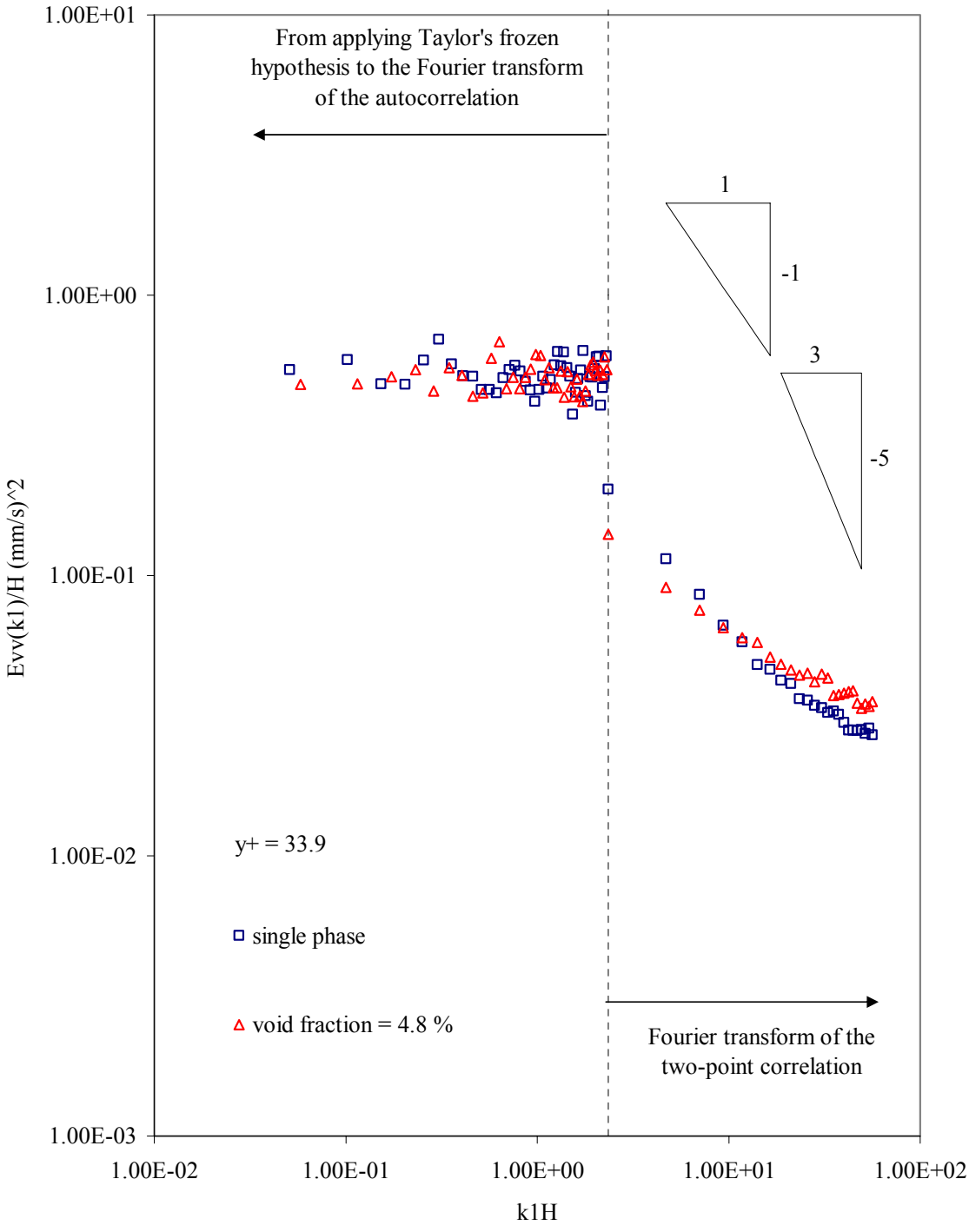

FIGURE C-11. Dimensional normal spectra versus non-dimensional wavenumber at y/H = 0.10 (without any correction).

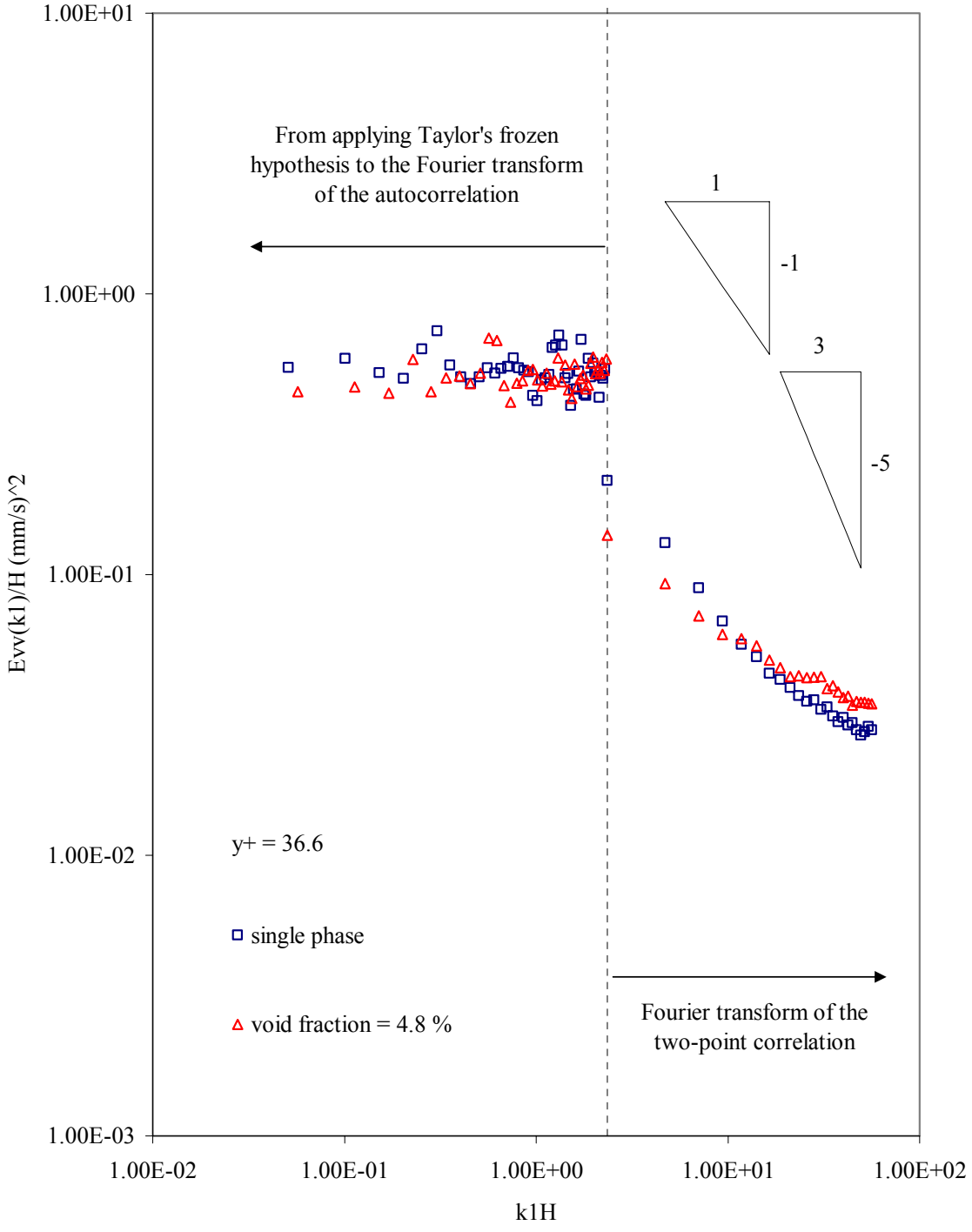

FIGURE C-11. Dimensional normal spectra versus non-dimensional wavenumber at y/H = 0.11 (without any correction).

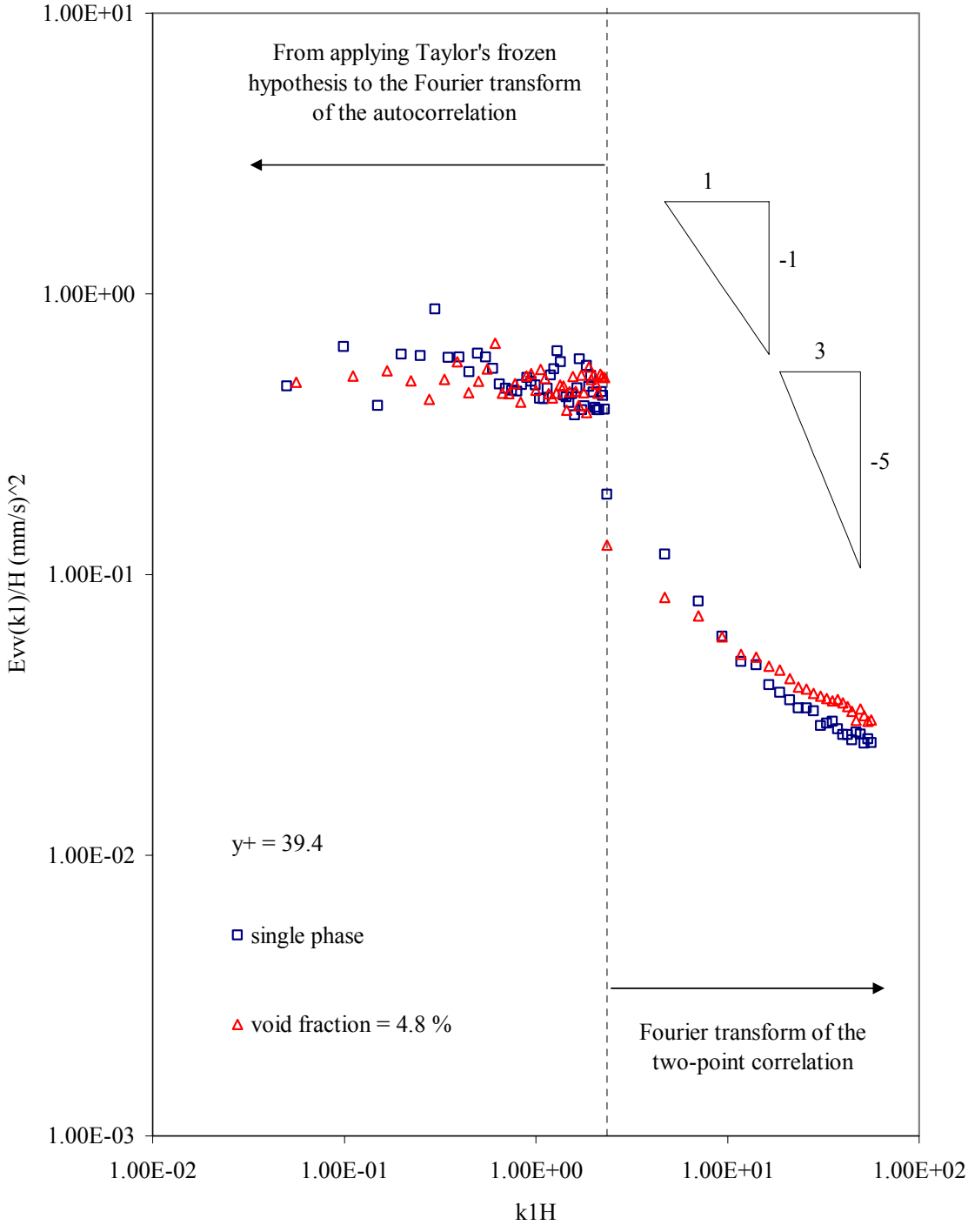

FIGURE C-12. Dimensional normal spectra versus non-dimensional wavenumber at y/H = 0.118 (without any correction).

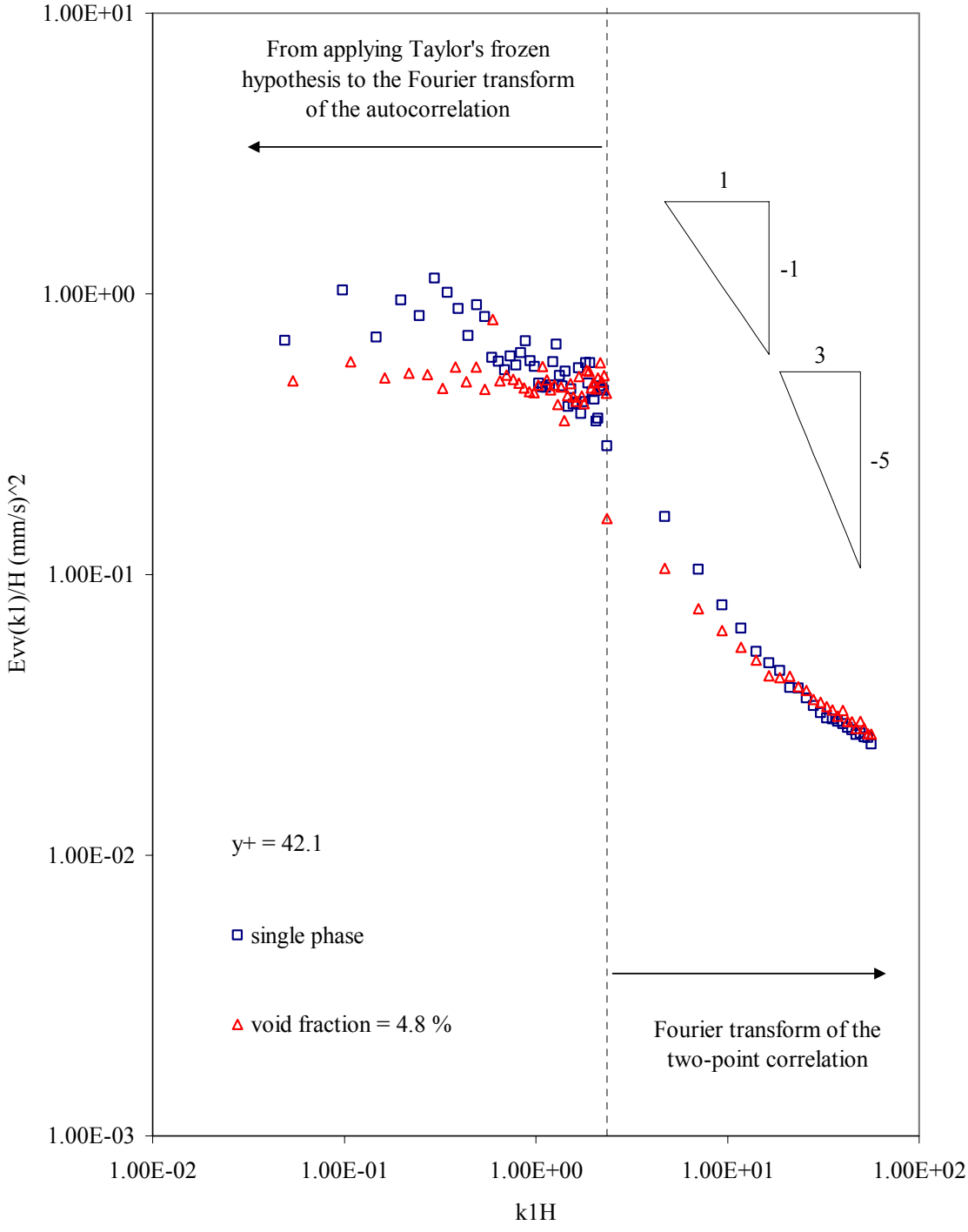

FIGURE C-13. Dimensional normal spectra versus non-dimensional wavenumber at y/H = 0.127 (without any correction).

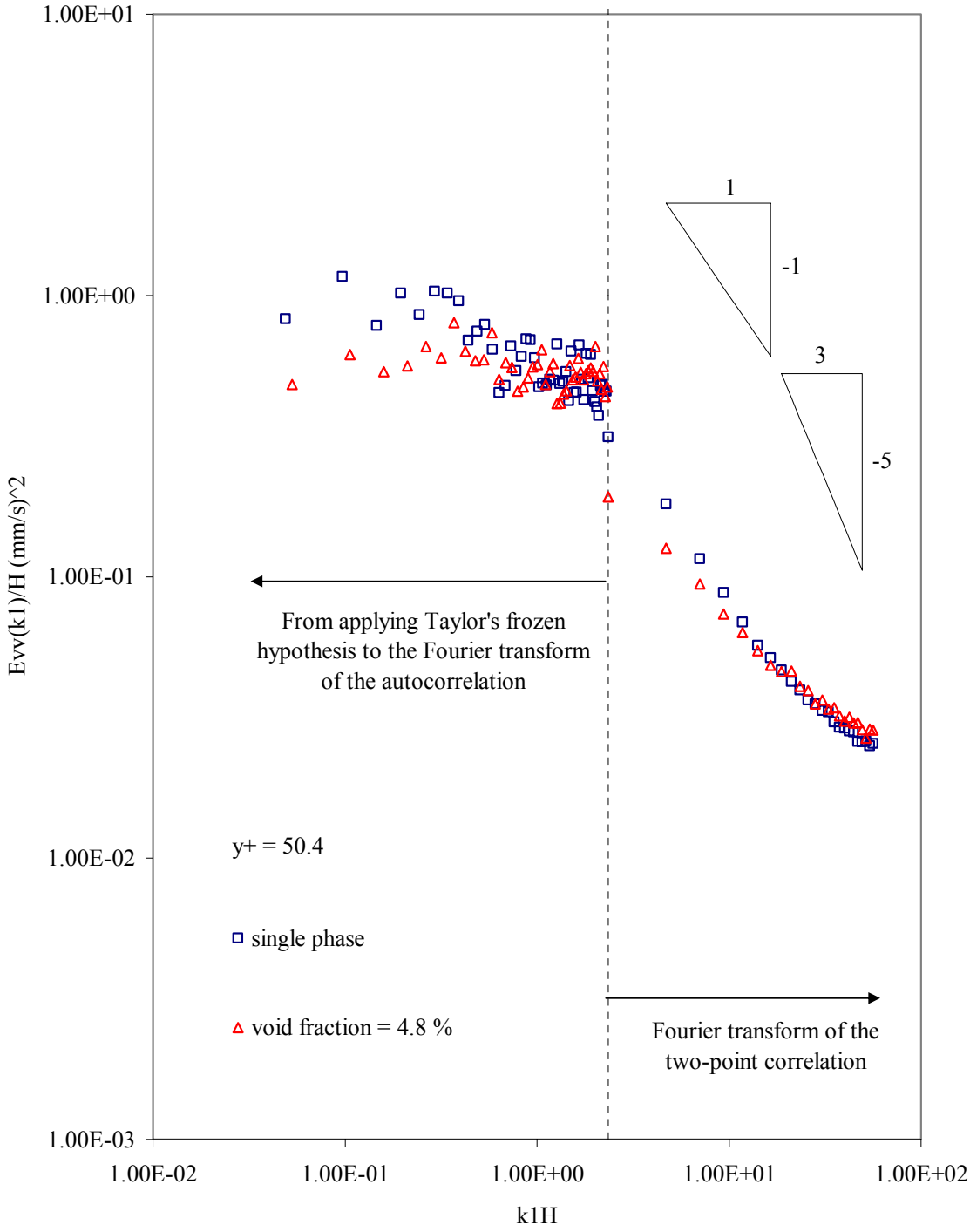

FIGURE C-14. Dimensional normal spectra versus non-dimensional wavenumber at y/H = 0.15 (without any correction).

APPENDIX D

This appendix shows the one dimensional spectra, E_{uv} (k_1) at different distance from the wall without any correction.

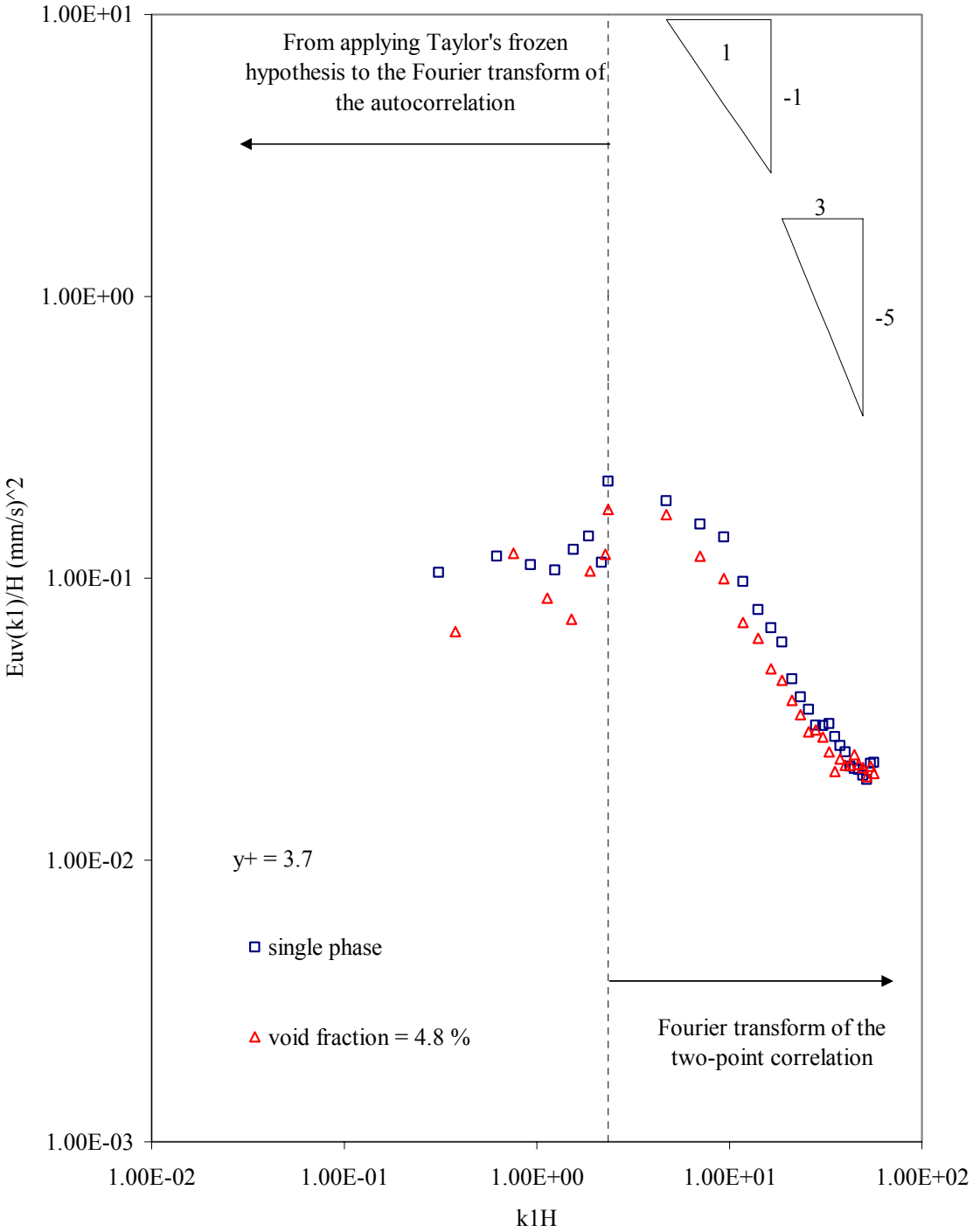

FIGURE D-1. Dimensional $E_{uv}(k_1)$ spectra versus non-dimensional wavenumber at y/H = 0.01 (without any correction).

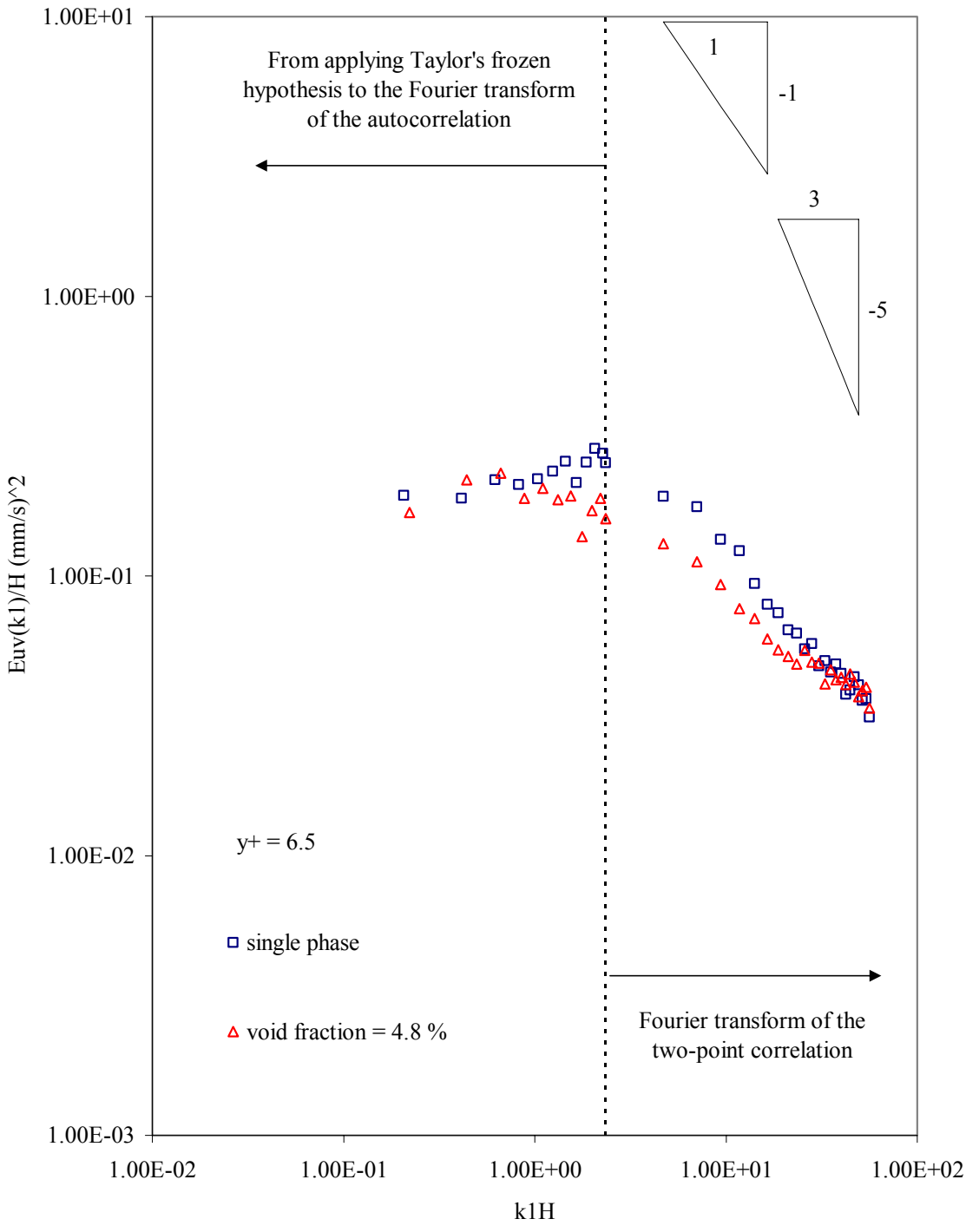

FIGURE D-2. Dimensional $E_{uv}(k_1)$ spectra versus non-dimensional wavenumber at y/H = 0.019 (without any correction).

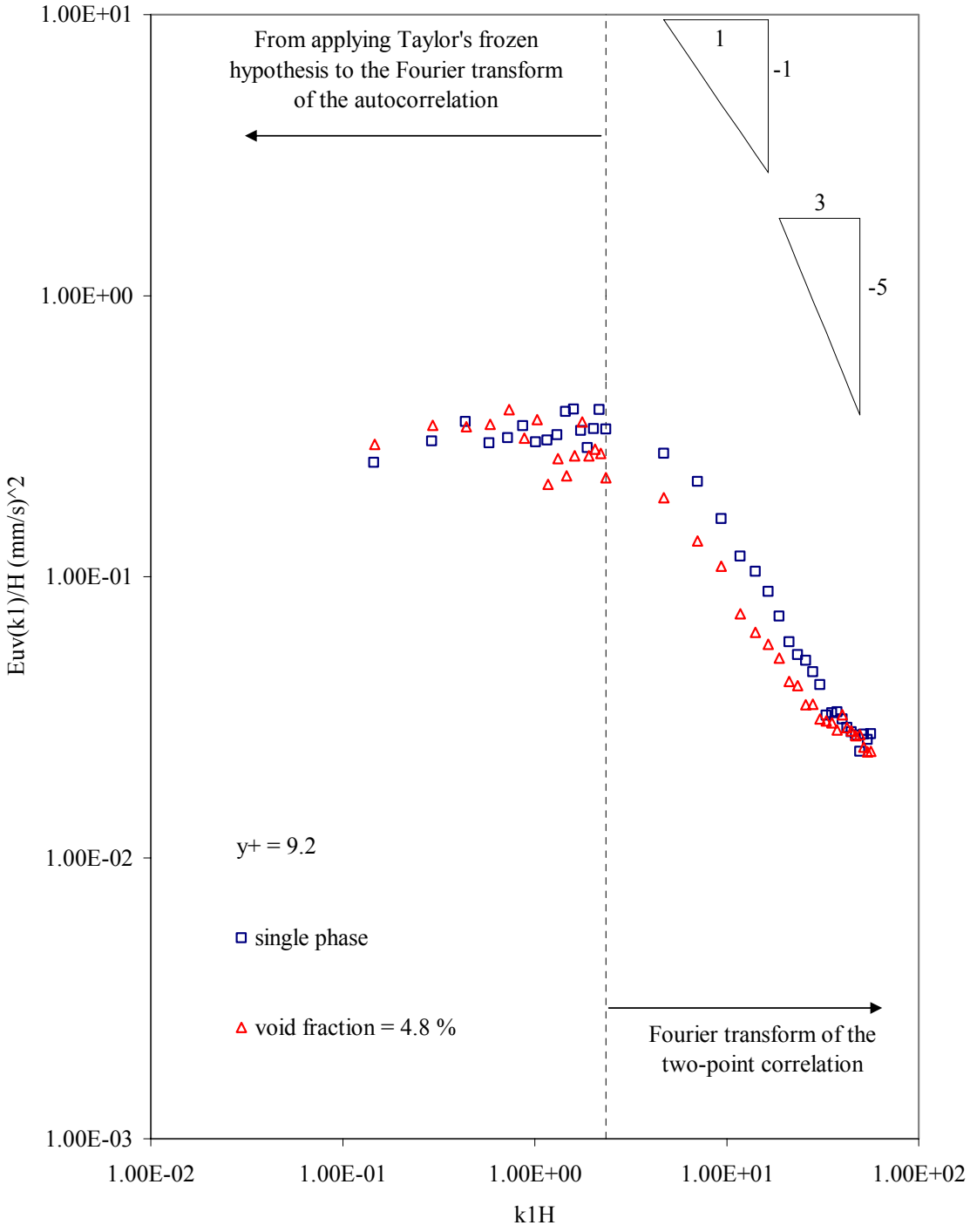

FIGURE D-3. Dimensional $E_{uv}(k_1)$ spectra versus non-dimensional wavenumber at y/H = 0.027 (without any correction).

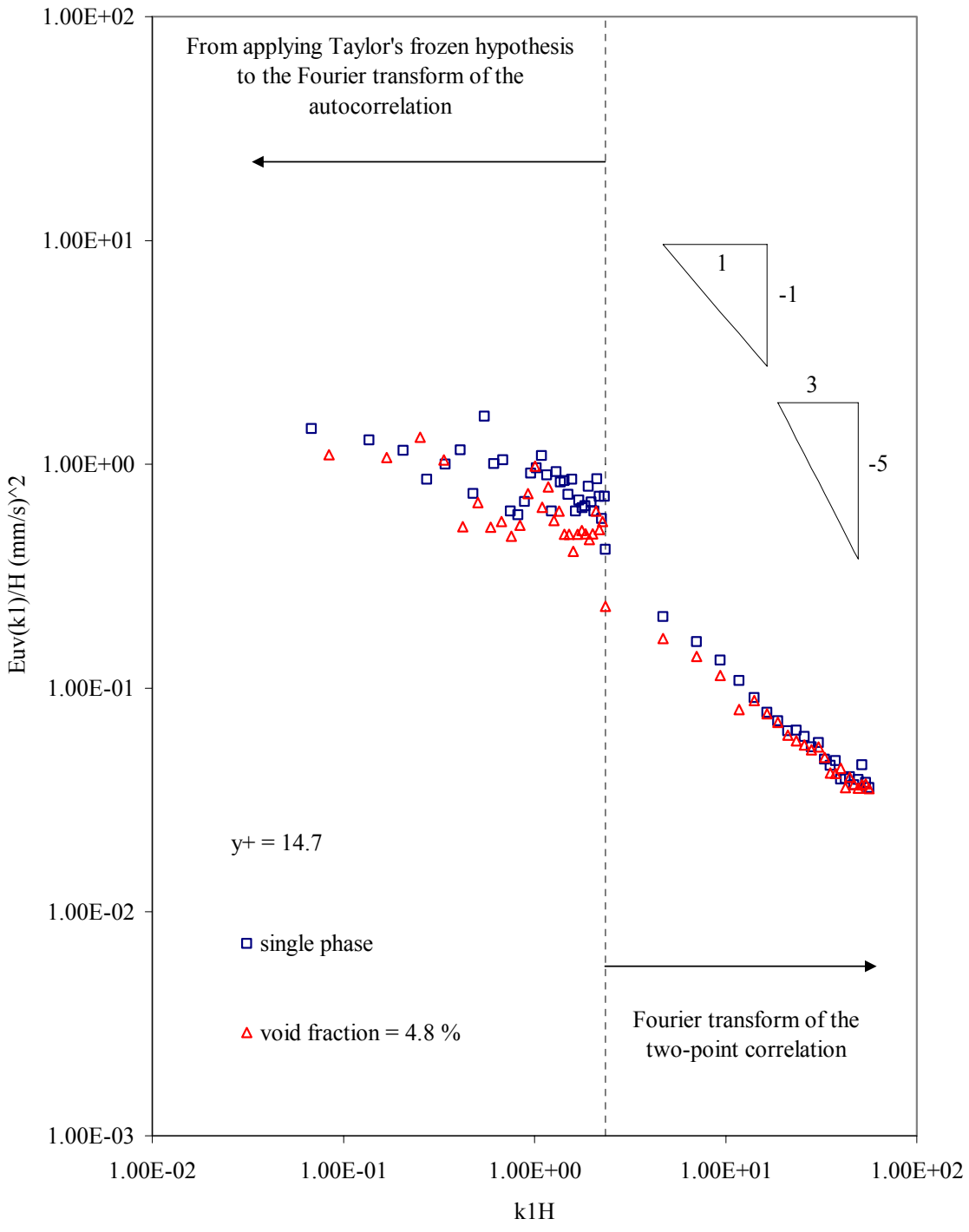

FIGURE D-4. Dimensional $E_{uv}(k_1)$ spectra versus non-dimensional wavenumber at y/H = 0.044 (without any correction).

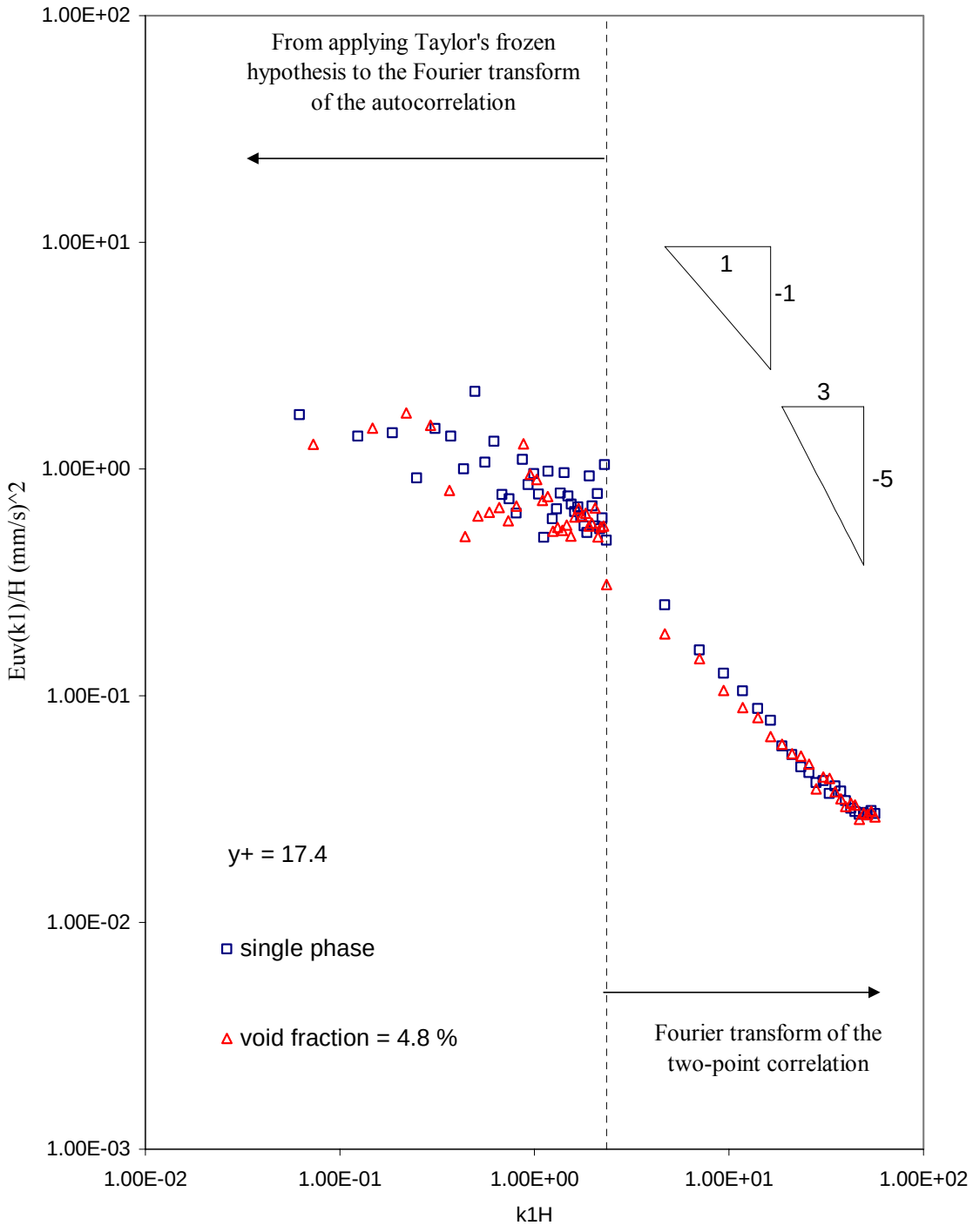

FIGURE D-5. Dimensional $E_{uv}(k_1)$ spectra versus non-dimensional wavenumber at y/H = 0.052 (without any correction).

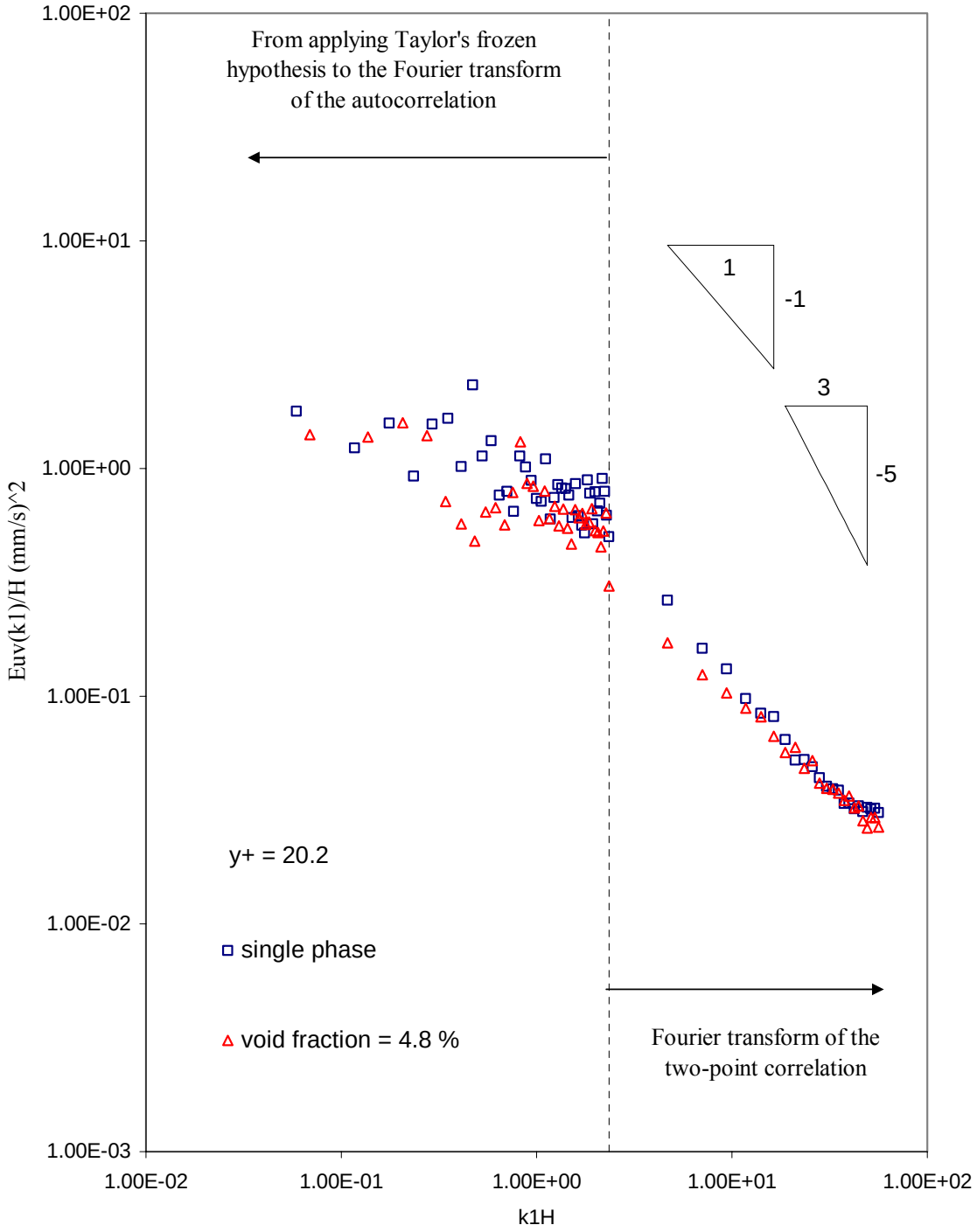

FIGURE D-6. Dimensional $E_{uv}(k_1)$ spectra versus non-dimensional wavenumber at y/H = 0.06 (without any correction).

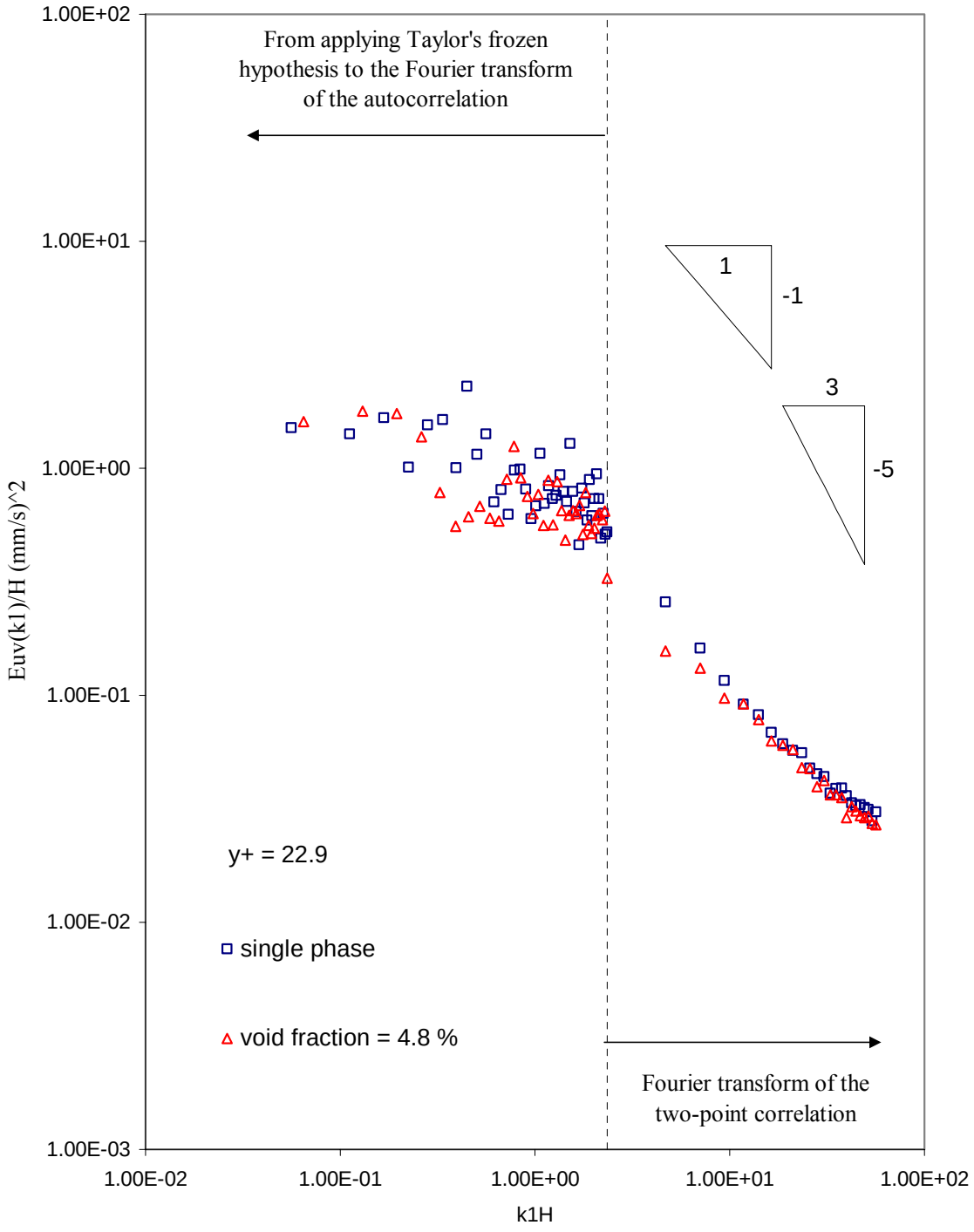

FIGURE D-7. Dimensional $E_{uv}(k_1)$ spectra versus non-dimensional wavenumber at y/H = 0.069 (without any correction).

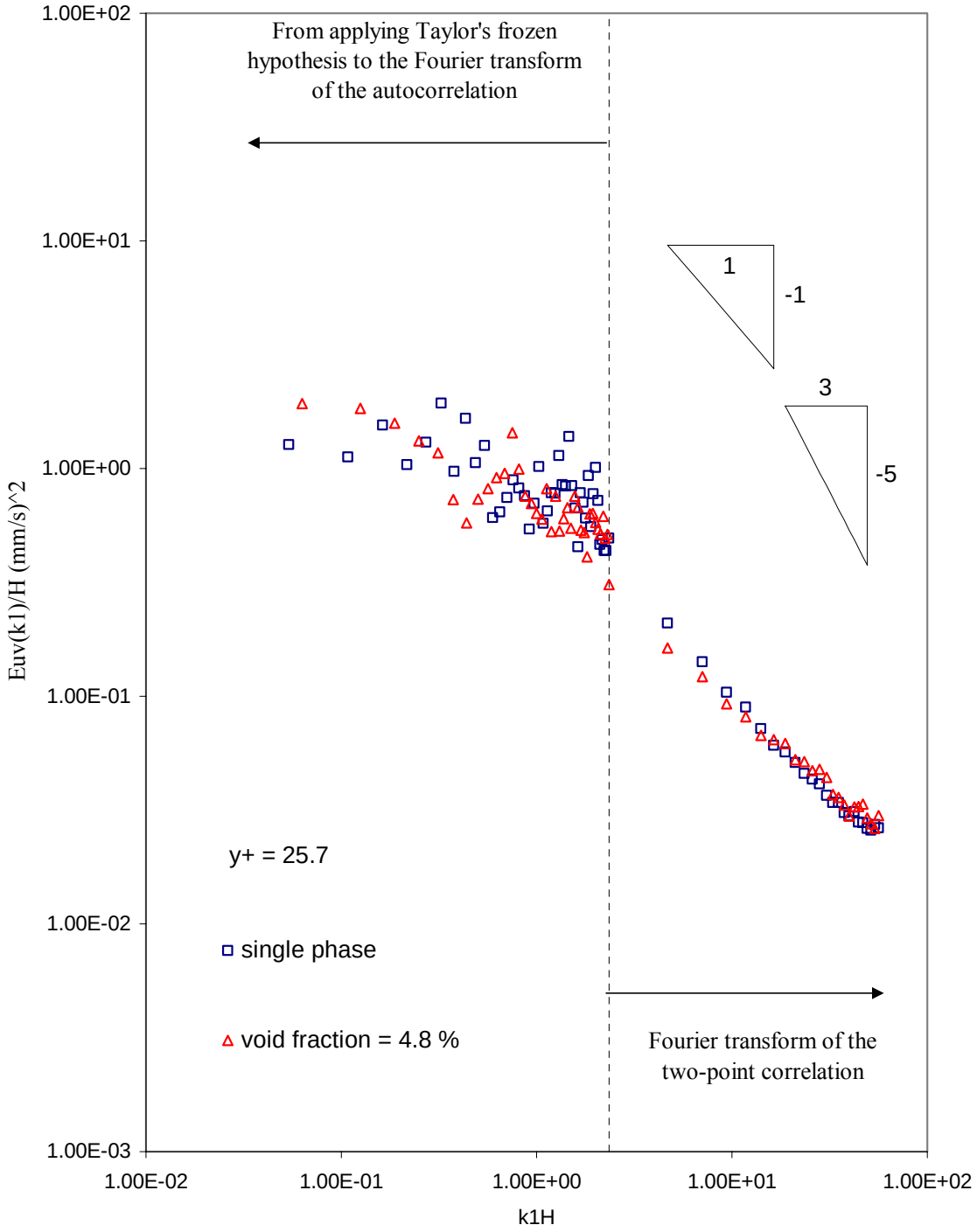

FIGURE D-8. Dimensional $E_{uv}(k_1)$ spectra versus non-dimensional wavenumber at y/H = 0.077 (without any correction).

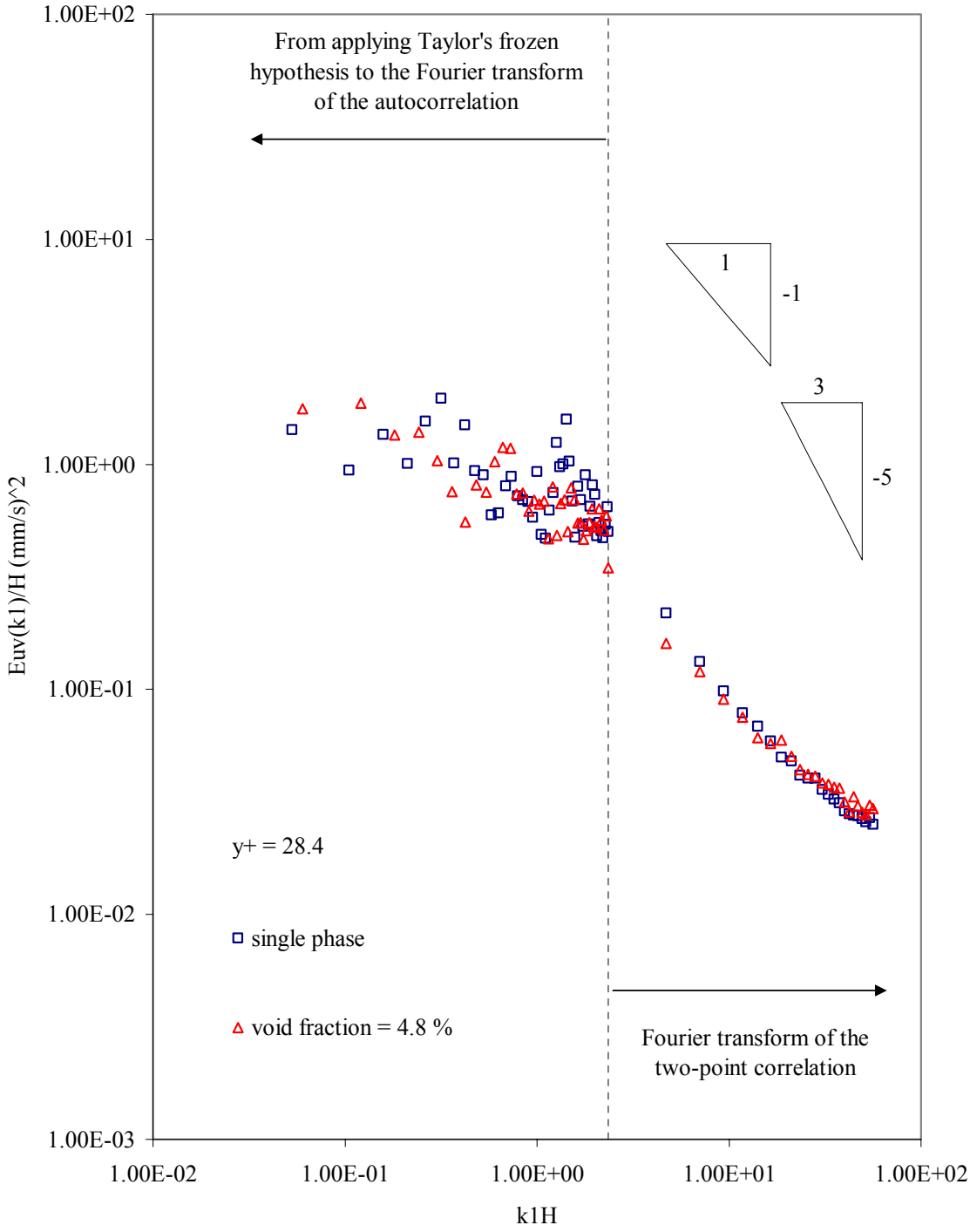

FIGURE D-9. Dimensional $E_{uv}(k_1)$ spectra versus non-dimensional wavenumber at y/H = 0.085 (without any correction).

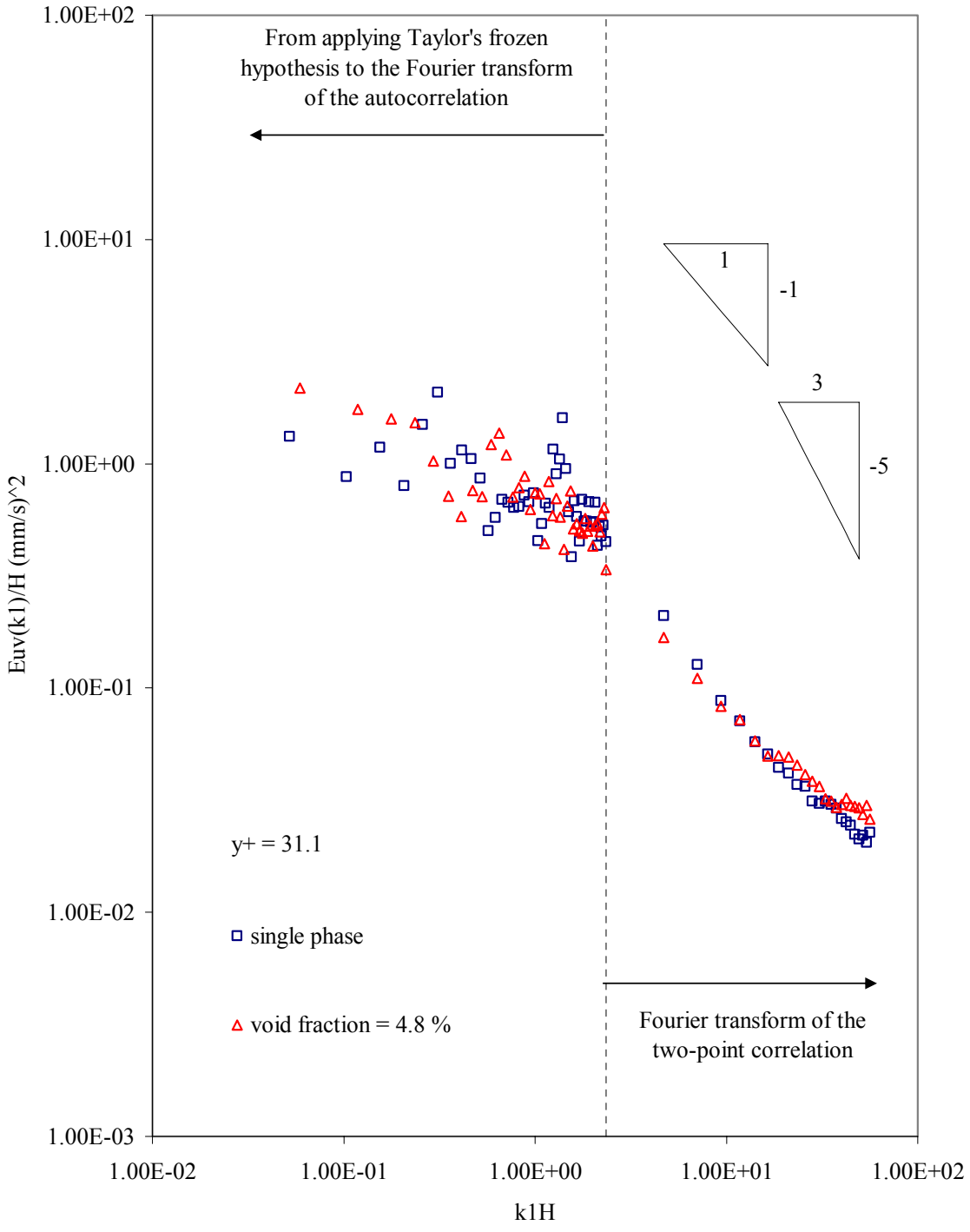

FIGURE D-10. Dimensional $E_{uv}(k_1)$ spectra versus non-dimensional wavenumber at y/H = 0.094 (without any correction).

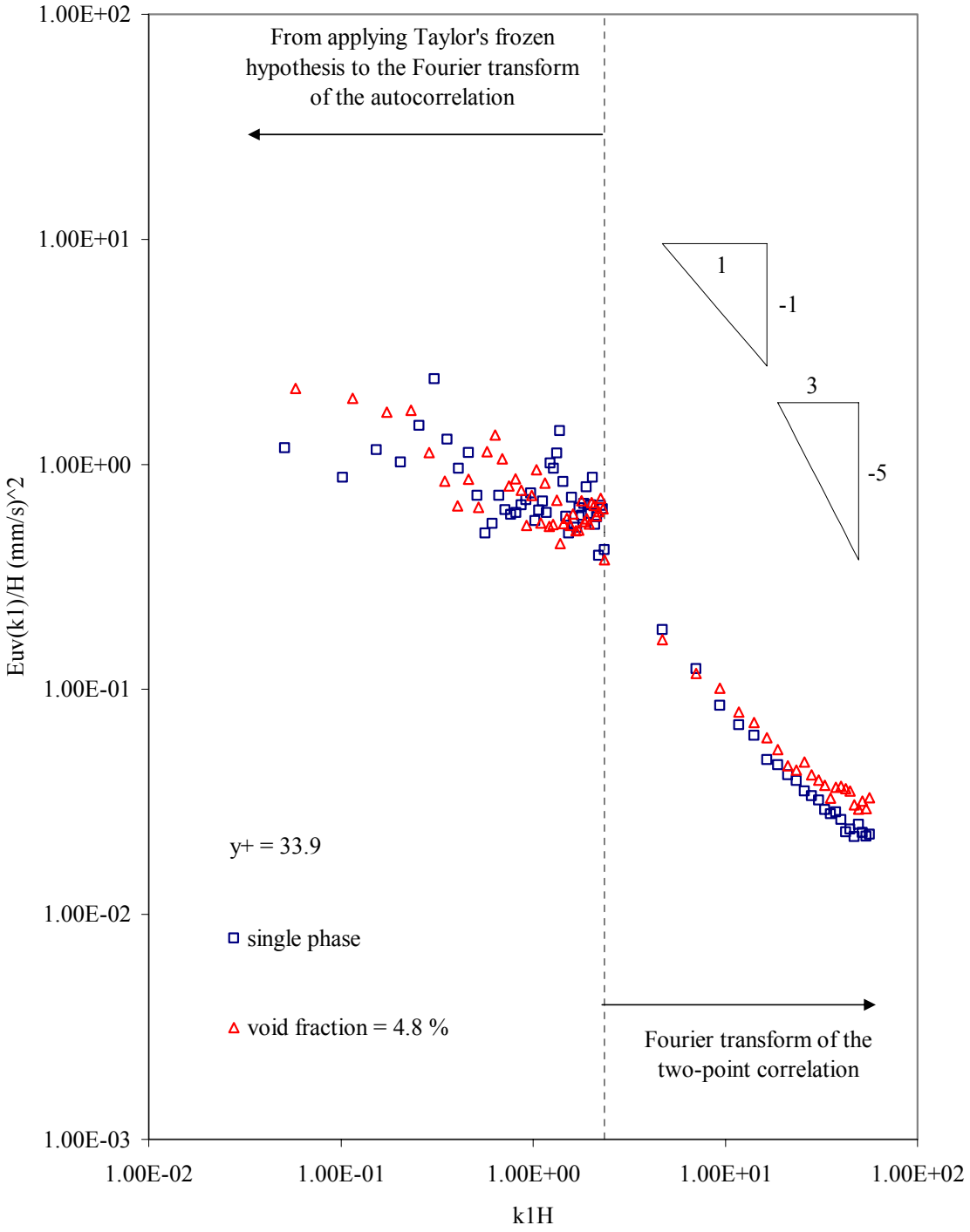

FIGURE D-11. Dimensional $E_{uv}(k_1)$ spectra versus non-dimensional wavenumber at y/H = 0.1 (without any correction).

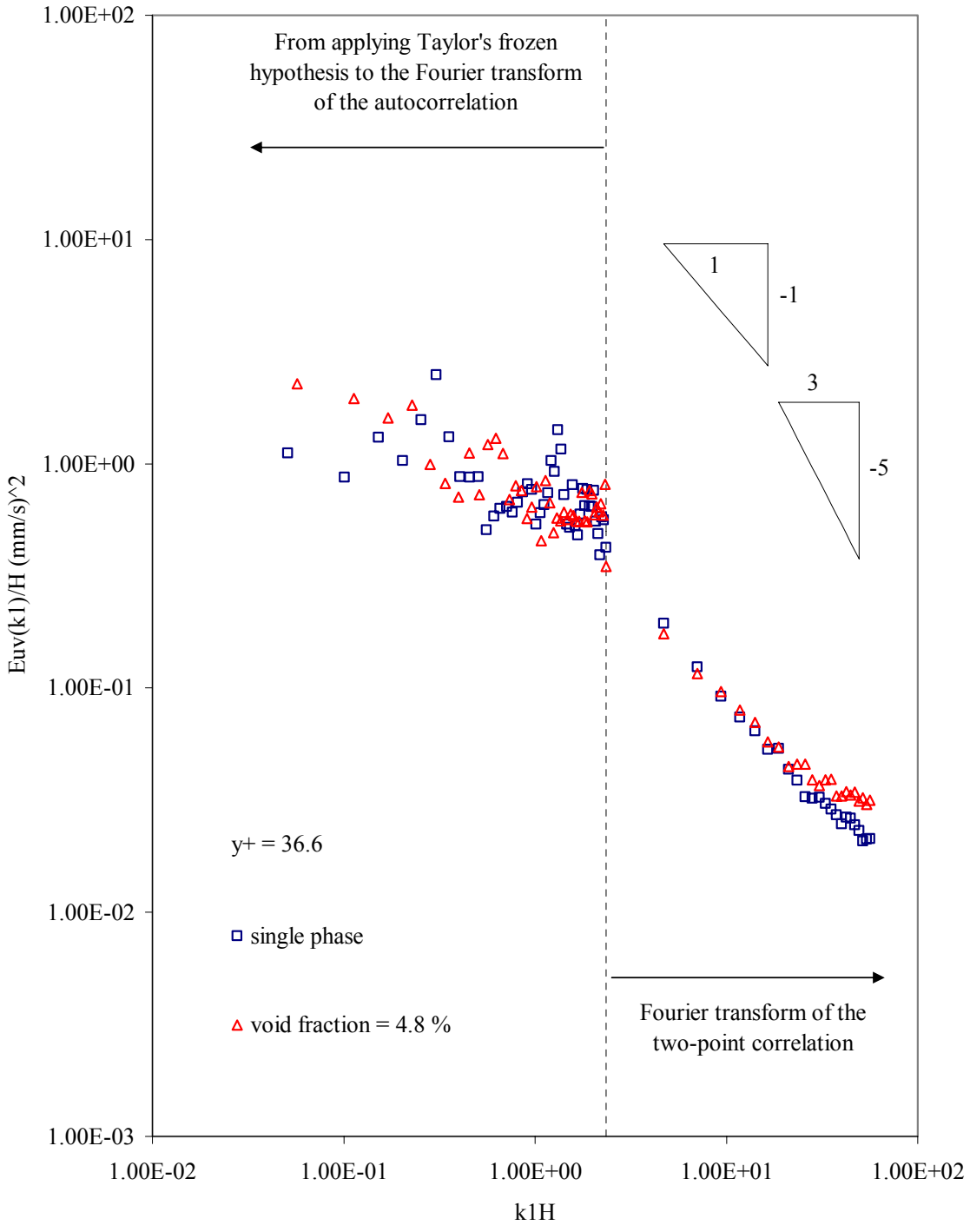

FIGURE D-12. Dimensional $E_{uv}(k_1)$ spectra versus non-dimensional wavenumber at y/H = 0.11 (without any correction).

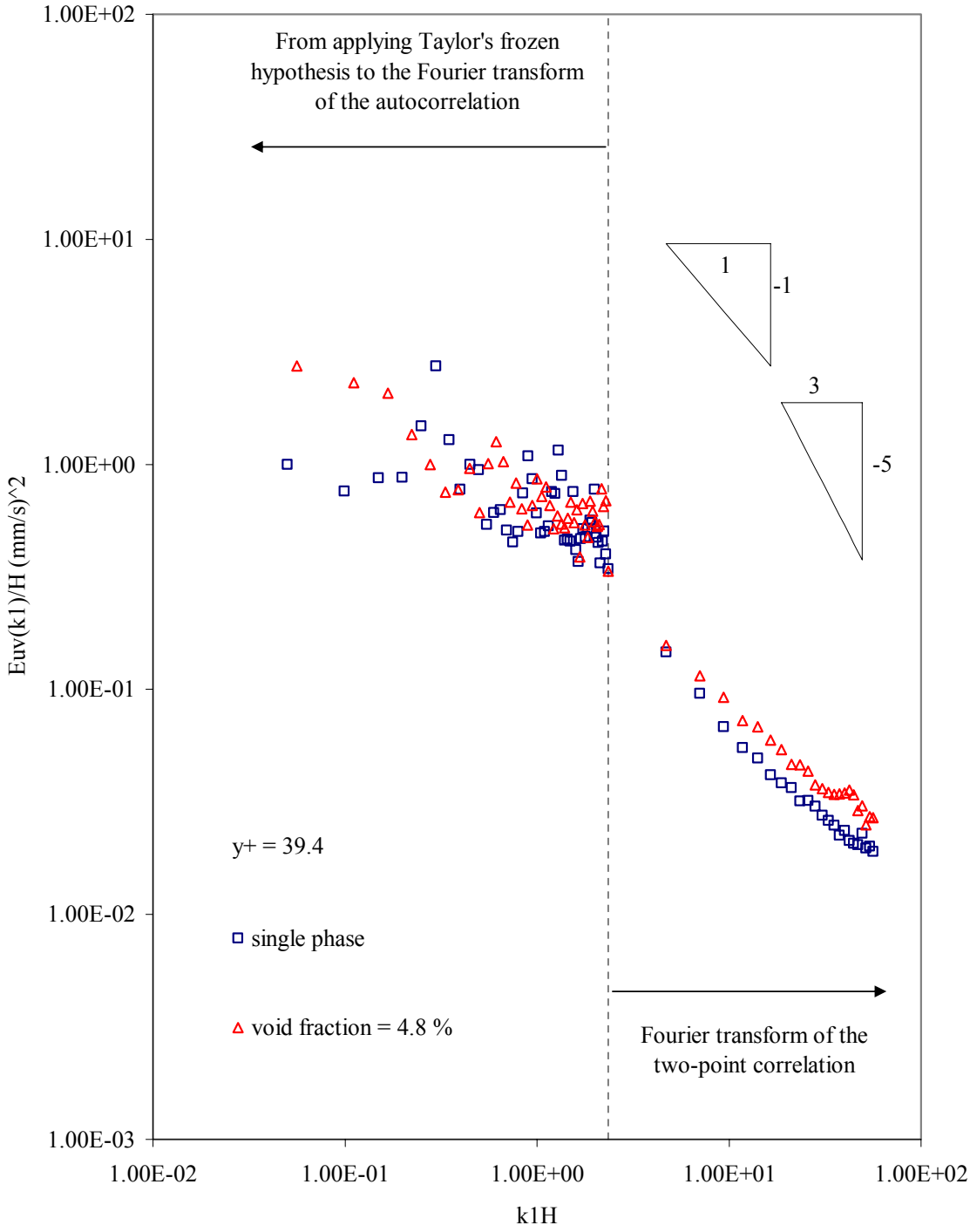

FIGURE D-13. Dimensional $E_{uv}(k_1)$ spectra versus non-dimensional wavenumber at y/H = 0.118 (without any correction).

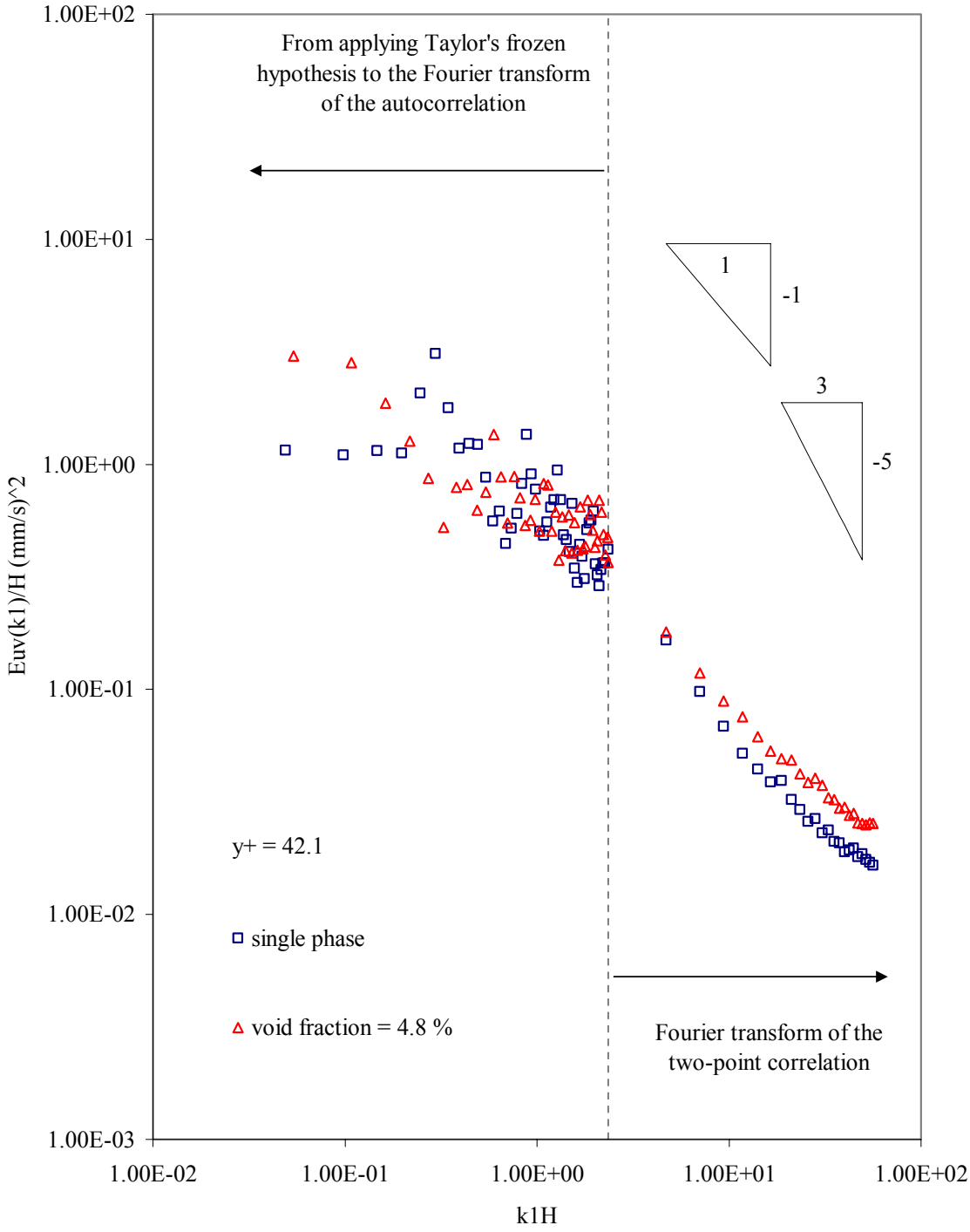

FIGURE D-14. Dimensional $E_{uv}(k_1)$ spectra versus non-dimensional wavenumber at y/H = 0.127 (without any correction).

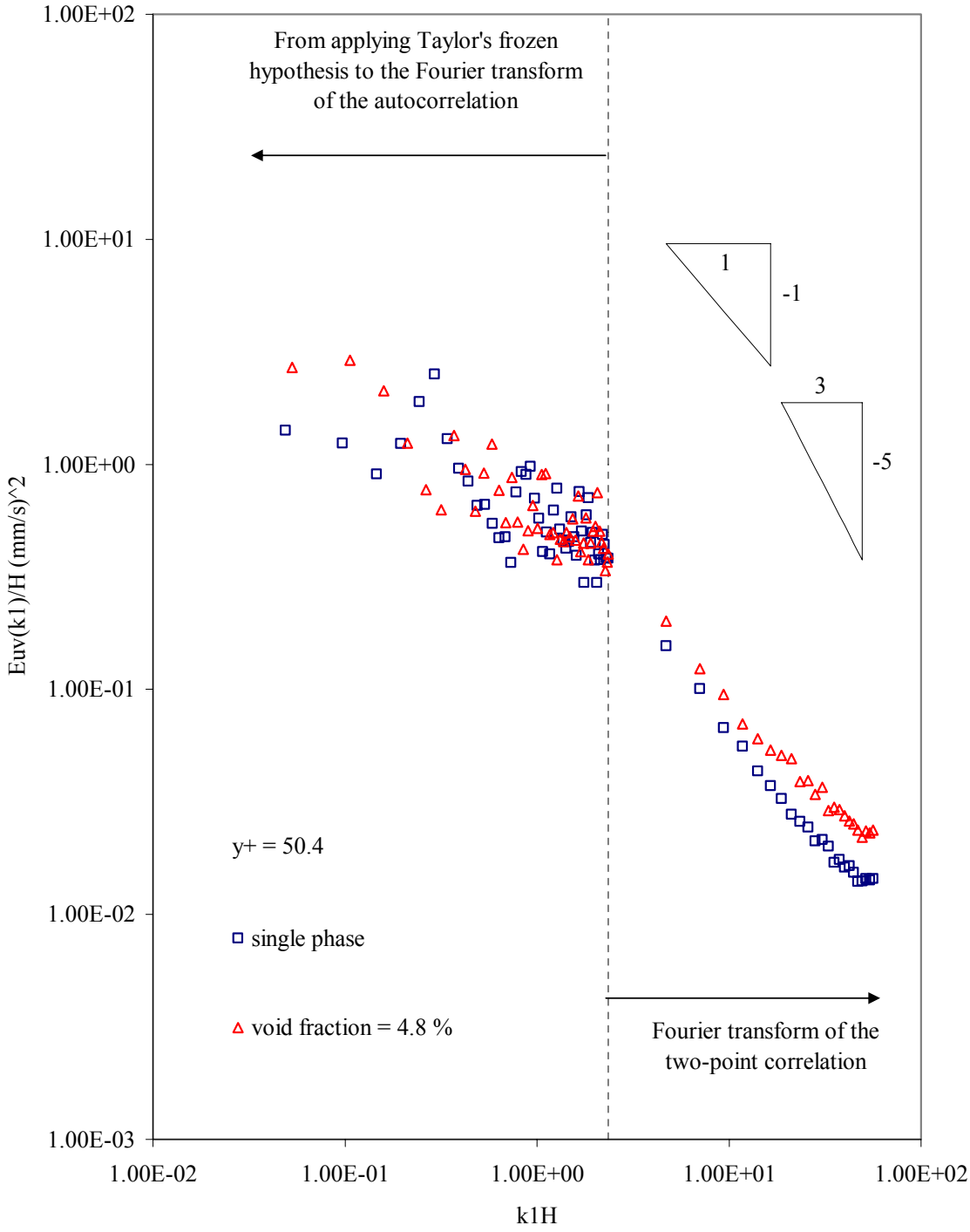

FIGURE D-15. Dimensional $E_{uv}(k_1)$ spectra versus non-dimensional wavenumber at y/H = 0.15 (without any correction).

VITA

Jose Alfredo Jimenez Bernal was born December 14, 1974 in Acapulco, Guerrero (Mexico) to Maria Asuncion Bernal Ortega and Tomas Jimenez Vazquez. He is married to Claudia Del Carmen Gutierrez Torres.

He attended High School Center of Technological Services No. 14 in Acapulco (CBtis 14) and graduated in 1989. He received a B.S. in mechanical and electrical engineering from Acapulco Institute of Technology (Mexico) under the direction of Professor Javier Gutierrez Avila and graduated as salutatorian in 1997. He received his M.S. in mechanical engineering from National Polytechnic Institute (Mexico) under the direction of Professor Pedro Quinto Diez in 2000 and his Ph.D. in mechanical engineering from Texas A&M University in 2004 under the direction of Professor Yassin A. Hassan.

He can be contacted through Dr. Yassin A. Hassan at Texas A&M University, Nuclear Engineering Department, College Station, Texas 77843-3123.